# Synthesis, Structure, and Physical Properties of Novel Iron Oxides Prepared by Topotactic Reactions

Takafumi Yamamoto

2012

# Contents

# *General Introduction*

## Background of This Work

### Iron

Given iron's abundance and low toxicity, exploring fundamentally new iron-based materials with new or improved functionalities is a significant issue. As shown below, iron-based materials show many attractive properties (e.g. ferro(ferri)magnetism, multiferroicity, spin state transition, and superconductivity), because of a wide variety of electronic configuration and coordination of iron.

The most of irons in solids are in divalent and trivalent states. In terms of binary iron oxides, $Fe_2O_3$, $Fe_3O_4$ and FeO are known. There are several kinds of $Fe^{3+}{}_2O_3$ with different crystal structures. Hematite $\alpha$-$Fe_2O_3$ is the most typical one and adopts a corundum structure with an octahedral coordinated iron (Figure 1a) [1]. $\varepsilon$-$Fe_2O_3$, which is relatively rare phase, has orthorhombic structure with an octahedral and tetrahedral coordinated irons (Figure 1b). Nanocrystal of $\varepsilon$-$Fe_2O_3$ has been recently synthesized by Ohkoshi and coworkers, and shows giant coercive field [2--4]. Magnetite $Fe_3O_4$ adopts a spinel structure in which $Fe^{3+}$ occupies the tetrahedral sites, whilst the octahedral sites are occupied by both $Fe^{3+}$ and $Fe^{2+}$ ions (Figure 1c) [5]. It exhibits thermally induced electron delocalization at the octahedral sites, resulting in metallic behavior, but becomes an insulator below 125 K due to the so-called Verway transition [6]. Wüstite $Fe_{1-y}O$ with a rock salt structure (Figure 1d) is known as a nonstoichiometric compound [7]. Due to the interest in earth science, the high pressure

behavior of Wüstite has been extensively studied [8]. It was revealed that Wüstite shows high spin to low spin transition and structural transition under high pressure [9,10].

Irons in divalent or trivalent states are also typically found in the many complex iron oxides. Ilmenite $FeTiO_3$ (Figure 2a) [11] and fayalite $Fe_2SiO_4$ (Figure 2b) [12] are common minerals with divalent iron in octahedral coordination. The high pressure study is of interest in earth science since their elements are major components of Earth's interior [13,14]. Brownmillerite $SrFeO_{2.5}$ consists of alternate stacking of an octahedral layer and a tetrahedral layer (Figure 2c). It is known as oxygen ion conductor at low temperatures (< 600K) [15]. Hexaferrites (with $Fe^{3+}$), which shows ferrimagnetic order with high magnetic anisotropy, have long been used in technological applications such as permanent magnets and microwave devices. Moreover, some hexaferrites recently have attracted attention for future multiferroic devises [16--18].

Superconductivity in iron-based materials is one of the most active research fields for solid state chemists and physicists in recent years. In 2008, Hosono and coworkers discovered superconductivity in fluorine-doped LaFeAsO at transition temperature $T_c$ = 26 K [19]. The crystal structure of LaFeAsO contains $Fe^{2+}As$ layers with tetrahedrally coordinated iron atoms in a tetragonal lattice, and these layers alternate with LaO layers along the *c*-axis (Figure 3). Applying pressure increases the $T_c$ up to 43 K [20] and replacement of the nonmagnetic La by magnetic rare earth elements substantially increases $T_c$ to 55 K [21].

**Perovskite Oxides with High Valence State of $Fe^{4+}$**

Not only typical irons but also unusual irons show interesting properties. There have been known a small class of perovskite oxides that contain iron in an unusually high valence state of $Fe^{4+}$ like $AFeO_3$ (A = Ca, Sr; Figure 4a, b). Their electronic properties are peculiar.

Normal $Fe^{2+}$ and $Fe^{3+}$ oxides such as $Fe^{2+}O$ and $LaFe^{3+}O_3$ are antiferromagnetic insulators governed by the Kanamori-Goodenough rule, while these $Fe^{4+}$ oxides exhibit a shift toward metallicity and ferromagnetism. $SrFe^{4+}O_3$ is a cubic metal and shows a proper screw spin structure with a propagation vector along [111] [22]. $CaFe^{4+}O_3$ shows a metal-to-insulator transition induced at 290 K by charge-disproportionation to $Fe^{3+}$ and $Fe^{5+}$ [23]. An A-site ordered perovskite family $ACu_3Fe_4O_{12}$ (A = Sr, Ca, La) [24--26] with $Fe^{4+}$ has been recently synthesized by using high pressure and high temperature technique (Figure 4c). They show novel properties, such as negative thermal expansion [24] and intersite charge transfer [25]. It is notable here that $Fe^{3+}\underline{L}$ ($t_2g^3eg^2\underline{L}$, $S = 2$), i.e., a charge transfer from O to Fe, is the realistic picture of $Fe^{4+}$ in these oxides. The $Fe^{4+}$ compounds are thus quite attractive from both experimental and theoretical view points [27], but the knowledge of the $Fe^{4+}$ physics is still far from satisfactory due to few model materials.

**Square Planar Iron Oxides**

In 2007, Tsujimoto et al. have synthesized an infinite layer iron oxide $SrFeO_2$ with square planar coordinated iron (Figure 5a) by topotactic reaction of perovskite $SrFeO_3$ using $CaH_2$ as a reducing agent [28]. Such metal hydride reduction for perovskite oxides was initiated by Rosseinsky and coworkers, who obtained square planar nickel oxide $LaNiO_2$ from perovskite $LaNiO_3$ by using NaH at 200 ˚C [29]. Since then, many highly reduced oxides were reported by the metal hydride reduction. Examples includes $Sr_3LaFe_{1.5}Co_{1.5}O_{7.5}$ [30], $La_3Ni_2O_6$ [31], $Y_2Ti_2O_6$, $REBaCo_2O_{5-x}$ (RE = Y, La) [32], $BaMnO_{2+x}$ [33].

In spite of the fact that an iron in materials exclusively adopts nonplanar coordination (i.e. $FeO_4$ tetrahedra, $FeO_6$ octahedra, $FeO_5$ pyramid and $FeO_5$ trigonal bypyramid), $SrFeO_2$ bears $FeO_4$ square planar square coordination. Surprisingly, $SrFeO_2$ allow a large amount of

chemical substitution without any distortion, up to 80% for (Sr,Ca)$FeO_2$ [34,35], and up to 30% for Sr(Fe,M)$O_2$ (M = Mn, Co). A further substitution of Ca results in a distortion of the $FeO_4$ square planar coordination towards tetrahedron (Figure 5b) [35]. $Sr_3Fe_2O_5$ (Figure 5c) [36] and $Sr_3Fe_2O_4Cl_2$ (Figure 5d) [37], which share with the structural feature of $SrFeO_2$, have been also synthesized. However, all the reported square planar coordinated iron oxides have been exclusively composed of a single iron site [28,35--39], thereby limiting variations in terms of Fe-O extended networks.

$SrFeO_2$ is an insulator and exhibits magnetic order of the *G*-type, with a Néel temperature ($T_N$) as high as 473 K [28]. Most importantly, the square planar coordinated iron forms more covalent bonds (to the oxide ligands and to neighboring iron ions) [40--42], than with iron in other coordination geometries. This characteristic is crucial for developing new and improved properties that work at high temperatures (thus important for future applications). Therefore, exploring new square planar coordinated iron oxides is of great importance.

**High Pressure Studies**

Pressure is a good parameter to tune structural and physical properties of solids since one can control atomic distances by external pressure. One important phenomenon under high pressure is a structural transition. By applying pressure, structural transitions occur in many compounds because a solid prefers denser crystal structure under high pressure. A structural modification sometimes results in new or improved properties, so that exploring a new crystal phase under high pressure is interesting not only in earth science but also in solid state science. For example, an elemental iron exhibits the pressure induced structural transition from body centered cubic (bcc) structure to hexagonal close packed (hcp) structure

accompanied with a magnetic transition from ferromagnetic to nonmagnetic state. The high-pressure nonmagnetic phase undergoes superconducting transition below 2 K [43].

A spin state transition is often induced by pressure. One of the reasons is the difference in volume of the high spin and the low spin species; high pressure often results in a high spin state to a low spin state transition since low spin species have denser than a high pressure one [44]. Among the metal ions that exhibit spin state transition, the largest numbers have been found for those with octahedral coordination. Examples includes (Mg,Fe)O [45], FeS [46], $(Mg,Fe)SiO_3$ [47], $CaFeO_3$ [48], and $Ca_2FeO_4$ [49].

However, a recently discovered pressure-induced spin transition in $SrFeO_2$ at $P_c$ = 33 GPa has several aspects distinct from conventional spin state transitions [50]. First, $SrFeO_2$ adopts a square planar coordination around iron (Figure 5a) [28], thus representing the first spin state transition in a four-fold coordinated metal center. Second, it is not a typical transition from a high-spin state ($S$ = 2) to a low-spin state ($S$ = 0), but to an intermediate-spin state ($S$ = 1). It is accompanied at the same time with an insulator-to-metal (I-M) and an antiferromagnetic-to-ferromagnetic (AFM-FM) transition. Although this unusual spin state transition is interested in the points mentioned above, the mechanism was an open question in contrast to conventional spin state transition.

**Outline of This Work**

This thesis reports (i) synthesis, structure, and physical properties of new square planar coordinated iron oxides obtained by topotactic reduction, (ii) structure and physical properties of square planar coordinated iron oxides under high pressure, (iii) synthesis, structure, and physical properties of new perovskite iron oxide with high valence state of $Fe^{4+}$ obtained by topotactic oxidation.

In Chapter 1, the A-site substitution effect on structural, thermal and magnetic properties of the infinite layer iron oxide $AFeO_2$ (A = alkali-earth elements) was studied. It is revealed that the Ba substitution is tolerable up to 30 %, although Ca can be substituted up to 100%. The Ba substitution shows little influence on the magnetic properties, in contrast to an expectation from the first principles calculations. The temperature, at which the oxidation from $AFeO_2$ to $AFeO_{2.5}$ occurs, and its transformation rate show a wide variation tuned solely by the out-of-plane distance.

In Chapter 2, new oxygen deficient perovskite $(Sr_{1-x}Ba_x)FeO_2$ ($0.4 \leq x \leq 1.0$) was reported. $(Sr_{1-x}Ba_x)FeO_2$ ($0.4 \leq x \leq 1.0$) has been successfully obtained by topotactic reduction with using $CaH_2$ and NaH. The new structure ($BaFeO_2$ structure) revealed that square planar coordination can coexist with other three- to six-fold coordination geometries. Powder neutron diffraction measurements revealed a *G*-type magnetic order with a drastic decrease of the Néel temperature compared to $SrFeO_2$, presumably due to the effect of oxygen disorder/defects. We also performed La substitution at the Ba-site, and found that the oxygen vacancies act as a flexible sink to accommodate heterovalent doping without changing the Fe oxidation and spin state, demonstrating the robustness of this new structure against cation substitution.

In Chapter 3, the effect of lanthanoid (Ln = Nd, Sm, Eu, Ho) substitution on the structural and magnetic properties of the infinite layer iron oxide $SrFeO_2$ was investigated. All the lanthanides examined have a similar solubility limit of ca. 30% but failed to inject electrons in the $FeO_2$ layer for different reasons. For Ln = Nd, Sm, and Ho, the substitution resulted in partial occupation of apical oxygen sites between $FeO_2$ layers to give a charge-compensated composition of $(Sr_{1-x}Ln_x)Fe^{2+}O_{2+x/2}$. A significant reduction of the Néel temperature is observed. In contrast, $(Sr_{1-x}Eu_x)FeO_2$ adopts the ideal infinite layer structure by forcing the europium ion to be divalent and the magnetic property hardly changes.

In Chapter 4, the pressure effect on the structural, magnetic and transport properties of the two-legged spin ladder $Sr_3Fe_2O_5$ have been studied. When pressure was applied, this material first exhibited a structural transition from *Immm* to *Ammm* at $P_s = 30 \pm 2$ GPa. This transition involves a phase shift of the ladder blocks from (1/2,1/2,1/2) to (0,1/2,1/2), by which a rock-salt-type (*B*1) SrO block with a seven-fold coordination around Sr changes into a CsCl-type (*B*2) block with eight-fold coordination, allowing a significant reduction of volume. However, the $S = 2$ antiferromagnetic state stays the same. Next, a spin state transition from $S = 2$ to $S = 1$, along with an AFM-FM transition was observed at $P_c = 34 \pm 2$ GPa, similar to that of $SrFeO_2$. A sign of an I-M transition was also observed at pressure around $P_c$. These results suggest a generality of the spin state transition in square planar coordinated $S = 2$ irons of *n*-legged ladder series $Sr_{n+1}Fe_nO_{2n+1}$ ($n = 1, 2, 3,\ldots$).

In Chapter 5, pressure induced structural transition of $A_2MO_3$ (A = Sr, Ca; M = Cu, Pd) with the intergrowth structure of rock salt (*B*1) AO blocks and corner-shared $MO_2$ square-planar blocks have been investigated. All the examined compounds exhibit a structural transition at $P_s = 29 \sim 41$ GPa involving a change in the A-site geometry to an 8-fold *B*2 coordination. This observation demonstrated that pressure induced structural transition in

$Sr_3Fe_2O_5$ independently occurs without respect to the spin state transition (and the AFM-FM, I-M transitions). Moreover, this study also demonstrated that the *B*1-to-*B*2 transition generally occurs in the intergrowth structures, as found in binary oxides or chalcogenides. An empirical relation of $P_s$ and the $R_c/R_a$ for the binary system holds well for the intergrowth structure also, which means that $P_s$ is predominantly determined by the rock salt blocks. However, a large deviation from the relation is found in $LaSrNiO_{3.4}$ where oxygen atoms partially occupy the apical site of the $MO_4$ square plane. We predict furthermore the occurrence of the same structural transition for Ruddlesden-Popper-type layered perovskite oxides $(AO)(AMO_3)_n$, under higher pressures.

In Chapter 6, a new perovskite oxide $BaFeO_3$ with an unusually high valence state of $Fe^{4+}$ was investigated. $BaFeO_3$ was synthesized by topotactic oxidation with using $O_3$ gas. $BaFeO_3$ shows a proper screw spin structure along [100] having a different propagation vector from that of $SrFeO_3$ with [111]. Furthermore, we have found that this material exhibits a complete saturation magnetization ($3.5\mu_B$) by the application of a tiny magnetic field (~0.3 T). Thus, this material represents the first example to show ferromagnetism at ambient pressure.

## References


[1] L. Pauling and S. B. Hendricks, J. Am. Chem. Soc. 47 (1925) 781.

[2] J. Jin, S. Ohkoshi, and K. Hashimoto, Adv. Mater. 16 (2004) 48.

[3] S. Ohkoshi, S. Sakurai, J. Jin, and K. Hashimoto, J. Appl. Phys. 97 (2005) 10K312.

[4] S. Ohkoshi, S. Kuroki, S. Sakurai, K. Matsumoto, K. Sato, and S. Sasaki, Angew. Chem. Int. Ed. 46 (2007) 8392.

[5] F. J. Berry, S. Skinner, and M. F. Thomas, J. Phys. : Condens. Matter 10 (1998) 215.

[6] E. Verwey, Nature 144 (1939) 327.

[7] B. Willis and H. Rooksby, Acta Crystallogr. 6 (1953) 827.

[8] H. Ozawa, F. Takahashi, K. Hirose, Y. Ohishi, and N. Hirao, Science 334 (2011) 792.

[9] M. Pasternak, R. Taylor, R. Jeanloz, X. Li, J. Nguyen, and C. McCammon, Phys. Rev. Lett. 79 (1997) 5046.

[10] J. F. Lin, V. V. Struzhkin, S. D. Jacobsen, M. Y. Hu, P. Chow, J. Kung, H. Liu, H. Mao, and R. J. Hemley, Nature 436 (2005) 377.

[11] B. A. Wechsler and C. T. Prewitt, Am. Mineral. 69 (1984) 176.

[12] J. R. Smyth, Am. Mineral. 60 (1975) 1092.

[13] S. H. Kirby, W. B. Durham, and L. A. Stern, Science 252 (1991) 216.

[14] L. Dobrzhinetskaya, H. W. Green II, and S. Wang, Science 271 (1996) 1841.

[15] W. Paulus, H. Schober, S. Eibl, M. Johnson, T. Berthier, O. Hernandez, M. Ceretti, M. Plazanet, K. Conder, and C. Lamberti, J. Am. Chem. Soc. 130 (2008) 16080.

[16] S. Ishiwata, Y. Taguchi, H. Murakawa, Y. Onose, and Y. Tokura, Science 319 (2008) 1643.

[17] S. H. Chun, Y. S. Chai, Y. S. Oh, D. Jaiswal-Nagar, S. Y. Haam, I. Kim, B. Lee, D. H. Nam, K. T. Ko, and J. H. Park, Phys. Rev. Lett. 104 (2010) 37204.

[18] Y. Kitagawa, Y. Hiraoka, T. Honda, T. Ishikura, H. Nakamura, and T. Kimura, Nat. Mater. 9 (2010) 797.

[19] Y. Kamihara, T. Watanabe, M. Hirano, and H. Hosono, J. Am. Chem. Soc. 130 (2008) 3296.

[20] H. Takahashi, K. Igawa, K. Arii, Y. Kamihara, M. Hirano, and H. Hosono, Nature 453 (2008) 376.

[21] R. Zhi-An, L. Wei, Y. Jie, Y. Wei, S. Xiao-Li, C. Guang-Can, D. Xiao-Li, S. Li-Ling, Z. Fang, and Z. Zhong-Xian, Chin. Phys. Lett. 25 (2008) 2215.

[22] T. Takeda, Y. Yamaguchi, and H. Watanabe, J. Phys. Soc. Jpn. 33 (1972) 967.

[23] P. Woodward, D. Cox, E. Moshopoulou, A. Sleight, and S. Morimoto, Phys. Rev. B 62 (2000) 844.

[24] I. Yamada, K. Tsuchida, K. Ohgushi, N. Hayashi, J. Kim, N. Tsuji, R. Takahashi, M. Matsushita, N. Nishiyama, and T. Inoue, Angew. Chem. Int. Ed. 123 (2011) 6709.

[25] Y. Long, N. Hayashi, T. Saito, M. Azuma, S. Muranaka, and Y. Shimakawa, Nature 458 (2009) 60.

[26] I. Yamada, K. Takata, N. Hayashi, S. Shinohara, M. Azuma, S. Mori, S. Muranaka, Y. Shimakawa, and M. Takano, Angew. Chem. Int. Ed. 120 (2008) 7140.

[27] M. Mostovoy, Phys. Rev. Lett. 94 (2005) 137205.

[28] Y. Tsujimoto, C. Tassel, N. Hayashi, T. Watanabe, H. Kageyama, K. Yoshimura, M. Takano, M. Ceretti, C. Ritter, and W. Paulus, Nature 450 (2007) 1062.

[29] M. Hayward, M. Green, M. Rosseinsky, and J. Sloan, J. Am. Chem. Soc. 121 (1999) 8843.

[30] A. Bowman, M. Allix, D. Pelloquin, and M. J. Rosseinsky, J. Am. Chem. Soc. 128 (2006) 12606.

[31] V. V. Poltavets, K. A. Lokshin, S. Dikmen, M. Croft, T. Egami, and M. Greenblatt, J. Am. Chem. Soc. 128 (2006) 9050.

[32] J. Seddon, E. Suard, and M. A. Hayward, J. Am. Chem. Soc. 132 (2010) 2802.

[33] J. Hadermann, A. M. Abakumov, J. J. Adkin, and M. A. Hayward, J. Am. Chem. Soc. 131 (2009) 10598.

[34] C. Tassel, T. Watanabe, Y. Tsujimoto, N. Hayashi, A. Kitada, Y. Sumida, T. Yamamoto, H. Kageyama, M. Takano, and K. Yoshimura, J. Am. Chem. Soc. 130 (2008) 3764.

[35] C. Tassel, J. M. Pruneda, N. Hayashi, *et al*, J. Am. Chem. Soc. 131 (2009) 221.

[36] H. Kageyama, T. Watanabe, Y. Tsujimoto, *et al*, Angew. Chem. Int. Ed. 47 (2008) 5740.

[37] E. Dixon and M. A. Hayward, Inorg. Chem. 49 (2010) 9649.

[38] L. Seinberg, T. Yamamoto, C. Tassel, *et al*, Inorg. Chem. 50 (2011) 3988.

[39] T. Yamamoto, Z. Li, C. Tassel, *et al*, Inorg. Chem. 49 (2010) 5957.

[40] K. Tomiyasu, H. Kageyama, C. Lee, *et al*, J. Phys. Soc. Jpn. 79 (2010) 034707.

[41] J. M. Pruneda, J. Íñiguez, E. Canadell, H. Kageyama, and M. Takano, Phys. Rev. B 78 (2008) 115101.

[42] H. J. Xiang, S. H. Wei, and M. H. Whangbo, Phys. Rev. Lett. 100 (2008) 167207.

[43] K. Shimizu, T. Kimura, S. Furomoto, K. Takeda, K. Kontani, Y. Onuki, and K. Amaya, Nature 412 (2001) 316.

[44] P. Gütlich, Y. Garcia, and H. A. Goodwin, Chem. Soc. Rev. 29 (2000) 419.

[45] J. Badro, G. Fiquet, F. Guyot, J. P. Rueff, V. V. Struzhkin, G. Vankó, and G. Monaco, Science 300 (2003) 789.

[46] J. P. Rueff, C. C. Kao, V. V. Struzhkin, J. Badro, J. Shu, R. Hemley, and H. Mao, Phys. Rev. Lett. 82 (1999) 3284.

[47] J. Badro, J. P. Rueff, G. Vankó, G. Monaco, G. Fiquet, and F. Guyot, Science 305 (2004) 383.

[48] M. Takano, S. Nasu, T. Abe, K. Yamamoto, S. Endo, Y. Takeda, and J. B. Goodenough, Phys. Rev. Lett. 67 (1991) 3267.

[49] M. Merlini, M. Hanfland, M. Gemmi, S. Huotari, L. Simonelli, and P. Strobel, Am. Mineral. 95 (2010) 200.

[50] T. Kawakami, Y. Tsujimoto, H. Kageyama, *et al*, Nat. Chem. 1 (2009) 371.

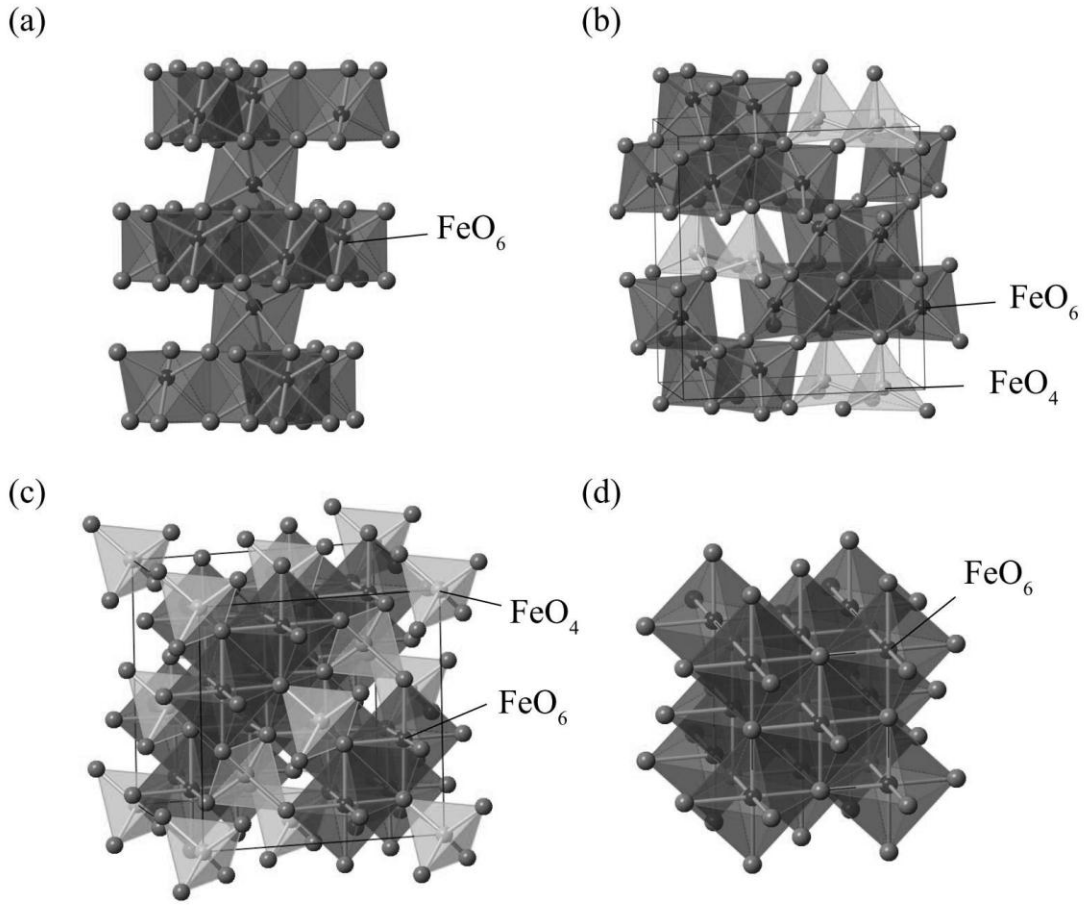


**Figure 1**. The structures of Hematite α-$Fe_2O_3$(a), ε-$Fe_2O_3$ (b), Magnetite $Fe_3O_4$ (c), Wüstite $Fe_{1-y}O$ (d).

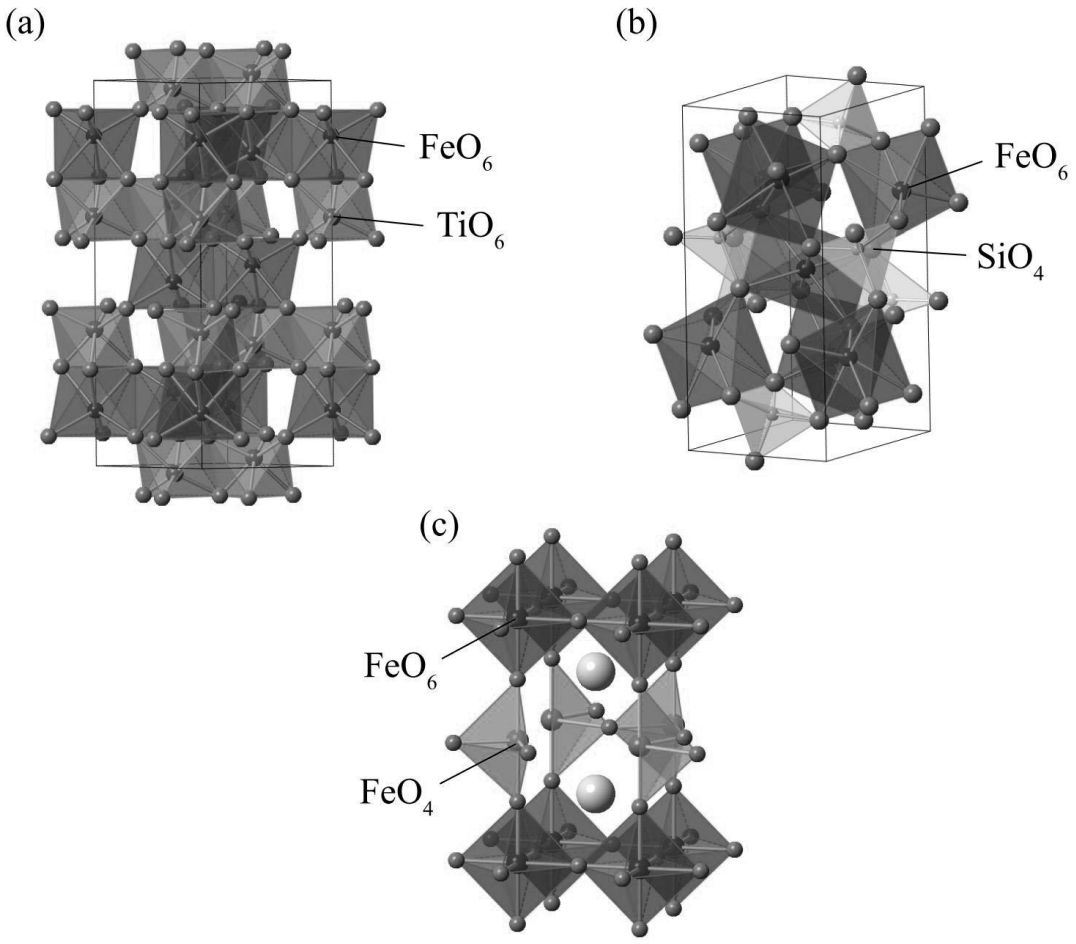


**Figure 2**. The structures of Ilmenite $FeTiO_3$ (a), fayalite $Fe_2SiO_4$ (2b), Brownmillerite $SrFeO_{2.5}$ (c).

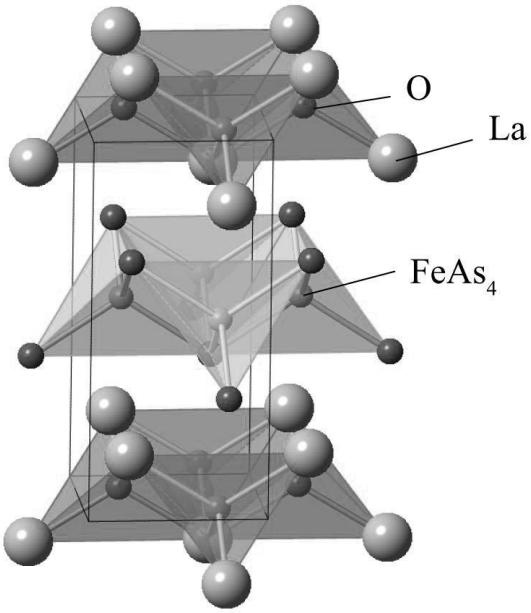


**Figure 3**. The structures of LaFeAsO.

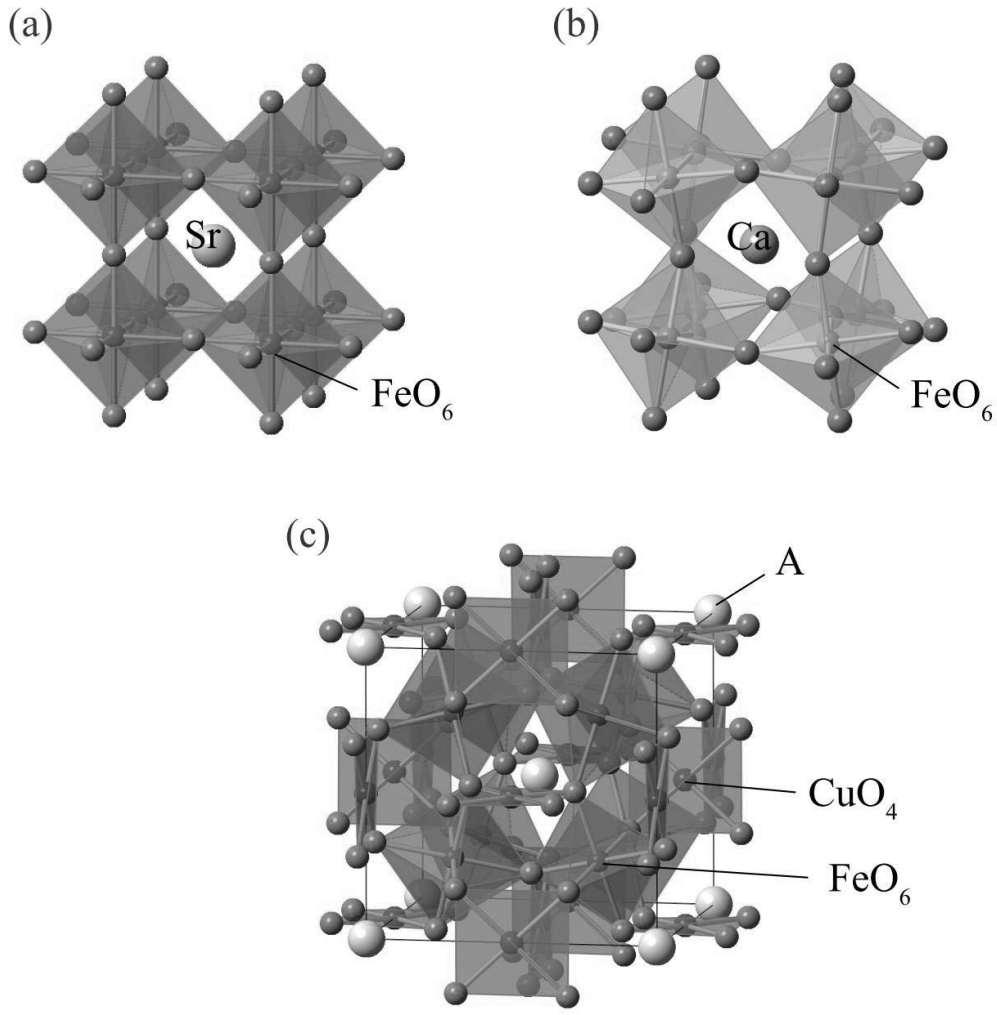


**Figure 4**. The structures of $SrFeO_3$ (a), $CaFeO_3$ (b), $ACu_3Fe_4O_{12}$ (c).

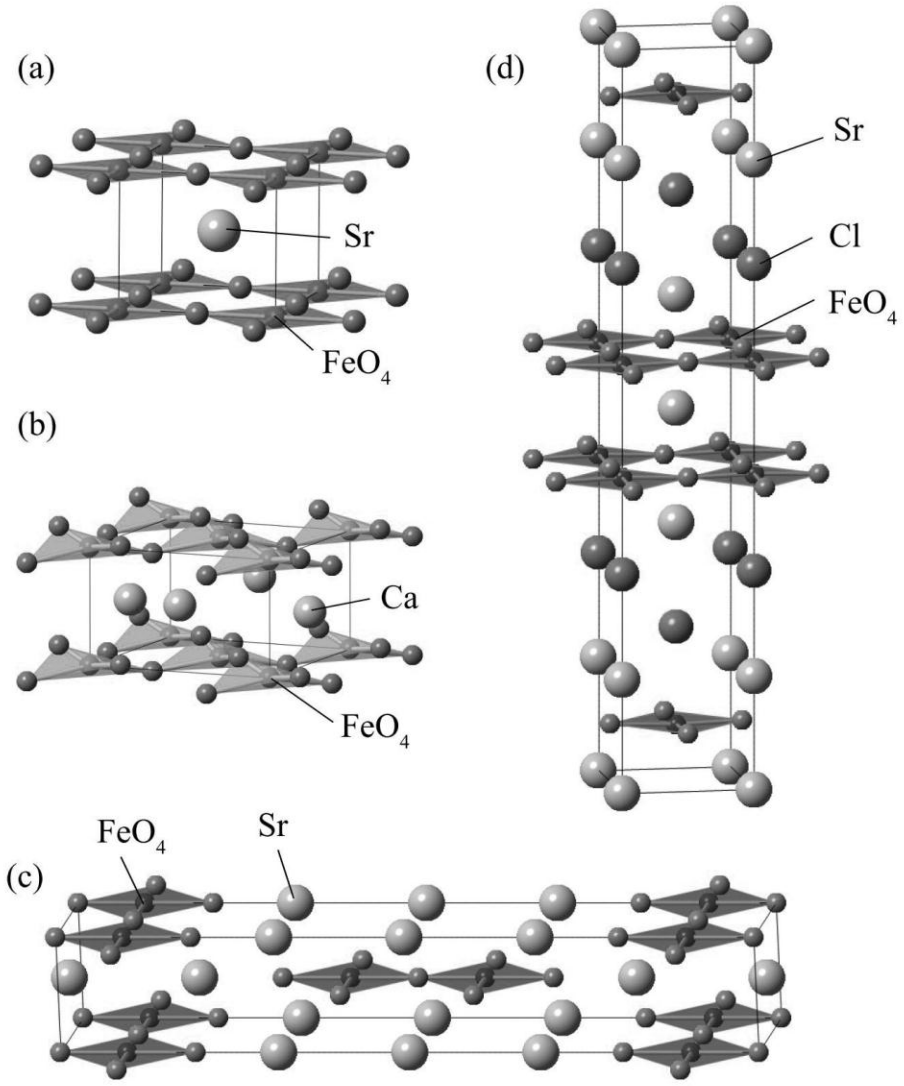


**Figure 5**. The structures of $SrFeO_2$ (a), $CaFeO_2$ (b), $Sr_3Fe_2O_5$ (c), $Sr_3Fe_2O_4Cl_2$ (d).

# *Chapter 1. Synthesis and Thermal Stability of the Solid Solution*

# *$AFeO_2$ (A = Ba, Sr, Ca)*

## 1.1. Introduction

Topochemical reactions such as ion exchange and intercalation reactions provide unique access to metastable crystalline oxide solids, novel structures and local coordination that cannot be obtained by conventional high temperature solid state reactions. Examples include $H[Ca_2Na_{n-3}Nb_nO_{3n+1}]$ ($3 \leq n \leq 7$) [1], $(CuX)LaNb_2O_7$ ($X$ = Cl, Br) [2], $H_{1.8}[Bi_{0.21}Sr_{0.80}Na_{0.95}Nb_3O_{10}]$ [3], which were prepared, respectively, from layered perovskites $K[Ca_2Na_{n-3}Nb_nO_{3n+1}]$, $RbLaNb_2O_7$ and $Bi_{1.8}Sr_{0.2}O_2[Bi_{0.2}Sr_{0.8}NaNb_3O_{10}]$. However, the reaction processes and driving forces that allow the modification of structures and composition at low temperature are still far from being satisfactorily understood. This is contrast to the well-known reaction mechanisms in synthetic organic chemistry. However, this is crucial for further developing topochemical routes and would ultimately help to lower working temperatures of solid oxide fuel cells and oxygen membranes.

An unprecedented $FeO_4$ square planar coordination has been recently realized in $SrFeO_2$ by reducing perovskite $SrFeO_3$ (Figure 1.1a) with $CaH_2$ at low temperatures [4]. As seen in Figure 1.1c, the structure of $SrFeO_2$ is made up of corner-shared $FeO_4$ square planes in between strontium atoms and is isostructural with the infinite layer (IL) structure $SrCuO_2$ [5,6]. Surprisingly, first-principles calculations revealed that this new material is a thermodynamically stable phase [7,8]. From the isomer shift of Mössbauer spectra, we found that the $Fe^{2+}$ in $SrFeO_2$ is indeed more strongly bonded to neighboring $O^{2-}$ than those of any

other existing divalent ferrous compounds. This utmost feature allows this material to achieve a magnetic order well above room temperature ($T_N$ = 473 K) [4] and explains why a spin-state transition is realized for the first time in a four-coordinated metal center [9,10]. This feature also preserves the square planes during structural changes, even if some distortion occurs. $SrFeO_2$ is susceptible to substantial positive chemical pressure; the substitution of the strontium site with calcium having a smaller ionic radius is possible up to as much as 80 %. A further and complete substitution to $CaFeO_2$ results in a considerable distortion of the $FeO_4$ square plane towards a tetrahedron [11,12]. The conversion from $SrFeO_3$ to $SrFeO_2$ (or vice versa) proceeds via the brownmillerite-type intermediate $SrFeO_{2.5}$ (Figure 1.1b) at temperatures as low as 400K [4], thereby involving not only extraction (insertion) of oxide ions but also drastic rearrangement of oxide ions in the basal framework.

In this chapter, we report on the negative chemical pressure effect on the structural and magnetic properties by the Sr-to-Ba substitution. Unlike the case of positive chemical pressure, the IL structure $(Sr_{1-y}Ba_y)FeO_2$ is found to exist only up to 30%. The substitutional and thermal stabilities as well as magnetic properties of this Ba-substituted and the Ca-substituted systems are discussed.

### 1.2. Experimental

First, we prepared oxygen deficit perovskite oxides $(Sr_{1-y}Ba_y)FeO_{3-\delta}$ ($0 < \delta < 0.5$) for $y$ = 0.1, 0.2, 0.3 and 0.4. Mixtures of stoichiometric amount of $SrCO_3$ (99.99 %), $BaCO_3$ (99.99 %) and $Fe_2O_3$ (99.99 %) were weighted, ground, pelletized and heated at 1473 K for 2 days in air with one intermediate grinding. Subsequently, the precursors of about 0.25 g were finely ground with two-molar excess of $CaH_2$ in an Ar-filled glove box, sealed in an evacuated Pyrex tube (volume 15 $cm^3$) with a residual pressure less than $1.3\times10^{-8}$ MPa, and

reacted at 553 K for 3 days. The residual $CaH_2$ and the byproduct CaO were removed by washing out with $NH_4Cl$ / methanol solution (0.15 mol/L). For the study of low-temperature powder X-ray diffraction (XRD) and thermogravimetry (TG), $(Sr_{1-x}Ca_x)FeO_2$ ($x$ = 0.0, 0.2, 0.4, 0.6, 0.8) were synthesized according to the procedure as described previously [11].

The sample purity was checked by XRD profile using a Mac Science M18XHF diffractometer equipped with a graphite monochromator and a Cu$K_\alpha$ radiation ($\lambda$ = 1.54056 Å). Low-temperature XRD data of $(Sr_{1-x}Ca_x)FeO_2$ and $(Sr_{1-y}Ba_y)FeO_2$ for $x$ = 0.0, 0.4, 0.8 and $y$ = 0.3 were collected for 10 – 290 K on a Mac Science MXP18 diffractometer equipped with a closed-cycle He refrigerator installed at the Institute for Solid State Physics, University of Tokyo. A monochromatized Cu$K_\alpha$ source was used and each scan was performed on a $2\theta$ range of 20 – 70° with an angular step of 0.02° and a counting time of 2.5°/sec. The peak positions were calibrated against Si as an internal standard, and the lattice parameters were obtained with a least-square method.

High-resolution synchrotron XRD experiments on $(Sr_{1-y}Ba_y)FeO_2$ ($y$ = 0.1, 0.2, 0.3) were performed at room temperature using a large Debye-Scherrer camera installed at the Japan Synchrotron Radiation Research Institute SPring-8 BL02B2. We used an imaging plate as a detector. Incident beams from a bending magnet were monochromatized to 0.42026 Å. The finely ground powder samples were filtered by a strainer with 32-μm-square holes and put into a Pyrex capillary of inner 0.1 mm diameter. The capillary was rotated during measurements to reduce preferential orientation. The obtained synchrotron XRD data were analyzed by the Rietveld method by using RIETAN-2000 program [13]. The agreement indices used were $R$-weighted pattern, $R_{wp} = [\sum w_i(y_{io} - y_{ic})^2/\sum w_i(y_{io})^2]^{1/2}$, $R$-pattern, $R_p = \Sigma|y_{io} - y_{ic}|/\Sigma(y_{io})$ and goodness of fit (GOF), $\chi^2 = [R_{wp}/R_{exp}]^2$, where $R_{exp} = [(N - P)/ \sum w_i y_{io}^2]^{1/2}$, $y_{io}$ and $y_{ic}$ are the observed and calculated intensities, $w_i$ is the weighting factor, $N$ is the total

number of $y_{io}$ data when the background is refined, and $P$ is the number of adjusted parameters.

Powder neutron diffraction (ND) experiment on $(Sr_{0.8}Ba_{0.2})FeO_2$ ($y$ = 0.2) at room temperature was carried out on the Kinken powder diffractometer with multicounters for High Efficiency and high Resolution MEasurementS, HERMES, of the Institute for Materials Research, Tohoku University, installed at a guide hall of JRR-3 reactor in the Japan Atomic Energy Agency (JAEA), Tokai [14]. The incident neutron with a wavelength of 1.82646 Å was monochromatized by the 331 reflection of vent Ge crystal. A 12'-blank-sample18' collimation was employed. A polycrystalline sample of 3 g mass was placed into a vanadium cylinder. The data were collected with a step-scan procedure using 150 neutron detectors in a $2\theta$ range from 3º to 153º with a step width of 0.1º.

Thermogravimetric data of $(Sr_{1-x}Ca_x)FeO_2$ ($x$ = 0.0, 0.2, 0.4, 0.6, 0.8) and $(Sr_{1-y}Ba_y)FeO_2$ ($y$ = 0.2) were collected using Rigaku Thermo plus (TG 8120). The sample of around 15 mg was put in a Pt pan and $\alpha$-$Al_2O_3$ was used as a reference material. The measurements were performed in heating the sample at 10 $Kmin^{-1}$. The samples after heated were identified by in-house XRD measurements.

Mössbauer spectra on $(Sr_{1-y}Ba_y)FeO_2$ for $y$ = 0.1, 0.2 and 0.3 were taken at room temperature in transmission geometry by using a $^{57}$Co/Rh $\gamma$-ray source. The source velocity was calibrated by $\alpha$-Fe as a reference material.

## 1.3. Results and Discussions

### *1.3.1. Crystal Structure*

Figure 1.2 shows the XRD patterns of samples obtained by hydride reduction from precurcer $(Sr_{1-y}Ba_y)FeO_{3-\delta}$ ($0 < \delta < 0.5$) for $y$ = 0 - 0.4. The XRD profiles for $0 \leq y \leq 0.3$ are

very similar to each other and are readily indexed on basis of the tetragonal unit cell without any peaks associated with impurities or super-reflections. However, the profile for $y$ = 0.4 is assigned as $(Sr_{0.6}Ba_{0.4})FeO_{2.5}$ with the $Ba_2Fe_2O_5$-type structure [15]. The lattice parameters $a$ = 6.829(1) Å, $b$ = 11.454(1) Å, $c$ = 23.11(4) Å and $\beta$ = 99.261(8)˚ are reasonable considering those of $BaFeO_{2.5}$ ($a$ = 6.969 Å, $b$ = 11.724 Å, $c$ = 23.408 Å, $\beta$ = 98.372˚) [15]. We could not obtain the IL $(Sr_{0.6}Ba_{0.4})FeO_2$ phase even with modified reaction temperature and time. The lattice parameters of the IL phase including the Ca substituted case are depicted in Figure 1.3 as a function of the average radius of the *A*-site cation, $r_A$, derived by assuming $r_{Ca}$ = 1.12 Å, $r_{Sr}$ = 1.26 Å and $r_{Ba}$ = 1.42 Å [16]. For comparison, theoretical lattice parameters of $CaFeO_2$, $SrFeO_2$ and $BaFeO_2$ obtained by first-principles calculations are presented [7,8]. The linear increase of the lattice parameters with $r_A$ suggests the successful formation of the IL structure. The lines obtained by the least-squares fit of the experimental data are located slightly higher than theoretically predicted values except the $c$ axis of the hypothetical IL phase $BaFeO_2$.

The synchrotron XRD data for the Ba-substituted samples ($y$ = 0.1, 0.2, 0.3) also show a simple tetragonal unit cell. Absence of any broadening, splitting of peaks, and super-reflections as found in $CaFeO_2$ [12] suggests formation of a well-crystallized and non-distorted IL structure. Accordingly, we performed Rietveld structural refinements for the synchrotron XRD data assuming, as an initial model, the ideal IL structure belonging to the *P*4/*mmm* space group with Sr/Ba on 1*d* (0.5, 0.5, 0.5), Fe on 1*a* (0, 0, 0) and O on 2*f* (0.5, 0, 0), where Ba and Sr atoms were set to be statistically disordered. All the refinements led to good fits, providing reasonable reliability factors $R_{wp}$ = 2.41 %, $\chi^2$ = 2.38 for $y$ = 0.1, $R_{wp}$ = 3.21%, $\chi^2$ = 3.80 for $y$ = 0.2 and $R_{wp}$ = 3.16%, $\chi^2$ = 3.18 for $y$ = 0.3 (see Figure 1.4 and Table 1.1). Reasonably small atomic displacement parameters ($B$) for each refinement indicate that the Ba/Sr, Fe and O atoms are positioned at the assumed sites.

In order to get more precise information on the oxygen position and its site occupation, we performed Rietveld refinement for the powder ND data of $(Sr_{0.8}Ba_{0.2})FeO_2$. The ND profile at room temperature included magnetic Bragg reflections, which were taken into account for the refinement, as will be discussed in detail later. The fit once again led to a reasonably small displacement parameter ($B$ = 1.12(8)) for oxygen atoms (and other atoms) and $R_{wp}$ = 7.41 %, $\chi^2$ = 2.20, as shown in Figure 1.5 and Table 1.1. When allowed to change, the oxygen occupancy factor was refined approximately to unity within error (1.005 (11)), indicating no oxygen deficiency. All these results together with the previous ones [11,12] led us to conclude that the ideal IL structure can tolerate up to 30% of the Ba-substitution and up to 80% of the Ca-substitution, namely with $r_A$ ranging from 1.15 to 1.31 Å. It is surprising that the solubility range of the IL structure is nearly the same as the cupric oxides $A$CuO$_2$ ($0 \le x < 0.9$, $0 \le y \le 0.33$) obtained by high temperature and high pressure synthesis [6].

The bond valence sum (BVS) calculations [17] based on the synchrotron XRD data gave ($A$, Fe) = (+1.95, +1.95) for $y$ = 0.1, (+1.99, +1.95) for $y$ = 0.2 and (+2.00, +1.93) for $y$ = 0.3. As shown in Figure 1.6, the BVS plotted as a function of $r_A$ follows a linear relation for both $A$ and Fe and hence validates once again the formation of the solid solution. Here, we would like to point out that while the Ca-substituted IL structure tolerates large deviation of the bond valences from the formal value (i.e., ($A$, Fe) = (+1.71, +2.15) for $x$ = 0.8) [11], the Ba-substituted IL structure is only accessible up to $y \sim 0.3$ with ($A$, Fe) = (+2.00, +1.93). This should be related to the difficulty of Fe to take an unstable valence state of +1. Since the BVS of Fe is determined almost exclusively by the Fe-O distance within the $FeO_2$ layer, the in-plane length is likely to determine the solubility range of the IL structure. Note however that the IL cuprates $A$CuO$_2$ show a different variation of BVS, ($A$, Cu) = (+1.94, +2.06) ~ (+2.41, +1.85), suggesting a different stabilization factor.

*1.3.2. Magnetic Properties*

The room-temperature $^{57}$Fe Mössbauer spectra of $(Sr_{1-y}Ba_y)FeO_2$ for $y$ = 0.1, 0.2 and 0.3, shown in Figure 1.7 consist of a single magnetically-split sextet together with a small paramagnetic doublet peak. The obtained spectra were fitted by a Lorentzian function and the results are summarized in Table 1.2. The doublet in each spectrum arises from a trivalent-iron-containing paramagnetic amorphous impurity formed by decomposition and over-reduction of the precursor $A$FeO$_{2.5}$ phase to Fe(0) that was then oxidized to Fe(III) upon exposure to air. Such an impurity phase was also observed upon the synthesis of $(Sr_{1-x}Ca_x)FeO_2$.[12] The values of isomer shift (*IS*) and quadrupole splitting (*QS*) for the sextet are very close to those of $SrFeO_2$ and the full width at half maximum (FWHM) is resolution limited, further supporting the structural analysis of the present compounds based on the ideal IL structure. The Ba-concentration dependence of the hyperfine field (*HF*) shows that the iron ion stays in a divalent high-spin ($S$ = 2) state and that the Néel temperature $T_N$ decreases only slightly with Ba-concentration. The same tendency is seen for $(Sr_{1-x}Ca_x)FeO_2$ ($x \leq 0.8$) [12]. Since the difference between $S_1$ and $S_2$ in Figure 1.7 is close to that of $SrFeO_2$ and to the value of *QS* above $T_N$ in $SrFeO_2$, the magnetic moments in the magnetically ordered state are considered to align perpendicularly to the $c$ axis, as in the case of $SrFeO_2$.

As mentioned above, the magnetic order for $(Sr_{0.8}Ba_{0.2})FeO_2$ at ambient temperature was also probed by the ND data. Well-developed magnetic reflections characterized as ((2$h$+1)/2, (2$k$+1)/2, (2$l$+1)/2), where $h$, $k$ and $l$ are integers, indicate the ($\pi$, $\pi$, $\pi$) type spin-structure. The Rietveld analysis demonstrated that the magnetic moments are 3.3 $\mu_B$ per iron and align in the *ab* plane in agreement with the Mössbauer results. A slight decrease of $T_N$ with $y$ is expected from the *HF* change. A linear extrapolation of the *HF* vs. $y$ curve to $y \rightarrow 1$ yielded

the *HF* of 36 T for the hypothetical phase $BaFeO_2$. This value is very close to *HF* = 35 T obtained for the distorted IL $CaFeO_2$ at room temperature [12]. It follows that $BaFeO_2$ would have a similar $T_N$ as $CaFeO_2$ ($T_N$ = 433 K), at most 40 K lower than that of $SrFeO_2$.

A decrease in $T_N$ in Ba-substituted IL compound has been anticipated from the theoretical studies by Xiang *et al* [8]. They showed that the dominating spin exchange paths of $SrFeO_2$ are $J_1$ = 8.68 meV and $J_2$ = 2.23 meV, where $J_1$ is the intralayer Fe-O-Fe superexchange and $J_2$ is the interlayer Fe-Fe exchange coupling constants [8]. They also considered the hypothetical phase $BaFeO_2$ and obtained $J_1$ = 5.81 meV and $J_2$ = 1.34 meV. In the framework of the mean-field theory and the Monte-Carlo simulation, it can be assumed that the $T_N$ scales linearly with $J_1$ so long as the $J_1/J_2$ ratio remains constant. Then, the $T_N$ of $BaFeO_2$ is estimated as 473×(5.81/8.68) = 303 K, which is, however, much lower than that estimated from the experimental data. The reason for the significant deviation between the theory and the experiment calls for further theoretical investigations. Here, the *IS* values for $y$ = 0.1, 0.2, 0.3 that scarcely alter from that for $SrFeO_2$ might give us a hint. Since *IS* provides information on how strongly Fe atom is bonded, the observation implies that the reduced $J_1$ and $J_2$ (with $y$) must be compensated by the increase of other further-neighbor exchange integrals.

### *1.3.3. Thermal Stability*

Low-temperature XRD measurements for $x$ = 0, 0.4, 0.8 and $y$ = 0.3 revealed the absence of any structural instabilities at low temperatures. For the quantitative estimation of the lattice stiffness [18--20], we calculated the Debye temperature $\theta_D$ using the Debye-Grüneisen model for the variation of unit-cell volume (see Figure 1.8), which is expressed as,

$$V(T) \cong V(0) + \int_0^T \frac{\gamma C_v}{B} dT \cong V(0) + \frac{9\gamma N k_B}{B} T\left(\frac{T}{\theta_D}\right)\int_0^{\theta_D/T} \frac{x^3}{e^x - 1} dx \qquad \text{- (1)}$$

where $V(0)$ is the unit-cell volume at 0 K, $\gamma$ is the Grüneisen parameter, $B$ is the bulk modulus, $k_B$ is the Boltzmann constant and $N$ is the number of atoms in the unit cell [21,22]. It is seen that the obtained values of $\theta_D$ are independent of composition within the experimental uncertainty, and are much smaller than that of $CaFeO_2$ with the distorted IL structure ($\theta_D$ = 733 K) [11].

The stability and reactivity of the IL structure at high temperature was investigated by the TG measurements in air up to 900 K (Figure 1.9). Compounds with a smaller $r_A$ ($x$ = 0.4, 0.6, 0.8) exhibited a single-step absorption of oxygen, while those with a larger $r_A$ ($x$ = 0.2, 0.0 and $y$ = 0.2) did a double-step absorption with a single plateau. Since the starting materials contain a tiny yet finite amount of amorphous impurity phase as revealed by the Mössbauer study, a direct determination of the oxygen content for the target compound from the raw data was not possible. Nevertheless, sample identification was carefully made by ex-situ XRD after rapid quenching of the furnace at any point of the TG curve and we found that the plateau corresponds to the $A$FeO$_{2.5}$ phase, and this phase for $x$ = 0.2, 0.0 and $y$ = 0.2 is further oxidized to become the pseudo-cubic oxygen-deficient perovskite. There is no intermediate phase between $A$FeO$_2$ and $A$FeO$_{2.5}$, as already pointed out for SrFeO$_2$.[4] With this knowledge, we normalized the raw TG data such that the oxygen content in the plateau region is 2.5 as shown in Figure 1.9.

Notably, the oxygen-absorbing temperature on forming $A$FeO$_{2.5}$ systematically changes with chemical substitution. We define here $T_O$, $T_{O'}$ and $T_{O''}$ as a temperature at which the normalized TG curve crosses $z$ = 0.25, 0.1 and 0.4, respectively, and are depicted as a function of $r_A$ in Figure 1.10. $T_O$ drops from 594 K for $(Sr_{0.2}Ca_{0.8})FeO_2$ to 527 K for

$(Sr_{0.8}Ba_{0.2})FeO_2$. Obviously, $T_O$ decreases in proportion with $r_A$. However, this would not mean that the IL structure becomes destabilized with increasing $r_A$ because $\theta_D$ of the IL compounds is independent of the substitution (except the distorted IL structure $CaFeO_2$) and also because $(Sr_{0.2}Ca_{0.8})FeO_2$ ($x$ = 0.8) with the most deviated valences of *A* and Fe has the highest $T_O$. It is most probable that the dominant factor for controlling oxygen absorption behavior is the lattice parameters controlled by *A*-site cation size. Considering the facts that the *c* axis is more susceptible to $r_A$ than the *a* axis and the oxygen pathways for the insertion of oxygen atoms may mainly involve the interlayer space between $FeO_2$ layers, we believe the *c* parameter contribute more to the oxygen absorbing temperature. However, one should recall that the conversion from the IL structure $SrFeO_2$ to the brownmillerite structure $SrFeO_{2.5}$ involves not only the insertion of oxygen atoms but also the reconstruction of the Fe-O framework [4]. Recent thin film studies have shown two distinct reaction pathways with different kinetic energies [23]. Furthermore, the slope for the $AFeO_2$ to $AFeO_{2.5}$ conversion becomes steeper with $r_A$; the difference between $T_{O''}$ and $T_{O'}$ is about 100 K for $(Sr_{0.2}Ca_{0.8})FeO_2$, while about 50 K for $(Sr_{0.8}Ba_{0.2})FeO_2$. Thus it might be possible that the oxygen migration pathways are also influenced by $r_A$.

### 1.4. Conclusion

We demonstrated that $SrFeO_2$ with the IL structure can tolerate only up to 30% substitution of Ba unlike the case of Ca-substitution. The long Fe-O distance caused by the Ba-substitution destabilizes the IL structure. The negative pressure effect does not drastically change the magnetic properties in contrast to the theoretical anticipation, meaning that iron atoms are still very strongly bonded to oxide ion. The oxidation temperature and rate are controllable to a great extent by *A*-site cation size. The importance of interstitial oxide ions

has been recently stressed for the design of oxygen ion conductors [24--27]. In the present compounds, no phase could be found between $A$FeO$_2$ and $A$FeO$_{2.5}$ although more oxidized phase SrFeO$_{3-\delta}$ ($0 < \delta < 0.5$) are known to exhibit high oxide ion conductivity. But, the elongated *c*-axis with respect to SrFeO$_2$ may allow further manipulation of structures, for example, by oxidative intercalation by chlorine gas.

## References


[1] A. Jacobson, J. W. Johnson, and J. Lewandowski, Inorg. Chem. 24 (1985) 3727.

[2] T. A. Kodenkandath, J. N. Lalena, W. L. Zhou, E. E. Carpenter, C. Sangregorio, A. Falster, W. Simmons Jr, C. J. O'Connor, and B. John, J. Am. Chem. Soc. 121 (1999) 10743.

[3] W. Sugimoto, M. Shirata, Y. Sugahara, and K. Kuroda, J. Am. Chem. Soc. 121 (1999) 11601.

[4] Y. Tsujimoto, C. Tassel, N. Hayashi, T. Watanabe, H. Kageyama, K. Yoshimura, M. Takano, M. Ceretti, C. Ritter, and W. Paulus, Nature 450 (2007) 1062.

[5] T. Siegrist, S. Zahurak, D. Murphy, and R. Roth, Nature 334 (1988) 231.

[6] M. Takano, Y. Takeda, H. Okada, M. Miyamoto, and T. Kusaka, Physica C 159 (1989) 375.

[7] J. M. Pruneda, J. Íñiguez, E. Canadell, H. Kageyama, and M. Takano, Phys. Rev. B 78 (2008) 115101.

[8] H. J. Xiang, S. H. Wei, and M. H. Whangbo, Phys. Rev. Lett. 100 (2008) 167207.

[9] T. Kawakami, Y. Tsujimoto, H. Kageyama, *et al*, Nat. Chem. 1 (2009) 371.

[10] M. H. Whangbo and J. Köhler, Nat. Chem. 1 (2009) 351.

[11] C. Tassel, T. Watanabe, Y. Tsujimoto, N. Hayashi, A. Kitada, Y. Sumida, T. Yamamoto, H. Kageyama, M. Takano, and K. Yoshimura, J. Am. Chem. Soc. 130 (2008) 3764.

[12] C. Tassel, J. M. Pruneda, N. Hayashi, *et al*, J. Am. Chem. Soc. 131 (2009) 221.

[13] F. Izumi and T. Ikeda, J. Cryst. Soc. Jpn. 42 (2000) 516.

[14] K. Ohoyama, T. Kanouchi, K. Nemoto, M. Ohashi, T. Kajitani, and Y. Yamaguchi, Jpn. J. Appl. Phys. 37 (1998) 3319.

[15] X. D. Zou, S. Hovmöller, M. Parras, J. M. González-Calbet, M. Vallet-Regí, and J. C. Grenier, Acta Cryst. A49 (1993) 27.

[16] R. Shannon, Acta Cryst. 32 (1976) 751.

[17] I. D. Brown and D. Altermatt, Acta Cryst. B41 (1985) 244.

[18] T. Okuda, A. Asamitsu, Y. Tomioka, T. Kimura, Y. Taguchi, and Y. Tokura, Phys. Rev. Lett. 81 (1998) 3203.

[19] L. Ghivelder, I. A. Castillo, M. Gusmao, J. Alonso, and L. Cohen, Phys. Rev. B 60 (1999) 12184.

[20] T. Tohei, A. Kuwabara, F. Oba, and I. Tanaka, Phys. Rev. B 73 (2006) 064304.

[21] T. Kiyama, K. Yoshimura, K. Kosuge, Y. Ikeda, and Y. Bando, Phys. Rev. B 54 (1996) 756.

[22] B. Dabrowski, M. Avdeev, O. Chmaissem, S. Kolesnik, P. Klamut, M. Maxwell, and J. Jorgensen, Phys. Rev. B 71 (2005) 104411.

[23] S. Inoue, M. Kawai, N. Ichikawa, H. Kageyama, W. Paulus, and Y. Shimakawa, Nat. Chem. 2 (2010) 213.

[24] E. Boehm, J. M. Bassat, M. C. Steil, P. Dordor, F. Mauvy, and J. C. Grenier, Solid State Sci. 5 (2003) 973.

[25] A. Demourgues, A. Wattiaux, J. C. Grenier, M. Pouchard, J. L. Soubeyroux, J. M. Dance, and P. Hagenmuller, J. Solid State Chem. 105 (1993) 458.

[26] X. Kuang, M. A. Green, H. Niu, P. Zajdel, C. Dickinson, J. B. Claridge, L. Jantsky, and M. J. Rosseinsky, Nat. Mater. 7 (2008) 498.

[27] A. Orera and P. Slater, Chem. Mater. 22 (2009) 675.

**Table 1.1.** Rietveld refinement for $(Sr_{1-y}Ba_y)FeO_2$ ($y$ = 0.1, 0.2, 0.3).

| | site | $y$ in $(Sr_{1-y}Ba_y)FeO_2$ | | | |
|---|---|---|---|---|---|
| | | 0.1 (SXRD) | 0.2 (SXRD) | 0.2 (ND) | 0.3 (SXRD) |
| $a$ (Å) | | 3.99794(3) | 4.00059(3) | 4.0014(1) | 4.00896(4) |
| $c$ (Å) | | 3.51198(3) | 3.54538(4) | 3.5457(2) | 3.58441(5) |
| $B$ in Sr/Ba (Å$^2$) | 1$d$ (0.5, 0.5, 0.5) | 0.428(8) | 0.49(1) | 0.76(7) | 0.50(1) |
| $B$ in Fe (Å$^2$) | 1$a$ (0, 0, 0) | 0.42(1) | 0.49(2) | 0.54(9) | 0.51(2) |
| $B$ in O (Å$^2$) | 2$f$ (0.5, 0, 0) | 0.58(4) | 0.64(5) | 1.12(8) | 0.74(5) |
| A-O (Å) | | 2.6607 | 2.6728 | 2.6732 | 2.6889 |
| Fe-O (Å) | | 1.9990 | 2.0003 | 2.0007 | 2.0045 |
| moment ($\mu_B$) | | | | 3.3 | |
| $R_{wp}$ (%) | | 2.42% | 3.21% | 7.41% | 3.16% |
| $R_p$ (%) | | 1.55% | 2.08% | 5.65% | 2.15% |
| $\chi^2$ | | 2.36 | 3.80 | 2.20 | 3.18 |

[a] SXRD and ND represent synchrotron X-ray diffraction and neutron diffraction. All the refinements were performed by using the ideal IL structure, $P4/mmm$ space group with $A$ = $(Sr_{1-y}Ba_y)$ on 1$d$, Fe on 1 and O on 2$f$.

**Table 1. 2.** Fitting parameters of Mössbauer spectra for $(Sr_{1-y}Ba_y)FeO_2$ ($y$ = 0.1, 0.2, 0.3).

| $y$ | $IS$ (mm/s) | $HF$ (T) | $QS$ (mm/s) | FWHM (mm/s) | Area (%) |
|---|---|---|---|---|---|
| 0.0 [4] | 0.498 | 40.1 | 1.16 | 0.28 | 100 |
| 0.1 | 0.493 | 39.6 | 1.15 | 0.31 | 91 |
| | (0.321) | (0.0) | (0.74) | (0.47) | (9) |
| 0.2 | 0.495 | 39.1 | 1.14 | 0.31 | 95 |
| | (0.321) | (0.0) | (0.72) | (0.47) | (5) |
| 0.3 | 0.497 | 39.0 | 1.15 | 0.31 | 94 |
| | (0.322) | (0.0) | (0.74) | (0.47) | (6) |

[a] $IS$, $HF$, $QS$, FWHM and Area represent isomer shift, hyperfine field, quadrupole splitting, full width at half maximum and area percentage of total fit, respectively. We used the values of $SrFeO_2$ in previous study [4]. The values in parentheses are from the paramagnetic amorphous impurity.

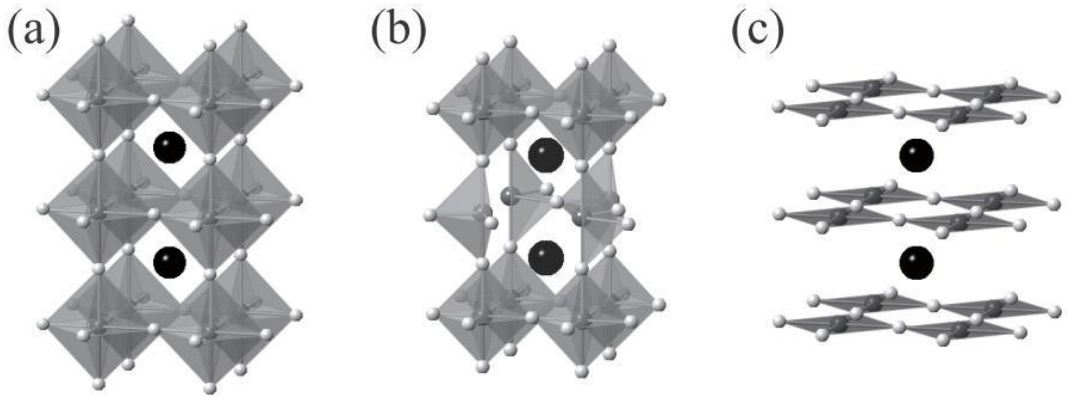


**Figure 1.1**. Schematic representation of the structures of perovskite $SrFeO_3$ (a), brownmillerite $SrFeO_{2.5}$ (b), infinite layer $SrFeO_2$ (c). Black, white and grey spheres represent Sr, Fe and O atoms, respectively.

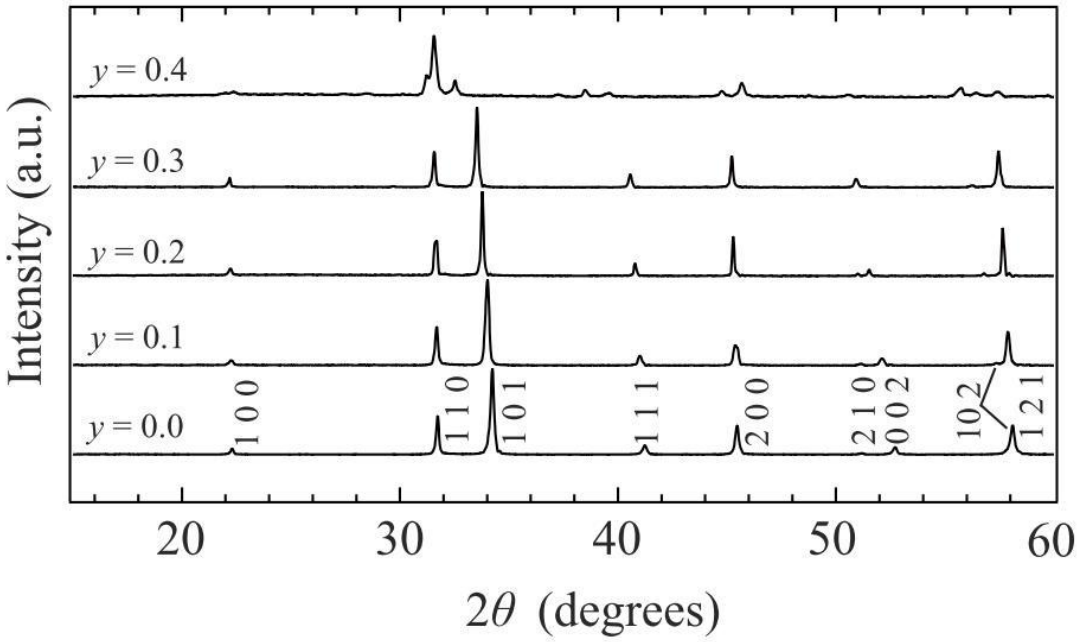


**Figure 1.2.** Powder XRD patterns of $(Sr_{1-y}Ba_y)FeO_2$. All the patterns except $y = 0.4$ could be indexed on the basis of the tetragonal IL structure. The $y = 0.4$ sample is identified as $(Sr_{0.6}Ba_{0.4})FeO_{2.5}$.

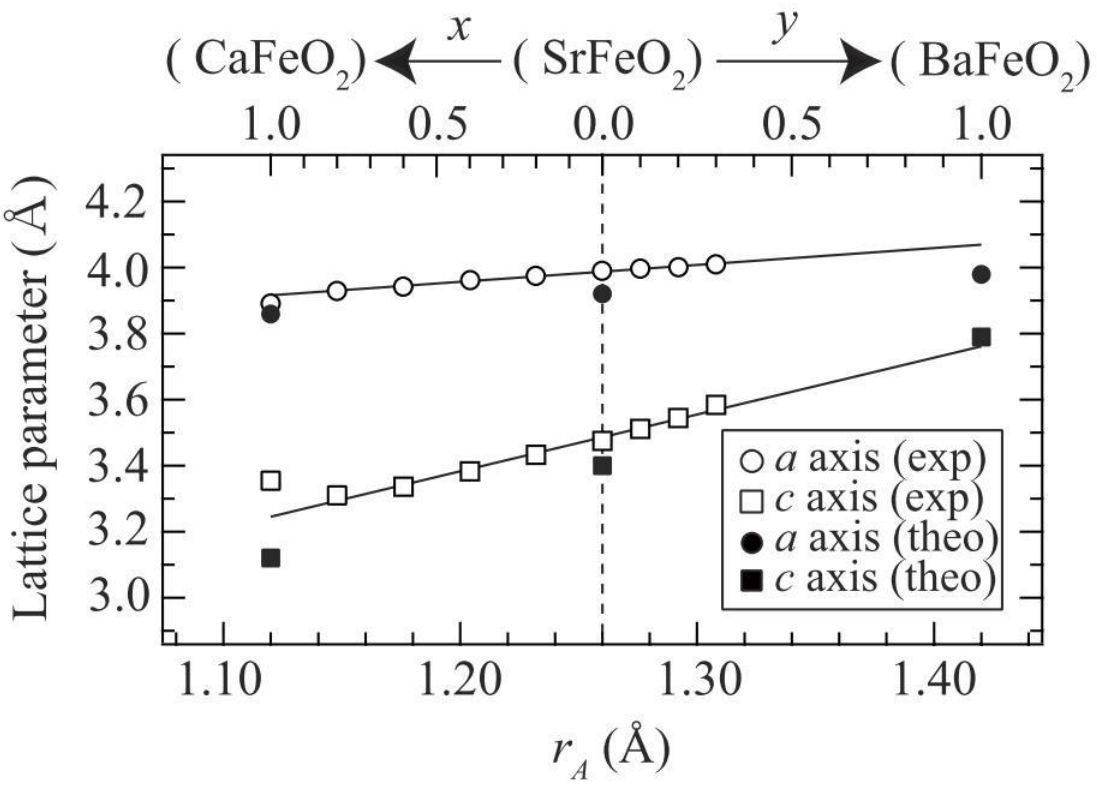


**Figure 1.3.** The lattice parameters of $(Sr_{1-x}Ca_x)FeO_2$ [11, 12] and $(Sr_{1-y}Ba_y)FeO_2$ (this study). Open symbols represent the experimental values, while closed symbols represent the theoretical ones [7, 8]. The error bars are within the size of the symbols. Solid lines were obtained by a least-squares fit. The deviation from the linear relation for $CaFeO_2$ is due to the distorted IL structure [12].

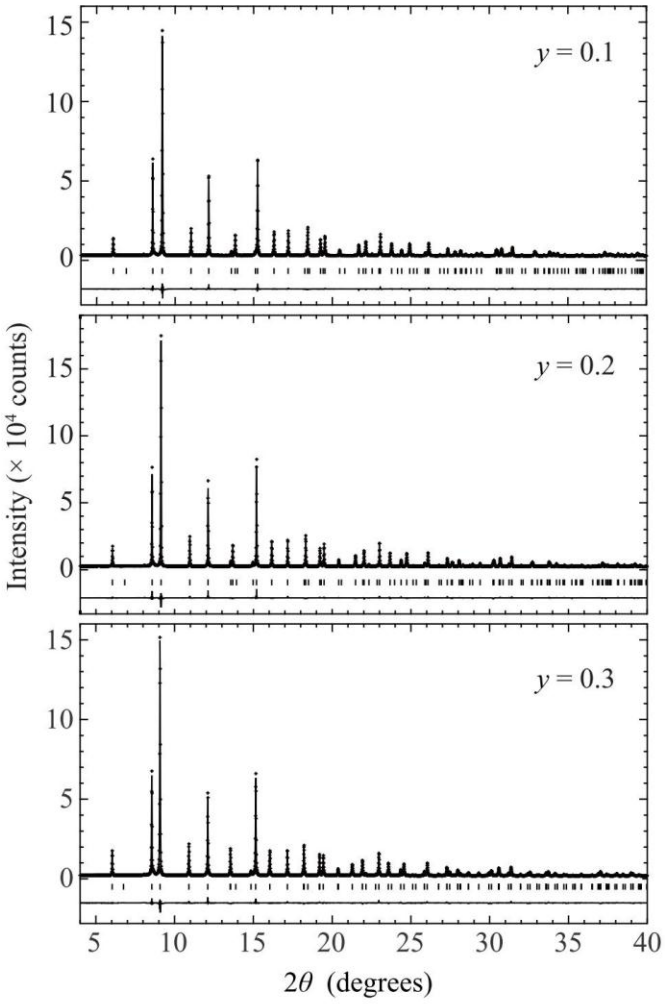


**Figure 1.4**. Structural characterization of $(Sr_{1-y}Ba_y)FeO_2$ ($y$ = 0.1, 0.2, 0.3) by the Rietveld refinement of synchrotron XRD data at room temperature. The overlying crosses and the solid line represent the observed and the calculated intensities. The bottom solid line represents the difference between the observed intensity and the calculated intensity. The ticks correspond to the position of the calculated Bragg peaks of $(Sr_{1-y}Ba_y)FeO_2$.

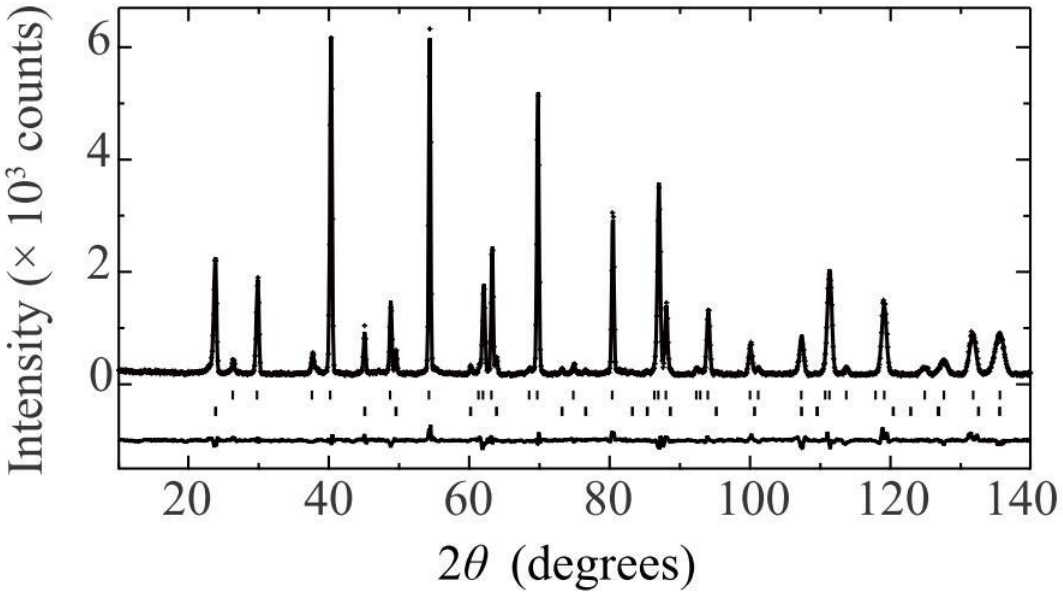


**Figure 1.5.** Structural characterization of $Sr_{0.2}Ba_{0.8}FeO_2$ ($y$ = 0.2) by the Rietveld refinement of ND data at room temperature. The upper and lower ticks correspond to the position of the calculated chemical and magnetic Bragg peaks of $(Sr_{0.8}Ba_{0.2})FeO_2$.

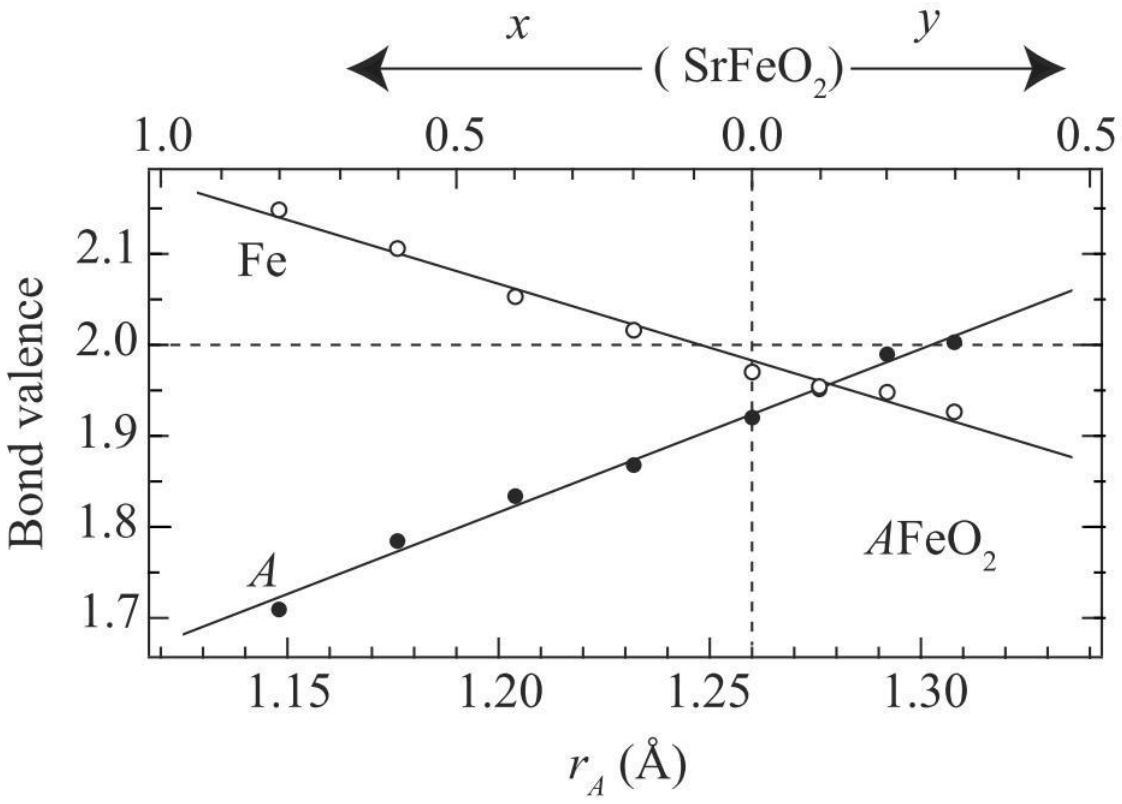


**Figure 1.6.** Bond valence sum for *A* (closed) and Fe (open) in $(Sr_{1-x}Ca_x)FeO_2$ or $(Sr_{1-y}Ba_y)FeO_2$. Here we assumed $r_o(A) = (1-y)\, r_o(Sr) + y\, r_o(Ba)$ where $r_o(Fe) = 1.734$ Å, $r_o(Ba) = 2.285$ Å, $r_o(Sr) = 2.118$ Å [17]. Solid lines were obtained by a least-squares fit. Values for $(Sr_{1-x}Ca_x)FeO_2$ were taken from the previous study [11].

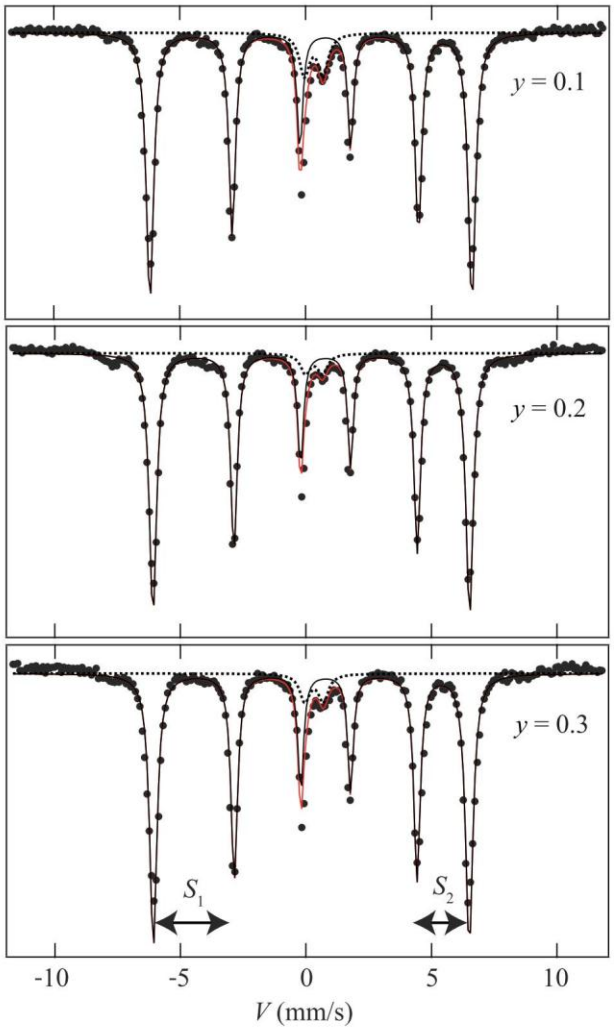


**Figure 1.7.** Mössbauer spectrum for $(Sr_{1-y}Ba_y)FeO_2$ ($y$ = 0.1, 0.2, 0.3) at room temperature. Circles denote the experimental data. A black solid line is the spectrum for$(Sr_{1-y}Ba_y)FeO_2$ and a broken line is that from an overreduced, decomposed impurity formed during the hydride reaction. A red line represents a total fit. $S_1$ and $S_2$ are the relative shifts of the peaks.

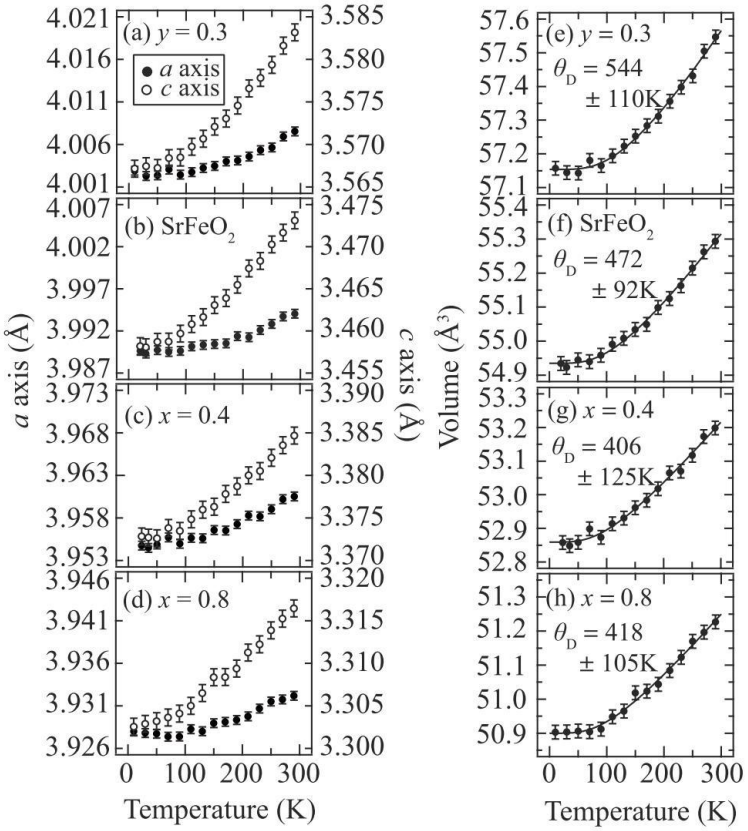


**Figure 1.8.** Lattice parameters and unit-cell volumes of $(Sr_{1-x}Ca_x)FeO_2$ and $(Sr_{1-y}Ba_y)FeO_2$ at low temperature. (a) – (d) Closed and open circles represent the *a* and *c* axes, respectively. (e) – (h) Circles represent the unit-cell volumes of $(Sr_{1-x}Ca_x)FeO_2$ and $(Sr_{1-y}Ba_y)FeO_2$ and solid lines represent the fit to the Debye-Grüneisen model with $\theta_D$ as an adjustable parameter. The present result of $SrFeO_2$ is in agreement with the result from previous study ($\theta_D$ = 395 K) [11] calculated from the low-temperature XRD measurement without calibrations by Si.

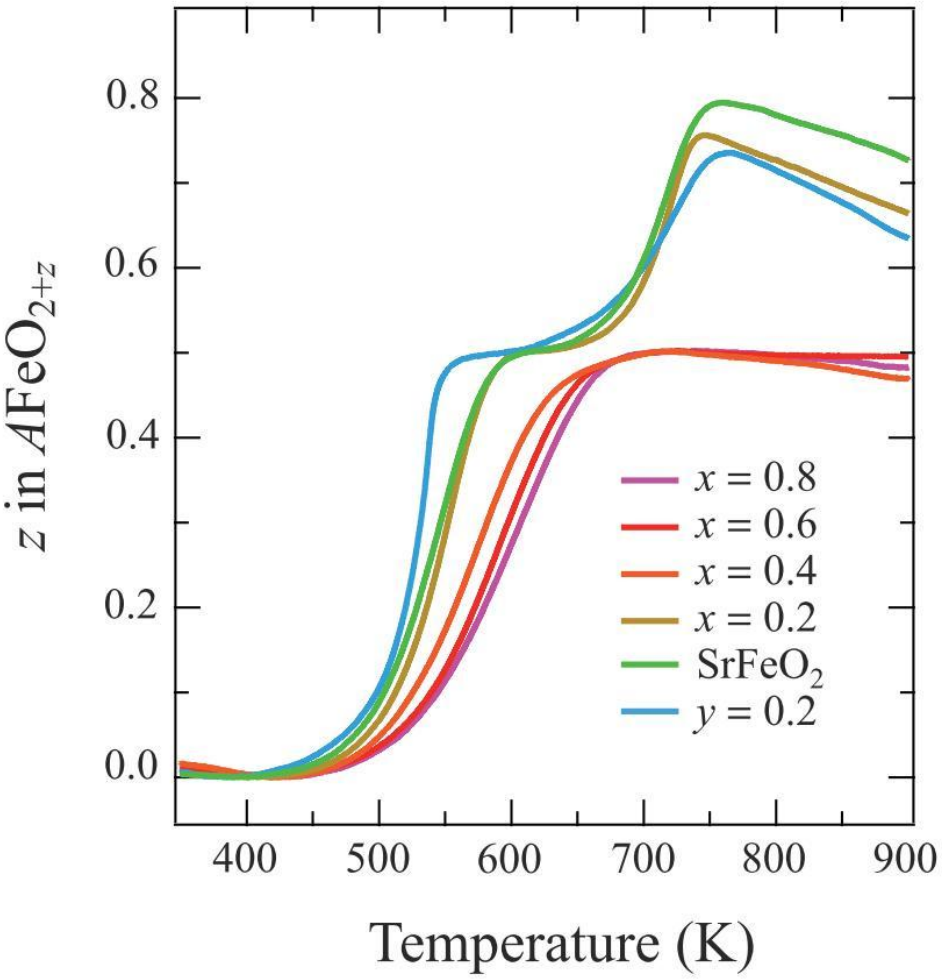


**Figure 1.9**. TG measurements of $(Sr_{1-x}Ca_x)FeO_2$ and $(Sr_{1-y}Ba_y)FeO_2$ performed in air. We normalized the raw TG data such that the plateaus correspond to the brownmillerite phase. It is to be noted that there is no intermediate phase for $0 < z < 0.5$ and hence the specimen in this $z$ range is nothing but $1-2z : 2z$ mixture of $A\text{FeO}_2$ and $A\text{FeO}_{2.5}$ phases.

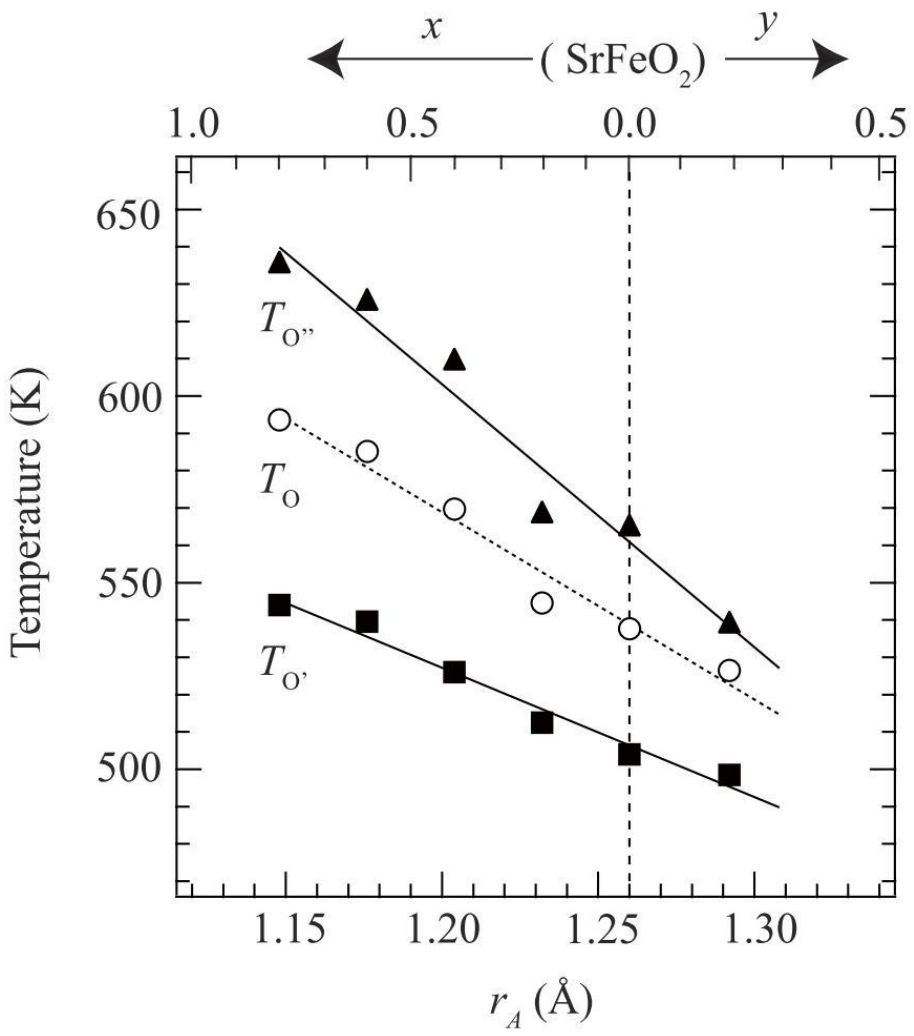


**Figure 1.10**. $r_A$ dependence of $T_O$, $T_{O'}$ and $T_{O''}$, the temperatures at which the TG curves cross $z$ = 0.25, 0.1 and 0.4 in Figure 9, respectively. Solid lines were obtained by a least-squares fit. We would like to note that there exists no intermediate phase between $z$ = 0 and 0.5 in $A\mathrm{FeO}_{2+z}$.

# *Chapter 2. $(Sr_{1-x}Ba_x)FeO_2$ $(0.4 \leq x \leq 1)$: a New Oxygen Deficient Perovskite Structure*

## 2.1. Introduction

Perovskite $ABO_3$ (Figure 2.1a) and spinel $AB_2O_4$ oxides represent two major classes in crystalline complex metal oxides, and are known to exhibit exotic properties such as giant magnetoresistance, high-$T_c$ superconductivity, metal-insulator transitions, and fast ion conductivity [1--10]. The rich diversity of chemical and physical properties in both structures is derived from their ability to accommodate various metal elements at both the A- and B-sites with a wide range of ionic radius and valence. Another characteristic, often found in the perovskite structure but rarely in the spinel structure, is the high tolerance for oxygen nonstoichiometry. For example, annealing a wide-gap insulator $SrTiO_3$ in a reducing atmosphere introduces a small amount of oxygen vacancies (i.e., electron doping), which eventually lead to superconductivity at low temperatures [11]. Proton conductivity arises from the creation of a large amount of oxygen vacancies by aliovalent A- or B-site substitution as found in $Sr(Zr_{1-\delta}Y_{\delta})O_{3-\delta/2}$ in wet atmosphere [12].

When the oxygen vacancy level in a perovskite ($\delta$ in $ABO_{3-\delta}$) is commensurate with respect to the underlying lattice, various types of oxygen vacancy order occur, often accompanied by breaking of translational symmetry, which is analogous to the metal-insulator (Mott) transition in electron systems [13]. Such order in oxygen vacancies has been typically observed when $\delta$ = 0.125 ($SrFeO_{2.875}$) [14], $\delta$ = 0.2 ($CaVO_{2.8}$) [15], $\delta$ = 0.25 ($SrFeO_{2.75}$, $Y_{1/2}Ba_{1/2}CoO_{2.75}$) [14, 16], and $\delta$ = 0.4 ($SrMnO_{2.6}$) [17]. Among them, $\delta$ = 0.5 ($ABO_{2.5}$) is a nexus of a number of structures with ordered oxygen vacancies. The brownmillerite structure,

for example $SrCoO_{2.5}$, known as a low temperature oxide conductor, consists of alternate stacks of $CoO_4$ tetrahedral layers and $CoO_6$ octahedral layers (Figure 2.1d).[18] The $LaNiO_{2.5}$ structure contains corner-shared $NiO_6$ octahedral chains along the tetragonal *c*-axis that are linked by $NiO_4$ square planes (Figure 2.1c) [19,20]. $(Y_{1/2}Ba_{1/2})CoO_{2.5}$ and $CaMnO_{2.5}$ consists only of $BO_5$ pyramids, but differ in that the former forms oxygen vacancy layers as a result of $Y^{3+}/Ba^{2+}$ order along the *c* axis (Figure 2.1e) [22], while the latter forms one-dimensional vacancy channels (Figure 2.1f) [17,21]. The $BaFeO_{2.5}$ structure contains three kinds of Fe coordination geometries, octahedra, pyramids, tetrahedra (Figure 2.1g) [23].

The infinite layer (IL) structure $ABO_2$ ($\delta$ = 1; Figure 2.1b) is the most oxygen-deficient perovskite, where relative to $ABO_3$, the apical oxygen atoms are completely removed to form $BO_4$ square planar coordination. $SrCuO_2$ [24] , $LaNiO_2$ [25], and $SrFeO_2$ [26] adopt this structure. Among them, $SrCuO_2$ was investigated intensively, exploiting high pressure synthesis, in order to electron-dope by lanthanide substitution [27,28] and to apply chemical pressure by Ba- or Ca-substitution for Sr [24]. The formation of $LaNiO_2$ is naturally understood because $Ni^+$ has the same $d^9$ electronic configurations as $Cu^{2+}$ with a half-filled $d_{x2-y2}$ orbital that favors square planar geometry. Though not Jahn-Teller active, $Fe^{2+}$ ($d^6$) ions in $SrFeO_2$, prepared through a low temperature $CaH_2$ reduction, bear square planar coordination. Interestingly, owing to the highly covalent nature in Fe-O interactions, this iron oxide can tolerate a large amount of A-site substitution; Ba-for-Sr substitution is possible up to 30% [29]. With Ca, the ideal IL structure remains up to 80%, beyond which the $FeO_4$ square planes become slightly distorted toward tetrahedra together with coherent rotation, providing a distorted IL structure [30, 31]. Other than the IL structure, the so-called 8-8-16 structure, $(La,Sr)CuO_2$ with two-, four- and five-coordinated copper was reported for $\delta$ = 1 (Figure 2.1h) [32].

Given iron's abundance and low toxicity, exploring novel iron oxides is a significant issue. The series of square planar coordinate iron oxides such as $SrFeO_2$ [24], $Sr_3Fe_2O_5$ [33], and $Sr_3Fe_2O_4Cl_2$ [34] is appealing because of their interesting properties including high Néel temperature (473 K) in $SrFeO_2$ and pressure-induced transitions (a spin state transition, an insulator-to-metal transition, and an antiferro-to-ferromagnetic transition) in $SrFeO_2$ [35] and $Sr_3Fe_2O_5$ [36], and a nontrivial spin structure in $Sr(Fe,Mn)O_2$ [37]. These properties originate from extremely strong covalent interactions of $Fe^{2+}$ ions in square planar coordination, as revealed by a small isomer shift (< 0.5 mm/s) in the Mössbauer spectroscopy [24]. Such covalent interactions should be important for applications that work at high temperatures. However, all the reported square planar coordinate iron oxides have been exclusively composed of a single iron site [26,29,31,33,34,38], thereby limiting variations in terms of Fe-O extended networks.

Compared to a conventional $H_2$ gas reaction [39,40], a low temperature reduction by metal hydrides ($CaH_2$, NaH, LiH) is a useful method to introduce more oxygen vacancies in transition metal oxides [41--43]. The reducing power of these metal hydrides is strong even at low temperatures (< 500 °C), while the use of low temperature helps the reaction to proceed topochemically. In this study, we report a novel oxygen vacancy ordered perovskite structure with the $ABO_2$ composition. The topochemical low temperature synthesis, and the chemical and structural characterization of $(Sr_{1-x}Ba_x)FeO_2$ ($0 \leq x \leq 1.0$) are presented. It was previously demonstrated that $(Sr_{1-x}Ba_x)FeO_2$ for $0 \leq x \leq 0.3$ crystallizes in the ideal IL structure [29]. However, we found here that additional Ba substitution induces a first-order structural transition involving a large, discontinuous lattice expansion. The resulting new structure is an oxygen deficient perovskite related in part to the $LaNiO_{2.5}$ structure, but with extensive oxygen defects and disorder (thus with various coordination geometries). Magnetic

properties and the effect of aliovalent A-site substitution ascribed, in part, to the flexible oxygen composition in this structural framework, are demonstrated.

## 2.2. Experimental

Precursor materials $(Sr_{1-x}Ba_x)FeO_{3-\delta}$ ($x$ = 0.4, 0.5, 0.6, 0.7, 0.8, 0.9 and 1.0; $\delta \leq 0.5$) were prepared by mixing stoichiometric amounts of $SrCO_3$ (99.99%), $BaCO_3$ (99.99%) and $Fe_2O_3$ (99.99%), pelletizing and heating at 1473 K in air for 48 h with one intermediate grinding. For $x$ = 0.9 and 1.0, the heat treatment in air led to a hexagonal perovskite phase $(Sr,Ba)Fe^{4+}O_3$ as reported [44]. We prevented formation of the hexagonal phase by heating the mixture in a reducing atmosphere to stabilize a phase with a lower iron valence; we successfully obtained a monoclinic phase $(Sr,Ba)Fe^{3+}O_{2.5}$ by heating at 1273 K for 24 h in flowing nitrogen with one intermediate grinding [23].

The obtained precursors were ground well with a two molar excess of $CaH_2$ in an Ar-filled glovebox, sealed in an evacuated Pyrex tube (volume 15 $cm^3$) with a residual pressure less than $1.3\times10^{-8}$ MPa, and reacted under various temperatures and durations as listed in Table 1. The residual $CaH_2$ and the CaO byproduct were removed by washing with an $NH_4Cl$/methanol solution (0.15 mol/L). It is seen from Table 1 that for $x$ = 0.4 - 0.9, the annealing temperature higher than 593 K and the reaction time longer than 3 days is required in order to complete the reaction. Note that $SrFeO_2$ can be prepared at 553 K within 1 day [26]. When $(Sr_{1-x}Ba_x)FeO_{3-\delta}$ ($x$ = 0.5 - 0.8) were heated with $CaH_2$ at lower temperatures, e.g., 573 K for 3 days, a small amount of a non-reacted $(Sr,Ba)FeO_{2.5}$ phase was obtained together with the new $(Sr,Ba)FeO_2$ phase. For $x$ = 0.4 and 0.9, one requires 14 days of reaction time at 593 K to isolate the pure phase.

However, the $CaH_2$ reduction of $BaFeO_{2.5}$ ($x$ = 1) failed in any conditions employed; the precursor decomposed to (Sr,Ba)O and Fe when reacted at 773 K, while no reaction occurred when reacted at 673 K. Consequently, we used NaH as an alternative reductant and obtained the $BaFeO_2$ phase; $BaFeO_{2.5}$ was ground with a two-molar excess of NaH in the Ar-filled glovebox, sealed in the same way, and reacted at 413 K for 3 days. The residual NaH and the NaOH byproduct were removed by washing with methanol.

It was observed that, when kept in air for a week, the $x$ = 0.5, 0.6, 0.7, 0.8 samples were partially oxidized, while the $x$ = 0.4, 0.9, and 1.0 compositions were much more air sensitive; storing in the Ar-filled glovebox (1 ppm < $H_2O$, 1 ppm < $O_2$) for several days resulted in oxidization back to (Sr,Ba)$FeO_{2.5}$. It is likely that the average A-site radius in the range of $x$ = 0.5 - 0.8 is accommodated best by the structure.

La substitution at the barium site was attempted with the ultimate motivation to dope electrons to the $Fe^{2+}O_2$ layer and induce metallic conductivity (superconductivity). The oxygen-deficient precursor perovskite $(Ba_{0.8}La_{0.2})FeO_{3-\delta}$ ($\delta$ < 0.5) was prepared by mixing stoichiometric amounts of $La_2O_3$ (99.9%), $BaCO_3$ (99.99%) and $Fe_2O_3$ (99.99%), pelletizing and heating at 1473 K for 24 h in air. Subsequently, the pellet was ground, pelletized and heated at 1573 K for 24 h in air. The obtained precursor was ground thoroughly with a two molar excess of NaH in the Ar-filled glovebox, sealed, and reacted at 443 K for 3 days. The final product, isolated by washing with methanol, was air sensitive as was $BaFeO_2$.

The sample purity of precursors and final products was checked by X-ray diffraction (XRD) using a M18XHF diffractometer (Mac Science) and a D8 ADVANCE diffractometer (Burker AXS) with Cu $K_\alpha$ radiation ($\lambda$ = 1.54056 Å). For structural refinements of $(Sr_{0.2}Ba_{0.8})FeO_2$, the most stable composition, high resolution synchrotron powder XRD experiments were performed at room temperature using a large Debye-Scherrer camera

installed at beamline BL02B2 of the Japan Synchrotron Radiation Research Institute (SPring-8). We used an imaging plate as a detector. Incident beams from a bending magnet were monochromatized to 0.7755 Å. The finely ground powder samples were sieved (32 μm) and put into a Pyrex capillary of 0.1 mm in inner diameter. The sealed capillary was rotated during measurements so as to reduce the effect of potential preferential orientation.

Powder neutron diffraction experiments on $(Sr_{0.4}Ba_{0.6})FeO_2$ and $(Sr_{0.2}Ba_{0.8})FeO_2$ were carried out on the Kinken powder diffractometer with multicounters for HERMES (High Efficiency and high Resolution MEasurementS) of the Institute for Materials Research, Tohoku University, installed at a guide hall of JRR-3 reactor in the Japan Atomic Energy Agency (JAEA), Tokai [45]. The incident neutron was monochromatized to 1.82646 Å by the 331 reflection of vent Ge crystal. A 12'-blank-sample-18' collimation was employed. A polycrystalline sample of 3 g was placed into a He-filled vanadium cylinder. The sample temperature was controlled from 20 K to 298 K. The data were collected with a step scan procedure using 150 $^3$He tube detectors in a $2\theta$ range from 3° to 153° with a step width of 0.1°.

The obtained synchrotron XRD and neutron diffraction data were analyzed by the Rietveld method using the RIETAN-FP program [46]. The agreement indices used were *R*-weighted pattern, $R_{wp} = [\sum w_i(y_{io} - y_{ic})^2/\sum w_i(y_{io})^2]^{1/2}$, *R*-pattern, $R_p = \Sigma|y_{io} - y_{ic}|/\Sigma(y_{io})$ and goodness of fit (GOF), $\chi^2 = [R_{wp}/R_{exp}]^2$, where $R_{exp} = [(N - P)/ \sum w_i y_{io}^2]^{1/2}$, $y_{io}$ and $y_{ic}$ are the observed and calculated intensities, $w_i$ is the weighting factor, $N$ is the total number of $y_{io}$ data when the background is refined, and $P$ is the number of adjusted parameters.

Thermogravimetric (TG) data of the reduced compounds were collected using a TG-DTA 2000S (Bruker AXS). Typically, 50 mg of sample was put in a Pt pan and $\alpha$-$Al_2O_3$ was used as a reference. The measurements were performed by heating the sample at 10 K/min under a

flow of oxygen with a flow rate of 100 mL/min. The samples after the measurements were identified by XRD measurements.

Mössbauer spectra on $(Sr_{1-x}Ba_x)FeO_2$ for $x$ = 0.5, 0.6, 0.7, 0.8 and the La-substituted sample after the reduction were taken at room temperature in transmission geometry using a $^{57}$Co/Rh $\gamma$-ray source. The source velocity was calibrated by $\alpha$-Fe as a reference material. Electrical resistivity of the La-substituted sample after the reduction was measured between 210 K and 298 K using a two-probe method. The sample was pelletized to a cylinder (6 $\phi \times$ 1 mm) and was sealed by a He-filled container. To check the effect of electrodes, the ohmic behavior of the sample was proved in a low-voltage regime. Activation energies were estimated from the temperature dependence of the resistivity above 230 K by Arrhenius plots.

## 2.3. Results and Discussions

### *2.3.1. Synthesis and Lattice Evolution*

The formation of the $(Sr,Ba)FeO_{3-\delta}$ precursors ($\delta \leq 0.5$) was confirmed by laboratory XRD (Figure 2.2a). All the diffraction peaks of the precursors ($x \leq 0.8$) were indexed in a pseudo cubic unit cell with $a \sim 3.9$ Å (when tiny superreflection peaks were neglected), while those of the precursors ($x$ = 0.9 and 1.0) were indexed in a monoclinic superstructure of $Ba_{28}Fe_{28}O_{70}$ ($BaFeO_{2.5}$), in consistency with the previous report [23]. No impurity phases were detected for all precursors. The lattice parameters for $x \leq 0.8$ increase with increasing $x$ (Figure 2.2b), which is consistent with the larger ionic radius of $Ba^{2+}$ (vs. $Sr^{2+}$). Non-linear $x$ dependence of the lattice parameters implies that the oxygen content varies with $x$.

Figure 2.3a shows the XRD patterns of the $x$ = 0.3–1.0 compounds after the hydride reduction. All the profiles are readily indexed on the basis of a tetragonal unit cell. It can be recognized that, relative to the $x$ = 0.3 sample crystallizing in the IL structure [29], the XRD

peaks for $x \geq 0.4$ are largely shifted to lower angles. In addition, several additional superreflections, related to the simple perovskite cell ($a_p \times b_p \times c_p$) by $2a_p \times 2a_p \times c_p$, are observed. No impurity could be found within the experimental resolution.

For the sake of comparison, the normalized lattice parameters, $a_p$ (= $a$/2) and $c$, are plotted in the whole $x$ range ($0 \leq x \leq 1$) in Figure 2.3b. A prominent jump of the lattice parameters is seen between $x$ = 0.3 and 0.4, strongly indicating a first-order structural phase transition from the IL structure to a new structure with much less density. For $x \geq 0.4$, both crystallographic axes increase linearly with $x$ (Vegard's law), meaning plausibly that, whatever the new structure is, it forms a solid solution and that the oxygen content is unvaried with $x$. The difference in the cell parameters between $x$ = 0.3 and 0.4 are 1.7% for $a$ and 5.7% for $c$. The larger increase along the $c$ axis suggests that the new phase of $x \geq 0.4$ contains apical oxygen atoms at least to a certain extent, in contrast to the IL structure where oxygen atoms are exclusively absent at the apical site of $BO_4$ square plane (B = $Cu^{2+}$, $Ni^{+}$, $Fe^{2+}$). For $x \leq 0.3$, the $c$ axis increases more steeply than the $a$ axis with $x$ ($\Delta c$(Å) = $0.36\Delta x$ vs. $\Delta a$(Å) = $0.06\Delta x$), reflecting the two dimensional nature of the IL structure. On the other hand, the lattice evolution for $0.4 \leq x$ is given by $\Delta a$(Å) = $0.18\Delta x$ and $\Delta c$(Å) = $0.15\Delta x$, indicating that the new structure is likely to be three dimensional.

As mentioned above, the linear increase of the lattice parameters for $x \geq 0.4$ suggests a constant oxygen content. The TG measurement was carried out to quantify the oxygen stoichiometry. The $x$ = 0.8 sample was chosen for this experiment because of its superior chemical stability. As shown in Figure 2.4, a double weight increase separated by a plateau was observed. A very similar behavior was obtained previously in $SrFeO_2$, $(Sr_{0.8}Ca_{0.2})FeO_2$, and $(Sr_{0.8}Ba_{0.2})FeO_2$ [29]. The XRD inspection after rapid quenching of the TG furnace revealed that the plateau in Figure 2.4 corresponds to the $(Sr_{0.2}Ba_{0.8})FeO_{2.5}$ phase with the

monoclinic $BaFeO_{2.5}$ structure [23], and this phase is, upon further heating, oxidized to the pseudo cubic oxygen-deficient perovskite $(Sr_{0.2}Ba_{0.8})FeO_{3-\delta}$ ($\delta < 0.5$). Supposing the oxygen content at the plateau is 2.5, then that of the initial phase can be calculated as 2.0. Thus, the chemical formula of the new phase ($x \geq 0.4$) as well as the IL phase ($x \leq 0.3$) can be defined as $(Sr_{1-x}Ba_x)FeO_2$. Moreover, the facile oxidation of $(Sr_{0.2}Ba_{0.8})FeO_2$ to $(Sr_{0.2}Ba_{0.8})FeO_{2.5}$ and $(Sr_{0.2}Ba_{0.8})FeO_{3-\delta}$ ($\delta < 0.5$) at low temperatures (< 600 K), and vice versa suggests a topochemical conversion; namely, the new phase is structurally related to the perovskite structure.

*2.3.2. Structural Refinements*

The structural refinement of synchrotron XRD and neutron diffraction was performed for $x = 0.8$. This composition was selected because of the highest chemical stability and also because of the highest crystallinity revealed by the laboratory XRD experiments. Shown in Figure 2.5a is the synchrotron XRD pattern, which could be indexed on a tetragonal $2a_p \times 2a_p \times c_p$ cell, with $a = 8.302$ Å and $c = 3.845$ Å, in consistency with the laboratory XRD data. No systematic extinct reflections were present. From this, one can derive possible tetragonal space groups as *P*4/*mmm*, *P*-42*m*, *P*-4*m*2, *P*4*mm*, *P*422, *P*4/*m*, *P*-4 and *P*4. There are several unindexed peaks at 9.1°, 14.7° and 18.7° (with intensities less than 0.5% of the main peak), which could not be assigned by assuming a lowered symmetry or a superstructure. Thus they come from tiny impurity phases. We initially built a structural model on the basis of the IL structure (space group *P*4/*mmm*), but using the $2a_P \times 2a_P \times c_P$ cell. The A-site was placed at (*x*, *x*, 1/2), where 20% of Sr and 80% of Ba atoms are randomly distributed. Three Fe atoms were placed at 1*a* (0, 0, 0), 1*c* (1/2, 1/2, 0), 2*f* (0, 1/2, 0), and two O atoms at 4*l* (*x*, 0, 0), 4*n*

($x$, 1/2, 0). Here, all the variable atomic coordinates were initially set as 1/4. This IL-derivative model resulted in a rather poor agreement at its best with $\chi^2 = 16.48$.

Accordingly, as a next step the symmetry was lowered to the maximum non-isomorphic sub-space groups for *P*4/*mmm*, that is, *P*-42*m*, *P*-4*m*2, *P*4*mm*, *P*422, and *P*4/*m*. Among them *P*4*mm* led to the best result, but the agreement factors were still poor ($\chi^2$ values became never better than 15.5). *P*4 and *P*-4, the maximum non-isomorphic sub-space groups, respectively for *P*4*mm*, *P*422, *P*4/*m* and for *P*-42*m*, *P*-4*m*2, *P*4/*m* did not improve the result as well. These results indicate that the real structure deviates significantly from the IL model assumed here.

To find a clue to reach a proper structural model, maximum entropy method (MEM) analysis was carried out by using the model with *P*4/*mmm* space group. Figure 2.6 clearly demonstrates the presence of finite electron density at the apical sites of the square planar iron center. This indicates that the new structure indeed contains apical oxygen atoms, unlike the IL structure. Note that the $c$ axis shows a prominent jump ($\Delta c \sim 0.20$ Å) upon the structural transition when going from the IL phase to the new phase (Figure 2.3b). This observation also supports a model in which the apical oxygen sites are occupied, at least to a certain extent. Consequently, we decided to start from a model with apical oxygen atoms. Namely, O(3) on 1*b* (0, 0, 1/2), O(4) on 1*d* (1/2, 1/2, 1/2) and O(5) on 2*e* (1/2, 0, 1/2) were added as the apical sites to the IL model. When the occupancy factors ($g$) of the oxygen sites were allowed to move, the $g$ value for O(5) always became close to zero, so it was fixed to zero in consequent refinements. On the other hand, the $g$ values for O(1) and O(3) became close to 1 within the error, so they were fixed to unity. It was conversely observed that the $g$ values for O(2) and O(4) reduced to ~0.6. Up to this point, we did not put any constraint on the total oxygen content. However, this analysis led to a total oxygen content being close to 2,

in a reasonable agreement with that obtained from the TG measurements (Figure 2.4). In addition, this model drastically improved the refinement with $\chi^2 = 8.14$.

Although the model involving apical oxygen sites led to the much better refinement, several atomic displacement parameters were relatively high, e.g., $U_{iso} \sim 0.03$ Å$^2$ for Fe(2) and $U_{iso} \sim 0.05$ Å$^2$ for Fe(3) and $U_{iso} \sim 0.2$ Å$^2$ for O(4). Since one vacancy at the O(2) site creates a Fe(2)$O_3$ coordination environment, Fe(2) would move away from the vacancy. Thus, the three-coordinate iron atom, Fe(2)', was placed at 4*n* (*x*, 1/2, 0), while the four-coordinate Fe(2) remained at the more symmetric 2*f* (0, 1/2, 0). This attempt gave $x \sim 0.042$ for Fe(2)' and reasonably small atomic displacement parameters of $U_{iso} < 0.01$ Å$^2$ were obtained for Fe(2) and Fe(2)'. In contrast, we could not reduce the *U* values of the Fe(3) and the O(4) sites by introduction of site disorder nor superstructure along the *c* axis. Therefore, anisotropic displacement parameters $U_{ij}$ were used for these sites, and highly anisotropic displacements were obtained; the Fe(3) atom is displaced along the *c* axis and the O(4) atom along the *c* axis and the *ab* plane.

In order to check this proposed structure, and in particular to obtain more precise information on the oxygen positions and their site occupancies, we performed Rietveld refinement using powder neutron diffraction data of the same compound, $(Sr_{0.2}Ba_{0.8})FeO_2$ (see Figure 2.5b). Like the synchrotron XRD, the neutron diffraction pattern at room temperature could be indexed on a tetragonal $2a_p \times 2a_p \times c_p$ cell. Note that tiny peaks at 9.5° and 43.7° result from unknown impurity phases. We started the refinement with the final model obtained from the synchrotron XRD data. During the refinement, the atomic parameters of the O atoms including occupancy factors were allowed to move, while those of Sr, Ba, and Fe atoms were fixed. Then, we returned to the synchrotron XRD data for mainly refining the atomic parameters of the A and Fe atoms, while retaining adjustable parameters

of O atoms. After this process was repeated several times, the oxygen content was converged to 2.04(1), which is very close to 2.0 obtained from the TG measurements. Therefore, we decided to fix the oxygen stoichiometry to 2. Agreement parameters for the neutron refinement are $R_p$ = 3.17%, $R_{wp}$ = 4.73%, $\chi^2$ = 4.14, $R_I$ = 2.20%, $R_F$ = 1.73% for the synchrotron XRD and $R_p$ = 4.43%, $R_{wp}$ = 5.63%, $\chi^2$ = 2.94, $R_I$ = 5.46%, $R_F$ = 3.56%. The other space groups with lower symmetry did not lead to better results, and we concluded that *P*4/*mmm* is the most likely space group. The final refinement results are summarized in Table 2.2 and the structure is represented in Figure 2.7.

From various experimental observations as addressed above, the compounds in all the range of $0.4 \leq x \leq 1.0$ should be isostructural. Let us call hereafter the refined structure the $BaFeO_2$ structure. The $BaFeO_2$ structure can be described as an "oxygen deficient" $LaNiO_{2.5}$ structure, which consists of octahedral chains interlinked by square planar units (Figure 2.1c). However, this similarity does not mean that the $BaFeO_2$ structure was formed by the mere and gradual deintercalation of oxide ions from a $LaNiO_{2.5}$ structure. First, $BaFeO_2$ is a line phase, which means that it has a defined composition and lattice parameters. Upon reduction of $BaFeO_{2.5}$ the oxygen content discontinuously changes from 2.5 and 2 (see Figure 2.8). In addition, the conversion of $BaFeO_2$ from $BaFeO_{2.5}$ ($Ba_{28}Fe_{28}O_{70}$; Figure 2.1g) [23] involves not only extraction of, but also rearrangement of oxide ions. Such a dynamic conversion involving framework rearrangement has also been observed in $SrFeO_2$ (from $SrFeO_{2.5}$), $LaNiO_2$ (from $LaNiO_{2.5}$)[19, 20] and $Sr_3Fe_2O_5$ (from $Sr_3FeO_6$) [26,33]. Because of the higher reactivity and air sensitivity, $BaFeO_2$ is oxidized back to $BaFeO_{2.5}$ even at room temperature, as in $CaFeO_2$ and $Sr_3Fe_2O_5$.

The coordination geometries around iron are illustrated in Figure 2.7c. There are four iron atoms, Fe(1), Fe(2) × 2, and Fe(3) in the unit cell. Fe(1) resides in a flattened $FeO_6$

octahedron with four long Fe(1)-O(1) bonds (2.352 Å) along the *a*(*b*) axis and two short Fe(1)-O(3) bonds (1.923 Å) along the *c* axis. Bond valence sum (BVS) calculations [47] for Fe(1) gave +1.95. The O(1) site is fully occupied while the occupancy of the O(2) site is 0.604, meaning that Fe(2)'$O_3$ trigonal planar and Fe(2)$O_4$ rhomboidally distorted square planar coordination geometries are randomly distributed, at a rate of 79:21. The four-coordinate Fe(2) has two short Fe(2)-O(1) bonds (1.799 Å) and two long Fe(2)-O(2) bonds (2.212 Å), giving the BVS of +2.23. The three-coordinate Fe(2)' has two Fe(2)'-O(1) bonds (1.833 Å) and one Fe(2)'-O(2) bond (1.863 Å), giving the BVS of +2.24. This indicates that Fe(2) and Fe(2)' are also divalent. Fe(3) would have an octahedral coordination, if one could neglect oxygen deficiencies at O(2) and O(4). However, taking the oxygen deficiencies into consideration, the average Fe(3) coordination number is 3.58, implying that the majority of the Fe(3) atoms should be in three- or four-fold coordination. The BVS calculations for the three- and four-coordinate Fe(3) gave +1.72-1.78 and +2.30-2.35, so that this iron site is likely to be divalent. In this way, the three kinds of iron are coordinated quite differently, but they are all divalent, which is once again consistent with the oxygen content of 2.

### *2.3.3. Mössbauer Spectroscopy*

To obtain more insight into local geometries around iron, $^{57}$Fe Mössbauer spectra were collected for $x$ = 0.5, 0.6, 0.7, and 0.8 at room temperature (Figures 2.9a). $BaFeO_2$ ($x$ = 1.0) was not measured because of its high air-sensitivity. At any concentration measured, the spectrum consists of four sets of paramagnetic doublets, which were well fitted by Lorentzian functions. The results are summarized in Figure 2.9b. All the Mössbauer parameters for $x$ = 0.5 - 0.8 are similar to each other, supporting the successful formation of the new phase as a solid solution.

The black subspectrum has a spectrum weight of 15% and has an isomer shift (*IS*) of ~0.35 mm/sec, which is a typical value for trivalent iron in a high spin state. Upon cooling the specimen below $T_N$, the shape of this doublet did not exhibit any splitting, while other doublets became sextets (not shown), implying that the former does not come from $(Sr_{0.2}Ba_{0.8})FeO_2$. Although no impurity phase was detected by laboratory XRD studies, it probably arises from a trivalent iron-containing paramagnetic amorphous impurity. It is probably formed by over-reduction and decomposition during the hydride reduction and then oxidation to Fe(III) upon exposure to air. We note that relative subspectrum area derived from amorphous impurity increased when a more severe reducing condition was employed (e.g., increased reaction temperature). Such an amorphous impurity phase was also observed in the Mössbauer spectroscopy of $(Sr,Ca)FeO_2$ and $(Sr_{1-x}Ba_x)FeO_2$ ($x \leq 0.3$) [29, 31]. Note that the Mössbauer specimen is different from that used for the TG measurement in Figure 2.4; when the impurity is ignored, the TG data for the Mössbauer specimen gives the oxygen content of 2.1, reasonably in consistent with the existence of the Fe(III) impurity phase of such amount.

The three other Mössbauer subspectra intrinsic to $(Sr,Ba)FeO_2$ are well consistent with the crystal structure proposed. Spectrum weights for yellow, green, blue curves in Figure 2.9a are 22%, 42%, 21%, respectively. The 1:2:1 ratio of the spectrum weight is what is expected from one Fe(1) ion, two Fe(2) (Fe(2)') ions and one Fe(3) ion in the unit cell. It is straightforward to determine which subspectrum corresponds to which iron site. The green subspectrum with the doubled intensity is assigned to Fe(2) and Fe(2)' in the distorted square planar and trigonal coordination. The yellow subspectrum has a narrow full width at half maximum (FWHM) of 0.30 mm/sec, which is close to instrumental resolution. This spectrum is thus assigned to the Fe(1) site because the $Fe(1)O_6$ octahedron is free from oxygen defects.

The *IS* value of ~0.8 mm/sec is typical for a divalent high-spin iron in an octahedral environment [48]. The blue subspectrum with a much wider FWHM of 0.42 mm/sec is assigned to the Fe(3) site because extensive oxygen defects are present around Fe(3).

We would like to point out again that the new (Sr,Ba)$FeO_2$ compound is a line phase and is reduced (oxidized) discontinuously from (to) (Sr,Ba)$FeO_{2.5}$. It is therefore different from the typical non-stoichiometric oxides, where the oxygen content continuously varies. In such a non-stoichiometric oxide system, more weakly bonded sites are subject to oxygen deficiency. What is observed in (Sr,Ba)$FeO_2$ is, however, opposed to this general trend; despite significant oxygen deficiency, Fe(2) (Fe(2)') and Fe(3) have smaller *IS* values of 0.24 and 0.29 mm/sec than Fe(1) and typical divalent iron in a high-spin state [48]. Namely, the iron ions with oxygen vacancies in (Sr,Ba)$FeO_2$ are far more covalently bonded.

Fe(2) is in the rhomboidally distorted square planar coordination and Fe(2)' is in the trigonal coordination. Therefore, the covalent bonding nature is not limited to the ideal square planar coordination, but is a common nature for iron in planar coordination geometry. In order to confirm this, we prepared $Sr_3La(Fe,Co)_3O_{7.5}$ [43] and performed a Mössbauer experiments to find that the trigonal planar site indeed has a similar value of *IS* = 0.32 mm/sec.

As mentioned above, the majority of Fe(3) atoms should be in three- and four-fold coordination. The small *IS* value of 0.29 mm/sec means that Fe(3) is also in planar geometry. If this is so, it is highly possible, despite the absence of long-range vacancy order, that the oxygen vacancies around Fe(3) are not statistically distributed at the octahedral site. Namely, two- and three-vacancies around a certain Fe(3) atom should *selectively* form, respectively, square planar and trigonal coordination. Such a selective local configuration is reminiscent of the recent work by Attfield et al., who demonstrated a *local* anion order, i.e., *cis*-

conformation of nitrogen atoms in $MO_4N_2$ octahedra in the absence of long-range anionic order [49].

### *2.3.4. $BaFeO_2$ Structure*

Although the oxygen content of the reduced materials is unvaried in the whole range of $x$ ($0 \leq x \leq 1$), the $BaFeO_2$ structure differs from the IL structure[24,27,28] and the distorted IL structure $CaFeO_2$ [31], in a number of points. One of the notable features is the ability of square planar coordination to coexist with other coordination polyhedra, giving a three-dimensional extended network. The present result provides a possibility that one can obtain iron oxides with various coordination geometries including square planes. The deformation from the ideal square plane is also distinct; while the Ca-for-Sr substitution of $SrFeO_2$ beyond the critical concentration (around 80%) leads to a tetrahedral distortion, the Ba-for-Sr substitution for $x \geq 0.4$ leads to a rhomboidal distortion. The strong covalency in $FeO_4$ square planar coordination, as probed by Mössbauer spectroscopy, would permit two types of distortion.

The distortion of $FeO_4$ square planes in the $CaFeO_2$ structure is accounted for by the smaller Ca ion less comfortable in the ideal IL structure, preferring to decrease the coordination number to six from eight [31]. By analogy, the $BaFeO_2$ structure might also be rationalized by the coordination environment around the Ba ion. However, this does not seem to be the case. The BVS of the A-site cation in $(Sr_{0.2}Ba_{0.8})FeO_2$ is +1.69, which is smaller than the theoretical value of +2, whereas +2.02 is obtained when a hypothetical IL structure of $(Sr_{0.2}Ba_{0.8})FeO_2$ is assumed, where the lattice parameters are determined by linear extrapolation of the curves in Figure 2.3b. This fact indicates that the key to stabilizing the $BaFeO_2$ structure and/or to destabilize the IL structure lies in the iron environment. In the

hypothetical IL structure of $(Sr_{0.2}Ba_{0.8})FeO_2$, the BVS of the iron ion is +1.81, which is smaller than the ideal value. It means that the Fe-O bond length now becomes too long to adopt the ideal square planar coordination. In the real structure of $(Sr_{0.2}Ba_{0.8})FeO_2$, the average BVS of iron in planar coordination is +2.23 for Fe(2) and +2.3 for Fe(3), implying that underbonding for A-site is less critical than for the Fe site. Note that the BVS of iron in the solubility limit for the IL phase, $(Sr_{0.7}Ba_{0.3})FeO_2$, is +1.93 [29], further reinforcing our discussion.

Apparently, the $BaFeO_2$ structure is structurally related to $LaNiO_{2.5}$ comprising of one-dimensional octahedral chains linked by square planar units (Figure 2.1c), but there exist several important differences. First, the stability of the oxygen defect ordered structure of $LaNiO_{2.5}$ with two different Ni coordination geometries is brought by appropriate spin configurations; the high-spin state ($S$ = 1) for the octahedral site and the low-spin state ($S$ = 0) for the square planar site [20]. However, in the $BaFeO_2$ structure, all the iron ions are divalent and in a high-spin state ($S$ = 2). Note also that $(La,Sr)CuO_2$, consisting of an ordered polyhedral network with two-, four- and five-fold coordination, has Cu in correspondingly different valance states, +1 and +2.

Another crucial difference concerns the connectivity of the octahedral chains. The planar Fe(2) site is either three or four-fold coordinated, resulting from the oxygen vacancies at O(2). More importantly, the significant oxygen deficiency at O(2) and O(4) around the otherwise octahedral Fe(3) site makes the average coordination number 3.56, a value close to that in the planar Fe(2) site. Thus it would be, in reality, inappropriate to consider Fe(3) as an octahedral site. The $BaFeO_2$ structure could be better described as a pillar-like structure with the Fe(1) octahedral chains bridged loosely by other lower-coordination polyhedra.

The $Fe(1)O_6$ chain-chain distance is rather long, at ~8 Å ($2a_p$). Therefore, why such a loose framework is formed is an interesting question. Fe(3) atom has a quite disordered coordination geometry with oxygen vacancies and is connected only by low-coordinate Fe(2) and Fe(3) atoms, along [100] and [001], respectively. The oxygen vacancies result in a random distribution of disconnected Fe(3)-(O)-Fe(3) and Fe(3)-(O)-Fe(2) bonds. Thus, this iron site will not play a crucial role for the stabilization of the loose framework, although Fe(2) and Fe(3) are covalently bonded resulting presumably from planar coordination geometries as mentioned earlier. What would be essential is the full occupation for the O(1) and O(3) sites, which provides a rigid 3D connection of [-Fe(1)-O(3)-] along the *c* axis and [-Fe(1)-O(1)-Fe(2)-O(1)-] along the *a*(*b*) axis (Figure 2.10). Depending on oxygen occupancy at the O(2) site, Fe(2) adopts square planar or trigonal coordination, but in each case it is connected by two neighboring $Fe(1)O_6$ octahedra. In other words, the Fe(2)-O(2) bonds give firm link with the Fe(1) chains. A similar situation is found in a triple-layered perovskite $Sr_3LaFe_{1.5}Co_{1.5}O_{7.5}$, where the inner perovskite layer, sandwiched by outer $BO_5$ pyramidal layers, consists of 68% of $BO_3$ trigonal coordination (B = Fe/Co) with a significant degree of randomness [43].

### *2.3.5. Physical Properties*

Both Mössbauer and neutron diffraction experiments revealed that $(Sr_{1-x}Ba_x)FeO_2$ ($x \geq 0.8$) is in a paramagnetic state at room temperature, in contrast to the IL structure with $T_N$ far beyond room temperature. When the temperature was decreased (Figure 2.11a), magnetic reflections were observed together with the nuclear reflections. Neutron data revealed a *G*-type spin order, which is the same magnetic structure as the IL phase. The temperature dependence of the neutron diffraction pattern in Figure 2.11b shows that $T_N$ is about 240 K.

From the Rietveld analysis for the $x = 0.8$ data at 20 K, the magnetic moments of all the irons, Fe(1), Fe(2) (Fe(2)'), and Fe(3), are 3.8 $\mu_B$/Fe in magnitude and align in the *ab* plane. Therefore, all the iron ions are in a divalent high-spin configuration, like the IL phase. The neutron diffraction pattern for $(Sr_{0.4}Ba_{0.6})FeO_2$ also shows the same type of spin order and similar magnetic moments of 3.8 $\mu_B$ at 20 K for all the iron sites. The $T_N$ is determined to be 240 K, which is the same as that for $x = 0.8$. These observations indicate that the $x$ dependence of magnetic properties is subtle, despite a non-negligible evolution of the lattice parameters.

The observed transition temperature of 240 K for $x = 0.6$ and 0.8 is much lower than those for $SrFeO_2$ ($T_N$ = 473 K) [26] and $CaFeO_2$ ($T_N$ = 420 K) [31]. The reduction in $T_N$ would result not only from the elongated iron-iron distance (along all the crystallographic directions) but also from the random oxygen deficiencies that break many Fe(2)-O(2)-Fe(3) and Fe(3)-O(4)-Fe(3) superexchange pathways. However, a closer look at the neutron diffraction patterns (Figure 2.11a) revealed that above $T_N$ weak but broad magnetic peaks persist, even at room temperature. No sign of splitting or broadening of the doublets was seen in the room-temperature Mössbauer spectrum. This suggests that a short-range magnetic correlation is already developed at temperatures well beyond $T_N$, but magnetic fluctuations should be faster than the Mössbauer time window ($> 10^{-8}$ s). It is also interesting to compare the magnetic properties of our system with $LaNiO_{2.5}$. Because of the high-spin ($S = 1$) and low-spin ($S = 0$) configurations at the octahedral and square-planar sites, the magnetic property of this nickelate is best characterized by quasi one-dimensional $S = 1$ chains made up of corner-shared $NiO_6$ octahedra along the *c* axis. Namely, although $Ni^{2+}$ ions are connected in the *ab* plane, the square-planar site acts as a non-magnetic separator, and as a result the magnetic order occurs at a rather low temperature ($T_N$ = 80 K) [20].

A trivalent lanthanum-substituted $BaFeO_2$ (**I**) was successfully obtained from the precursor $(Ba_{0.8}La_{0.2})FeO_{3-\delta}$ ($\delta < 0.5$). The XRD pattern of **I** could be indexed in the same tetragonal unit cell as $BaFeO_2$ (Figure 2.12a), and the lattice parameters ($a$ = 8.268 Å and $c$ = 3.846 Å) are slightly smaller than $a$ = 8.375 Å and $c$ = 3.879 Å in $BaFeO_2$. Superreflections corresponding to the $2a_p \times 2a_p \times c_p$ cell are present. These facts indicate that **I** is isostructural with $BaFeO_2$. Because **I** is air sensitive and easily oxidized back to $(Ba_{0.8}La_{0.2})FeO_{3-\delta}$, the Mössbauer spectrum of **I** includes very broad peaks possibly arising from oxidized $(Ba_{0.8}La_{0.2})FeO_{3-\delta}$, as shown in Figure 2.12b. Nevertheless, ignoring this broad background, we were able to fit the spectrum well, as summarized in Figure 2.12b. All the fitted parameters of the subspectra are similar to those of $(Sr_{1-x}Ba_x)FeO_2$ ($x \geq 0.4$), suggesting that all the iron ions in **I** are in similar environments to those in $(Sr_{1-x}Ba_x)FeO_2$ ($x \geq 0.4$), having all the iron sites being divalent and high-spin state. To account for this, the chemical formula must be $(Ba_{0.8}La_{0.2})FeO_{2.1}$. Here, the excess oxygen may occupy the vacant sites at O(2) and O(4) such that the iron valence state of +2 remains unaltered. In general, for a given (fixed) $y$, the reduced phase has a defined composition of $(Ba_{1-y}La_y)FeO_{2+y/2}$.

This compensated composition of $(Ba_{0.8}La_{0.2})FeO_{2.1}$ implies, in part, a failure of electron doping by the La-for-Sr substitution. Nevertheless, as shown in Figure 2.12c, the electrical resistance $\rho$ is measurable, in contrast to $(Sr_{1-x}Ba_x)FeO_2$ ($0 \leq x \leq 1$). The resistivity for $SrFeO_2$ is out of range of our experimental system, and becomes only measurable when pressurized above 15 GPa [35]. The room temperature resistivity of **I** is high in magnitude (~ MΩ cm) and shows a semiconducting behavior with the activation energy of 0.21 eV. Note that a small amount of the amorphous impurity phase can be found in the Mössbauer spectrum. At this point, we cannot totally exclude a possibility that the impurity phase accounts for the resistivity decrease. However, since the amount of impurity estimated from

Mössbauer data is comparable to that of $(Sr_{1-x}Ba_x)FeO_2$ ($0.4 \leq x \leq 1.0$), the lanthanum substitution plus additional oxygen insertion might result in a large change in the electronic structure with a reduced band gap. Theoretical investigation is needed for further understanding of the La-substitution effect on the electronic and physical properties.

## 2.4. Conclusion

$(Sr_{1-x}Ba_x)FeO_2$ ($0.4 \leq x \leq 1.0$) with a novel perovskite-related structure was successfully obtained by low temperature topotactic reaction with calcium hydride ($0.4 \leq x \leq 0.9$) and sodium hydride ($x = 1.0$). The new structure is partly analogous to the $LaNiO_{2.5}$ structure with one-dimensional chains of octahedra linked by planar units, but differs in that one of the octahedral sites has a significant amount of oxygen vacancies and that all the iron ions have the same spin and valence state. Unlike recently reported iron oxides with square planar coordination, this structure demonstrates the ability of the iron square planar coordination to coexist with other types of coordination. Thus, it is expected that a large family of square–planar based iron oxides will be prepared in future. The Mössbauer spectra indicate that the Fe(2) and Fe(3) ions have extremely strong covalency, and this may contribute to the formation of the unique structure. At the same time, the rigidity of a 3D Fe-O-Fe connection which consists of [-Fe(1)-O(3)-] along the *c* axis and [-Fe(1)-O(1)-Fe(2)-O(1)-] along the *a*(*b*) axis acts to strengthen the framework. The extreme covalency of planar coordinate iron and its preferential valence (+2) stabilize this compound as a line phase with a defined composition, despite the presence of structural disorders and partial occupations.

The structural conversion between $BaFeO_2$ and $BaFeO_{2.5}$ involves a complex rearrangement of the oxygen framework at low temperature. The recent work on $CaFeO_{2.5}$-$CaFeO_2$ thin films [50] revealed different oxygen migration pathways with selective kinetics.

Revealing the reaction mechanism (pathway) between $BaFeO_2$ and $BaFeO_{2.5}$ will also be an important subject for future study. We also obtained the La-substituted $BaFeO_2$ and showed that the additional oxygen atoms are incorporated into the structure. The importance of interstitial oxide ions has been recently stressed for the design of oxygen ion conductors [51--54]. The $BaFeO_2$ structure is hence interesting in connection to oxygen ion conductivity.

## References

[1] R. Von Helmolt, J. Wecker, B. Holzapfel, L. Schultz, and K. Samwer, Phys. Rev. Lett. 71 (1993) 2331.

[2] Y. Moritomo, A. Asamitsu, H. Kuwahara, and Y. Tokura, Nature 380 (1996) 141.

[3] S. Jin, T. H. Tiefel, M. McCormack, R. A. Fastnacht, R. Ramesh, and L. H. Chen, Science 264 (1994) 413.

[4] R. E. Cohen, Nature 358 (1992) 136.

[5] P. Lacorre, J. B. Torrance, J. Pannetier, A. I. Nazzal, P. W. Wang, and T. C. Huang, J. Solid State Chem. 91 (1991) 225.

[6] J. A. Alonso, M. J. Martínez-Lope, M. T. Casais, M. A. G. Aranda, and M. T. Fernández-Díaz, J. Am. Chem. Soc. 121 (1999) 4754.

[7] M. Takano, S. Nasu, T. Abe, K. Yamamoto, S. Endo, Y. Takeda, and J. B. Goodenough, Phys. Rev. Lett. 67 (1991) 3267.

[8] D. C. Johnston, H. Prakash, W. H. Zachariasen, and R. Viswanathan, Mater. Res. Bull. 8 (1973) 777.

[9] M. Isobe and Y. Ueda, J. Phys. Soc. Jpn. 71 (2002) 1848.

[10] M. Nishizawa, T. Ise, H. Koshika, T. Itoh, and I. Uchida, Chem. Mater. 12 (2000) 1367.

[11] J. F. Schooley, W. R. Hosler, and M. L. Cohen, Phys. Rev. Lett. 12 (1964) 474.

[12] H. Matsumoto, Y. Furya, S. Okada, T. Tanji, and T. Ishihara, Electrochem. Solid-State Lett. 10 (2007) 11.

[13] E. Abrahams and G. Kotliar, Science 274 (1996) 1853.

[14] J. P. Hodges, S. Short, J. D. Jorgensen, X. Xiong, B. Dabrowski, S. M. Mini, and C. W. Kimball, J. Solid State Chem. 151 (2000) 190.

[15] Y. Ueda and N. Nakayama, Solid State Ionics 108 (1998) 303.

[16] D. Akahoshi and Y. Ueda, J. Solid State Chem. 156 (2001) 355.

[17] L. Suescun, O. Chmaissem, J. Mais, B. Dabrowski, and J. D. Jorgensen, J. Solid State Chem. 180 (2007) 1698.

[18] R. Le Toquin, W. Paulus, A. Cousson, C. Prestipino, and C. Lamberti, J. Am. Chem. Soc. 128 (2006) 13161.

[19] J. A. Alonso, M. J. Martínez-Lope, J. L. García-Muñoz, and M. T. Fernández, Physica B 234 (1997) 18.

[20] J. A. Alonso, M. J. Martínez-Lope, J. L. García-Muñoz, and M. T. Fernández-Díaz, J. Phys. : Condens. Matter 9 (1997) 6417.

[21] K. R. Poeppelmeier, M. E. Leonowicz, and J. M. Longo, J. Solid State Chem. 44 (1982) 89.

[22] T. Vogt, P. M. Woodward, P. Karen, B. A. Hunter, P. Henning, and A. R. Moodenbaugh, Phys. Rev. Lett. 84 (2000) 2969.

[23] X. D. Zou, S. Hovmöller, M. Parras, J. M. González-Calbet, M. Vallet-Regí, and J. C. Grenier, Acta Cryst. A49 (1993) 27.

[24] M. Takano, Y. Takeda, H. Okada, M. Miyamoto, and T. Kusaka, Physica C 159 (1989) 375.

[25] M. Crespin, P. Levitz, and L. Gatineau, J. Chem. Soc. Faraday Trans. 79 (1983) 1181.

[26] Y. Tsujimoto, C. Tassel, N. Hayashi, T. Watanabe, H. Kageyama, K. Yoshimura, M. Takano, M. Ceretti, C. Ritter, and W. Paulus, Nature 450 (2007) 1062.

[27] N. Ikeda, Z. Hiroi, M. Azuma, M. Takano, Y. Bando, and Y. Takeda, Physica C 210 (1993) 367.

[28] M. G. Smith, A. Manthiram, J. Zhou, J. B. Goodenough, and J. T. Markert, Nature 351 (1991) 549.

[29] T. Yamamoto, Z. Li, C. Tassel, *et al*, Inorg. Chem. 49 (2010) 5957.

[30] C. Tassel, T. Watanabe, Y. Tsujimoto, N. Hayashi, A. Kitada, Y. Sumida, T. Yamamoto, H. Kageyama, M. Takano, and K. Yoshimura, J. Am. Chem. Soc. 130 (2008) 3764.

[31] C. Tassel, J. M. Pruneda, N. Hayashi, *et al*, J. Am. Chem. Soc. 131 (2009) 221.

[32] K. Otzschi, K. Koga, and Y. Ueda, J. Solid State Chem. 115 (1995) 490.

[33] H. Kageyama, T. Watanabe, Y. Tsujimoto, *et al*, Angew. Chem. Int. Ed. 47 (2008) 5740.

[34] E. Dixon and M. A. Hayward, Inorg. Chem. 49 (2010) 9649.

[35] T. Kawakami, Y. Tsujimoto, H. Kageyama, *et al*, Nat. Chem. 1 (2009) 371.

[36] T. Yamamoto, C. Tassel, Y. Kobayashi, *et al*, J. Am. Chem. Soc. 133 (2011) 6036.

[37] R. Tamura, N. Kawashima, T. Yamamoto, C. Tassel, and H. Kageyama, Phys. Rev. B 84 (2011) 214408.

[38] L. Seinberg, T. Yamamoto, C. Tassel, *et al*, Inorg. Chem. 50 (2011) 3988.

[39] M. Hayward, M. Green, M. Rosseinsky, and J. Sloan, J. Am. Chem. Soc. 121 (1999) 8843.

[40] M. Hayward, E. Cussen, J. Claridge, M. Bieringer, M. Rosseinsky, C. Kiely, S. Blundell, I. Marshall, and F. Pratt, Science 295 (2002) 1882.

[41] V. V. Poltavets, K. A. Lokshin, S. Dikmen, M. Croft, T. Egami, and M. Greenblatt, J. Am. Chem. Soc. 128 (2006) 9050.

[42] J. Seddon, E. Suard, and M. A. Hayward, J. Am. Chem. Soc. 132 (2010) 2802.

[43] A. Bowman, M. Allix, D. Pelloquin, and M. J. Rosseinsky, J. Am. Chem. Soc. 128 (2006) 12606.

[44] S. Morimoto, K. Kuzushita, and S. Nasu, J. Magn. Magn. Mater. 272-276 (2004) 127.

[45] K. Ohoyama, T. Kanouchi, K. Nemoto, M. Ohashi, T. Kajitani, and Y. Yamaguchi, Jpn. J. Appl. Phys. 37 (1998) 3319.

[46] F. Izumi and K. Momma, Solid State Phenom. 130 (2007) 15.

[47] I. D. Brown and D. Altermatt, Acta Cryst. B41 (1985) 244.

[48] N. N. Greenwood and T. C. Gibb, Mössbauer Spectroscopy (1971) Chapman and Hall: London.

[49] M. Yang, J. Oró-Solé, J. A. Rodgers, A. B. Jorge, A. Fuertes, and J. P. Attfield, Nat. Chem. 3 (2010) 47.

[50] S. Inoue, M. Kawai, N. Ichikawa, H. Kageyama, W. Paulus, and Y. Shimakawa, Nat. Chem. 2 (2010) 213.

[51] E. Boehm, J. M. Bassat, M. C. Steil, P. Dordor, F. Mauvy, and J. C. Grenier, Solid State Sci. 5 (2003) 973.

[52] A. Demourgues, A. Wattiaux, J. C. Grenier, M. Pouchard, J. L. Soubeyroux, J. M. Dance, and P. Hagenmuller, J. Solid State Chem. 105 (1993) 458.

[53] X. Kuang, M. A. Green, H. Niu, P. Zajdel, C. Dickinson, J. B. Claridge, L. Jantsky, and M. J. Rosseinsky, Nat. Mater. 7 (2008) 498.

[54] A. Orera and P. Slater, Chem. Mater. 22 (2009) 675.

**Table 2.1.** Reaction conditions for $(Sr_{1-x}Ba_x)FeO_2$.

| $x$ | Reaction temperature (K) | Reaction time (days) | Reducing agent | Obtained phase |
|---|---|---|---|---|
| 0.0 [a] | 553 | 1 | $CaH_2$ | IL |
| 0.1, 0.2, 0.3[a] | 553 | 3 | $CaH_2$ | IL |
| 0.4 | 593 | 14 | $CaH_2$ | $BaFeO_2$-type |
| 0.5, 0.6, 0.7, 0.8 | 593 | 3 | $CaH_2$ | $BaFeO_2$-type |
| 0.9 | 593 | 14 | $CaH_2$ | $BaFeO_2$-type |
| 1.0 | 413 | 3 | NaH | $BaFeO_2$-type |

[a] We used the values for $x$ = 0.0 – 0.3 in previous studies [26, 29].

**Table 2.2.** Crystallographic data for $(Sr_{0.2}Ba_{0.8})FeO_2$ ($Z$ = 4).[a]

| atom | site | occupancy ($g$) | $x$ | $y$ | $z$ | $U_{iso}$ /Å$^2$ | $U_{11}$ = $U_{22}$ /Å$^2$ | $U_{33}$ /Å$^2$ |
|---|---|---|---|---|---|---|---|---|
| Sr(1) | 4*k* | 0.2 | 0.23667(3) | 0.23667(3) | 0.5 | 0.0098(1) | | |
| Ba(1) | 4*k* | 0.8 | 0.23667(3) | 0.23667(3) | 0.5 | 0.0098(1) | | |
| Fe(1) | 1*a* | 1 | 0 | 0 | 0 | 0.0106(7) | | |
| Fe(2) | 2*f* | 0.208(6) | 0 | 0.5 | 0 | 0.0078(6) | | |
| Fe(2)’ | 4*n* | 0.396(3) | 0.0421(3) | 0.5 | 0 | 0.0078(6) | | |
| Fe(3) | 1*c* | 1 | 0.5 | 0.5 | 0 | | 0.029(1) | 0.91(3) |
| O(1) | 4*l* | 1 | 0.2833(4) | 0 | 0 | 0.023(1) | | |
| O(2) | 4*n* | 0.604(3) | 0.2665(8) | 0.5 | 0 | 0.032(2) | | |
| O(3) | 1*b* | 1 | 0 | 0 | 0.5 | 0.003(1) | | |
| O(4) | 1*d* | 0.583(13) | 0.5 | 0.5 | 0.5 | | 0.29(3) | 0.16(3) |

[a] Space group: *P*4/*mmm*; $a$ = 8.30241(4) Å, $c$ = 3.84506(2) for synchrotron XRD data, and $a$ = 8.3017(2) Å, $c$ = 3.84632(9) Å for neutron diffraction data. [b]

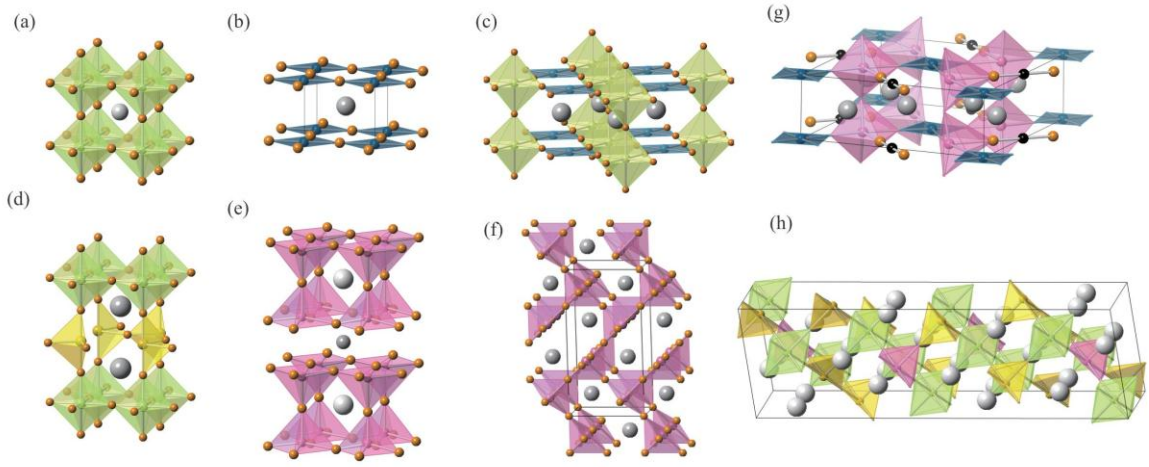


**Figure 2.1**. Structures of perovskite $ABO_3$ and perovskite $ABO_{3-\delta}$ with ordered oxygen vacancies. Perovskite $ABO_3$ with octahedra (a), infinite layer $ABO_2$ ($\delta$ = 1) with square planes (b). Various $ABO_{2.5}$ ($\delta$ = 0.5) structures are shown in (c)-(g). $LaNiO_{2.5}$ with octahedra and square planes (c), Brownmillerite $ABO_{2.5}$ with octahedra and tetrahedra (d), $YBaCoO_{2.5}$ with pyramids (e), $CaMnO_{2.5}$ with pyramids (f), and $BaFeO_{2.5}$ with octahedra, pyramids and tetrahedra (g). The $(La,Sr)CuO_2$ structure is shown in (h). White and gray spheres represent A-site cations. B-site cations lie in the center of the polyhedra and black spheres in (h) represent two-coordinate copper ions.

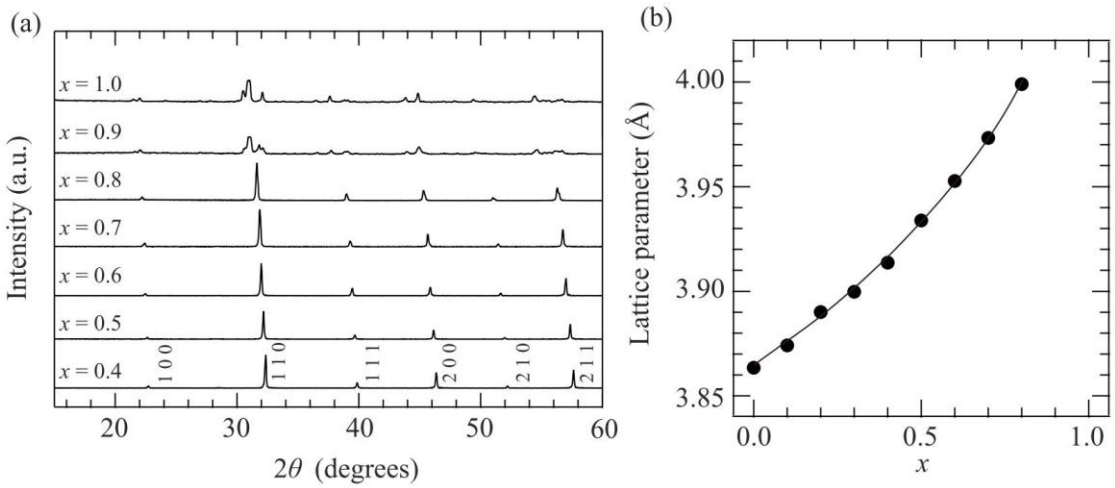


**Figure 2.2**. (a) XRD patterns of the precursors before reduction. The patterns for $x$ = 0.4, 0.5, 0.6, 0.7, and 0.8 could be assigned as cubic perovskite $(Sr_{1-x}Ba_x)FeO_{3-\delta}$ ($\delta < 0.5$), and those for $x$ = 0.9 and 1.0 could be assigned as $(Sr_{1-x}Ba_x)FeO_{2.5}$ with a monoclinic $BaFeO_{2.5}$ structure [23]. (b) Lattice parameters of $(Sr_{1-x}Ba_x)FeO_{3-\delta}$ ($0 \leq x \leq 0.8$). The lattice parameters for $x$ = 0.0 – 0.3 were those obtained from previous studies [26, 29]. The solid line is a guide to the eye. The XRD patterns for $x$ = 0.9 and 1.0 are readily indexed on the basis of a monoclinic unit cell with lattice parameters $a$ = 6.978(4) Å, $b$ = 11.015(7) Å, $c$ = 23.117(16) Å, $\beta$ = 98.22(4)°, $V$ = 1758.6(19) Å$^3$ for $x$ = 0.9 and $a$ = 6.950(1) Å, $b$ = 11.555(2) Å, $c$ = 23.567(3) Å, $\beta$ = 97.53(1)°, $V$ = 1876.3(5) Å$^3$ for $x$ = 1.0.

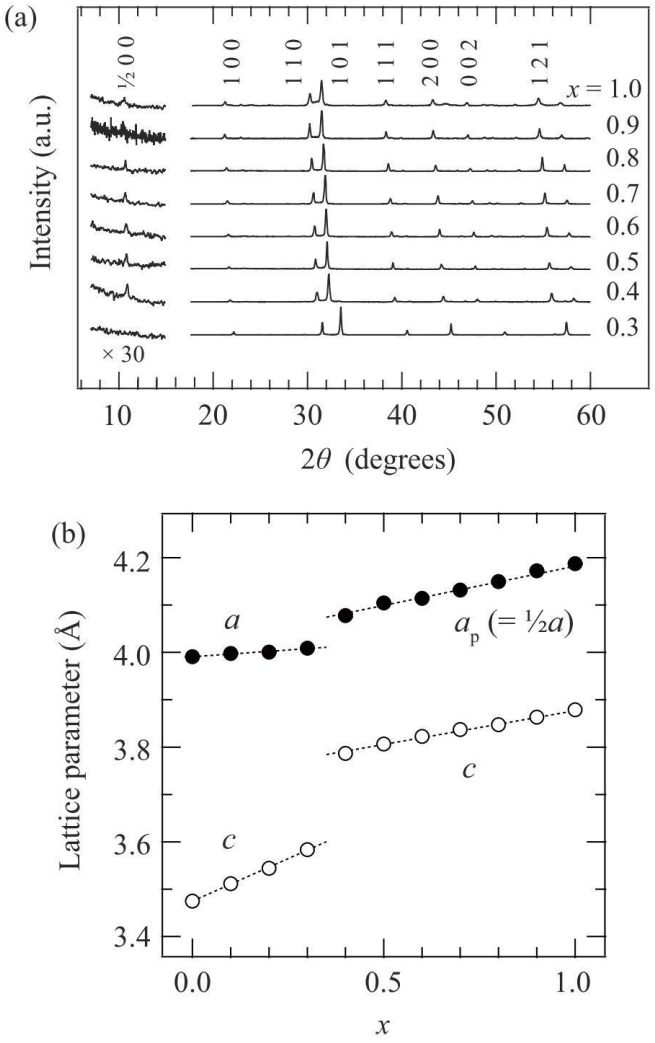


**Figure 2.3.** (a) XRD patterns of $(Sr_{1-x}Ba_x)FeO_2$ ($0.3 \leq x \leq 1.0$). All patterns could be indexed by a tetragonal system. (b) The *a* (closed) and *c* (open) parameters of $(Sr_{1-x}Ba_x)FeO_2$ ($0 \leq x \leq 1$). For comparison, the unit cell of the new structure ($0.4 \leq x \leq 1$) is represented as the perovskite cell ($a_p = 1/2a$). The error bars are within the size of the symbols. The data for $x$ = 0.0 – 0.3 are taken from previous studies [26, 29].

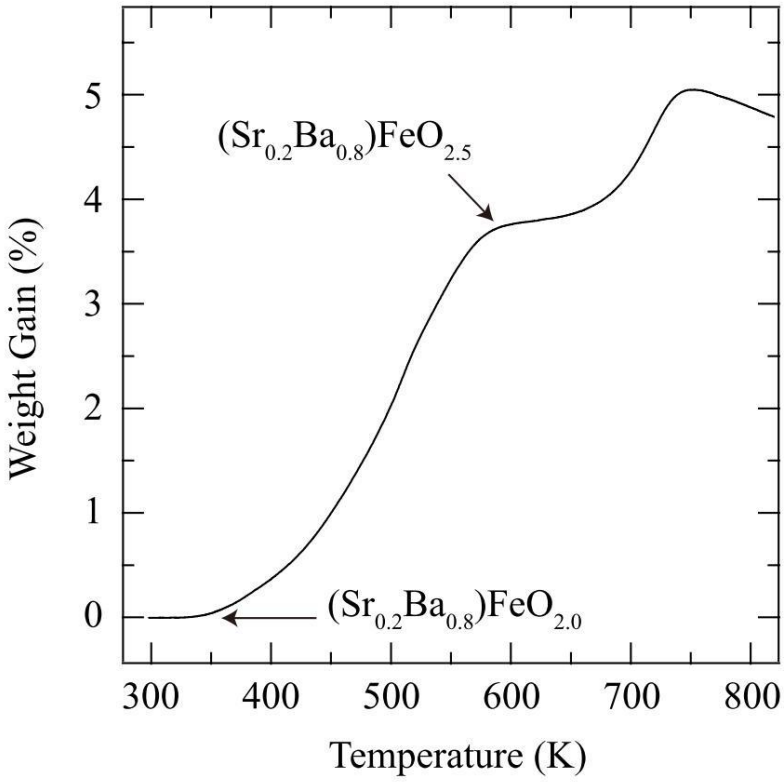


**Figure 2.4.** Oxidation behavior of $(Sr_{0.2}Ba_{0.8})FeO_2$ ($x$ = 0.8) under a flow of oxygen gas.

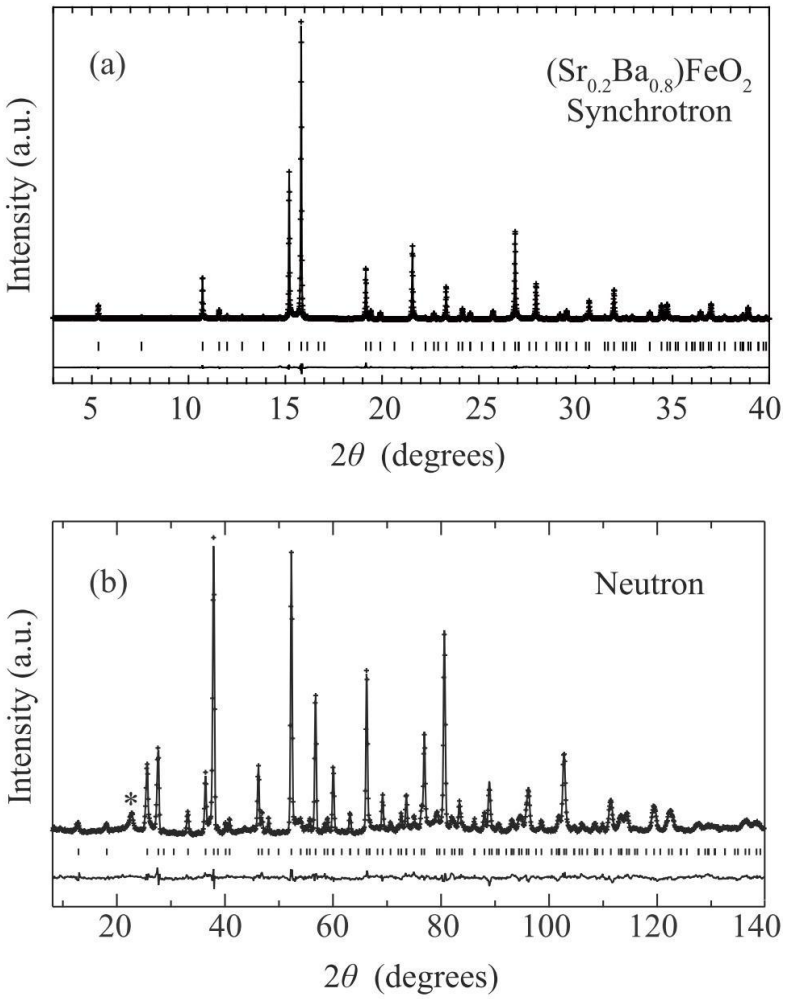


**Figure 2.5.**. (a) Structural characterization of $(Sr_{0.2}Ba_{0.8})FeO_2$ by Rietveld refinement of synchrotron XRD data at room temperature with $\lambda$ = 0.7755 Å ($R_p$ = 3.17%, $R_{wp}$ = 4.73%, $\chi^2$ = 4.14, $R_I$ = 2.20%, $R_F$ = 1.73%), and (b) that of neutron diffraction data at room temperature with $\lambda$ = 1.82646 Å ($R_p$ = 4.43%, $R_{wp}$ = 5.63%, $\chi^2$ = 2.94, $R_I$ = 5.46%, $R_F$ = 3.56%). The overlying crosses and the solid lines represent the observed intensities and the calculated intensities. The bottom solid lines represent the residual intensities. The ticks correspond to the position of the calculated Bragg peaks of the main phase $(Sr_{0.2}Ba_{0.8})FeO_2$. The asterisk in (b) corresponds to a short range magnetic reflection of $(Sr_{0.2}Ba_{0.8})FeO_2$, which was included as the background of the refinement.

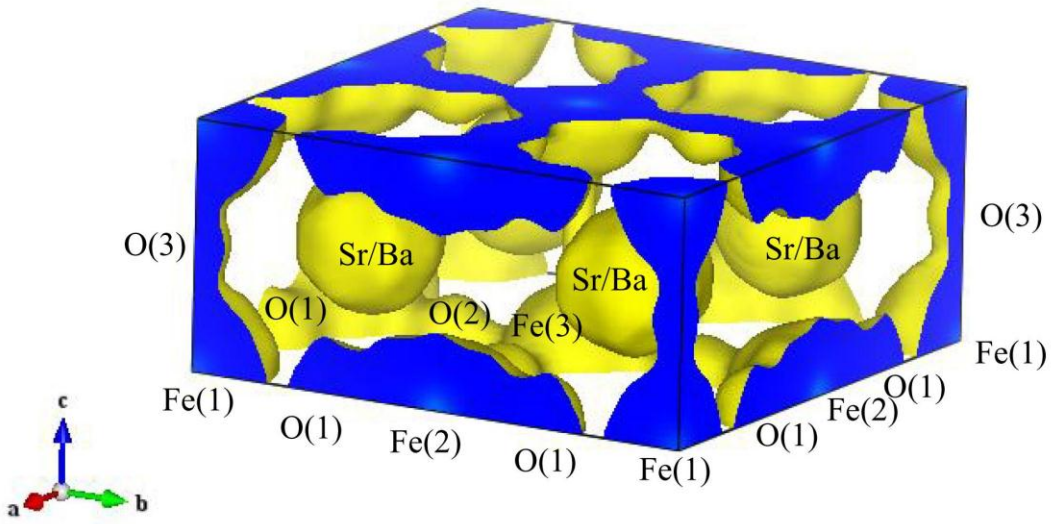


**Figure 2.6.** Electron density map by maximum entropy method (MEM) analysis, showing electron density at the apical sites.

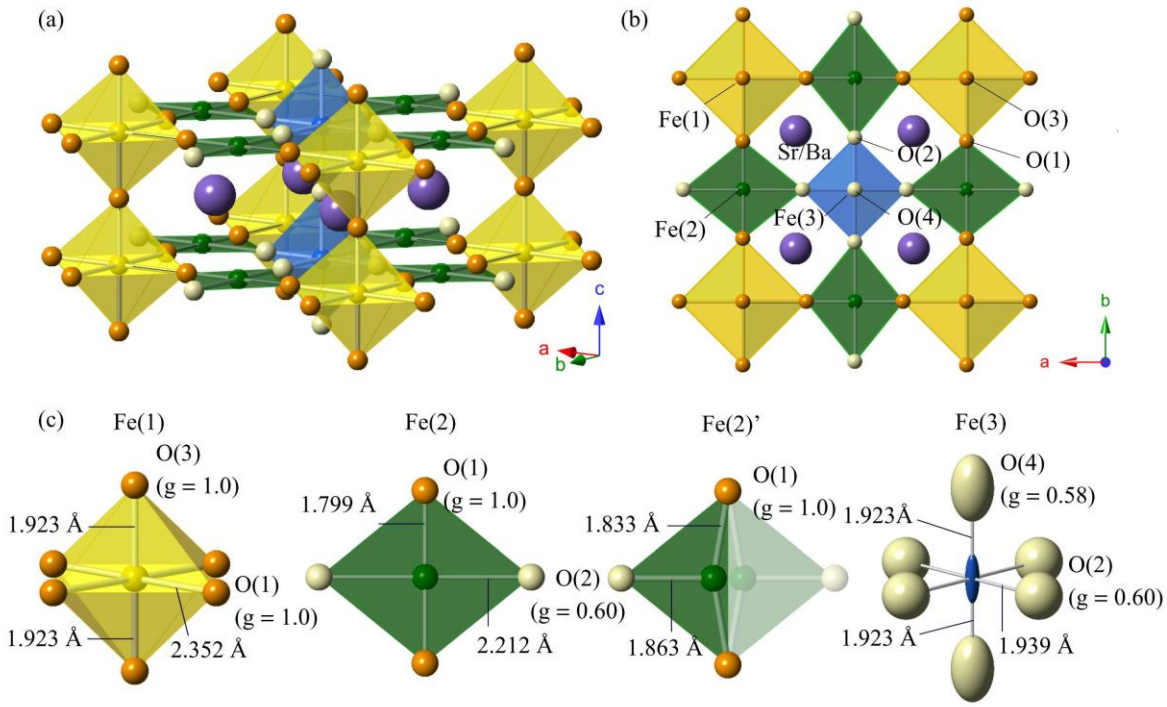


**Figure 2.7.** Structure of $(Sr_{0.2}Ba_{0.8})FeO_2$. Purple, yellow, green, and blue, spheres represent Ba/Sr, Fe(1), Fe(2), and Fe(3) atoms, respectively. Orange spheres represent fully occupied O(1) and O(3) atoms ($g$ = 1.0), while dilute yellow spheres represent partially occupied O(2) and O(4) atoms ($g$ < 1.0), where $g$ represents the site occupancy factor. (a) The structure of $(Sr_{0.2}Ba_{0.8})FeO_2$. (b) [001] projection. Fe(2)' is neglected in (a) and (b). (c) Coordination environment around each iron. The displacement ellipsoids are depicted in coordination environment around Fe(3).

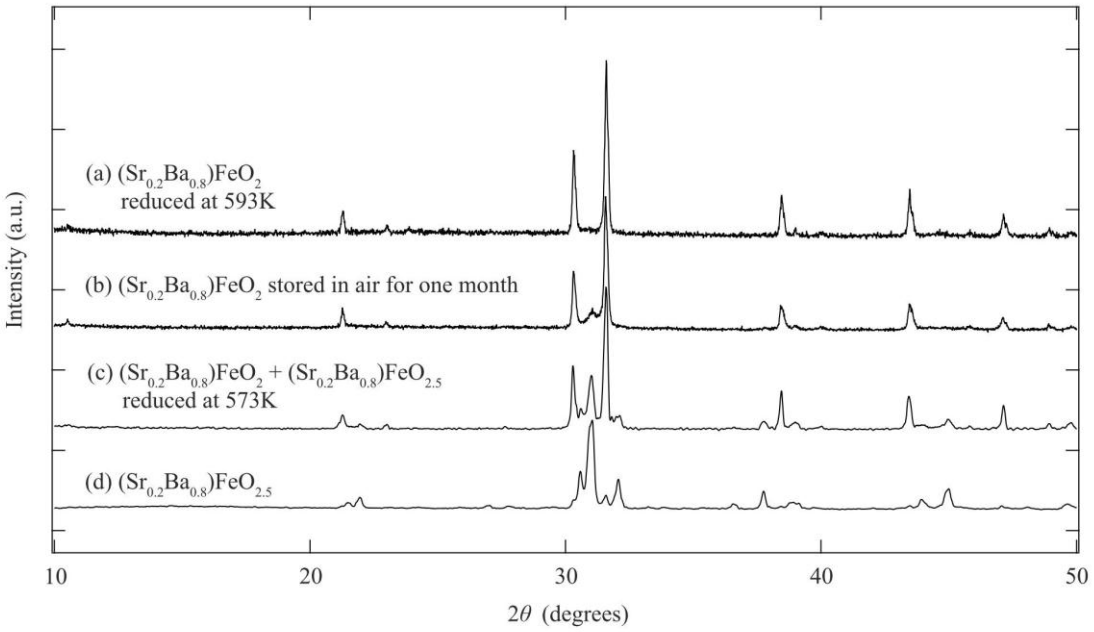


**Figure 2.8.**. XRD patterns for the $x$ = 0.8 samples in various conditions: (a) obtained by a reaction at 593 K for 3 days, (b) obtained by a reaction at 593 K for 3 days after storage in air for one month, (c) obtained by a reaction at 573 K for 3 days, and (d) $(Sr_{0.2}Ba_{0.8})FeO_{2.5}$. The data of (a) and (b) were obtained using a D8 ADVANCE diffractometer (Bruker AXS), and those of (c) and (d) using a M18XHF diffractometer (Mac Science). In (c) and (d), peaks from Cu $K_{\alpha 2}$ radiation are removed.

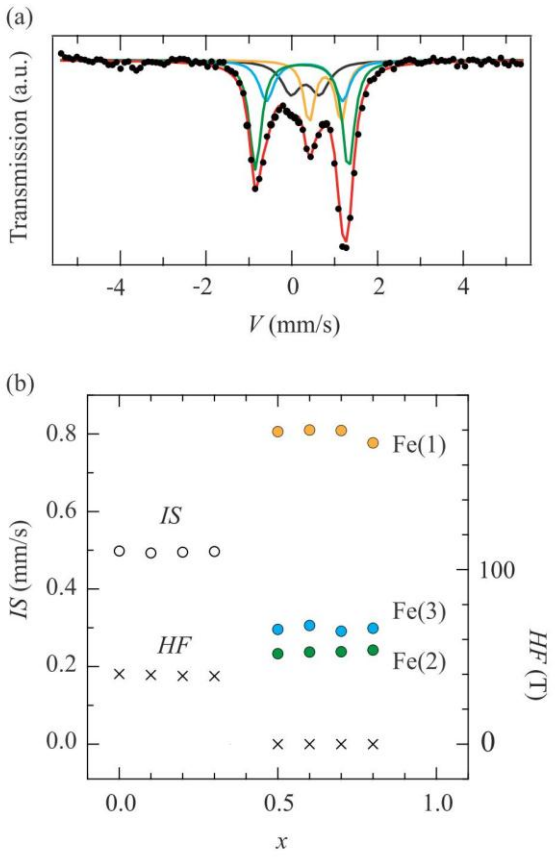


**Figure 2.9.** (a) Mössbauer spectrum for $x$ = 0.8 at room temperature. Circles denote the experimental data. The spectrum was fitted by four components; yellow, green, and blue lines represent subspectra from Fe(1), Fe(2), Fe(3), respectively. The black line represents an overreduced, decomposed amorphous impurity formed during the hydride reaction. The red line represents the total fitted spectrum. (b) Hyperfine field (*HF*) and isomer shift (*IS*) of $(Sr_{1-x}Ba_x)FeO_2$. The cross marks and the open circles represent *HF* and *IS*. Closed yellow, green, and blue circles represent *IS* of Fe(1), Fe(2), and Fe(3), respectively.

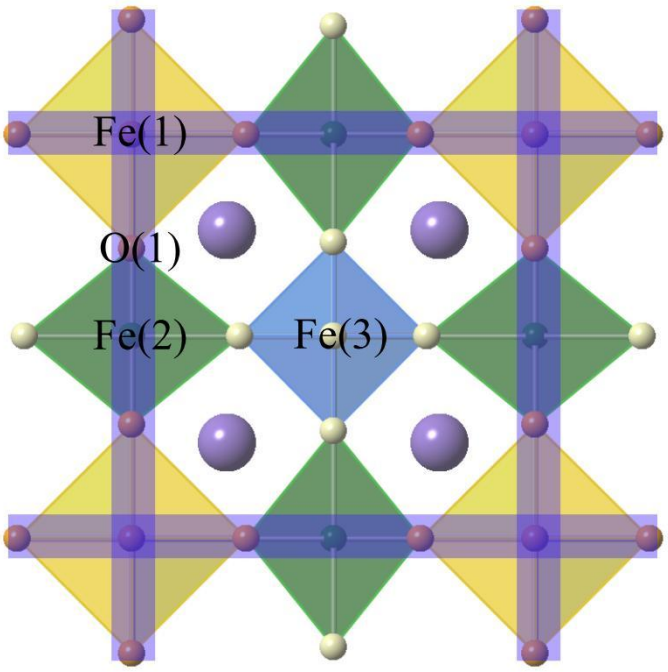


**Figure 2.10.** The [001] projection of the $BaFeO_2$ structure, where the blue band highlights the in-plane Fe-O-Fe connections free from oxygen deficiency.

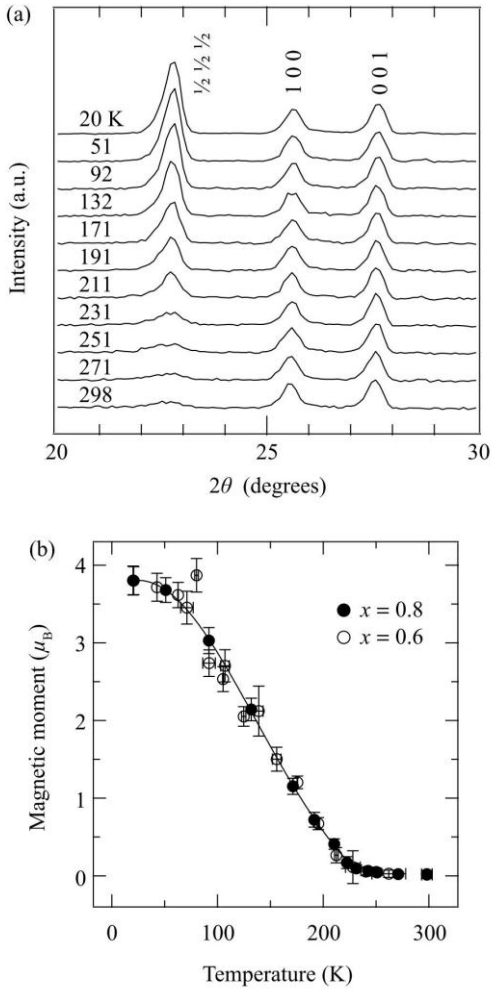


**Figure 2.11.** (a) The temperature evolution of neutron diffraction profile for $x = 0.8$ showing the magnetic Bragg reflection $(½\ ½\ ½)_p$, together with the nuclear Bragg reflections $(100)_p$ and $(001)_p$. (b) Temperature dependence of the magnetic moment in $(Sr_{1-x}Ba_x)FeO_2$ for $x$ = 0.6 (open), 0.8 (closed). Néel temperature ($T_N$) for both $x$ = 0.6 and 0.8 compounds are determined to be about 240 K. The solid line is a guide to the eyes.

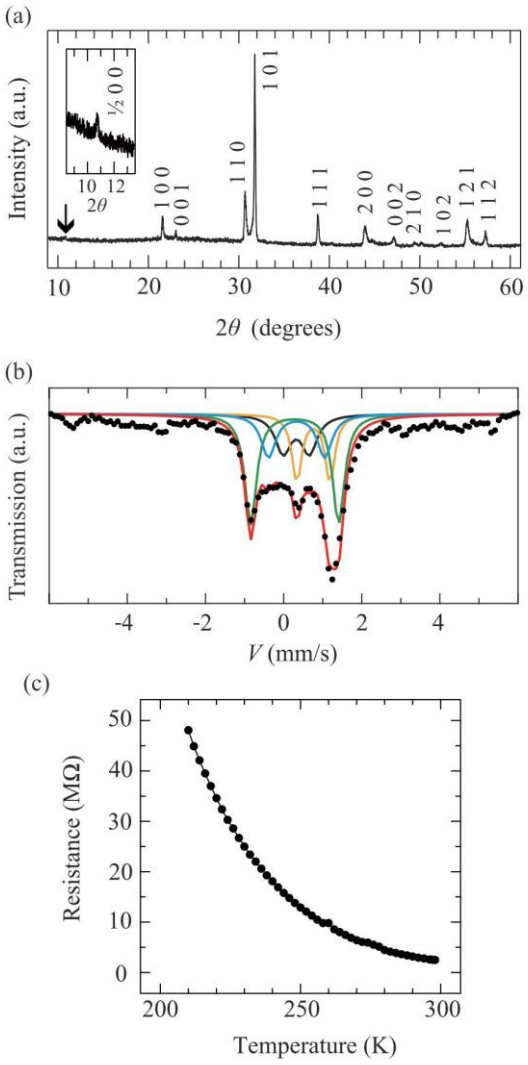


**Figure 2.12.** (a) XRD patterns of $(Ba_{0.8}La_{0.2})FeO_{2+\delta}$ collected at our laboratory. It could be indexed by a tetragonal system with the lattice parameter $a$ = 8.268 Å and $c$ = 3.846 Å. (b) Mössbauer spectrum for $(Ba_{0.8}La_{0.2})FeO_{2+\delta}$ at room temperature. Circles denote the experimental data. The spectrum was fitted by four parameters; yellow, green, and blue lines represent spectra from Fe(1), Fe(2), Fe(3) in $(Ba_{0.8}La_{0.2})FeO_{2+\delta}$, respectively. The black line represents an overreduced, decomposed impurity formed during the hydride reaction. The red line represents the total of the four components. (c) The temperature dependence of the resistance.

# *Chapter 3. An Infinite Layer Structure with Partially Filled Apical Oxygen*

## 3.1. Introduction

$SrCuO_2$ [1], an infinite layer (IL) structure with stacked $CuO_2$ layers being separated only by Sr atoms (without insulating and/or spacing layers), represents the simplest parent structure of the cupric high-temperature superconductors (Figure 3.1). The non-doped $SrCuO_2$ is a half-filled Mott insulator with the G-type magnetic order, but it becomes a superconductor when moderate carriers are injected into the $CuO_2$ layer, as reported with the electron-doped system $(Sr_{1-x}Nd_x)CuO_2$ [2].

Recently, $SrFeO_2$, which is isostructural with $SrCuO_2$, was prepared by a topotactic reduction of a perovskite $SrFeO_3$ with calcium hydride [3]. $SrFeO_2$ is an insulator and exhibits magnetic order also of the G-type, with a Néel temperature ($T_N$) as high as 473 K [3], due to strong in-plane and out-of-plane exchange interactions [4--6]. The strong exchange interactions allow a large amount of A-site substitution without any symmetry change, up to 80% for $(Sr,Ca)FeO_2$ [7,8], and up to 30% for $(Sr,Ba)FeO_2$ [9]. A further substitution of Ca results in a distortion of the $FeO_4$ square planar coordination towards tetrahedron [8]. $(Sr,Ba)FeO_2$ beyond 30% substitution level leads to a highly oxygen-deficient $LaNiO_{2.5}$-related structure with rhomboidally distorted square planar coordination [10].

$SrFeO_2$ ($d^6$) and $SrCuO_2$ ($d^9$) have different spin quantum numbers, $S = 2$ and $S = 1/2$, respectively. In addition, $SrFeO_2$ shares structural features with the recently discovered iron pnictide superconductors [11] in that the iron ions are coordinated 4-fold and form a two-dimensional square lattice. Thus, carrier doping to this insulating iron oxide is of great

interest. In order to inject carriers, the B-site (Fe-site) substitution in $SrFeO_2$ was investigated [12,13]. It is shown that the substitution by Mn ($d^5$) and Co ($d^7$) is possible up to 30% and gives rise to interesting properties such as a random fan-out state in $Sr(Fe_{0.7}Mn_{0.3})O_2$ resulting from competing ferro- and antiferromagnetic interactions. Unfortunately, all the substituted compounds remain insulating. Metallic conductivity in $SrFeO_2$ has been achieved, instead, by applying pressure beyond $P_c$ = 33 GPa [14]. This insulator-metal transition is accompanied by transitions in spin state ($S$ = 2 to $S$ = 1) and in spin structure (antiferromagnetic to ferromagnetic phase). Here, shortening of the distance between face-to-face $FeO_4$ square planes and thus enhanced out-of-plane Fe-Fe interaction plays a crucial role in the drastic change in the electronic structures at $P_c$.

Recently, Matsuyama et al. reported the synthesis and physical properties of epitaxial thin films of $(Sr,Eu)FeO_2$ [15]. The Eu-substituted films show a drastic reduction in resistivity though still semiconducting. Based on X-ray absorption spectra showing dominant contribution of $Eu^{3+}$ states, they concluded that electrons supplied by the $Eu^{3+}$-for-$Sr^{2+}$ substitution are attributable to electric conductivity. However, the resistivity of the undoped $SrFeO_2$ film is already substantial (~1 kΩcm at room temperature (RT)), in contradiction to the results on powder sample [14] as well as the first principles calculations with a band gap of ~1 eV [5,6]. We recall that europium ion can adopt both divalent and trivalent states and that the X-ray absorption spectroscopy is highly sensitive to surface states. Furthermore, precise structural and compositional analysis for thin film samples is in general limited. Therefore, whether the Eu-substitution leads to electron doping to give $(Sr_{1-x}Eu^{3+}_x)Fe^{(2-x)+}O_2$ is not clear and should be subject for further investigations.

In this study, we prepared powder samples of lanthanoid (Ln) substituted $SrFeO_2$ by Nd, Sm, and Ho that adopt exclusively trivalent state, in addition to Eu. Structural and physical

properties were investigated by synchrotron X-ray diffraction (XRD), neutron diffraction, pair distribution function (PDF) analysis, and $^{151}$Eu- and $^{57}$Fe-Mössbauer spectroscopy. It is found that Eu ions in (Sr,Eu)$FeO_2$ are all divalent, resulting in the same electronic configurations of iron as $SrFeO_2$ and thus the sample is insulating. However, unlike Eu-substitution, the substitution of $Nd^{3+}$, $Sm^{3+}$, $Ho^{3+}$ for $Sr^{2+}$ is compensated by partial occupation of apical oxygen sites between $FeO_2$ layers, resulting in an insulating state with a composition of $(Sr_{1-x}Ln_x)Fe^{2+}O_{2+x/2}$. Such an IL structure with partial apical oxygen atoms has not been reported so far.

### 3.2. Experimental

Precursor perovskites $(Sr_{1-x}Ln_x)FeO_{3-\delta}$ (Ln = Nd, $x$ = 0.1, 0.2, 0.3, 0.35; Ln = Sm, $x$ = 0.1, 0.2, 0.3, 0.35; Ln = Eu, $x$ = 0.1, 0.15, 0.2, 0.3, 0.4, 0.5; Ln = Ho, $x$ = 0.05, 0.1, 0.15, 0.2, 0.25, 0.3; $\delta \leq 0.5$) were prepared by mixing stoichiometric amounts of $SrCO_3$ (99.99%, Rare Metallic Co., Ltd.), pre-dried $Ln_2O_3$ (99.99%, Rare Metallic Co., Ltd.) and $Fe_2O_3$ (99.99%, Rare Metallic Co., Ltd.), pelletizing and heating at 1473 K in air for 48 h with one intermediate grinding. The obtained precursors were ground well with a two molar excess of $CaH_2$ in an Ar-filled glovebox, sealed in an evacuated Pyrex tube (volume 15 cm$^3$) with a residual pressure less than $2.0\times10^{-8}$ MPa, and reacted at various temperatures and durations as listed in Table 3.1. The residual $CaH_2$ and CaO byproduct were removed by washing with a 0.1 mol/L $NH_4Cl$ / methanol solution.

The purity of the precursors and the final products was checked by XRD using a D8 ADVANCE diffractometer (Burker AXS) and a Cu $K_\alpha$ radiation ($\lambda$ = 1.54056 Å). High-resolution synchrotron XRD experiments were performed at RT using the large Debye-Scherrer camera installed at the beamlines BL02B2 and BL15XU of the Japan Synchrotron

Radiation Research Institute (SPring-8). We used an imaging plate as a detector. Incident beams from a bending magnet were monochromatized to 0.342673 Å and 0.399633 Å for $(Sr_{0.8}Eu_{0.2})FeO_2$ and $(Sr_{0.75}Ho_{0.25})FeO_{2.125}$, respectively. Finely ground powder samples were sieved through a 32 μm mesh sieve and put into a Pyrex capillary (0.1 mm inner diameter). The sealed capillary was rotated during measurements to reduce the effect of preferential orientation.

The powder neutron diffraction experiment on $(Sr_{0.75}Ho_{0.25})FeO_{2.125}$ at RT was carried out at the Echidna neutron diffractometer at the OPAL reactor, ANSTO [16]. A polycrystalline sample (3 g) was placed into a vanadium cylinder. The data were collected with a step scan procedure using 128 neutron detectors in a $2\theta$ range from 2.75º to 163.95º with a step width of 0.05º. The neutron beam was monochromatized to a wavelength of 1.6220(5) Å by using a Ge335 monochromator crystal. The primary and secondary collimators were left open.

The synchrotron XRD and neutron diffraction data collected were analyzed by the Rietveld method using a RIETAN-FP program [17]. The agreement indices used were $R_{wp} = [\sum_i w_i(y_{io} - y_{ic})^2/\sum_i w_i(y_{io})^2]^{1/2}$, $R_p = \Sigma_i|y_{io} - y_{ic}|/\Sigma_i(y_{io})$, $R_I = \Sigma_K|I_0(h_K) - I(h_K)|/\Sigma_K I_0(h_K)$, $R_F = \Sigma_K||F_0(h_K)| - |F(h_K)||/\Sigma_K|F_0(h_K)|$, where $y_{io}$ and $y_{ic}$ are the observed and calculated intensities, $w_i$ is the weighting factor, $I_0(h_K)$ and $I(h_K)$ are the estimated and calculated integrated intensities, $F_0(h_K)$ and $F(h_K)$ are the estimated and calculated crystal structure factors.

The pair distribution functions for $SrFeO_2$, $(Sr_{0.8}Eu_{0.2})FeO_2$ and $(Sr_{0.8}Ho_{0.2})FeO_{2.1}$ were obtained at RT from high energy powder XRD experiments carried out at the SPring-8 beam line BL04B2 ($\lambda$ = 0.20154 Å). Powder data were obtained to a large $Q_{max}$ (25 $Å^{-1}$), then corrected for several parameters including scattering of the quartz capillary and normalization, followed by a Fourier transform to obtain the atomic pair distribution $G(r)$.

The data were fitted using a PDFgui program [18], on the basis of the crystallographic models obtained from the XRD/neutron Rietveld analysis.

$^{57}$Fe-Mössbauer spectra on the $(Sr_{1-x}Eu_x)FeO_2$ ($x$ = 0.1, 0.2, 0.3) and $(Sr_{1-x}Ho_x)FeO_{2+x/2}$ ($x$ = 0.05, 0.1, 0.2, 0.25, 0.3) samples were taken at RT in transmission geometry using a $^{57}$Co/Rh $\gamma$-ray source. $^{151}$Eu-Mössbauer spectra on $(Sr_{1-x}Eu_x)FeO_2$ ($x$ = 0.1, 0.2, 0.3) were taken at RT in transmission geometry using a $^{151}SmF_3$ $\gamma$-ray source. The source velocity was calibrated, respectively, by $\alpha$-Fe, $EuF_3$ as a standard for $^{57}$Fe- and $^{151}$Eu-Mössbauer experiments.

### 3.3. Results and Discussions

*3.3.1 Synthesis and Lattice Evolution*

The precursor perovskite solid solutions $(Sr_{1-x}Ln_x)FeO_{3-\delta}$ ($\delta < 0.5$) could be obtained up to 35% for Ln = Nd, Sm, 50% for Eu, and 30% for Ho. Single-phase formation in the corresponding $x$ range was confirmed by laboratory XRD (Figure 3.2). The diffraction peaks of the precursors were indexed in a cubic unit cell, in consistency with the previous report [19]. A deviation of the lattice parameter evolution from the Vegard's law implies that the amount of oxygen vacancy $\delta$ changes with $x$ [20].

Upon hydride reduction, the IL-like tetragonal structures were successfully obtained for compositions up to 30% for Nd and Ho, 35% for Sm, and 40% for Eu. No impurity phase was detected from the laboratory XRD data. The XRD profiles of the reduced compounds were readily indexed on the basis of the tetragonal unit cell of $SrFeO_2$ ($a \sim 3.9$ Å and $c \sim 3.5$ Å), as shown in Figure 3.3. Lattice parameters calculated by Le Bail analysis are plotted as a function of $x$ in Figure 3.4, together with the data for $SrFeO_2$ ($x$ = 0) [3]. For Eu substitution, both the $a$ and $c$ axes were almost constant with $x$. The Shannon's ionic radii of $Sr^{2+}$, $Eu^{2+}$

and $Eu^{3+}$ with 8-fold coordination are 1.26 Å, 1.25 Å and 1.066 Å, respectively [21]. This strongly indicates that the substituted europium ions are divalent (i.e., $(Sr_{1-x}Eu^{2+}_x)Fe^{2+}O_2$), in marked contrast to the recent thin film study claiming the trivalent europium state (i.e., $(Sr_{1-x}Eu^{3+}_x)Fe^{(2-x)+}O_2$) [15].

On the contrary, for Nd, Sm, and Ho, the volumes increase continuously with increasing *x*. As long as the IL structure is considered, this observation does not agree with the geometrical consideration: the ionic radii of $Nd^{3+}$, $Sm^{3+}$ and $Ho^{3+}$ with 8-fold coordination are, respectively, 1.109 Å, 1.079 Å and 1.015 Å [21] are much smaller than $Sr^{2+}$. There is a tendency for these systems that the increase of the *c* axis is more significantly than the decrease of the *a* axis. These facts suggested that additional oxygen ions are positioned at the apical site of Fe atoms (see Figure 3.1). We note that the RT resistivity of a hand-pressed pellet of all the reduced compounds are very high (> 1 MΩcm), implying no electron doping occurred by the Ln-for-Sr substitution. Thus, the heterovalent substitution causes the incorporation of additional oxygen so as to retain the divalent iron state. Namely, the chemical formula is expected to be $(Sr_{1-x}Ln^{3+}_x)Fe^{2+}O_{2+x/2}$ (Ln = Nd, Sm, Ho).

### *3.3.2 Structure and Magnetic properties of $(Sr_{1-x}Eu_x)FeO_2$*

Rietveld analysis has been performed for the synchrotron XRD data on 20% Eu-substituted sample. The observed peak widths are comparable with $SrFeO_2$ [3], demonstrating high crystallinity. The diffraction data can be indexed in a tetragonal unit cell as shown earlier. Tiny impurity peaks are present, arising from an incompletely reduced phase ($\delta < 0.5$). No superreflections as observed in $CaFeO_2$ were detected [8]. The Rietveld structural refinement was performed using the ideal IL structure with the *P*4/*mmm* space group as a starting model, where the Sr and Eu atoms were distributed randomly on the 1*d* site. The thermal parameters

of all atoms were allowed to vary. The refinement converged rapidly, yielding reasonable thermal parameters and discrepancy factors. When the occupancy factor ($g$) of the oxygen site was refined, it became 1.0 within the statistical error. Thus, the $g$ value was subsequently fixed at full occupancy. In the end we obtained agreement factors of $R_p$ = 5.17%, $R_{wp}$ = 7.29%, $R_I$ = 1.81%, and $R_F$ = 1.64% (Figure 3.5 and Table 3.2). The other space groups with lower symmetry did not lead to better results, so we conclude that $(Sr_{0.8}Eu_{0.2})FeO_2$ adopts the IL structure. Bond valence sum (BVS) calculations [22] for Sr, Eu and Fe gave, respectively, +1.93, +1.71 and +1.98. Thus, both europium and iron are reasonably assigned as divalent, which agrees with the result from the ionic size considerations discussed earlier.

The $^{57}$Fe Mössbauer spectroscopy revealed that the spectra for the reduced Eu samples ($x$ = 0.1, 0.2 and 0.3) at RT consist of a single, well-defined sextet (Figure 3.6a). Isomer shift (*IS*), hyperfine field (*HF*), quadrupole splitting (*QS*), and full width at half maximum (*FWHM*) are almost constant and are close to those of $SrFeO_2$ (Table 3.3). This is consistent with the structural refinement and suggests that iron ions are divalent in high spin state and that the magnetic order is well developed as in the case of $SrFeO_2$. $^{151}$Eu Mössbauer spectra at RT (Figure 3.6b) demonstrate that the europium ions are mostly divalent, but a trivalent component was also observed (11 ~ 23%). We could not find any sign of monovalent iron by $^{57}$Fe Mössbauer spectra. In addition, the Eu substitution does not influence on the transport properties, unlike the thin film study, meaning that the iron ion is divalent in $(Sr_{1-x}Eu_x)FeO_2$. Therefore, we speculate that $Eu^{3+}$ observed in the Mössbauer spectra derives from partial oxidation of europium ions; it is possible that $(Sr_{1-x}Eu_x)FeO_2$ oxidized to $(Sr_{1-x}Eu_x)FeO_{2+\delta}$ ($\delta$ ~ 0.02) after synthesis and before the Mössbauer measurements. In fact, we obtained $(Sr_{0.7}Eu_{0.3})FeO_{2+\delta}$ by decreasing reduction temperature compared with synthesis of $(Sr_{0.7}Eu_{0.3})FeO_2$ (the reduction temperatures are 613K and 568K, respectively, for

$(Sr_{0.7}Eu_{0.3})FeO_2$ and $(Sr_{0.7}Eu_{0.3})FeO_{2+\delta}$). The volume of $(Sr_{0.7}Eu_{0.3})FeO_{2+\delta}$ is slightly the larger than that of $(Sr_{0.7}Eu_{0.3})FeO_2$ (Figure 3.7). $(Sr_{0.7}Eu_{0.3})FeO_{2+\delta}$ is insulator, so that the chemical formula is expected to be $(Sr^{2+}_{0.7}Eu^{2+}_{0.3-2\delta}Eu^{3+}_{2\delta})Fe^{2+}O_{2+\delta}$ ($0 < \delta \leq 0.15$).

Note that Matsuyama et al. synthesized Eu-substituted $SrFeO_2$ in the form of thin film [15]. They reported a decrease of the resistivity by the Eu-substitution and successful carrier doping. They argued that the electron carriers are supplied by $Eu^{3+}$ ions substituting for divalent sites, because X-ray absorption spectra demonstrated that $Fe^{2+}$ and $Eu^{3+}$ state are dominant. However, we have obtained the opposite result. Mössbauer spectra demonstrated that the $Eu^{2+}$ state is dominant and we did not observe any sign of carrier doping. It is possible that the thin film allows formation of metastable phase of $(Sr_{1-x}Eu^{3+}_x)Fe^{(2-x)+}O_2$ due to a lattice strain or a surface effect. However, whether the Eu-substitution in the thin film $SrFeO_2$ leads to electrons doping is still questionable and should be subject to further investigations.

### *3.3.3 Structure and Magnetic properties of $(Sr_{1-x}Ln_x)FeO_{2+x/2}$ (Ln = Nd, Sm, Ho)*

The synchrotron XRD measurement of 25% Ho-substituted sample has been performed for the Rietveld analysis. The observed peak widths are comparable with $SrFeO_2$ [3], demonstrating high crystallinity. The diffraction data can be indexed in a tetragonal unit cell as shown earlier. Tiny impurity peaks are present, arising from an incompletely reduced phase ($\delta < 0.5$). No superreflections as observed in $CaFeO_2$ were detected [8]. First, the Rietveld structural refinement was performed using the ideal IL structure as the Eu-substituted sample. The thermal parameters of all atoms were allowed to vary. In contrast to the Ln = Eu case, the refinement result of the 25% Ho data was rather poor ($R_I$ = 9.51%, $R_F$ = 6.98%). Hence, according to the model suggested earlier, the apical oxygen site O(2) on 1*b*

(0, 0, 0.5) was added to the IL structure. When the *g* values of O(1) and O(2) sites were allowed to refine, they became, respectively, 1.0 and 0.15. This implies the full/partial occupation of equatorial/apical oxygen site. Note that the same attempt for Ln = Eu led to a contrasting consequence; the *g* value for O(2) became close to zero within the error, indicating the absence of apical oxygen. In the refinement of the 25% Ho sample, large isotropic displacement parameters ($U_{iso} > 0.04$) were found in O(1) and O(2), indicating local displacements.

In order to obtain more precise information on the oxygen positions and their site occupancies, we performed neutron Rietveld refinement of 25% Ho sample, starting with the final structure obtained from the synchrotron XRD. Anisotropic displacement parameters were included since large $U_{iso}$ values for the oxygen atoms were obtained from the synchrotron refinement. The refinement converged rapidly, yielding large components of the anisotropic displacement parameters along the *c* axis for the oxygen atoms. Then, we returned to the synchrotron XRD data for refining the thermal parameters of the Sr, Ho, and Fe atoms, while retaining adjustable parameters of the O atoms. Subsequently, we refined the neutron diffraction data again, fixing the thermal parameters of Sr, Ho, and Fe atoms. After this stepwise process was repeated several times, the *g* value of O(2) was converged to 0.11(3), which is very close to the proposed composition of $(Sr_{0.75}Ho_{0.25})FeO_{2.125}$. The agreement parameters are $R_p$ = 3.32%, $R_{wp}$ = 2.40%, $R_I$ = 6.16%, $R_F$ = 6.17% for the synchrotron XRD and $R_p$ = 5.59%, $R_{wp}$ = 4.88%, $R_I$ = 6.61%, $R_F$ = 3.71% for the neutron diffraction. The other space groups with lower symmetry did not lead to better results, so *P*4/*mmm* is the most likely space group. The final refinement results are summarized in Table 3.4 and Figure 3.8. The obtained structure is shown in Figure 3.9a.

Although the anisotropic displacement parameters $U_{33}$ for the oxygen atoms in $(Sr_{0.75}Ho_{0.25})FeO_{2.125}$ are high, attempts to displace the oxygen atoms from the ideal sites did not improve the fitting of Rietveld refinement. Therefore, in order to obtain insight into the local geometry, more appropriate measurement for analysis of the local structure is needed. Thus, pair distribution functions (PDF) analysis was performed for $(Sr_{0.8}Ho_{0.2})FeO_{2.1}$. For comparison, PDF analysis was also made for $SrFeO_2$ and $(Sr_{0.7}Eu_{0.3})FeO_2$ with the ideal IL structure, and the results are shown in Figures 3.10 and 3.11. The PDF patterns of $(Sr_{0.7}Eu_{0.3})FeO_2$ are very similar to those of $SrFeO_2$. The PDF analysis using the ideal IL model provided good agreement parameters, $R_{wp}$ of 9.0% and 8.9%, at short range (1.5−5 Å), and 16.3% and 14.4% at long range (10−20 Å) for $SrFeO_2$ and $(Sr_{0.7}Eu_{0.3})FeO_2$, respectively. This suggests that the structure of $(Sr_{0.7}Eu_{0.3})FeO_2$ is free from local distortion and disorder. On the other hand, the PDF patterns of $(Sr_{0.8}Ho_{0.2})FeO_{2.1}$ are obviously different from $SrFeO_2$, both in the short range and long range. For example, peaks centered at 2.0 Å and 2.6 Å representing, respectively, Fe−O and A−O bonding, are asymmetric (see insets of Figure 3.11). As expected, the calculated pattern when assuming the ideal IL model disagreed considerably from the experimental one at local range, especially around 2.0 Å (inset of Figure 3.11a). Thus, as suggested by the Rietveld refinement, the apical oxygen site O(2) with $g = 0.1$ was included. This caused $R_{wp}$ to reduce from 14.2% to 12.5% at local range and from 13.2% to 12.8% at long range (Figures 3.11c and 3.11d). A slight disagreement around the peaks at 2.0-2.5 Å indicates the presence of local distortion from the ideal site. To further improve the refinement for $(Sr_{0.8}Ho_{0.2})FeO_{2.1}$, we allowed the site disorder of O(1) and O(2) along the *c* axis. Although the site disorder of O(2) site did not lead better refinement, that of O(1) atoms from 2*f* (0.5, 0, 0) to 4*i* (0.5, 0, 0.07(2)) improved the refinement at local range

($R_{wp}$ = 10.9%; Figure 3.11e). Here, no obvious improvement was seen at long range ($R_{wp}$ = 13.3%; Figure 3.11f).

The result of the PDF analysis indicates that the insertion of the apical oxygen induces the displacement of the equatorial oxygen where the equatorial oxygen atoms and the iron atoms are not coplanar (Figure 3.9b). As a result, some $FeO_4$ square planar units are distorted by neighbouring $FeO_5$ pyramid. For example, if a $FeO_5$ pyramid shares equatorial oxygen with a $FeO_4$ square plane, there is probably distortion such that the shared oxygen is not coplanar within the $FeO_4$ unit any more. We previously demonstrated that the square planar $FeO_4$ can be distorted towards tetrahedron by Ca-substitution [8] and to a rhomboidal shape by Ba-substitution [10]. In the present compounds, the distortion of the square planar $FeO_4$ consists of random displacements of oxygen along the *c*-axis.

In $(Sr_{1-x}Ho_x)FeO_{2+x/2}$, the square planar $FeO_4$ coexists with pyramidal coordination, while it can coexist with $FeO_6$ octahedral coordination and $FeO_3$ trigonal coordination by Ba-substitution [10]. Therefore, the present study proves flexibility and the square planar iron to coexist with the other coordination in an iron oxide network as demonstrated by the previous works [8,10].

Ho-substitution influences on the Fe Mössbauer spectrum to a greater extent (Figure 3.12a), in contrast to substitution by europium. The *HF* decreases with *x*, and finally becomes 0 for *x* = 0.3 (Figure 3.12b). This is consistent with the neutron diffraction measurement which demonstrates *G*-type spin order with 1.2$\mu_B$ per iron at room temperature for *x* = 0.25. These results indicate that the Néel temperature ($T_N$) drastically decreases with *x*. The *IS* and *QS* values do not change by the Ho-substitution of $x \leq 0.25$, indicating that the square planar iron is divalent in a high spin state in $(Sr_{1-x}Ho_x)FeO_{2+x/2}$ ($x \leq 0.25$). In *x* = 0.3, three components exist. The largest subspectrum (black line) has the *IS* of ~0.5 mm/sec and *QS* of ~1.0 mm/sec,

which is the similar values as $x \leq 0.25$ (Tables 3.5 and 3.6). Thus, this subspectrum can be assigned as square planar $Fe^{2+}$ in a high spin state. The green subspectrum has a spectrum weight of 15% and has an *IS* of ~0.0 mm/sec, which is a typical value for iron metal. Although no impurity phase was detected by XRD studies, it is probably an amorphous phase formed by over-reduction and decomposition during the hydride reduction, since the reaction temperature for $x = 0.3$ is 100 K higher than that of $x \leq 0.25$ (Table 3.1). The blue subspectrum has a spectrum weight of 12% and has an *IS* of ~0.8 mm/sec, which is a typical value for a divalent high-spin iron. Due to a existence of apical oxygen, there should exist about 30% of pyramidal coordination in $(Sr_{0.7}Ho_{0.3})FeO_{2.15}$. We speculate that the blue spectrum is assigned as the pyramidal irons. However, the amount of pyramidal $Fe^{2+}$ is small compared with the expected value of 30%. We could not reasonably explain this discrepancy. However, there exists a Fe metal impurity in the spectrum for $x = 0.3$. In addition, spectra of the square planar irons and the pyramidal irons overwrap with each other. Thus, a measurement of a pure sample is needed in order to discuss in more details. Here, we could not detect spectrum from the pyramidal irons in $x \leq 0.25$ because the spectra are broad and the amount of the pyramidal irons are smaller than $x = 0.3$.

We previously demonstrated that the lattice parameters have little influence on the $T_N$ [9] and the distortion which occurs in $CaFeO_2$ does not decrease the $T_N$ largely [8]. Therefore, the decrease of $T_N$ by the Ho-substitution may be a result from the pyramidal coordinate iron. As pointed out above, the iron in the pyramidal coordination is typical divalent high spin state, and is bonded much weakly as compared with the square planar iron with strong covalency. In fact, the $T_N$ of FeO with a typical divalent high spin iron is approximately 200K [23] which is much lower than that of $SrFeO_2$ (473K) [3]. Note that difference of the crystal structure between FeO and $SrFeO_2$ also have an influence on the $T_N$. Thus, theoretical

investigation is needed for further understanding of the apical oxygen effect on the physical properties.

$(Sr_{1-x}Ho_x)FeO_{2+x/2}$ crystallizes in the IL structure with partially filled apical oxygen as shown in Figure 3.9a. Here, the lattice parameter evolutions with $x$ for all the Ho- Nd- and Sm-substituted compounds are similar (Figure 3.4). In addition, all the compounds are insulator. Thus, we also assume that all the Nd- and Sm-substituted compounds also adopt the similar structure with the chemical formulas of $(Sr_{1-x}Ln^{3+}_x)Fe^{2+}O_{2+x/2}$ (Ln = Nd, Sm, Ho). This means that reduction from precursor is stopped at just $Fe^{2+}$ state, and Fe ion is never reduced beyond divalent. Namely, hole-doping in square planar iron is the difficult. Here, we note that structural analyses for the individual compositions are needed to confirm the individual structures since the lattice parameters do not show Vegard's law (Figure 3.4).

In previous studies, all the IL-based compounds $AFeO_2$ ($A = Sr_{1-x}Ca_x$, $Sr_{1-y}Ba_y$ where $0 \le x \le 1$ and $0 \le y \le 0.3$) were reduced directly from, and oxidized directly back to brownmillerite ($AFeO_{2.5}$) phase [9]. Therefore, this compound represents the first example of the IL related structure that oxygen content slightly deviates from 2. In the IL cuprates, there have been many studies on A-site substitution and deficiency for carrier doping [2,24], but no one seems to show partial occupation of apical oxygen. In the IL nickelate $LaNiO_2$, domains of a partially oxidized phase with a stoichiometry of $LaNiO_{2.09}$ have been observed [25]. This is occasional intergrowths (i.e. lamellar defects) of pyramidal layers among the square plane layers, due to incomplete reduction [25]. In contrast, $(Sr_{1-x}Ln^{3+}_x)Fe^{2+}O_{2+x/2}$ can be considered as a terminal reduction product consisting of a single crystallographic phase with no defects. In $(Sr_{1-x}Ln_x)FeO_{2+x/2}$, the intercalated oxygen atoms are randomly distributed in the interlayer. Based on the concept of the bond valence [22], the intercalated oxygen atoms are more likely to be around the randomly distributed Ln atoms. The reduction of an A-site ordered

perovskite, e.g. $YSr_2Fe_3O_8$ [26], may be interesting for comparison with this study, since the intercalated oxygen atoms possibly (partially) ordered unlike the present compounds.

### 3.4. Conclusion

We showed that the A-site substitution in the IL structure $SrFeO_2$ is tolerable up to ca. 30% for all Ln (= Nd, Sm, Eu, Ho). For the Nd, Sm and Ho substitution, an increase of out-of-plane cell parameters is observed, which is explained by an insertion of apical oxygen atoms to compensate for trivalent doping. This compound represents the first example of the IL related structure that oxygen content slightly deviates from 2. On the other hand, $(Sr_{1-x}Eu_x)FeO_2$ adopts an ideal infinite layer structure by forcing the europium ions to be divalent. The Ho-substitution results in a significant reduction of the Néel temperature, while the Eu-substitution has a little influence on the magnetic property. Although this represents a success of heterovalent A-site substitution into square planar iron oxide, we failed to inject carriers into a $FeO_2$ layer, indicating significant stability of a divalent iron in the square-planar-based iron oxide. However, this is a contrast result with a previous report of a thin film sample [15]. Thus, further research on thin films should be needed.

## References


[1] M. Takano, Y. Takeda, H. Okada, M. Miyamoto, and T. Kusaka, Physica C 159 (1989) 375.

[2] M. G. Smith, A. Manthiram, J. Zhou, J. B. Goodenough, and J. T. Markert, Nature 351 (1991) 549.

[3] Y. Tsujimoto, C. Tassel, N. Hayashi, T. Watanabe, H. Kageyama, K. Yoshimura, M. Takano, M. Ceretti, C. Ritter, and W. Paulus, Nature 450 (2007) 1062.

[4] K. Tomiyasu, H. Kageyama, C. Lee*, et al*, J. Phys. Soc. Jpn. 79 (2010) 034707.

[5] J. M. Pruneda, J. Íñiguez, E. Canadell, H. Kageyama, and M. Takano, Phys. Rev. B 78 (2008) 115101.

[6] H. J. Xiang, S. H. Wei, and M. H. Whangbo, Phys. Rev. Lett. 100 (2008) 167207.

[7] C. Tassel, T. Watanabe, Y. Tsujimoto, N. Hayashi, A. Kitada, Y. Sumida, T. Yamamoto, H. Kageyama, M. Takano, and K. Yoshimura, J. Am. Chem. Soc. 130 (2008) 3764.

[8] C. Tassel, J. M. Pruneda, N. Hayashi*, et al*, J. Am. Chem. Soc. 131 (2009) 221.

[9] T. Yamamoto, Z. Li, C. Tassel*, et al*, Inorg. Chem. 49 (2010) 5957.

[10] T. Yamamoto, Y. Kobayashi, N. Hayashi*, et al*, J. Am. Chem. Soc. accepted.

[11] Y. Kamihara, T. Watanabe, M. Hirano, and H. Hosono, J. Am. Chem. Soc. 130 (2008) 3296.

[12] L. Seinberg, T. Yamamoto, C. Tassel*, et al*, Inorg. Chem. 50 (2011) 3988.

[13] M. Retuerto, F. Jiménez-Villacorta, M. J. Martínez-Lope, M. T. Fernández-Díaz, and J. A. Alonso, Inorg. Chem. 50 (2011) 1929.

[14] T. Kawakami, Y. Tsujimoto, H. Kageyama*, et al*, Nat. Chem. 1 (2009) 371.

[15] T. Matsuyama, A. Chikamatsu, Y. Hirose, T. Fukumura, and T. Hasegawa, Appl. Phys. Express 4 (2011) 3001.

[16] K. D. Liss, B. Hunter, M. Hagen, T. Noakes, and S. Kennedy, Physica B 385 (2006) 1010.

[17] F. Izumi and K. Momma, Solid State Phenom. 130 (2007) 15.

[18] C. Farrow, P. Juhas, J. Liu, D. Bryndin, E. Božin, J. Bloch, T. Proffen, and S. Billinge, J. Phys. : Condens. Matter 19 (2007) 335219.

[19] P. Battle, T. Gibb, and S. Nixon, J. Solid State Chem. 79 (1989) 86.

[20] K. Roh, K. Ryu, and C. Yo, J. Mater. Sci. 30 (1995) 1245.

[21] R. Shannon, Acta Cryst. 32 (1976) 751.

[22] I. D. Brown and D. Altermatt, Acta Cryst. B41 (1985) 244.

[23] C. McCammon, J. Magn. Magn. Mater. 104 (1992) 1937.

[24] N. Ikeda, Z. Hiroi, M. Azuma, M. Takano, Y. Bando, and Y. Takeda, Physica C 210 (1993) 367.

[25] M. Hayward, M. Green, M. Rosseinsky, and J. Sloan, J. Am. Chem. Soc. 121 (1999) 8843.

[26] A. Azad, A. Zakaria, F. Ahmed, S. Paranjpe, and A. Das, J. Magn. Magn. Mater. 214 (2000) 251.

**Table 3.1.** Synthesis conditions for hydride reduction of $(Sr_{1-x}Ln_x)FeO_{3-\delta}$ ($\delta < 0.5$)

| Ln | $x$ | Reaction temperature (K) | Reaction time (days) |
|---|---|---|---|
| Nd | 0.1, 0.2 | 568 | 6 |
| | 0.3 | 673 | 8 |
| | 0.35[a] | 723 | |
| Sm | 0.1, | 553 | 3 |
| | 0.2 | 568 | 5 |
| | 0.3 | 623 | 4 |
| | 0.35 | 673 | 7 |
| Eu | 0.1, 0.15, 0.2 | 553 | 3 |
| | 0.3 | 613 | 6 |
| | 0.4, 0.5[a] | 723 | 7 |
| Ho | 0.05, 0.1, | 623 | 1 |
| | 0.15, 0.2, 0.25 | 623 | 4 |
| | 0.3 | 723 | 2 |

[a] Reduction was unsuccessful for $x = 0.35$ (Nd) and $x = 0.5$ (Eu).

**Table 3.2.** Crystallographic data for $(Sr_{0.8}Eu_{0.2})FeO_2$.[a]

| atom | site | $g$ | $x$ | $y$ | $z$ | $U_{iso}$ /Å$^2$ |
|---|---|---|---|---|---|---|
| Sr(1) | 1*d* | 0.8 | 0.5 | 0.5 | 0.5 | 0.0057(2) |
| Eu(1) | 1*d* | 0.2 | 0.5 | 0.5 | 0.5 | 0.0057(2) |
| Fe(1) | 1*a* | 1 | 0 | 0 | 0 | 0.0051(3) |
| O(1) | 2*f* | 1 | 0.5 | 0 | 0 | 0.0059(9) |

[a] Space group: *P*4/*mmm*; $a = 3.98905(2)$ Å, $c = 3.47234(2)$ Å.

**Table 3.3.** Fitting parameters of $^{57}$Fe and $^{151}$Eu Mössbauer spectra for $(Sr_{1-x}Eu_x)FeO_2$ ($x$= 0.1, 0.2, 0.3). [a]

$^{57}$Fe

| *x* | *IS* (mm/s) | *HF* (T) | *QS* (mm/s)[b] | FWHM (mm/s) | Area (%) |
|---|---|---|---|---|---|
| 0.0[c] | 0.489 | 40.1 | 1.16 | 0.28 | 100 |
| 0.1 | 0.498 | 39.7 | 1.13 | 0.30 | 100 |
| 0.2 | 0.508 | 39.9 | 1.08 | 0.30 | 100 |
| 0.3 | 0.499 | 39.8 | 1.12 | 0.30 | 100 |

$^{151}$Eu ($Eu^{2+}$)

| *x* | *IS* (mm/s) | *HF* (T) | *QS* (mm/s)[b] | FWHM (mm/s) | Area (%) |
|---|---|---|---|---|---|
| 0.1 | -12 | 0.0 | 0.0 | 3.1 | 77.2 |
| 0.2 | -12 | 0.0 | 0.0 | 0.30 | 86.6 |
| 0.3 | -12 | 0.0 | 0.0 | 3.1 | 88.8 |

$^{151}$Eu ($Eu^{3+}$ from impurity)

| *x* | *IS* (mm/s) | *HF* (T) | *QS* (mm/s)[b] | FWHM (mm/s) | Area (%) |
|---|---|---|---|---|---|
| 0.1 | 0.672 | 0.0 | 0.0 | 3.0 | 22.8 |
| 0.2 | 0.747 | 0.0 | 0.0 | 3.0 | 13.4 |
| 0.3 | 0.399 | 0.0 | 0.0 | 3.0 | 11.2 |

[a] *IS*, *HF*, *QS*, FWHM and Area represent isomer shift, hyperfine field, quadrupole splitting, full width at half maximum and area percentage of total fit, respectively. [b] $S_1$-$S_2$. [c] We use the value of $SrFeO_2$ in pervious study [3].

**Table 3.4.** Crystallographic data for $(Sr_{0.75}Ho_{0.25})FeO_{2.11(3)}$.[a]

| atom | site | *g* | *x* | *y* | *z* | $U_{11}$/Å$^2$ | $U_{22}$/Å$^2$ | $U_{33}$/Å$^2$ |
|---|---|---|---|---|---|---|---|---|
| Sr(1) | 1*d* | 0.75 | 0.5 | 0.5 | 0.5 | 0.0259(5) | 0.0259(5) | 0.0246(6) |
| Ho(1) | 1*d* | 0.25 | 0.5 | 0.5 | 0.5 | 0.0259(5) | 0.0259(5) | 0.0246(6) |
| Fe(1) | 1*a* | 1 | 0 | 0 | 0 | 0.0067(6) | 0.0067(6) | 0.030(1) |
| O(1) | 2*f* | 0.980(8) | 0.5 | 0 | 0 | 0.021(1) | 0.032(2) | 0.097(2) |
| O(2) | 1*b* | 0.15(1) | 0 | 0 | 0.5 | 0.009(7) | 0.009(7) | 0.11(3) |

[a] Space group: *P*4/*mmm*; $a$ = 3.95349(9) Å, $c$ = 3.57172(9) Å for synchrotron XRD data, $a$ = 3.9566(2) Å, $c$ = 3.5392(2) Å for neutron diffraction data. $U_{12} = U_{13} = U_{23} = 0$. The magnetic structure is of *G*-type with 1.2 $\mu_B$ per iron.

**Table 3.5.** Fitting parameters of $^{57}$Fe and Mössbauer spectra for $(Sr_{1-x}Ho_x)FeO_{2+x/2}$ ($x$ = 0.05, 0.1, 0.2, 0.25). [a]

| *x* | *IS* (mm/s) | *HF* (T)[b] | *QS* (mm/s)[c] |
|---|---|---|---|
| 0.0[d] | 0.489 | 40.1 | 1.16 |
| 0.05 | 0.495 | 38.7 | 1.13 |
| 0.1 | 0.503 | 36.7 | 1.15 |
| 0.2 | 0.475 | 27.2 | 1.08 |
| 0.25 | 0.498 | 9.9 | 1.05 |

[a] *IS*, *HF*, and *QS* represent isomer shift, hyperfine field, and quadrupole splitting, respectively. [b]Average value. [c]$S_1$-$S_2$. [d]We use the value of $SrFeO_2$ in pervious study [3].

**Table 3.6.** Fitting parameters of $^{57}$Fe and Mössbauer spectra for $(Sr_{0.7}Ho_{0.3})FeO_{2.15}$($x$ = 0.3).

| | *IS* (mm/s) | *HF* (T) | *QS* (mm/s) | FWHM | Area (%) |
|---|---|---|---|---|---|
| square planar $Fe^{2+}$ | 0.513 | 0 | 1.02 | 0.55 | 73 |
| typical $Fe^{2+}$ | 0.779 | 0 | 1.96 | 0.55 | 12 |
| Fe metal impurity | -0.020 | 31.2 | 0.10 | 0.60 | 15 |

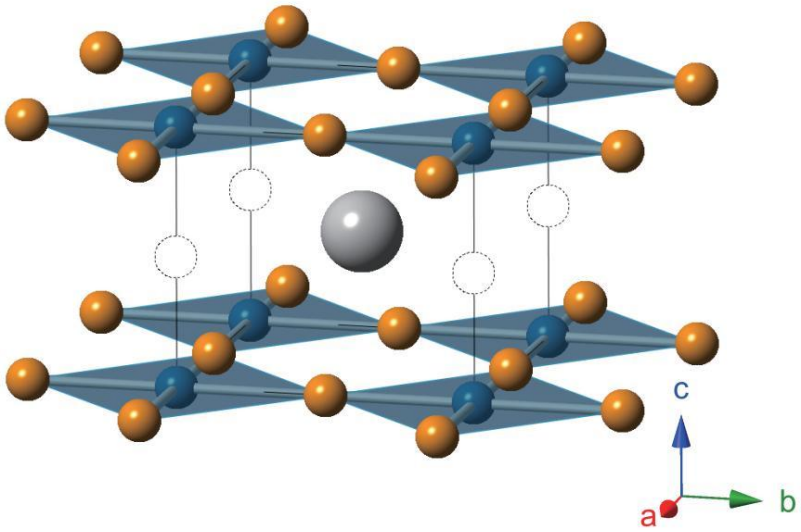


**Figure 3.1**. The infinite layer structure $ABO_2$. Orange, gray and blue spheres represent O, A-site, B-site atoms. Dotted circles represent vacant apical oxygen sites.

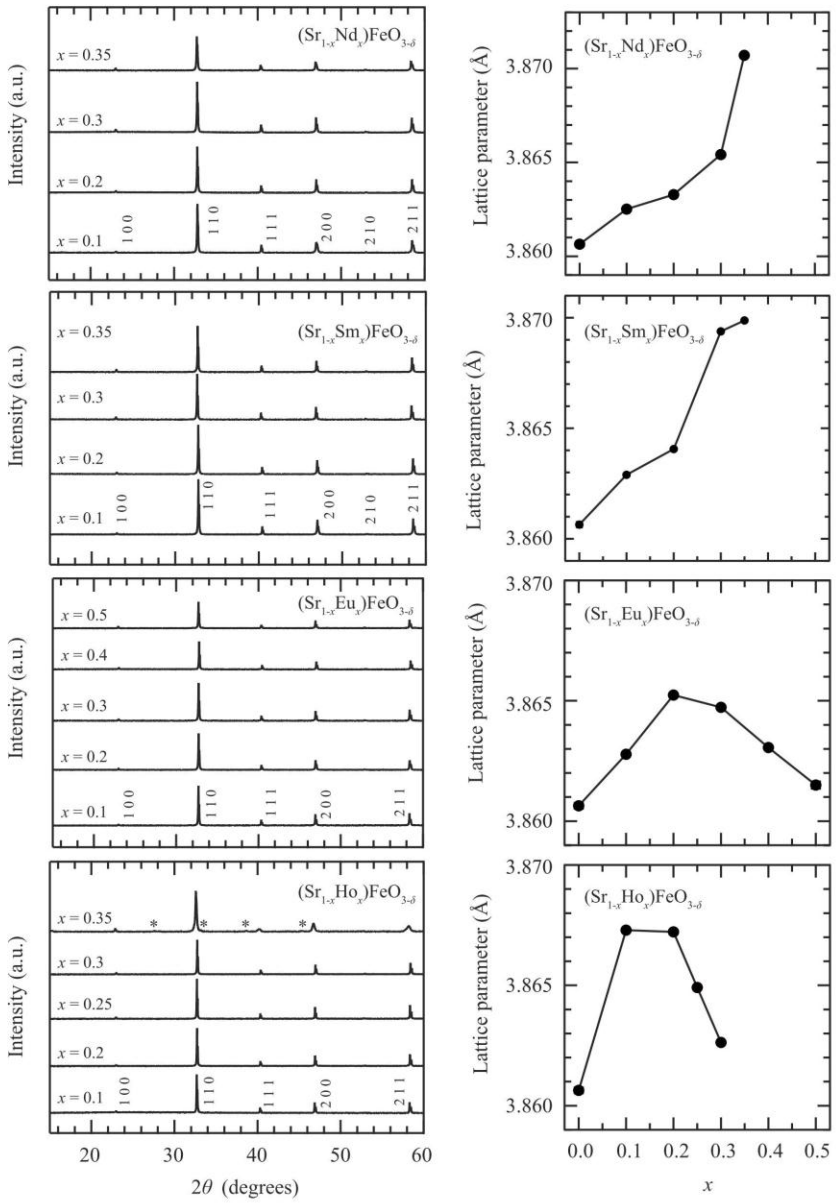


**Figure 3.2.** (Right figures) XRD patterns of the precursors $(Sr_{1-x}Ln_x)FeO_{3-\delta}$ (Ln = Nd, Sm, Eu, Ho) before reduction. All the patterns could be assigned as cubic perovskite. * indicates unknown impurity phase. (Left figures) Lattice parameters of $(Sr_{1-x}Ln_x)FeO_{3-\delta}$.

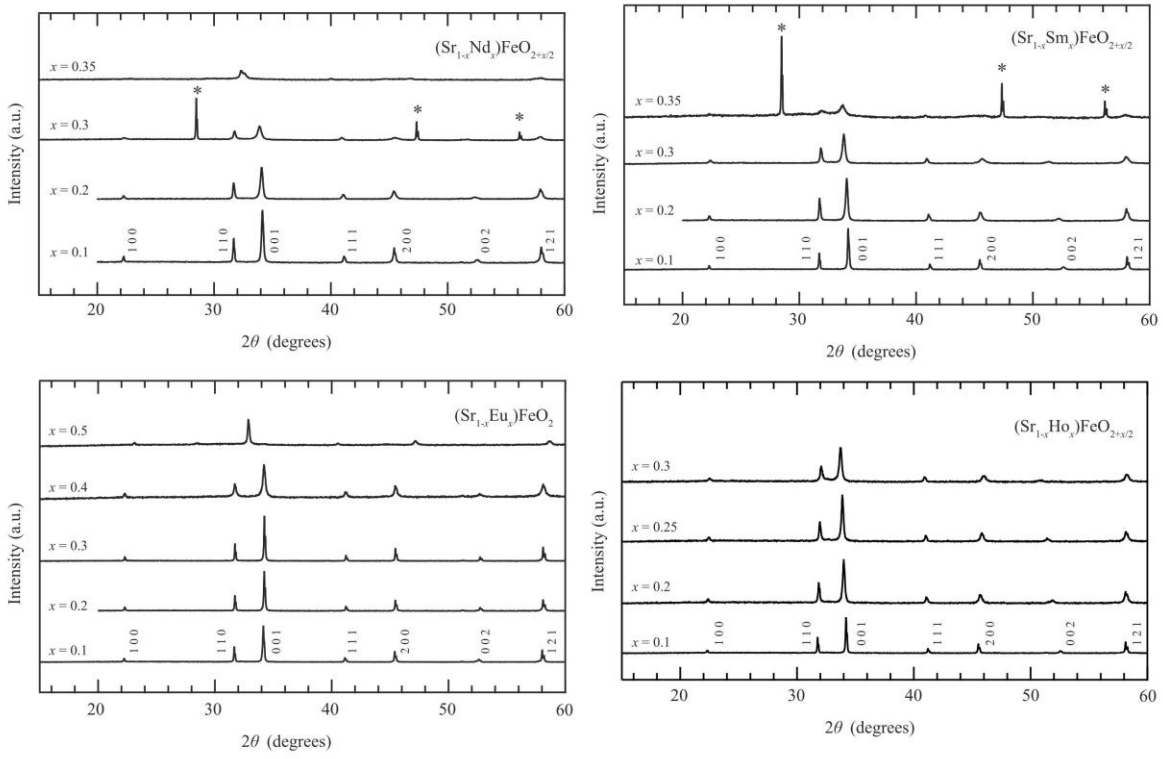


**Figure 3.3**. XRD patterns of $(Sr_{1-x}Ln_x)FeO_{2+x/2}$ (Ln = Nd, Sm, Eu, Ho) after reduction. All patterns could be indexed by a tetragonal system. * indicates Si peaks as a standard material.

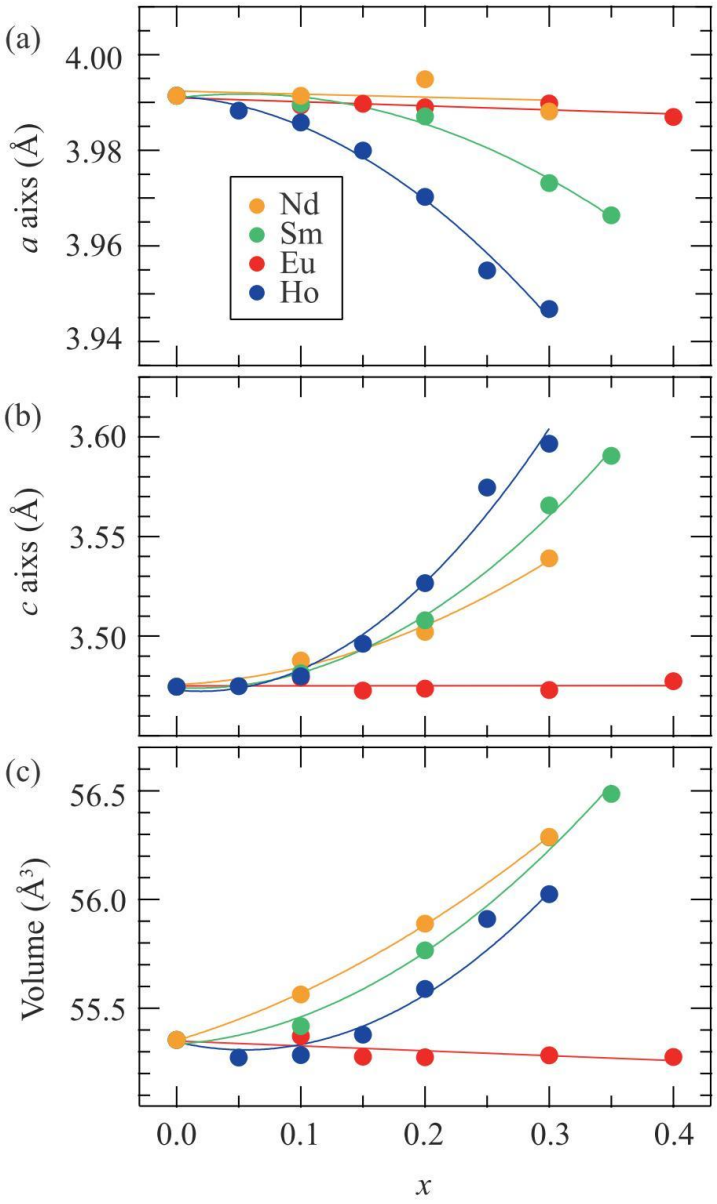


**Figure 3.4.** The lattice parameters (a, b) and the volume (c) for $(Sr_{1-x}Ln_x)FeO_{2+\delta}$ (Ln = Nd (yellow), Sm (green), Eu (red), Ho(blue)) as a function of lanthanide doping $x$. The lines are guides to the eye. The data for $x = 0.0$ are taken from the previous study [3].

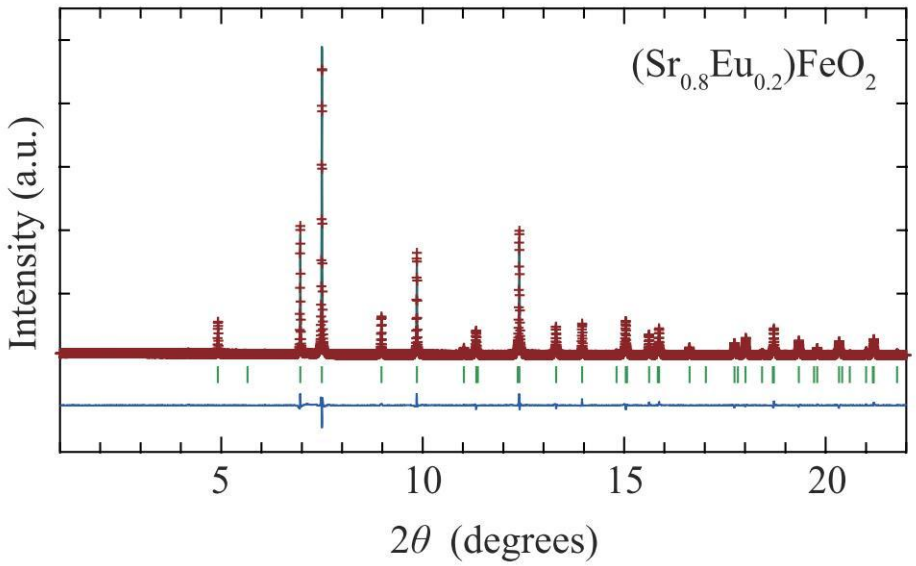


**Figure 3.5**. Structural characterization of $(Sr_{0.8}Eu_{0.2})FeO_2$ by Rietveld refinement of synchrotron XRD data at room temperature ($R_{wp}$ = 7.29%, $R_I$ = 1.81%, $R_F$ = 1.64%). The overlying crosses and the solid lines represent the observed intensities and the calculated intensities. The bottom solid line represents the residual. The ticks correspond to the position of the calculated Bragg peaks.

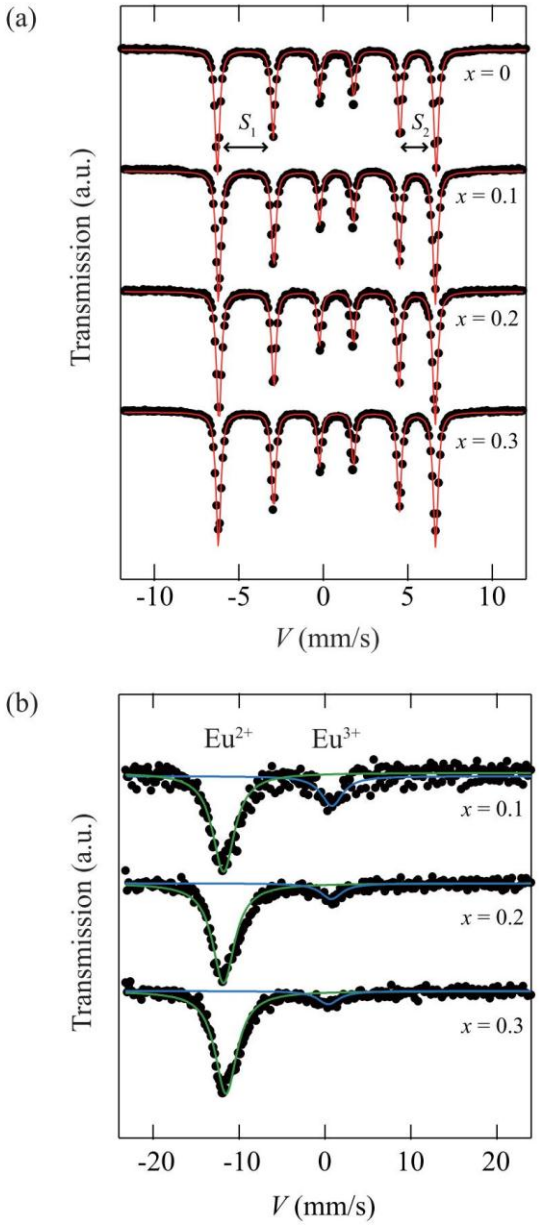


**Figure 3.6**. $^{57}$Fe (a) and $^{151}$Eu (b) Mössbauer spectra for $(Sr_{1-x}Eu_x)FeO_2$ ($x$= 0.1, 0.2, 0.3) at room temperature. Circles denote the experimental data. (a) The red lines represent fitting curves. (b) The green and blue lines represent fitting curves for $Eu^{2+}$ and $Eu^{3+}$. The spectrum for europium should split into several peaks due to quadrupole interaction. However, we used a single fitting curve for simplicity.

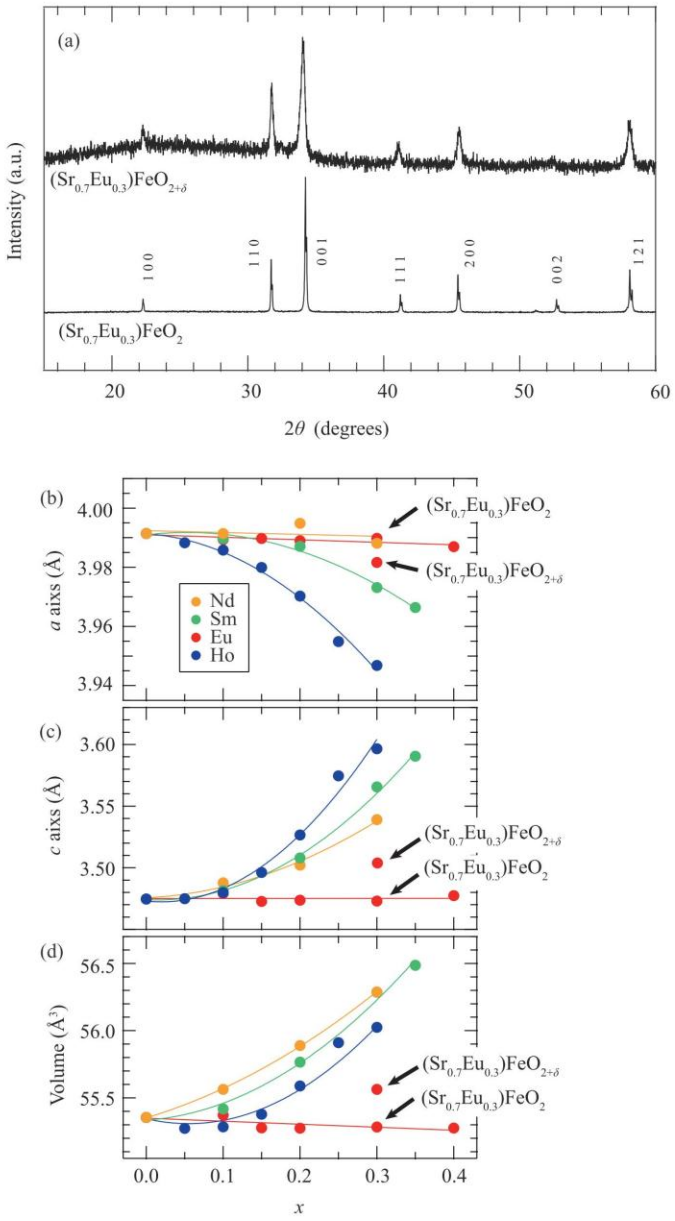


**Figure 3.7**. (a) Comparison of XRD patterns of $(Sr_{0.7}Eu_{0.3})FeO_2$ and $(Sr_{0.7}Eu_{0.3})FeO_{2+\delta}$. $(Sr_{0.7}Eu_{0.3})FeO_2$ and $(Sr_{0.7}Eu_{0.3})FeO_{2+\delta}$ were synthesized at 613 K for 6 days and at 568 K for 6 days, respectively. The patterns could be indexed by a tetragonal system but the lattice parameters are slightly different. (b)-(d) Comparison of the lattice parameters and the volume. The *c* axis of $(Sr_{0.7}Eu_{0.3})FeO_{2+\delta}$ is slightly larger than that of $(Sr_{0.7}Eu_{0.3})FeO_2$, suggesting existence of the apical oxygen.

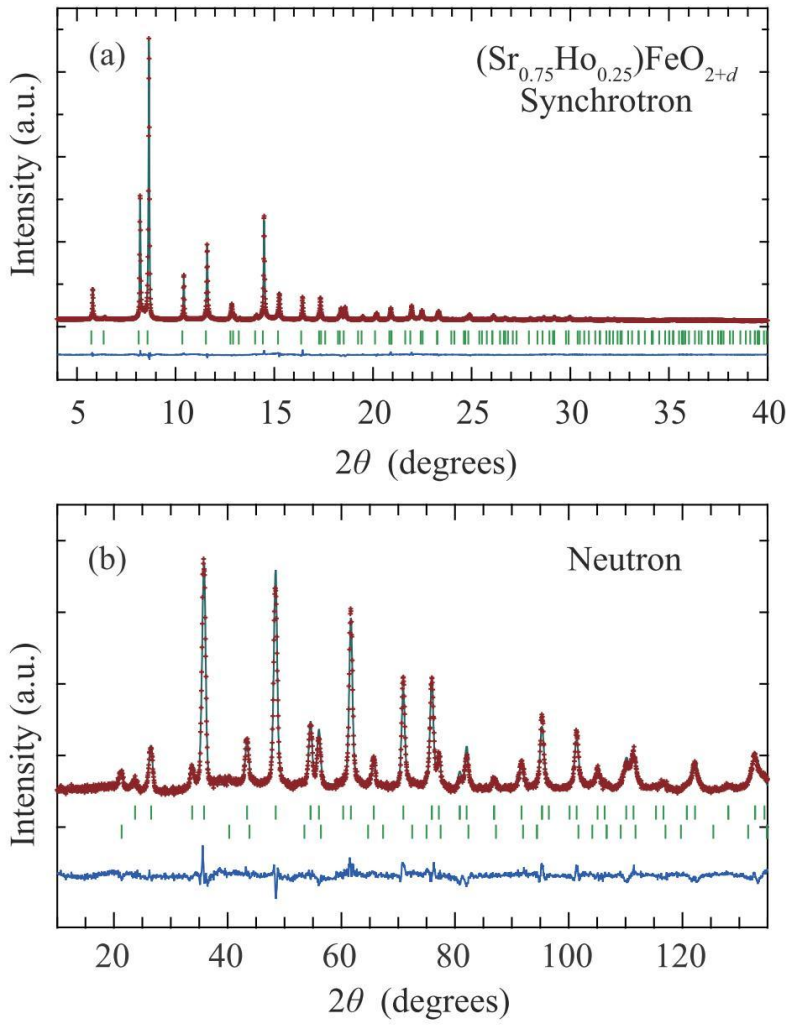


**Figure 3.8**. (a) Structural characterization of $(Sr_{0.75}Ho_{0.25})FeO_{2.125}$ by Rietveld refinement of synchrotron XRD data at room temperature ($R_p$ = 3.32%, $R_{wp}$ = 2.40%, $R_I$ = 6.16%, $R_F$ = 6.17%), and (b) that of neutron diffraction data at room temperature ($R_p$ = 5.59%, $R_{wp}$ = 4.88%, $R_I$ = 6.61%, $R_F$ = 3.71%). The upper and lower ticks in (b) correspond to the position of the calculated structural and magnetic Bragg peaks.

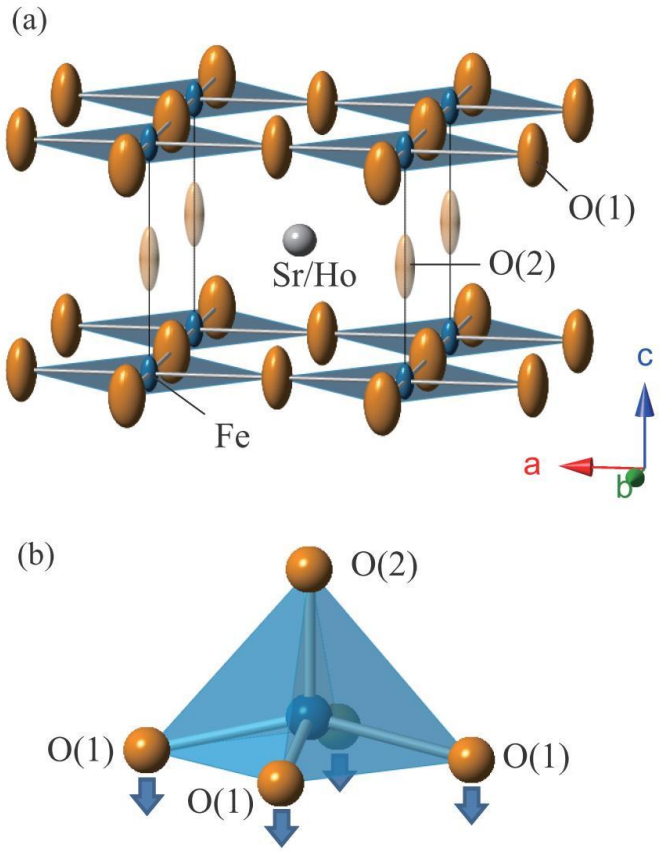


**Figure 3.9.** (a) Structure of $(Sr_{0.75}Ho_{0.25})FeO_{2.125}$ depicted by thermal ellipsoids. Orange, gray and blue spheres represent O, A-site, Fe atoms. (b) A local structure around $FeO_5$ pyramid. The insertion of the apical oxygen induces the displacement to direction of the arrows.

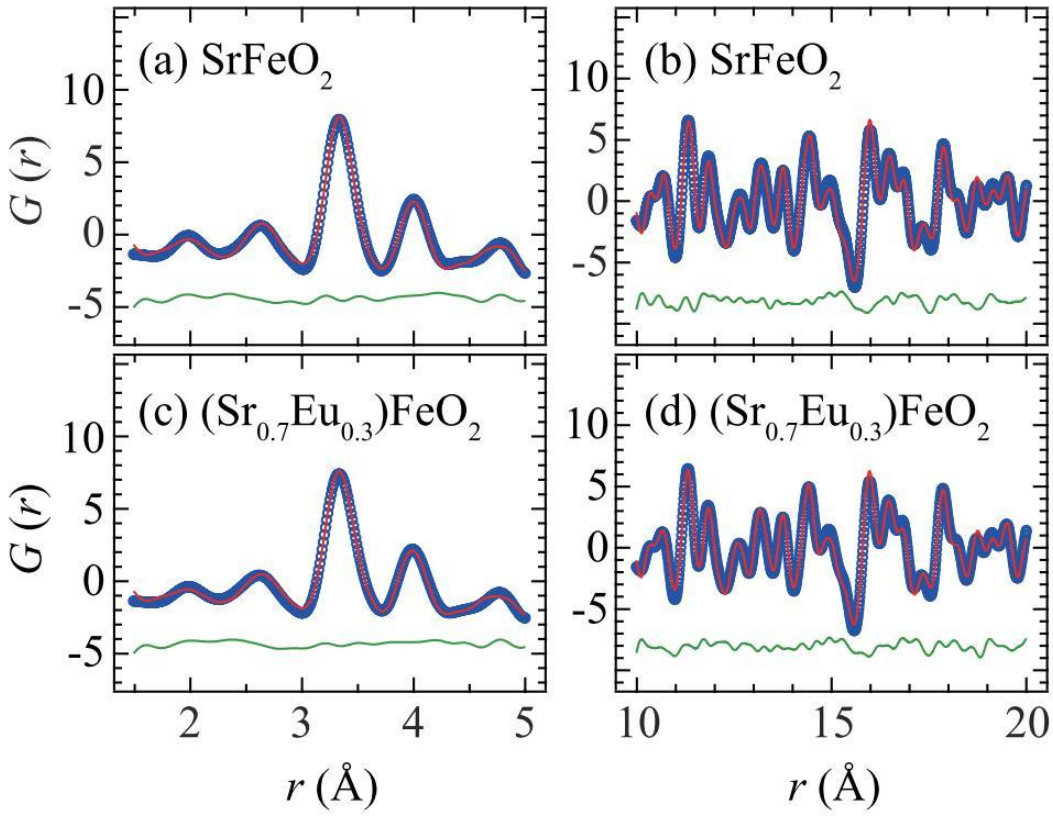


**Figure 3.10**. PDF analyses for $SrFeO_2$ at local range (1.5-5 Å) (a) and long range (10-20 Å) (b), for $(Sr_{0.7}Eu_{0.3})FeO_2$ at local range (c) and long range (d). The overlying circles and the solid lines represent the observed $G(r)$ intensities and the calculated $G(r)$ intensities. The bottom solid lines represent the residual.

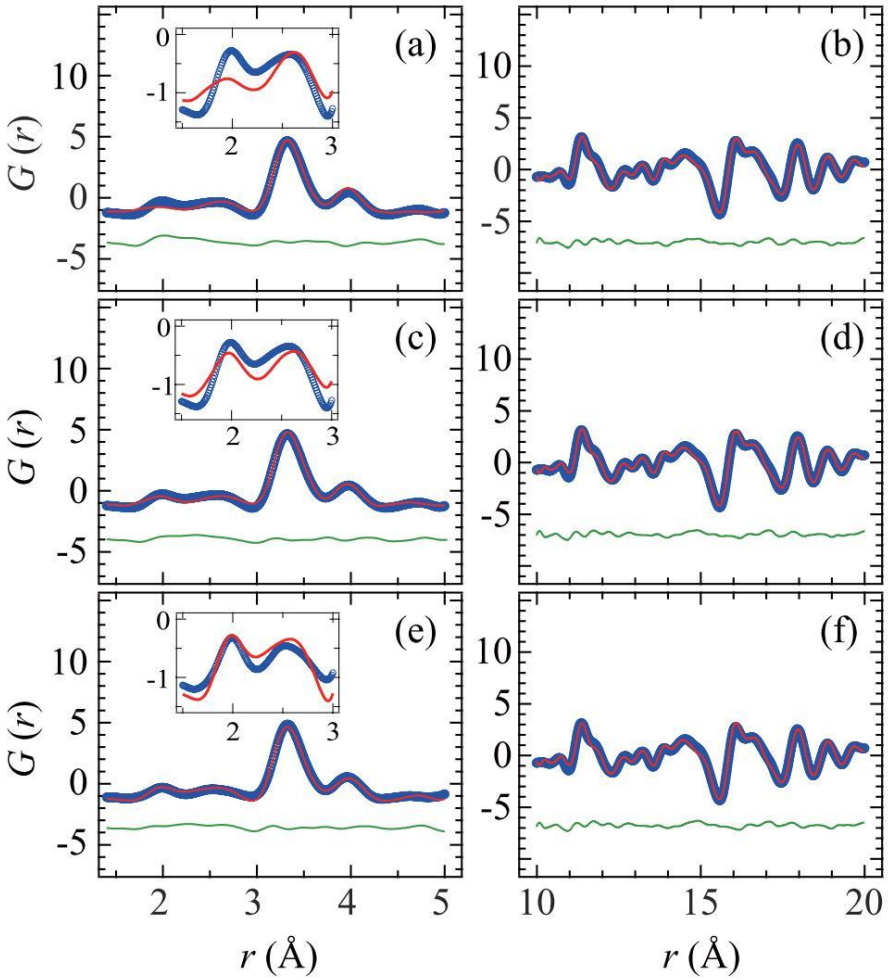


**Figure 3.11.** PDF analyses for $(Sr_{0.8}Ho_{0.2})FeO_2$ with at the IL structure at local range (a) and long range (b), for $(Sr_{0.8}Ho_{0.2})FeO_{2.1}$ with the structure obtained by the Rietveld refinement at local range (c) and long range (d), for $(Sr_{0.8}Ho_{0.2})FeO_{2.1}$ with the displaced model at local range (e) and long range (f). Insets in (a), (c), (d) show extended patterns around peaks representing Fe−O (~2.0 Å) and A−O (~2.6 Å).

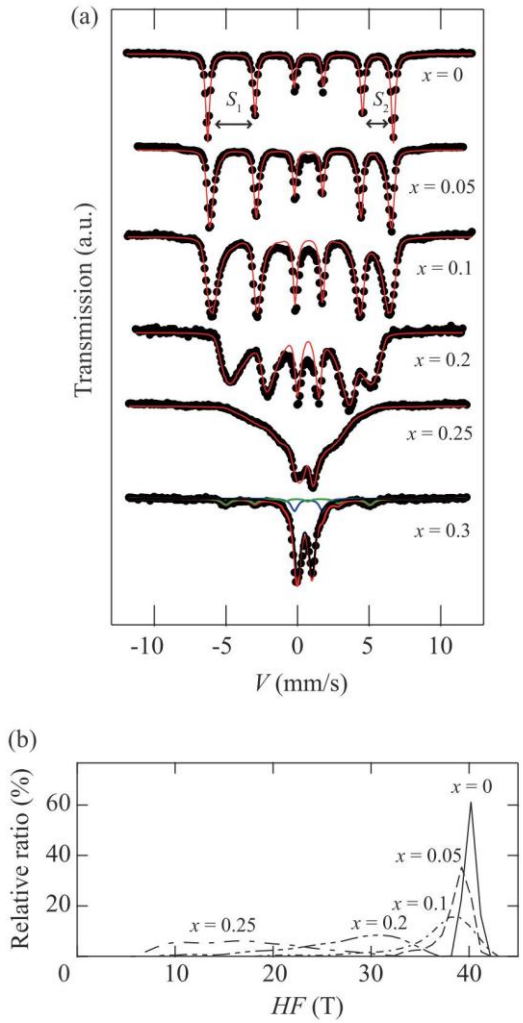


**Figure 3.12**. $^{57}$Fe Mössbauer spectra for $(Sr_{1-x}Ho_x)FeO_{2+x/2}$ ($x$= 0.05, 0.1, 0.2, 0.25) at room temperature. Circles denote the experimental data. The red lines represent total fitting curves. The black, blue and green line in $x$ = 0.3 represent square planar $Fe^{2+}$, typical $Fe^{2+}$ and amorphous Fe metal impurity, respectively. (b) A distribution of the hyperfine field *HF*. The relative area is plotted with an interval of 1T.

# *Chapter 4. Pressure-Induced Structural, Magnetic and Transport Transitions in the Two-Legged Ladder $Sr_3Fe_2O_5$*

## 4.1. Introduction

Spin state transitions or spin crossover have been intensely investigated in various fields not only for their fundamental details [1] but also due to potential applications in information storage, optical switches, visual displays, and so on [1,2]. Generally, this transition can be rationalized by the competition between the two energies in metal center: the intra-atomic exchange energy that favors a high spin state and the crystal field energy that favors a low spin state [3]. Thousands of examples, including minerals and biomolecules, are now found to have spin state transitions [4--8], but they are almost exclusively limited to those with octahedrally coordinated 3*d* transition metal ions.

A recently discovered pressure-induced spin transition in $SrFe(II)O_2$ at $P_c$ = 33 GPa has several aspects distinct from conventional spin state transitions [9]. First, $SrFeO_2$ adopts a square planar coordination around iron (Figure 4.1a) [10], thus representing the first spin state transition in a four-fold coordinated metal center. Second, it is not a typical transition from a high-spin state ($S$ = 2) to a low-spin state ($S$ = 0), but to an intermediate-spin state ($S$ = 1). Last but not least is that it is accompanied at the same time with an insulator-to-metal (I-M) and an antiferromagnetic-to-ferromagnetic (AFM-FM) transition (involving possibly a partial charge transfer from O 2*p* to Fe 3*d* leading to $d^{6.5}$ electronic configurations). These facts indicate that many-body effects derived from the interplay between charge, orbital, and spin degrees of freedom in a strongly correlated electron system are of great importance, which is in stark contrast to conventional cases, where the overall physics behind a spin state

transition can be in principle explained by a single (or several) octahedrally coordinated metal(s).

After the synthesis of $SrFeO_2$, subsequent studies reported several new compounds with the $FeO_4$ square planar motif; (Sr,Ba,Ca)$FeO_2$ [11--13], $Sr_3Fe_2O_5$ [14], and $Sr_3Fe_2O_4Cl_2$ [15]. Here, $SrFeO_2$ and $Sr_3Fe_2O_5$ belong, respectively, to $n = \infty$ and $n = 2$ of the $S = 2$ $n$-legged ladder series $Sr_{n+1}Fe_nO_{2n+1}$ ($n$ = 1, 2, 3,…). The former has the infinite layer structure consisting of two-dimensional (2d) $FeO_2$ layers that are separated by Sr atoms (Figure 4.1a), while in the latter two consecutive rock salt layers (SrO) cut the 2d infinite layers into two-legged ladders ($Sr_2Fe_2O_4$) (Figure 4.1b). As it is well known, magnetic and transport properties in a strongly correlated electron system are largely influenced by the topology and dimensionality of the lattice. A representative example is found in the relevant system, $S$ = 1/2 $n$-legged spin ladder series $Sr_{n-1}Cu_nO_{2n-1}$, prepared under high pressures [16]. $SrCuO_2$ ($n = \infty$), whose magnetism is characterized by a square-lattice Heisenberg antiferromagnet, shows a ($\pi$, $\pi$, $\pi$) magnetic order like $SrFeO_2$, but becomes a superconductor when appropriate carriers are injected into the $CuO_2$ plane [17]. The two-legged ladder $SrCu_2O_3$ ($n$ = 2) has a non-magnetic (spin-singlet) ground state with a finite gap to the first excited triplet states, but the three-legged ladder $Sr_2Cu_3O_5$ ($n$ = 3) has gapless excitations [18], verifying a predicted even- or odd-number leg dependence by Dagotto and Rice [19].

In this context, $Sr_3Fe_2O_5$ provides a unique opportunity to understand how dimensionality is related to the physical properties in the $S$ = 2 spin ladder system. The effect of dimensional reduction has been already seen by the reduction of the Néel temperature from $T_N$ = 473 K for $SrFeO_2$ [10] to $T_N$ = 296 K for $Sr_3Fe_2O_5$ [20], but external stimuli such as magnetic field, light and pressure may induce new phenomena. In this paper, we demonstrate the structural,

magnetic and transport studies on $Sr_3Fe_2O_5$ under high pressure. We observed a spin state transition from $S = 2$ to $S = 1$, an antiferromagnetic-to-ferromagnetic transition at a nearly identical pressure with $SrFeO_2$. We have also found evidence of an insulator-to-metal transition. These facts indicate the robustness of the transitions to the dimensionality. However, unlike $SrFeO_2$ [10], we observed a structural transition involving a change of a stacking sequence of the ladder blocks.

### 4.2. Experimental

A powder sample of $Sr_3Fe_2O_5$ was synthesized by hydride reaction of a slightly oxygen deficient $Sr_3Fe_2O_{7-x}$ ($x \sim 0.4$) with $CaH_2$. The $Sr_3Fe_2O_{7-x}$ precursor was prepared by a high temperature ceramic method from $SrCO_3$ (99.99%), $BaCO_3$ (99.99%) and $Fe_2O_3$ (99.99%) by heating a pelletized stoichiometric mixture at 1273 K in air for 48 hours with one intermediate grinding. For reduction, $Sr_3Fe_2O_{7-x}$ and a four molar excess of $CaH_2$ were finely ground in an Ar-filled glove box, sealed in an evacuated Pyrex tube, and heated at 598 K for 1 day. Residual $CaH_2$ and the CaO byproduct were removed from the final reaction phase by washing them out with an $NH_4Cl$/methanol solution. For more details, refer to the literature [14]. In order to obtain better statistics for the $^{57}$Fe Mössbauer spectroscopy measurements, $^{57}$Fe-enriched $Sr_3Fe_2O_5$ ($^{57}$Fe consisting of about 50% of the total Fe amount) was prepared.

The high-pressure $^{57}$Fe Mössbauer measurements were performed up to 100 GPa using a Bassett-type diamond-anvil cell (DAC) [21]. The powder sample and small ruby chips were inserted in a 200 μm hole of a Re gasket. Daphne7474 was used as a pressure-transmitting medium. A point γ-ray source of $^{57}$Co in a rhodium matrix of 370 MBq and another one of 925 MBq with active areas of 1 mm and 5 mm in diameter, respectively, were used. The velocity scale of the spectrum was relative to α-Fe at room temperature (RT). We estimated

the pressure distribution along the sample by measuring fluorescence of ruby chips dispersed in the sample. We found that the pressure gradient at the sample was not more than 5 GPa at maximal pressures. Experiments under the external magnetic field up to 3 T were carried out with the magnetic field applied along the γ-ray propagation direction. For examination of the intermediate-pressure phase, we employed a DAC with a 180 μm hole of a Re gasket in order to obtain a smaller pressure gradient.

Four-probe dc resistance measurements up to 67 GPa were carried out between 5 K and 300 K with Pt electrodes. The sample/metal-gasket cavity was coated with an insulating mixture of $Al_2O_3$ and NaCl combined with epoxy. The initial sectional area and the distance between probes were about 60 × 50 $\mu m^2$ and 50 μm. Applied pressure was calibrated by means of fluorescence manometer on ruby chips placed around the sample.

Powder X-ray diffraction (XRD) profiles at high pressures up to 39 GPa at RT were recorded using Mo-$K_\alpha$ radiation from a 5.4 kW Rigaku rotating anode generator equipped with a 100 μm collimator. A powder sample of $Sr_3Fe_2O_5$ was loaded into a 180 μm diameter hole of a pre-indented rhenium gasket of the diamond-anvil cell. Helium was used as a pressure-transmitting medium. The shift of ruby fluorescence was used to determine the pressure. The pressure gradient at the sample increased slowly with pressure, but was not more than 0.5 GPa at the maximum pressure. The diffracted X-rays were collected with an imaging plate. More details of the experimental setup are reported elsewhere [22]. Three diffraction peaks, (015), (105), (110) for the low-pressure phase and (015), (104), (111) for the high-pressure phase, were used to refine the cell parameters.

High-resolution synchrotron XRD experiments at high pressures up to 36.7 GPa were performed at RT using angle-dispersive X-ray diffractometry installed in the NE1 synchrotron beam line of the Photon Factory - Advanced Ring for Pulse X-rays (PF-AR) at

the High Energy Accelerator Research Organization (KEK), Japan. The incident X-ray beam was monochromatized to a wavelength of 0.41310 Å. The X-ray beam size was collimated to a diameter of about 50 μm. The angle-dispersive X-ray diffraction patterns were obtained on an imaging plate. The pressure gradient at the sample, estimated in the same way as described above, was not more than 1.0 GPa at maximal pressures. The observed intensities on the imaging plates were integrated as a function of $2\theta$ using the Fit2d code to obtain conventional, one-dimensional diffraction profiles. The obtained synchrotron XRD data were analyzed by the Rietveld method using RIETAN-FP program [23].

### 4.3. Results and Discussions

Typical $^{57}$Fe Mössbauer spectra at high pressures are shown in Figure 4.2. At 0.5 GPa, the spectrum at RT consists of doublet peaks with an isomer shift *IS* of 0.47 mm/s and a quadrupole splitting *QS* of 1.26 mm/s, indicating a paramagnetic state as well as square-planar coordination geometry for a high-spin $Fe^{2+}$, which is consistent with a previous study.[14] When more pressure was applied at RT, the doublet immediately changed to six well-defined peaks, indicating the presence of magnetic order. The value of $S_1$–$S_2$ as indicated in the spectrum at 7 GPa of Figure 4.2 is 1.48 mm/s, which is very close to the *QS* value at 0.5 GPa in the paramagnetic state. A gradual and linear decrease in *IS* with pressure (Figure 4.3) is in accordance with the trend observed in many iron compounds including $SrFeO_2$ [4,9], and can be interpreted in terms of a gradually increased hybridization of iron 3*d* orbitals with the 2*p* orbitals of the oxygen neighbors.

With increasing pressure up to 30 GPa, the split of the sextet increases (see the 26 GPa spectrum in Figure 4.2), implying the increase of $T_N$, which should result from increased magnetic interactions through the decrease of cell parameter. Indeed, the temperature-

dependent Mössbauer measurements at pressures up to 10 GPa reveals that $T_N$ has a linear increase with pressure in this pressure region (Figures 4.4). One can see from the top panel of Figure 4.3 that the hyperfine field $H_{hf}$ steeply increases up to 10 GPa as anticipated, but then saturates above 20 GPa to ~ 32 T. This value is much smaller than 43.7 T at 4 K in an ambient pressure (corresponding to the fully saturated moment for $S = 2$) [14] and 41.6 T at 4K and 23 GPa (Figure 4.5). The tendency of $T_N$ to saturate above 20 GPa is not consistent with the pressure dependence of the cell parameters. All the crystallographic axes continuously decrease with pressure as will be shown later. At 10 GPa, $T_N$ rises up to 365 K (22% increase with respect to the ambient pressure data). Remarkably, $H_{hf}$ for $SrFeO_2$ is nearly independent of both pressures [9] and Sr-to-Ca substitution [12], in spite of the fact that *a* and *c* in $SrFeO_2$ [9] and *a* and *b* in $Sr_3Fe_2O_5$ (as will be shown later) behave similarly as a function of pressure before the transition arrives. The variability of $T_N$ for $Sr_3Fe_2O_5$ with pressure can be explained in terms of geometrical frustration in the ladder arrangement due to the *I*-centered lattice.

The spectrum at 7 GPa contains a small portion of a doublet with similar *IS* and *QS* values (0.64 mm/s and 1.41 mm/s, respectively) to those of the sextet (0.42 mm/s and 1.48 mm/s), as seen in Figure 4.2. The doublet-to-sextet ratio slightly increases at 26 GPa. At each pressure measured in this study, the doublet vanishes at 9 K so that this component is not considered to arise from impurity phase but from $Sr_3Fe_2O_5$ having a lower $T_N$ ($T_N$ < RT). Note that we did not observe such a coexistence with a paramagnetic component in the previous high-pressure study of $SrFeO_2$ [9]. This means that a structural strain caused by nonhydrostatic stress would be more prominent in $Sr_3Fe_2O_5$ than in $SrFeO_2$. Under our experimental conditions, solidification of a pressure medium (Daphne7474) inevitably results in nonhydrostatic pressure to the $Sr_3Fe_2O_5/SrFeO_2$ samples. Given the intergrowth structure

composed of different units (i.e., rock-salt and ladder blocks), such an effect in $Sr_3Fe_2O_5$ would be much stronger than in $SrFeO_2$. Even a small amount of strain might cause a substantial reduction of $T_N$ due to the geometrical frustration in the magnetic lattice as already pointed out.

When further pressure was applied, a drastic change in the Mössbauer spectra appeared (see Figure 4.2), featured by a reduction of the hyperfine field ($H_{hf}$ = 13.5 T at 38 GPa, RT), suggesting an intermediate-spin ($S$ = 1) state as was observed in the high-pressure phase of $SrFeO_2$ [9]. When the sample was cooled to 9 K, $H_{hf}$ increased to 18.4 T, which is nearly half of that of the low-pressure phase, thereby confirming that the iron ions are in the intermediate spin state. Figure 4.3 displays that the obtained *IS* and *QS* values are close to those of the intermediate-spin state of $SrFeO_2$ [9], demonstrating that the iron is in a square planar geometry having only one crystallographically equivalent site. The relatively large $H_{hf}$ value in the intermediate-spin state at RT indicates well-developed magnetic order. Despite the pressure gradient of ~ 5 GPa, a careful analysis of the relative spectrum weight gave a rough estimate of the transition pressure $P_c$ as 34 ± 3 GPa, which is surprisingly close to that of $SrFeO_2$ [9]. When a magnetic field was applied parallel to the γ ray direction, the intensities of the second and fifth lines of the sextet at 44 GPa showed a remarkable decrease at 1.5 T (not shown) and disappeared at 3 T (see Figure 4.2), indicating that the high-pressure phase ($P > P_c$) is a FM state. The AFM-FM transition at $P_c$ was also found in $SrFeO_2$ [9]. The spectral features of the $S$ = 1 state remain up to the maximum pressure of 100 GPa applied in this study. This shows that the $S$ = 1 FM state is quite robust, as in the case of $SrFeO_2$ [9].

Given the high-spin to intermediate-spin state transition and the AFM-to-FM transition in $Sr_3Fe_2O_5$, an I-M transition, which was observed in $SrFeO_2$ [9], is intuitively expected. The electrical resistivity of $Sr_3Fe_2O_5$ performed under pressure is shown in Figure 4.6. The

resistivity is unmeasurably high below 15 GPa, due to a large band gap as theoretically suggested [24]. However, it became measurable above 15 GPa and then remarkably decreases. It is reduced by five orders of magnitude at 60 GPa. Such a large decrease in the resistivity suggests the presence of an I-M transition at $P_c$, although the temperature dependence of the electrical resistance ($\Delta R/\Delta T$) does not become positive even at 67 GPa. It should be noted that the observation of metallic behavior ($\Delta R/\Delta T > 0$) in a powder sample is in general difficult in low dimensional materials as demonstrated by $Na_{1/3}V_2O_5$ [25]. Moreover, the obscurity of the transition may be a result of surface damage due to the air sensitivity of $Sr_3Fe_2O_5$ [14] and pressure inhomogeneity. It is well known that divalent iron oxides are all insulators [26,27]. According to first principles calculations, the unusual metallic state of $SrFeO_2$ under high pressure is accompanied by the charge transfer from O 2*p* to Fe 3*d*, resulting in $d^6$ to $d^{6.5}$ electronic configurations [9]. Accordingly, it is natural to expect that the electric conductivity in $Sr_3Fe_2O_5$ is also attributed to the charge transfer. However, despite such evidence pointing towards an I-M transition, the resistivity data is still ambiguous, and first principles calculations for $Sr_3Fe_2O_5$ would shed more light on this issue.

A pressure-induced spin state transition always involves a volume reduction at $P_c$ [8,9]. In order to probe this, we carried out high pressure XRD experiments at RT up to 38.8 GPa (see Figure 4.7a). In $SrFeO_2$, we previously reported that the diffraction patterns do not show any spectacular change at $P_c$ – the anomaly at $P_c$ is recognizable only when the cell parameters are plotted as a function of *P* [9]. In the case of $Sr_3Fe_2O_5$, however, we unexpectedly found a drastic change in the diffraction pattern above 30 GPa. From $P$ = 2.2 to 29.0 GPa, all diffraction peaks (excluding rhenium peaks) could be assigned to an *I*-centered orthorhombic structure. The diffraction patterns above 30 GPa could be also indexed on the basis of the orthorhombic unit cell (e.g., $a$ = 3.00 Å, $b$ = 3.78 Å, $c$ = 19.09 Å at 38.8 GPa) but have

different extinction conditions. It is seen from Figure 4.7a, for example, that the originally extinct (104) and (111) peaks in the low-pressure structure (space group *Immm*) appear, while the originally allowed (105) and (110) peaks disappear. It follows that the new structure induced by pressure has an *A*-centered orthorhombic lattice. When releasing the pressure, the high-pressure structure remained at pressures above 28.4 GPa, and then completely returned to the original low-pressure structure at pressures below 25.5 GPa without any loss in crystallinity, suggesting that the structural transition is of first-order, reversible and topotactic.

As depicted in Figures 4.7b-d, all the axes decrease smoothly before the structural transition arrives. The pressure dependence of the volume for the low-pressure structure (Figure 4.7e) can be fitted well by the Birch-Murnaghan equation of the state [28], yielding the bulk modulus of $K$ = 94 GPa, which is slightly smaller than that of $SrFeO_2$ ($K$ = 126 GPa) [9]. The volume reduction at 30 GPa is about 4%. Remarkably, while the *a* and *c* axes decrease during this transition, the *b* axis (i.e., the leg direction) increases. Due to the small pressure distribution within the sample (< 0.5 GPa) for the XRD experiments, the structural transition pressure $P_s$ can be precisely determined as 30 ± 2 GPa based on the data during compression. In the case of $SrFeO_2$, we employed almost the same experimental setup as the present study, and obtained a perfect agreement of $P_c$ [9], at which the anomaly was found in Mössbauer (33 ± 3 GPa) and XRD (33 ± 1 GPa) measurements, but in $Sr_3Fe_2O_5$ there is an apparent discrepancy between $P_s$ (= 30 ± 2 GPa) obtained from the XRD measurements and $P_c$ (= 34 ± 3 GPa) obtained from the Mössbauer measurement, a strong indication that the structural transition and the spin state transition are independent. In support of this interpretation, we see a large drop of the *b* axis at 34 ± 2 GPa (see Figure 4.7c), which coincides with $P_c$. The volume reduction at $P_c$ is as much as 3%. The presence of the intermediate phase (i.e., the

two critical pressures at 30 GPa and 34 GPa) was further confirmed by careful Mössbauer measurements as discussed later.

The high-pressure structure up to 36.7 GPa was determined using synchrotron XRD data (Figures 4.8). As expected, the XRD patterns measured above $P_s$ could be indexed on the *A*-centered orthorhombic cell ($a$ = 3.014(4) Å, $b$ =3.800(7) Å, $c$ = 19.11(3) Å at 36.7 GPa), and several small reflections from unknown impurities were found. Earlier, we already explained from the Mössbauer spectra that the irons in the high-pressure structure are in a square planar geometry having only one crystallographically equivalent site. In addition, the structural transition is reversible with only small hysteresis, indicating that the two structures are topotactically related with each other. All these observations led us to consider that the structural transition from the *I*- to *A*-centered space group is caused by a change in the stacking sequence of the two-legged ladder (or the original perovskite) blocks. In the *I*-centered structure of $Sr_3Fe_2O_5$ below $P_s$ (or that of its precursor $Sr_3Fe_2O_7$), the two-legged ladder (or perovskite) blocks are phase-shifted from each other by (1/2, 1/2, 1/2) (see Figure 4.1b). In the *A*-centered structure above $P_s$, we expected that the adjacent ladder blocks are staggered only in the *b* and *c* directions, giving a phase shift of (0, 1/2, 1/2) as shown in Figure 4.1c.

Possible space groups for the high-pressure phase are *Ammm*, *A*2*mm*, *Am*2*m*, *Amm*2 and *A*222. Among these candidates, *Ammm* is the maximal non-isomorphic subspace group for *Immm*, the space group for the low-pressure structure. Accordingly, we chose *Ammm* as the initial space group for refinement of the high-pressure structure. Assuming Sr(1) to be at 2*c* (0.5, 0.5, 0), Sr(2) at 4*j* (0.5, 0.5, *z*), Fe at 4*i* (0, 0, *z*), O(1) at 2*a* (0, 0, 0), O(2) at 4*i* (0, 0, *z*) and O(3) at 4*i* (0, 0, *z*), we refined the structural parameters while the occupancy factors were

constrained to unity. The refinements converged well, providing $R_{wp}$ = 0.90%, $\chi^2$ = 0.89 (see Figure 4.8). These small agreement indices as well as the small atomic displacement parameters *B* for all atoms suggest that the refined structure is reasonable. Other candidate space groups with lower symmetry did not give any appreciable improvement in the structural refinement, so we conclude that the structure with *Ammm* as summarized in Table 4.1 is the best choice.

The inter-atomic distances for the refined structure are listed in Figure 4.9 and Table 4.2. The $FeO_4$ square planar coordination at ambient pressure consists of four almost equivalent bonds (~ 2.0 Å), while that at 36.7 GPa has a distortion with three long bonds (1.97(1) Å and 1.912(5)Å) and one short bond (1.62(5) Å), as shown in Figure 4.9. The mean Fe-O distance of 1.85 Å is close to that for $SrFeO_2$ at 39.2 GPa (1.88 Å). The Sr-O distance at 36.7 GPa ranges from 2.20 Å to 2.65 Å, which is acceptable in this pressure region considering previous studies [9,29--31]. As for Sr(1), Sr(2) is eight-fold coordinated to oxygen atoms in the CsCl-type structure (Figures 4.1c and 4.9). The mean bond distance around Sr(1) (2.53 Å) is slightly longer than that for $SrFeO_2$ at 39.2 GPa (2.41 Å). However, that of Sr(2) (2.43 Å) is very close to 2.41 Å.

We see now that $Sr_3Fe_2O_5$ undergoes a pressure-induced structural transition involving a phase shift of the two-legged ladder blocks. The change of the stacking sequence at $P_s$ leads to the increase of the oxygen coordination number of Sr(2) from seven to eight (see Figures 4.1b and 4.1c), while maintaining the $FeO_4$ square planar coordination. The new structure adopts the intergrowth of a two-legged ladder with CsCl type structure. In geology, the structural transition from the *B*1(NaCl) type to the *B*2(CsCl) type was intensively studied by both theoretical [32,33] and experimental [34,35] methods due to the possible occurrence of

this transition in the earth's lower mantle, which could affect the transmission of seismic waves. Indeed, *AX* materials (*A* = Be, Mg, Ca, Sr, Ba, *X* = O, S, Se, Te) with the *B*1 structure undergo or are predicted to undergo structural transitions to the *B*2 structure with observed or expected critical pressures ranging from 5 GPa to 1000 GPa, depending on the ionic radii of *A* [34--36]. In SrO [37], the *B*1 to *B*2 transition occurs at 36 GPa which is close to $P_s$ (= 30 GPa) observed in $Sr_3Fe_2O_5$. Moreover, the atomic distances (Sr-Sr, O-O and Sr-O) of the two compounds above $P_s$ are similar; those of SrO at 37 GPa are, respectively, 2.89 Å, 2.89 Å and 2.50 Å while Sr(2)-Sr(2), O(3)-O(3) and the mean Sr(2)-O distance of $Sr_3Fe_2O_5$ at 36.7 GPa are 2.752(7) Å, 3.05(6) Å and 2.43 Å. All these facts validate the observed transition in $Sr_3Fe_2O_5$. It is also interesting to point out that Dion-Jacobson type layered perovskite oxides $A$LaNb$_2$O$_7$ (*A* = alkali metal) exhibit a similar structural modification [38], where the stacking sequence of the perovskite blocks can be varied by the ionic radius of the *A* ion, instead of pressure. *A* = Cs, K and Li, respectively, give *P*-, *A*-, *I*-centered structures with eight, six and four-fold coordination around the *A* ion, while maintaining the perovskite blocks.

The new structure above $P_s$ consists of *infinite* $Fe_2O_5$ layers intervened by Sr atoms along the *a* direction with the sequence [– $Fe_2O_5$ – $Sr_3$ – $Fe_2O_5$ – $Sr_3$ –] (Figure 4.1c). In the low-pressure structure (Figure 4.1b), each $Fe_2O_7$ rung is collinearly aligned with the neighboring Sr(2) atoms along [001], while in the high-pressure phase each $Fe_2O_7$ rung is connected to two $Fe_2O_7$ rungs of neighboring ladders in a zigzag manner. It is this staggered arrangement that permits a distinct decrease of *c* during the structural transition (~0.4 Å). Also, the alternating stacking of $(Fe_2O_5)^{6-}$ and $(Sr_3)^{6+}$ in the high-pressure structure would effectively reduce the stack distance along the *a* axis ($\Delta a$ ~0.1 Å). On the contrary, the large reduction in *a* and *c* axes by the phase shift is partly compensated by the increase of the *b* axis (the leg

direction) about ~0.05 Å. The elongation of this axis is rationalized as the relief of coulomb repulsion between adjacent Sr(2) ions and between adjacent O(1) ions (see the arrows in Figure 4.1), both of which become considerably shorter upon the structural transition (Sr(2)-Sr(2): 3.5 Å → 2.8 Å; O(1)-O(1): ~3.3 Å→ ~3.1 Å).

There remains a question about magnetic properties of the intermediate-pressure phase ($P_s < P < P_c$). Thus we decided to perform Mössbauer measurements in this pressure region using a different batch. In this measurement, we used a DAC with the smaller sample hole in order to obtain a smaller pressure gradient. As shown in Figure 4.10, the RT spectrum at 31 GPa consists of sextet (57%) and doublet (43%). The $H_{hf}$ for the sextet component is 32.4 T at RT and is 40.2 T at 4 K, indicating persistence of the high-spin state, but we notice that $S_1$–$S_2$ (1.10 mm/s) is different from that at 26 GPa (see Figure 4.10) and is rather close to those at $P > P_c$ as demonstrated in Figure 4.3. Since $QS$ (= $S_1$-$S_2$) provides relevant information on the local structure around iron, the sextet component can be assigned as intrinsic to the intermediate-pressure phase ($P_s < P < P_c$). The doublet component has nearly the same $IS$ and $QS$ values as the sextet at 31 GPa so that it is also ascribed as intrinsic to the intermediate-pressure phase. We deduce that structural strains induced by the structural transition might be a possible reason of why the spin-ordered coexists with the disordered states in the intermediate-pressure phase.

The low-temperature spectrum at 31 GPa consists of only a single set of sextet, meaning that the paramagnetic phase also experiences magnetic order. By the application of magnetic field of 3 T, the sextet becomes markedly broadened, which indicates that the intermediate-pressure phase is in an AFM state as the low-pressure phase. The magnetic moments align parallel to the $FeO_4$ square planar unit, as in the low-pressure $S = 2$ AFM and high-pressure $S = 1$ FM phases. It is not possible to determine the magnetic structure of the intermediate

AFM phase from the Mössbauer data, but the *G*-type order as observed at ambient pressure [14] is likely to be preserved because a change in the spin structure in $SrFeO_2$ takes place together with the spin state transition.

It is interesting that the spin state transition in $Sr_3Fe_2O_5$ occurs at almost the same pressure as $SrFeO_2$ [9], an observation pointing that the dimensionality has little influence on the spin state transition. Whangbo and Köhler argued that the face-to-face $FeO_4$ square planar arrangement is essential for the occurrence of the spin state transition in $SrFeO_2$ [3]. In accordance with their argument, $Sr_3Fe_2O_5$ containing the same face-to-face arrangement exhibits the spin state transition. However, close inspections of the structures of $SrFeO_2$ and $Sr_3Fe_2O_5$ have found several aspects to be addressed. First, the distance between adjacent face-to-face $FeO_4$ square planar units (i.e., $a$ for $Sr_3Fe_2O_5$ and $c$ for $SrFeO_2$) is considered as the most crucial factor for the spin state transition, but the spin state transition occurs when $c$ = 3.09 Å for $SrFeO_2$ and $a$ = 3.04 Å for $Sr_3Fe_2O_5$. The structural transition helps to shorten $a$, and the length at $P_s$ is close to $c$ for $SrFeO_2$ at $P_c$. The second concerns the shape of the $FeO_4$ square planar coordination; in $SrFeO_2$ all four Fe-O bonds are equal in length [9], but this is not the case in $Sr_3Fe_2O_5$ below $P_s$, and further distortion becomes more prominent above $P_s$ (Figure 4.9). Owing to the short Fe-O(1) length, the iron atom is shifted toward O(3), which results in a deviation of the Fe-O(2)-Fe bridging angle from the ideal value 180 ° (e.g., 167 ° at 36.7 GPa). Third, the *d*-orbital occupation and electronic configuration should be affected by the deformed structure of $FeO_4$. In the $S$ = 1 state of $SrFeO_2$, the $d_{xy}$ and $d_{yz}$ for the spin-down channel are equally filled (half-filled) [9], but this balance might be disturbed in $Sr_3Fe_2O_5$. All these factors can more or less contribute to changing $P_c$, so that it is possible that our observation can be a mere accidental coincidence. Therefore, a systematic and

comprehensive study of the other ladder series $Sr_{n+1}Fe_nO_{2n+1}$ including $Sr_2FeO_3$ and $Sr_4Fe_3O_7$ (not yet synthesized) is strongly desired.

As demonstrated already, the structural transition in $Sr_3Fe_2O_5$ can be explained quite adequately by structural terms so that we consider that the two transitions occur independently (although the proximity of $P_s$ and $P_c$ in $Sr_3Fe_2O_5$ superficially suggests some interplays between them). If this is the case, we can in turn predict a pressure-induced structural transition for compounds that share structural features with $Sr_3Fe_2O_5$. Among the candidate materials are $A_2CuO_3$ ($A$ = Ca, Sr, Ba) [39,40] and $Sr_2PdO_3$[41], all having the *Immm* space group with the intergrowth structure of $A$O rock-salt block and $CuO_2$ ($PdO_2$) chain (or one-legged ladder) blocks, being isostructural with the hypothetical compound $Sr_2FeO_3$. Another candidate, $K_2NiO_2$, is tetragonal (*I*4/*mmm*), which differs from the aforementioned $A_2CuO_3$ structure by the absence of bridging oxygen, yielding a two-fold dumbbell coordination around Ni [42]. It is interesting to check whether the orthorhombicity is necessary or not for the structural transition from the *I*- to *A*-centered lattice.

### 4.4. Conclusion

$Sr_3Fe(II)_2O_5$ exhibits a spin state transition from $S$ = 2 to $S$ = 1 state at $P_c$ = 34 GPa with an AFM-FM transition. Signs suggesting an I-M transition were also observed at pressure around $P_c$. $SrFeO_2$ shows the same behavior, suggesting a general intrinsic character for square planar coordinated iron oxides. The critical pressure $P_c$ is insensitive to the dimensionality, but further studies especially using other systems $Sr_{n+1}Fe_nO_{2n+1}$ are needed to understand the spin-ladder physics for $S$ = 2. Most importantly, unlike $SrFeO_2$, we also observed a pressure-induced structural transition at $P_s$ = 30 GPa, which involves a change in the stacking sequence of the ladder blocks. The SrO block of the original seven-fold rock-salt

structure adopts the eight-fold CsCl structure. This allows an efficient contraction of the volume. Ever since the prediction of superconductivity in the $S$ = 1/2 two-legged ladder system by Dagotto *et al*. [43], the search for superconductivity has been vigorously performed and $(Sr_{1-x}Ca_x)_{14}Cu_{24}O_{41}$ was found to show superconductivity under high-pressure although its $T_c$ is low [44]. The successful metallization of $S$ = 2 $Sr_3Fe_2O_5$ under high pressure would also provide hope that further pressurization could lead to superconductivity.

## References


[1] P. Gütlich, A. Hauser, and H. Spiering, Angew. Chem. Int. Ed. 33 (1994) 2024.

[2] O. Kahn and C. J. Martinez, Science 279 (1998) 44.

[3] M. H. Whangbo and J. Köhler, Nat. Chem. 1 (2009) 351.

[4] M. Takano, S. Nasu, T. Abe, K. Yamamoto, S. Endo, Y. Takeda, and J. B. Goodenough, Phys. Rev. Lett. 67 (1991) 3267.

[5] M. Abbate, J. Fuggle, A. Fujimori, L. Tjeng, C. Chen, R. Potze, G. Sawatzky, H. Eisaki, and S. Uchida, Phys. Rev. B 47 (1993) 16124.

[6] J. A. Real, E. Andrés, M. C. Munoz, M. Julve, T. Granier, A. Bousseksou, and F. Varret, Science 268 (1995) 265.

[7] G. J. Halder, C. J. Kepert, B. Moubaraki, K. S. Murray, and J. D. Cashion, Science 298 (2002) 1762.

[8] J. F. Lin, V. V. Struzhkin, S. D. Jacobsen, M. Y. Hu, P. Chow, J. Kung, H. Liu, H. Mao, and R. J. Hemley, Nature 436 (2005) 377.

[9] T. Kawakami, Y. Tsujimoto, H. Kageyama, *et al*, Nat. Chem. 1 (2009) 371.

[10] Y. Tsujimoto, C. Tassel, N. Hayashi, T. Watanabe, H. Kageyama, K. Yoshimura, M. Takano, M. Ceretti, C. Ritter, and W. Paulus, Nature 450 (2007) 1062.

[11] C. Tassel, T. Watanabe, Y. Tsujimoto, N. Hayashi, A. Kitada, Y. Sumida, T. Yamamoto, H. Kageyama, M. Takano, and K. Yoshimura, J. Am. Chem. Soc. 130 (2008) 3764.

[12] C. Tassel, J. M. Pruneda, N. Hayashi, *et al*, J. Am. Chem. Soc. 131 (2009) 221.

[13] T. Yamamoto, Z. Li, C. Tassel, *et al*, Inorg. Chem. 49 (2010) 5957.

[14] H. Kageyama, T. Watanabe, Y. Tsujimoto, *et al*, Angew. Chem. Int. Ed. 47 (2008) 5740.

[15] E. Dixon and M. A. Hayward, Inorg. Chem. 49 (2010) 9649.

[16] Z. Hiroi, M. Azuma, M. Takano, and Y. Bando, J. Solid State Chem. 95 (1991) 230.

[17] M. G. Smith, A. Manthiram, J. Zhou, J. B. Goodenough, and J. T. Markert, Nature 351 (1991) 549.

[18] M. Azuma, Z. Hiroi, M. Takano, K. Ishida, and Y. Kitaoka, Phys. Rev. Lett. 73 (1994) 3463.

[19] E. Dagotto and T. M. Rice, Science 271 (1996) 618.

[20] N. Hayashi, H. Kageyama, Y. Tsujimoto, T. Watanabe, S. Muranaka, T. Ono, S. Nasu, Y. Ajiro, K. Yoshimura, and M. Takano, J. Phys. Soc. Jpn. 79 (2010) 123709.

[21] W. A. Bassett, T. Takahashi, and P. W. Stook, Rev. Sci. Instrum. 38 (1967) 37.

[22] A. K. Arora, T. Yagi, N. Miyajima, and T. A. Mary, J. Appl. Phys. 97 (2005) 013508.

[23] F. Izumi and K. Momma, Solid State Phenom. 130 (2007) 15.

[24] H. J. Koo, H. Xiang, C. Lee, and M. H. Whangbo, Inorg. Chem. 48 (2009) 9051.

[25] H. Yamada and Y. Ueda, J. Phys. Soc. Jpn. 68 (1999) 2735.

[26] R. D. Shannon, D. B. Rogers, C. T. Prewitt, and J. L. Gillson, Inorg. Chem. 10 (1971) 723.

[27] M. Derzsi, P. Piekarz, P. T. Jochym, J. Łażewski, M. Sternik, A. M. Oleś, and K. Parlinski, Phys. Rev. B 79 (2009) 205105.

[28] F. Birch, J. Appl. Phys. 9 (1938) 279.

[29] D. Errandonea, J. Pellicer-Porres, F. J. Manjón, *et al*, Phys. Rev. B 72 (2005) 174106.

[30] D. Errandonea, R. S. Kumar, X. Ma, and C. Tu, J. Solid State Chem. 181 (2008) 355.

[31] M. Fischer, B. Bonello, J. P. Itie, A. Polian, E. Dartyge, A. Fontaine, and H. Tolentino, Phys. Rev. B 42 (1990) 8494.

[32] K. Chang and M. L. Cohen, Phys. Rev. B 30 (1984) 4774.

[33] D. Alfe, M. Alfredsson, J. Brodholt, M. Gillan, M. Towler, and R. Needs, Phys. Rev. B 72 (2005) 014114.

[34] R. Jeanloz, T. J. Ahrens, H. K. Mao, and P. M. Bell, Science 206 (1979) 829.

[35] T. A. Grzybowski and A. L. Ruoff, Phys. Rev. B 27 (1983) 6502.

[36] C. Narayana, V. J. Nesamony, and A. L. Ruoff, Phys. Rev. B 56 (1997) 14338.

[37] Y. Sato and R. Jeanloz, J. Geophys. Res. 86 (1981) 11773.

[38] M. Sato, J. Abo, T. Jin, and M. Ohta, J. Alloys Compounds 192 (1993) 81.

[39] K. Kojima, Y. Fudamoto, M. Larkin, G. Luke, J. Merrin, B. Nachumi, Y. Uemura, N. Motoyama, H. Eisaki, and S. Uchida, Phys. Rev. Lett. 78 (1997) 1787.

[40] W. K. Wong-Ng, K. Davis, and R. S. Roth, J. Am. Ceram. Soc. 71 (1988) C64.

[41] Y. Nagata, T. Taniguchi, G. Tanaka, M. Satho, and H. Samata, J. Alloys Compounds 346 (2002) 50.

[42] H. Rieck and R. Hoppe, Z. Anorg. Allg. Chem. 400 (1973) 311.

[43] E. Dagotto, J. Riera, and D. Scalapino, Phys. Rev. B 45 (1992) 5744.

[44] T. Nagata, M. Uehara, J. Goto, J. Akimitsu, N. Motoyama, H. Eisaki, S. Uchida, H. Takahashi, T. Nakanishi, and N. Môri, Phys. Rev. Lett. 81 (1998) 1090.

**Table 4.1.** Structural parameters for $Sr_3Fe_2O_5$ at 36.7 GPa obtained by Rietveld refinement.

| atom | site | *g* | *x* | *y* | *z* | *B* /Å$^2$ |
|---|---|---|---|---|---|---|
| Sr(1) | 2*c* | 1 | 0.5 | 0.5 | 0 | 0.4(2) |
| Sr(2) | 4*j* | 1 | 0.5 | 0.5 | 0.1979(3) | 0.4(2) |
| Fe | 4*i* | 1 | 0 | 0 | 0.1029(7) | 1.5(2) |
| O(1) | 2*a* | 1 | 0 | 0 | 0 | 0.6(4) |
| O(2) | 4*i* | 1 | 0 | 0 | 0.614(2) | 0.6(4) |
| O(3) | 4*i* | 1 | 0 | 0 | 0.188(3) | 0.6(4) |

[a] space group : *Ammm*, $a$ = 3.0108(4) Å, $b$ =3.8004(4) Å, $c$ = 19.113(3) Å,
$R_{wp}$ = 0.90%, $R_p$ = 0.66%, $\chi^2$ = 0.89
$R_I$ = 4.98%, $R_F$ = 3.28%,

**Table 4.2.** Interatomic distances for $Sr_3Fe_2O_5$ at 36.7GPa.

| | Distance (Å) |
|---|---|
| Sr(1)–O(1) × 4 | 2.4243(2) |
| Sr(1)–O(2) × 4 | 2.65(4) |
| Sr(2)–O(2) × 2 | 2.20(3) |
| Sr(2)–O(3) × 2 | 2.65(4) |
| Sr(2)–O(3) × 4 | 2.432(4) |
| Fe–O(1) × 1 | 1.97(1) |
| Fe–O(2) × 2 | 1.912(5) |
| Fe–O(3) × 1 | 1.62(5) |

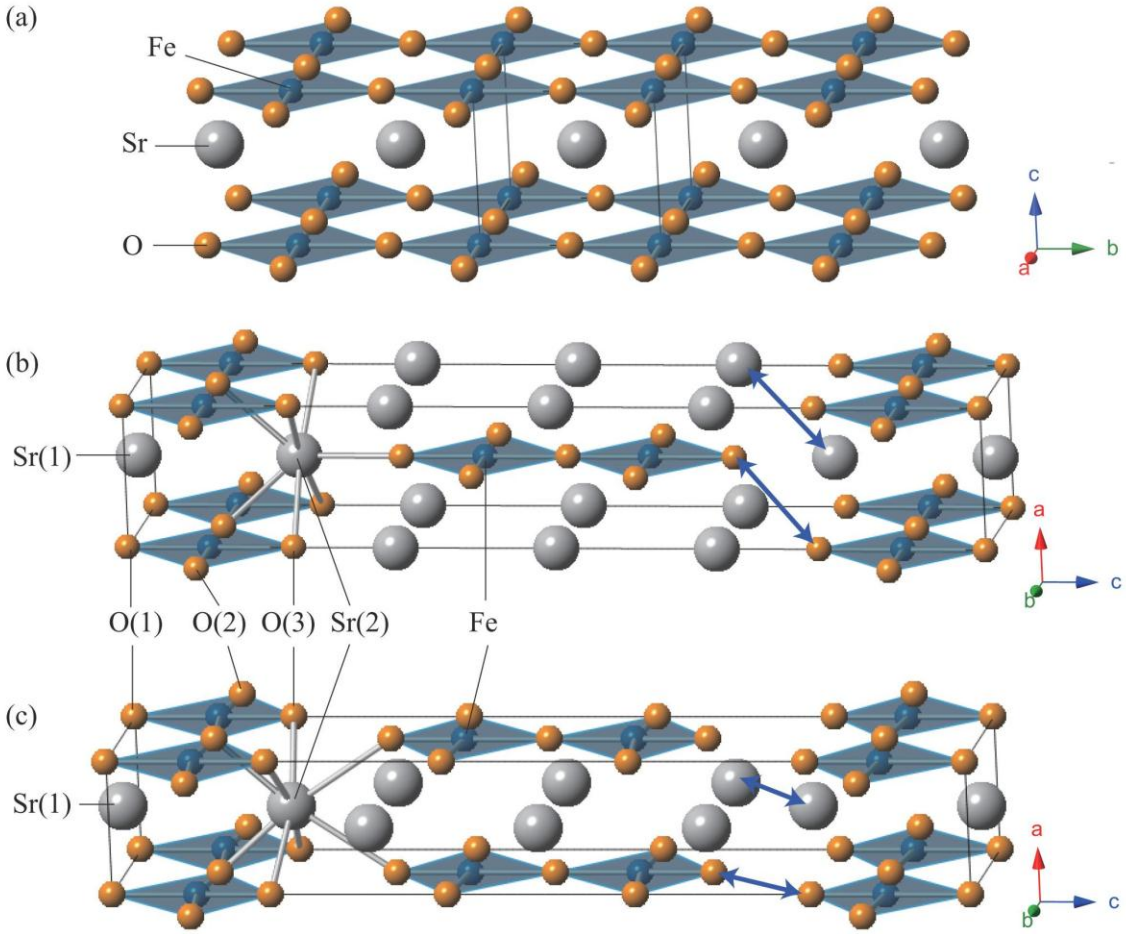


**Figure 4.1**. Comparison of the structure of (a) $SrFeO_2$, and $Sr_3Fe_2O_5$ at (b) low pressure ($P < P_s$) and (c) high pressure ($P_s < P$). White, blue, and orange spheres represent Sr, Fe and O atoms, respectively. Blue arrows represent the adjacent Sr(2)-Sr(2) and O(2)-O(2).

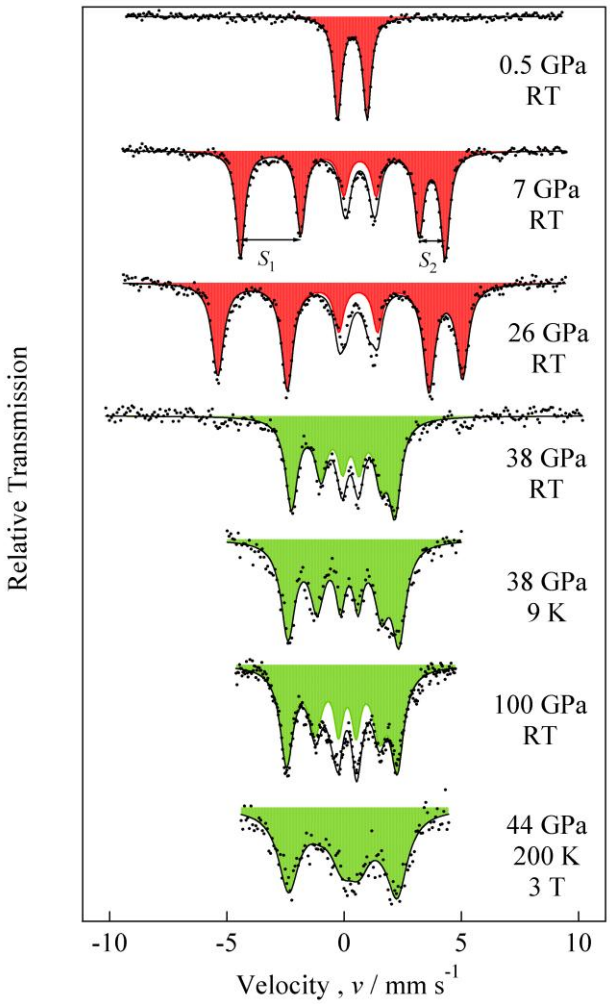


**Figure 4.2.** Observation of the spin state transition in $Sr_3Fe_2O_5$ by high-pressure $^{57}Fe$ Mössbauer experiments. The red spectra correspond to the $S$ = 2 state, and the green to the $S$ = 1 state. The solid lines represent the total fitted curves. The difference between the first and second peaks and the fifth and sixth peaks, $S_1$–$S_2$, represents $QS$ (see text for more detail).

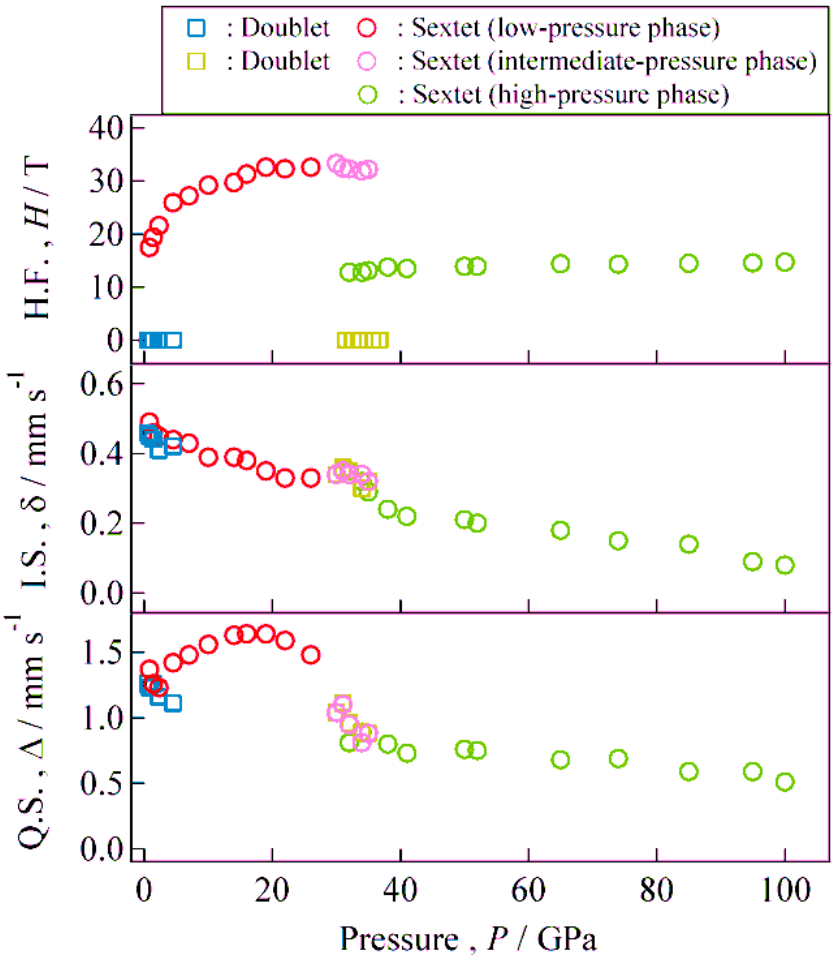


**Figure 4.3**. Pressure dependence of Mössbauer parameters of $Sr_3Fe_2O_5$, $H_{hf}$ (top), *IS* (middle), *QS* (bottom) at RT.

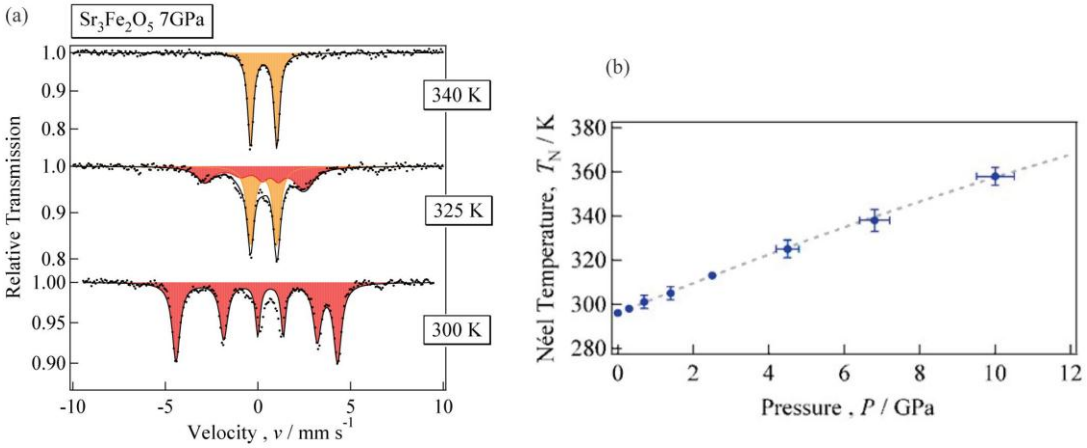


**Figure 4.4**. (a) Temperature dependence of $^{57}$Fe Mössbauer spectra at 7 GPa. (b) Pressure dependence of $T_N$ as determined by the $^{57}$Fe Mössbauer spectra at elevated temperatures.

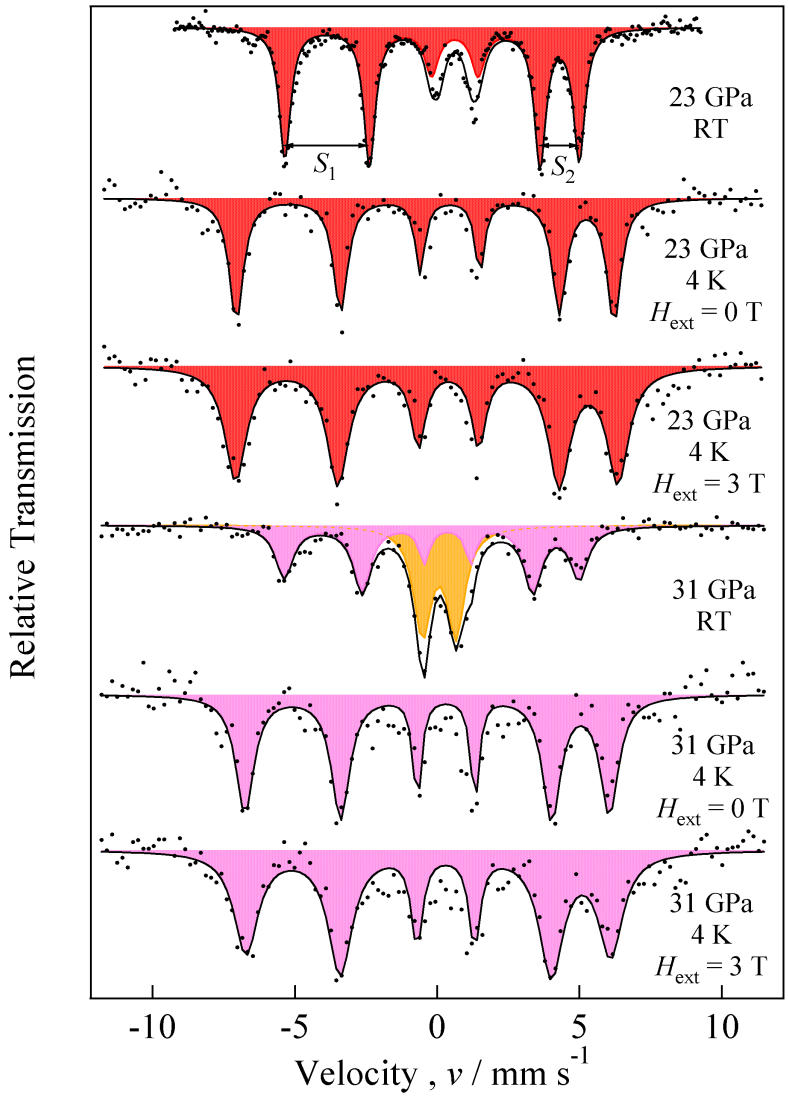


**Figure 4.5**. Temperature and magnetic field dependence of $^{57}$Fe Mössbauer spectra for $Sr_3Fe_2O_5$.

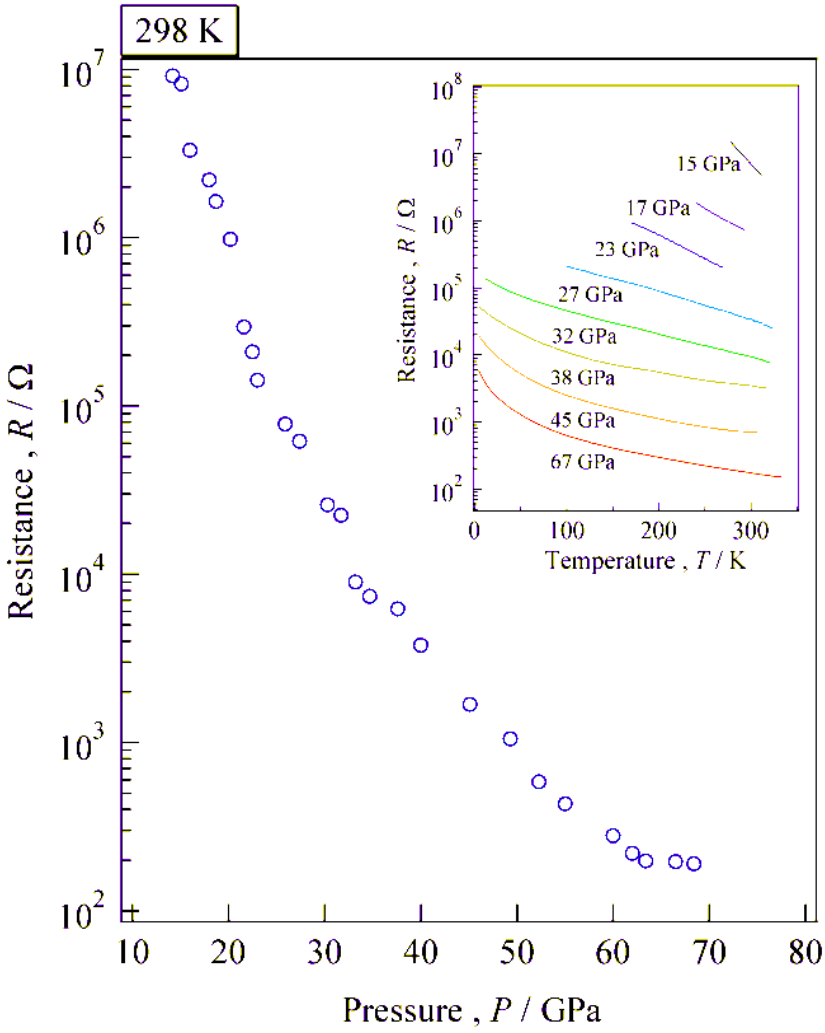


**Figure 4.6**. Room temperature electrical resistance as a function of *P*. Inset shows temperature dependence of the electrical resistance under high pressure.

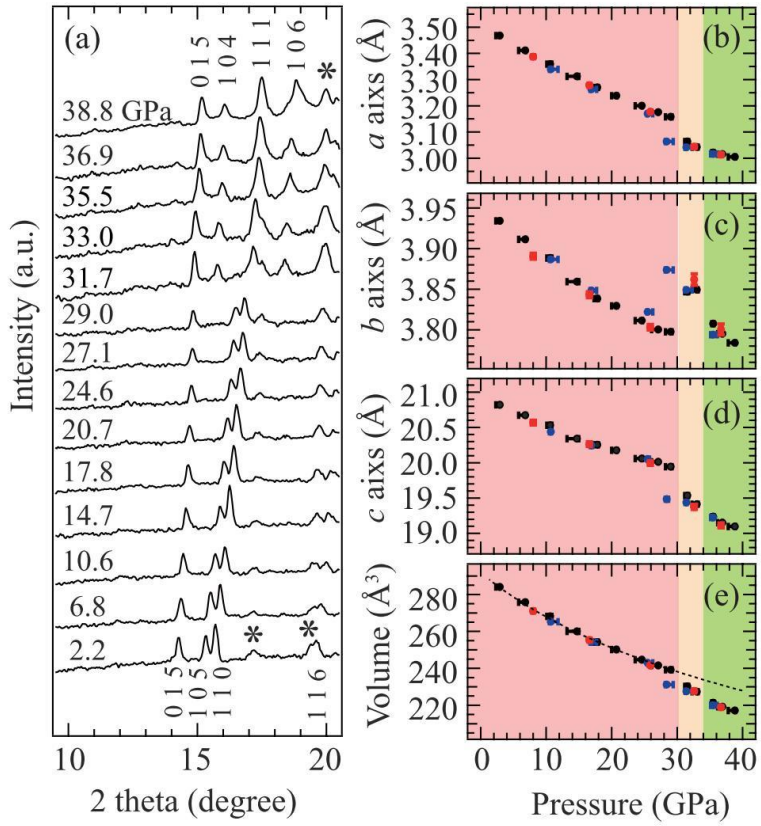


**Figure 4.7.** (a) Powder XRD patterns of $Sr_3Fe_2O_5$ at various pressures at RT, indexed on the orthorhombic unit cell. Asterisks correspond to peaks from rhenium. Pressure dependence of (b)-(d) the lattice parameters and (e) the volume. Black circles represent the data obtained upon increasing pressure using laboratory XRD, blue circles represent those obtained upon releasing pressure using laboratory XRD, and red circles represent those obtained using synchrotron XRD. The dotted line in panel (e) represents Birch-Murnaghan fitting below $P_s$.

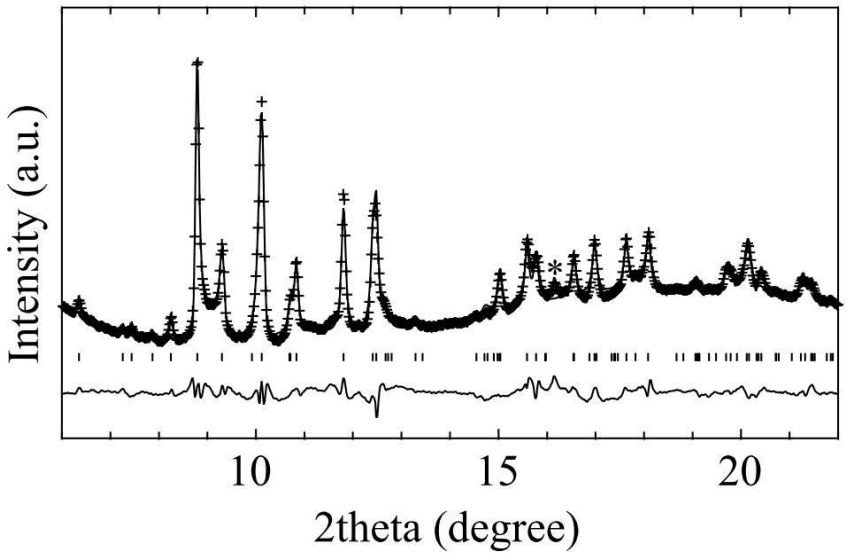


**Figure 4.8**. Structural characterization of $Sr_3Fe_2O_5$ by the Rietveld refinement of the synchrotron XRD data at 36.7 GPa and RT. The overlying crosses and the solid line represent the observed and the calculated intensities. The bottom solid line represents the difference between the observed intensity and the calculated intensity. The ticks correspond to the position of the calculated Bragg peaks of high-pressure phase of $Sr_3Fe_2O_5$. Asterisk indicates reflection from unknown impurity.

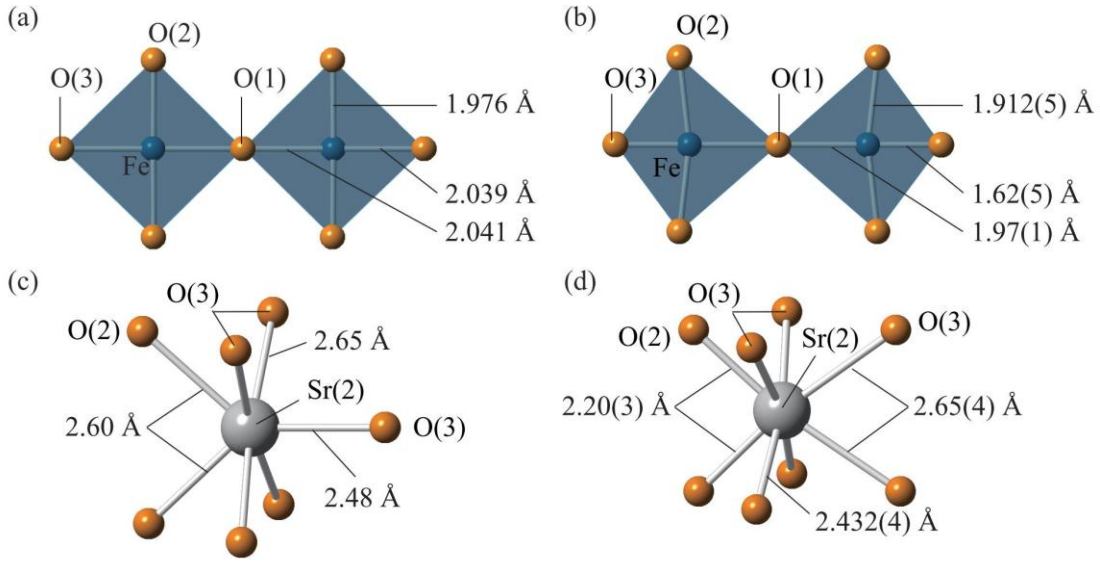


**Figure 4.9**. Coordination around Fe and Sr(2). (a) Iron coordination in the low-pressure structure at ambient pressure, and (b) the high-pressure structure at 36.7 GPa. (c) Sr(2) coordination in the low-pressure structure at ambient pressure, and (d) the high-pressure structure at 36.7 GPa.

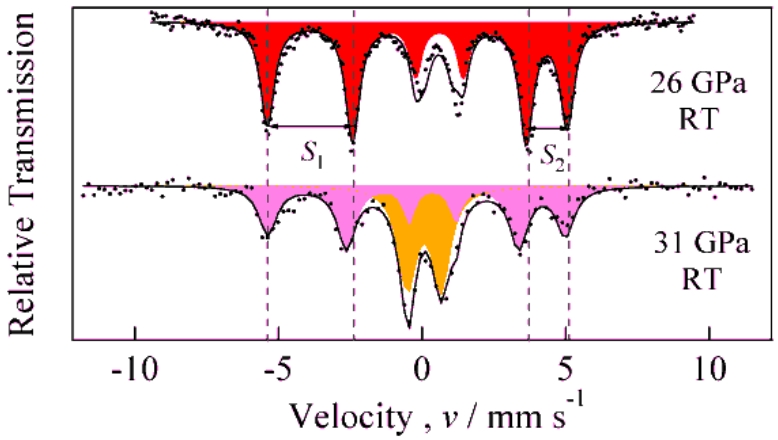


**Figure 4.10**. $^{57}$Fe Mössbauer spectra in the $S$ = 2 state at RT. The red spectrum corresponds to the low-pressure phase, and the pink and orange to the intermediate-pressure phase.

# *Chapter 5. B1-to-B2 Structural Transitions in Rock Salt Intergrowth Structures*

## 5.1. Introduction

Crystal structures of minerals under high pressure have long been of great interest in structural chemistry and geology. For example, silica $SiO_2$ has various polymorphs depending on temperature and pressure [1--4]. The recent discovery of post-perovskite structure in $MgSiO_3$ may account for the D" seismic discontinuity [5]. Among a numerous number of pressure-induced structural transitions, the transition from *B*1(NaCl) to *B*2(CsCl) is perhaps the most systematically studied system and best understood both from experimental and theoretical point of view. This is because both *B*1 and *B*2 structures are simple ionic structures and MgO is believed to exhibit this transition in the Earth's lower mantle. So far, many ionic binary compounds AX (A = Ca, Sr, Ba: X = O, S, Se, Te) with the *B*1-type structure at ambient pressure are known to or predicted to transform to the *B*2-type structure at high pressure [6--18]. It was furthermore revealed that, for a given X, the logarithm of transition pressure $P_s$ shows a linear dependence on ratio of the cation/anion radius, $R_A/R_X$ (see Figure 5.1) [6--8].

Pressure-induced magnetic/transport transitions have been recently observed at $P_c$ = 33 GPa in the infinite layer structure $SrFeO_2$, that is, a spin-state transition (from high-spin state to intermediate-spin state), an insulator-to-metal transition, and an antiferromagnetic-to-ferromagnetic transition [19]. The two-legged spin ladder structure $Sr_3Fe_2O_5$, an intergrowth compound composed of alternate stacking of the SrO rock salt block and the $(SrFeO_2)_2$ ladder block along the *c* axis, also undergoes these three transitions at the nearly same

pressure of $P_c$ = 34 GPa [20]. Unexpectedly, the latter compound shows an additional structural transition from *Immm* to *Ammm* at $P_s$ = 30 GPa [20]. The structural transition is of 1st order and is characterized by the phase shift of the neighboring ladder blocks from (1/2,1/2,1/2) to (0,1/2,1/2). With this phase shift of the ladder block, the coordination geometry around strontium changes from the 7-fold rock salt arrangement to the 8-fold CsCl arrangement. Therefore, this structural transition can be characterized as a *B*1-to-*B*2 transition within an intergrowth compound.

However, whether or not the *B*1-to-*B*2 transition is universal to structurally related intergrowth compounds is uncertain. Several considerations show that one cannot easily preclude the scenario that the $FeO_4$ square planes (or the ladder subunit in $Sr_3Fe_2O_5$) take a leading role in the structural transition. A series of *n*-legged spin ladder $Sr_{n-1}Cu_nO_{2n-1}$ (*n* = 2, 3,…) [21,22], obtained by high pressure synthesis, can be viewed as "quasi" infinite layer structures composed of the $(Cu_nO_{2n-1})^{2(n-1)-}$ layers intervened by $(n-1)Sr^{2+}$. Notice that the high pressure form of $Sr_3Fe_2O_5$ also forms the "quasi" infinite layer structure composed of $(Fe_2O_5)^{6-}$ layers intervened by $3Sr^{2+}$. Furthermore, the preservation of the piled ladders upon transition may be ascribed to Fe-Fe interactions between face-to-face $FeO_4$ square planes (i.e. metal-metal bonding), which are experimentally and theoretically shown to be strong [23--26]. The metal-metal bonding would become stronger under high pressure. Another source of complication is the proximity of $P_s$ and $P_c$: the structural transition might be driven by certain interplay between energetically close states (*S* = 2 antiferromagnetic insulator vs *S* = 1 ferromagnetic metal).

In this study, we investigated the presence of pressure-induced structural transitions in one-dimensional (1D) compounds $A_2MO_3$ (A = Sr, Ca; M = Cu, Pd) [27,28]. The crystal structure is shown in Figure 5.2a. $A_2MO_3$ is an intergrowth structure of the AO rock salt

blocks and the 1D chains of corner-shared $MO_2$ squares (or one-legged ladders), and adopt the *Immm* space group. In $A_2Cu(II)O_3$, only 3d $x^2$–$y^2$ orbital is active and the metal-metal bonding between face-to-face $CuO_4$ square planes is negligibly small, in contrast to the case of $Sr_3Fe_2O_5$. All examined $A_2MO_3$ compounds exhibit the same type of structural transitions as $Sr_3Fe_2O_5$, which provides a unique opportunity to discuss the intrinsic nature of this transition and quantitative comparison with the well-studied binary systems. In addition, the effect of the partial oxygen filling at the apical vacant site was investigated through $LaSrNiO_{3.4}$. The electrical properties of $Sr_2CuO_3$ between the low- and high pressure phases are compared for investigating the effect on the physical properties.

### 5.2. Experimental

Powder samples of $Sr_2CuO_3$, $Ca_2CuO_3$ and $Sr_2PdO_3$ were synthesized by the high temperature ceramic method [27,28]. Stoichiometric amounts of $SrCO_3$ (99.99%), $CaCO_3$ (99.99%), CuO (99.99%), and PdO (99.99%) were mixed, pelletized, and fired at 1173 K for 24 hours. Subsequently, the pellets were ground, re-pelletized, and heated at 1223 K for 24 hours. The sample purities were checked by X-ray diffraction (XRD) measurement using a D8 ADVANCE diffractometer (BRUKER) equipped with a graphite monochromator and Cu $K_{\alpha 1}$ radiation ($\lambda$ = 1.54056 Å). As shown in Figure 5.3, all the diffraction patterns were represented by the *Immm* space group, in consistency with previous reports [27,28]. No impurity peaks were detected.

A powder sample of $LaSrNiO_{3.4}$ was synthesized topochemically by reducing a single-layered Ruddlesden-Popper type perovskite $LaSrNiO_4$. The $LaSrNiO_4$ precursor was prepared by a high temperature ceramic method from $SrCO_3$ (99.99%), predried $La_2O_3$ (99.99%) and NiO (99.99%). A pelletized stoichiometric mixture was heated at 1373 K in air

for 24 hours, and at 1673 K in $O_2$ flowing for 48 hours after an intermediate grinding. For reduction, $LaSrNiO_4$ and a two molar excess of $CaH_2$ were finely ground in a $N_2$-filled glove box, sealed in an evacuated Pyrex tube, and heated at 623 K for 24 hours. Residual $CaH_2$ and CaO byproduct were removed from the final reaction phase by washing with a 0.05 mol/L $NH_4Cl$/methanol solution. The tetragonal and orthorhombic lattice parameters of the precursor and the reduced phases are, respectively, $a$ = 3.82699(5) Å, $c$ = 12.4569(2) Å and $a$ = 3.6856(3) Å, $b$ = 3.8670(3) Å, $c$ = 12.708(1) Å. Oxygen amount of the reduced material was examined by thermogravimetric (TG) measurement using a TG-DTA 2000S (Bruker AXS). 50.8 mg of the sample was put in a Pt pan and $\alpha$-$Al_2O_3$ was used as a reference. The measurements were performed by heating the sample at 10 K/min under a flow of oxygen with a flow rate of 100 ml/min. Figures 5.4 demonstrates that the composition was calculated as $LaSrNiO_{3.4}$. This stoichiometry is supported by the dependence of the lattice parameters on the oxygen content as reported in the literature for $LaSrNiO_{4-x}$, which was obtained by $H_2$ gas reduction from $LaSrNiO_4$ [29].

High resolution powder synchrotron XRD experiments under high pressures were performed at room temperature up to 37 GPa for $Sr_2CuO_3$, 51 GPa for $Ca_2CuO_3$ and 35 GPa for $Sr_2PdO_3$ using angle-dispersive X-ray diffractometry using the NE1A synchrotron beam line of the Photon Factory - Advanced Ring for Pulse X-rays (PF-AR) at the High Energy Accelerator Research Organization (KEK), Japan. Helium was used as a pressure transmitting medium for $Sr_2CuO_3$ and $Sr_2PdO_3$, while a 4:1 methanol:ethanol mixture was used for $Ca_2CuO_3$. The pressure gradients within the samples were not more than 8 GPa for $Sr_2CuO_3$, 4 GPa for $Ca_2CuO_3$ and 1 GPa for $Sr_2PdO_3$ at maximum pressures applied in this study. The incident X-ray beam was monochromatized to a wavelength of 0.4115 Å for $Sr_2CuO_3$ and 0.4114 Å for $Ca_2CuO_3$. For $Sr_2PdO_3$, the first batch was measured with a

wavelength of 0.4115 Å, until the used DAC was broken at 24GPa. The second batch was measured with a wavelength of 0.4114 Å in a pressure range from 19 GPa to 35GPa. The beam was collimated to a diameter of about 50 μm. The angle-dispersive XRD patterns were obtained on an imaging plate.

The observed synchrotron XRD intensities on the imaging plates were integrated as a function of $2\theta$ using the Fit2d code [30] to obtain one-dimensional diffraction profiles. The data at the highest pressure applied to each compound were analyzed by the Rietveld method using the RIETAN-FP program [31]. The agreement indices used were the weighted pattern $R$, $R_{wp} = [\sum w_i(y_{io} - y_{ic})^2/\sum w_i(y_{io})^2]^{1/2}$, pattern $R$, $R_p = \Sigma|y_{io} - y_{ic}|/\Sigma(y_{io})$ and goodness of fit (GOF), $\chi^2 = [R_{wp}/R_{exp}]^2$, where $R_{exp} = [(N - m)/ \sum w_i y_{io}^2]^{1/2}$, $y_{io}$ and $y_{ic}$ are the observed and calculated intensities, $w_i$ is the weighting factor, $N$ is the total number of $y_{io}$ data when the background is refined, and $m$ is the number of adjusted parameters.

Powder synchrotron XRD experiments for $LaSrNiO_{3.4}$ at pressures up to 70 GPa were performed at room temperature using angle-dispersive X-ray diffractometry using BL10XU of SPring-8. The powder sample was loaded into a 90 μm hole of pre-indented rhenium gaskets of the diamond anvil cells. A 4:1 methanol:ethanol mixture was used as a pressure transmitting medium. The Raman shift of diamond was used to determine the pressure [32]. The incident X-ray beam was monochromatized to a wavelength of 0.41417 Å. The beam was collimated to a diameter of about 30 μm.

The temperature dependence of the electric resistivity of $Sr_2CuO_3$ was carried out between 150 K and 300 K by a standard four-probe dc resistance method in various constant pressures up to 40 GPa. Pt electrodes were used and the sample/metal gasket cavity was coated with an insulating mixture of $Al_2O_3$ and NaCl combined with epoxy. Applied pressures were measured by means of a fluorescence manometer on ruby chips placed around the samples.

In these electrical resistance measurements, the initial sectional area was about 60 μm × 50 μm and the distance between probes was 50 μm.

### 5.3. Results and Discussions

The high pressure synchrotron XRD measurements of $Sr_2PdO_3$, $Sr_2CuO_3$, and $Ca_2CuO_3$ at room temperature are carried out. Selected synchrotron XRD patterns are shown in Figure 5.5. Upon exclusion of weak unknown impurity peaks, the diffraction patterns of these compounds in the low pressure regime could be assigned to the orthorhombic *I*-centered unit cell, consistent with the reported data at ambient pressure [27,28]. As is expected, the $2\theta$ angles of the reflection peaks gradually increase with increasing pressure, resulting from contraction of the lattice. For all the compounds examined, the further application of pressure finally results in drastic change in the diffraction patterns featured by a discontinuous change in the cell constants and by modified reflection conditions compatible with the orthorhombic *A*-centered lattice. There is a pressure region where the low and high pressure phases coexist, mainly resulting from a pressure gradient across the specimen. We determined $P_s$ as a pressure where the volume fractions of the two phases become close (Figure 5.6). The obtained values are 29 GPa for $Sr_2PdO_3$, 30 GPa for $Sr_2CuO_3$, and 41GPa for $Ca_2CuO_3$.

The cell constants of the Cu- and Pd-compounds, which are determined by the least-squares method using well-separated reflections in the synchrotron XRD profiles, are plotted as a function of pressure in Figures 5.7a-c. The pressure dependence of the volume below $P_s$ (Figure 5.7d) can be fitted well by the Birch-Murnaghan equation of state [33]. The bulk modulus for $Ca_2CuO_3$, $K = 151 \pm 1$ GPa, is in a reasonable agreement with a previous study where $K = 165$ GPa [34]. Much smaller bulk moduli were obtained when the A-site is strontium ($K = 99 \pm 3$ GPa for $Sr_2CuO_3$ and $Sr_2PdO_3$), suggesting that the compressibility is

predominantly influenced by the A-site. The number of ladder legs should not affect lattice compressibility because the low pressure phase of the two-legged ladder $Sr_3Fe_2O_5$ has a similar value of $K$ = 94 GPa [20].

Reflecting topotactic nature of the structural transition, when the applied pressure is gradually reduced, the high pressure diffraction patterns completely returned back to the low pressure diffraction patterns without any loss in crystallinity at 20 GPa for $Sr_2PdO_3$ and 30 GPa for $Ca_2CuO_3$. Even when the pressure was quenched from the pressure above $P_s$, what we found was the original low pressure phase. As shown in Figures 5.7a-c, the lattice evolution at $P_s$ is anisotropic: The *a* and *c* axes exhibit a discontinuous decrease, while the *b* axis (i.e., the $MO_2$ chain direction) exhibits a discontinuous increase. This is indeed what has been observed in $Sr_3Fe_2O_5$ [20]. The change in the *a* and *b* axes at $P_s$ is about –4% and +2% for $Sr_2PdO_3$ and –4% and +3% for $Sr_2CuO_3$ and $Ca_2CuO_3$, which are comparable to –3% and +2% for $Sr_3Fe_2O_5$ [20]. All of these observations suggest that the structural transitions in $Sr_2PdO_3$, $Sr_2CuO_3$ and $Ca_2CuO_3$ are analogous to that in $Sr_3Fe_2O_5$. Namely, the structural transition is described by a phase shift of the neighboring $MO_2$ chains from (1/2,1/2,1/2) to (0,1/2,1/2), which allows a change in the A-site coordination environment from the *B*1-type to *B*2-type geometry (Figures 5.2).

The high pressure $A_2MO_3$ structure was refined using the synchrotron XRD data at 34.7 GPa for $Sr_2PdO_3$, at 37.4 GPa for $Sr_2CuO_3$, and at 51.3 GPa for $Ca_2CuO_3$, assuming the space group *Ammm* (as in $Sr_3Fe_2O_5$ [20]). The atoms are placed at 4*j* (0.5, 0, *z*) for A = Sr or Ca, 2*a* (0, 0, 0) for M = Cu or Pd, 4*i* (0, 0, *z*) for O(1), and 2*b* (0, 0.5, 0) for O(2). During the refinements, the occupancy factors were constrained to unity. All the refinements converged well, yielding $R_p$ = 0.75%, $R_{wp}$ = 1.21%, $\chi^2$ = 2.83 $R_{Bragg}$ = 0.97%, $R_F$ = 0.46% for $Sr_2PdO_3$, $R_p$ = 0.90%, $R_{wp}$ = 1.20%, $\chi^2$ =2.49 $R_I$ = 0.57%, $R_F$ = 0.31% for $Sr_2CuO_3$, and $R_p$ = 0.69%,

$R_{wp}$ = 1.24%, $\chi^2$ = 1.59 $R_I$ = 1.08%, $R_F$ = 0.49% for $Ca_2CuO_3$ (Figure 5.8). The atomic displacement parameters *B* for each atom are acceptable. The final structural parameters together with reliability factors based on the *Ammm* space group are summarized in Table 5.1. We note that other lower symmetry space groups which satisfy the reflection conditions for the high pressure phase (i.e. *A*2*mm*, *Am*2*m*, *Amm*2 and *A*222) did not improve the structural refinements.

The inter-atomic distances for the refined structures are listed in Table 5.2. The A-site ions in the low pressure phase are coordinated to 7 oxygen atoms (A-O(1) × 1, A-O(1) × 4, A-O(2) × 2) in the *B*1-type arrangement (Figure 5.2a), while in the high pressure phase they are coordinated to 8 oxygen atoms (where A-O(1) × 1 → A-O(1) × 2) in the *B*2-type arrangement (Figure 5.2b). The A-O distances (2.226 Å ~ 2.564 Å) for the high pressure phase are acceptable considering known compounds in this pressure region [10,19,20,35--37]. The Cu-O distances (1.84 Å ~ 2.016 Å) for the high pressure phases are also comparable to those found in previous studies [38,39].

Now that the proposed high pressure structure of $A_2MO_3$ is confirmed, we can say that the pressure-induced *B*1-to-*B*2 transition generally occurs in the rock salt/spin-ladder intergrowth compounds and is not restricted to iron oxides and/or two-legged ladder structure . Namely, we can propose that $(AO)(AMO_2)_n$ ($n$ = 1, 2, 3…) with the AO rock salt unit and the $(AMO_2)_n$ *n*-legged spin ladder unit, if synthesized, would exhibit the same type of transition. It also gives a proof that the structural transition in $Sr_3Fe_2O_5$ at 30 GPa is independent to other magnetic/transport transitions at 34 GPa.

We may further expect that the *B*1-to-*B*2 transition is more general and is observed for intergrowth structures having a rock salt sublayer. Among possible candidates are $K_2NiO_2$ [40] and $A_2ZnN_2$ (A = Sr, Ba) [41], the structures of which differ from the $A_2MO_3$ structure

by the absence of bridging oxygen (thus *I*4/*mmm*), yielding a two-fold dumbbell coordination around Ni and Zn. The structure of $Ba_3ZnN_2O$ is built up from the intergrowth structure between the BaO rock salt block and $Ba_2ZnN_2$ block [42]. Misfit layer compounds $(MS)_nTS_2$ (M = Sn, Pb, Bi, rare earth elements; T = Nb, Ta ; $n$ = 1.08 – 1.19) are intergrowth structures between distorted MS rock salt blocks and $TS_2$ blocks [43]. Delafossite $CuFeO_2$ consists of a FeO rock salt block and linearly coordinated CuO block. Xu *et al.* reported the high pressure transition leading to an increase of Cu coordination at 23 GPa [38], instead of a *B*1-to-*B*2 transition in the FeO block. Further high pressure possibly leads to the *B*1-to-*B*2 transition.

Let us now quantitatively compare the *B*1-to-*B*2 structural transition between binary systems and the intergrowth systems. It is known from experimental and theoretical studies in binary oxides or chalcogenides (AX) that for a given X, log $P_s$ follows a linear pressure dependence on $R_A/R_X$ (Figure 5.1) [6--8,44]. Figure 5.9 shows the empirical relation for X = oxygen, where $\log P_s = -2.0\ R_A/R_O + 3.2$. It is remarkable that the critical pressures for the intergrowth compounds $A_2MO_3$ and $Sr_3Fe_2O_5$ are located just on the line. This means that $P_s$ is determined solely by $R_A/R_O$ in the AO block. Insensitivity of the ladder block to $P_s$ in turn implies that the ladder subunit at ambient pressure is a favorable form at high pressure. The structural stability of the ladder subunit under high pressure is understandable because it should have high compressibility along the out-of-plane direction as a result from the complete absence of apical oxygen. In support of this, a preliminary experiment showed that the infinite layer structure $SrFeO_2$ consisting only of the infinite-legged ladder block does not show any structural transition at least up to 100 GPa.

When the vacant apical oxygen site of the $MO_4$ square plane is partially filled, does this type of structural transition occur, and if it does, how and to what extent is $P_s$ influenced? To answer these questions, we performed a high pressure synchrotron XRD measurement on

$LaSrNiO_{3.4}$. Here, $LaSrNiO_3$ without apical oxygen is isostructural with $Sr_2CuO_3$. At ambient pressure, $LaSrNiO_{3.4}$ adopts the orthorhombic *I*–centered space group, sharing the same structural feature with $Sr_2CuO_3$, but differing in that the apical oxygen site at 2*d* (0.5, 0, 0) is partially (i.e., 40%) and randomly occupied (Figure 5.10). The ratio $R_A/R_O$ in $LaSrNiO_{3.4}$ is 0.86 ($R_A$ is the average ionic radius of $La^{3+}$ and $Sr^{2+}$). Then $P_s$ is estimated as 30 GPa on the basis of the $P_s$-$R_A/R_O$ line in Figure 5.9. However, the synchrotron XRD patterns of $LaSrNiO_{3.4}$ at 44 GPa and 55 GPa shown in Figure 5.11 could still be assigned to the *I*-centered orthorhombic unit cell. A set of new peaks assigned to the *A*-centered orthorhombic unit cell emerged at 63 GPa together with those of the original *I*-centered unit cell. The 70 GPa profile indicates the completion of the structural transition. Since the strongest reflections, (110) for the low pressure phase and (111) for the high pressure phase, are of comparable intensity at 63 GPa, $P_s$ should be around this pressure. The lattice parameters at 55 GPa and 70 GPa are, respectively, $a$ = 3.401(2) Å, $b$ = 3.637(2) Å, $c$ = 11.99(2) Å and $a$ = 3.124(2) Å, $b$ = 3.727(2) Å, $c$ = 10.568(7) Å. The increased $b$ axis, a characteristic feature of the *B*1-to-*B*2 transition, is observed. In addition, as a consequence of the partial occupation at the apical vacant site, the distance between the face-to-face square planes ($a$ axis) is considerably longer as compared with those of other compounds, e.g. 2.7496(3) Å (= $a$) for $Ca_2CuO_3$ at 51.3GPa, 2.947 Å (= $c$) for $SrFeO_2$ at 70.4GPa (unpublished data).

$P_s$ ~ 63 GPa for $LaSrNiO_{3.4}$ is twice higher than that estimated from the empirical relation for the binary rock salt systems and for the rock salt/ladder intergrowth compounds (see Figure 5.9). Obviously, $P_s$ is affected by the partial occupancy at the apical site. Given the less efficient contraction of the $a$ axis in the pressure study of $LaSrNiO_{3.4}$, it is naturally considered that $P_s$ depends on the amount of apical oxygen in $LaSrNiO_{3+x}$; the more the apical oxygen atoms there are, the higher $P_s$ becomes. Ultimately, the fully ocqupied

compound $LaSrNiO_4$ ($x$ = 1; $K_2NiO_4$–type structure), or in more general terms, Ruddlesden-Popper phase $A_{n+1}B_nO_{3n+1}$ ($n$ = 1, 2, 3,…) should undergo the same type of structural transition at elevated pressures. A simple linear extrapolation of the critical pressures (63 GPa for $LaSrNiO_{3.4}$ and 30 GPa for $LaSrNiO_3$) gives $P_s$ ~120 GPa for $LaSrNiO_4$, - a pressure range at which synchrotron XRD experiments are currently accessible [4].

Ruddlesden-Popper type layered perovskite compounds have offered a wide range of chemical and physical properties, including superconductivity in $(La,Sr)CuO_4$ [45] and $Sr_2RuO_4$ [46], colossal magnetoresistitivy (CMR) in $(La,Sr)_{n+1}Mn_nO_{3n+1}$ [47], itinerant ferromagnetism in $Sr_3Ru_2O_7$ [48], Mott insulating behavior derived from the strong spin-orbit coupling in $Sr_2IrO_4$ [49], and photo catalysis in $Sr_2TiO_4$. As far as the authors' are aware, this type of structural transition has not been reported yet. Thus it is very interesting to investigate if the structural transition occurs generally in Ruddlesden-Popper compounds or not. It is expected that the phase change of adjacent perovskite blocks can change the electronic structures, leading to new or improved chemical and physical properties.

The ambient pressure phase of $Sr_2CuO_3$ is well known as a prototypical 1D spin-1/2 Heisenberg antiferromagnet with $T_N/J_{intra}$ ~ 0.002 (where $J_{inta}$ is the intra-chain superexchange interaction) [50,51]. The staggered arrangement of the adjacent $CuO_2$ chains renders the Cu $d_{x2-y2}$ orbitals to be only weakly overlapped between the chains, strongly enhancing the one-dimensionality of the magnetic interactions. Upon the structural transition, the adjacent chains align in a uniform manner to form a $(CuO_3)^{4-}$ "quasi" infinite layer structure. As a result, the inter-chain interaction via a Cu-O-O-Cu super-super-exchange interaction path within each $(CuO_3)^{4-}$ layer would not be negligible, making the system a quasi 2D antiferromagnet.

In order to detect a sign of possible effects of increase in dimensionality, we investigated the transport properties of $Sr_2CuO_3$ at elevated pressure. Shown in Figure 5.12 is the pressure dependence of room-temperature resistance $\rho$(RT) of $Sr_2CuO_3$. Reflecting a wide band gap (~ 2 eV) in the ambient pressure structure,[52,53] $\rho$(RT) at 2 GPa is about $10^6$ Ω (roughly corresponding to $10^3$ to $10^4$ Ωcm). $\rho$(RT) decreases slowly towards ~ 20 GPa, and then decreases rather steeply above $P_s$, an indication of a reduced band gap and/or an increased electron mobility/carrier number in the high pressure phase. The anomaly associated with the structural transition is not so obvious, which is understood in terms of a large pressure distribution along the sample and the use of hand-pressed pellet, as was seen in $SrFeO_2$ and $Sr_3Fe_2O_5$ [19,20]. A crude estimation of the activation energy, as calculated from temperature dependence of the resistances, gave ~ 0.21 eV below $P_s$ and ~ 0.18 eV above $P_s$ (Figure 5.13). We would like to recall that in the two-legged ladder structure $(Sr,Ca)_{14}Cu_{24}O_{41}$, pressure induces dimensional crossover from 1D to 2D as well as charge-transfer from the chain to the ladder, and as a consequence superconductivity appears [54]. At present, it is not clear yet if the reduced band gap in $Sr_2CuO_3$ above $P_s$ is explained by the dimensional increase from 1D to 2D. Carrier doping into the $(CuO_3)^{4-}$ layer, for example, by Na-for-Sr substitution may eventually induce metallic conductivity. Because of experimental limits at high pressure, first principles calculations would be definitely useful for understanding the electronic structures and the nature of the chemical bonds between the magnetic moments.

### 5.4. Conclusion

We have demonstrated that the intergrowth structures $A_2MO_3$ (A = Sr, Ca; M = Cu, Pd) exhibit a pressure-induced structural transition with the space group changing from *Immm* to *Ammm*, involving change of the structure of AO block from rock salt structure to CsCl

structure. Together with $Sr_3Fe_2O_5$, the present study demonstrates the generality of the *B*1-to-*B*2 structural transition in the intergrowth structure of $(AO)(AMO_2)_n$ ($n$ = 1, 2, 3…). It is remarkable that the critical pressures $P_s$ for the intergrowth compounds are determined solely by $R_A/R_O$, showing quantitatively the same trend as the binary AO compounds, which make it possible to predict $P_s$ of other related compounds. Given the *B*1-to-*B*2 structural transition in binary chalcogenides [6--18], the rock-salt/ladder intergrowth chalcogenides may also exhibit the *B*1-to-*B*2 structural transition with $P_s$ scaled by $R_A/R_S$, $R_A/R_{Se}$, and $R_A/R_{Te}$. Introduction of oxygen atom at the apical site leads to a significantly deviation from the $P_s$ vs $R_A/R_O$ relation. It is expected that the high pressure structures consisting of "quasi" infinite layers have different electronic structures due to inter-ladder(chain) interaction within the layer, leading to new or improved chemical and physical properties. Unfortunately, we have not successfully quenched the high pressure phase, which is an important step for investigating detailed properties and future applications. Recently, the high pressure *B*2 structure of KI crystal was obtained even at ambient pressure using nanospaces of single-walled carbon nanohorns.[55] Thus, novel techniques may be necessary, and hold the key for tapping into high pressure materials for widespread use.

## References

[1] K. T. Park, K. Terakura, and Y. Matsui, Nature 336 (1988) 670.

[2] D. Andrault, G. Fiquet, F. Guyot, and M. Hanfland, Science 282 (1998) 720.

[3] D. M. Teter, R. J. Hemley, G. Kresse, and J. Hafner, Phys. Rev. Lett. 80 (1998) 2145.

[4] Y. Kuwayama, K. Hirose, N. Sata, and Y. Ohishi, Science 309 (2005) 923.

[5] M. Murakami, K. Hirose, K. Kawamura, N. Sata, and Y. Ohishi, Science 304 (2004) 855.

[6] K. Syassen, Phys. Status Solidi 91 (1985) 11.

[7] S. Ekbundit, A. Chizmeshya, R. LaViolette, and G. H. Wolf, J. Phys. : Condens. Matter 8 (1996) 8251.

[8] C. Narayana, V. J. Nesamony, and A. L. Ruoff, Phys. Rev. B 56 (1997) 14338.

[9] L. Liu and W. A. Bassett, J. Geophys. Res. 77 (1972) 4934.

[10] R. Jeanloz, T. J. Ahrens, H. K. Mao, and P. M. Bell, Science 206 (1979) 829.

[11] Y. Sato and R. Jeanloz, J. Geophys. Res. 86 (1981) 11773.

[12] T. A. Grzybowski and A. L. Ruoff, Phys. Rev. B 27 (1983) 6502.

[13] T. A. Grzybowski and A. L. Ruoff, Phys. Rev. Lett. 53 (1984) 489.

[14] H. G. Zimmer, H. Winzen, and K. Syassen, Phys. Rev. B 32 (1985) 4066.

[15] T. A. Grzybowski and A. L. Ruoff, Mater. Res. Soc. Symp. Proc. (1984) 43.

[16] S. T. Weir, Y. K. Vohra, and A. L. Ruoff, Phys. Rev. B 33 (1986) 4221.

[17] H. Luo, R. G. Greene, and A. L. Ruoff, Phys. Rev. B 49 (1994) 15341.

[18] H. Luo, R. G. Greene, K. Ghandehari, T. Li, and A. L. Ruoff, Phys. Rev. B 50 (1994) 16232.

[19] T. Kawakami, Y. Tsujimoto, H. Kageyama, *et al*, Nat. Chem. 1 (2009) 371.

[20] T. Yamamoto, C. Tassel, Y. Kobayashi, *et al*, J. Am. Chem. Soc. 133 (2011) 6036.

[21] M. Takano, Y. Takeda, H. Okada, M. Miyamoto, and T. Kusaka, Physica C 159 (1989) 375.

[22] Z. Hiroi, M. Azuma, M. Takano, and Y. Bando, J. Solid State Chem. 95 (1991) 230.

[23] J. M. Pruneda, J. Íñiguez, E. Canadell, H. Kageyama, and M. Takano, Phys. Rev. B 78 (2008) 115101.

[24] H. J. Xiang, S. H. Wei, and M. H. Whangbo, Phys. Rev. Lett. 100 (2008) 167207.

[25] H. J. Koo, H. Xiang, C. Lee, and M. H. Whangbo, Inorg. Chem. 48 (2009) 9051.

[26] K. Tomiyasu, H. Kageyama, C. Lee, *et al*, J. Phys. Soc. Jpn. 79 (2010) 034707.

[27] M. T. Weller and D. R. Lines, J. Solid State Chem. 82 (1989) 21.

[28] Y. Nagata, T. Taniguchi, G. Tanaka, M. Satho, and H. Samata, J. Alloys Compounds 346 (2002) 50.

[29] M. Crespin, C. Landron, P. Odier, J. M. Bassat, P. Mouron, and J. Choisnet, J. Solid State Chem. 100 (1992) 281.

[30] J. Hammersley, Fit2d user manual. ESRF: Grenoble, France. (1996).

[31] F. Izumi and K. Momma, Solid State Phenom. 130 (2007) 15.

[32] Y. Akahama and H. Kawamura, J. Appl. Phys. 96 (2004) 3748.

[33] F. Birch, J. Appl. Phys. 9 (1938) 279.

[34] G. M. Zhang, W. J. Mai, F. Y. Li, Z. X. Bao, R. C. Yu, T. Q. Lu, J. Liu, and C. Q. Jin, Phys. Rev. B 67 (2003) 212102.

[35] D. Errandonea, J. Pellicer-Porres, F. J. Manjón, *et al*, Phys. Rev. B 72 (2005) 174106.

[36] D. Errandonea, R. S. Kumar, X. Ma, and C. Tu, J. Solid State Chem. 181 (2008) 355.

[37] M. Fischer, B. Bonello, J. P. Itie, A. Polian, E. Dartyge, A. Fontaine, and H. Tolentino, Phys. Rev. B 42 (1990) 8494.

[38] W. M. Xu, G. K. Rozenberg, M. P. Pasternak, *et al*, Phys. Rev. B 81 (2010) 104110.

[39] P. Dera, A. Jayaraman, C. T. Prewitt, and S. A. Gramsch, Phys. Rev. B 65 (2002) 134105.

[40] H. Rieck and R. Hoppe, Z. Anorg. Allg. Chem. 400 (1973) 311.

[41] H. Yamane and F. J. DiSalvo, J. Solid State Chem. 119 (1995) 375.

[42] H. Yamane and F. J. DiSalvo, J. Alloys Compounds 234 (1996) 203.

[43] G. A. Wiegers, A. Meetsma, S. Van Smaalen, *et al*, Solid State Commun. 70 (1989) 409.

[44] R. Shannon, Acta Cryst. 32 (1976) 751.

[45] R. J. Cava, R. B. Van Dover, B. Batlogg, and E. A. Rietman, Phys. Rev. Lett. 58 (1987) 408.

[46] Y. Maeno, H. Hashimoto, K. Yoshida, S. Nishizaki, T. Fujita, J. G. Bednorz, and F. Lichtenberg, Nature 372 (1994) 532.

[47] Y. Moritomo, A. Asamitsu, H. Kuwahara, and Y. Tokura, Nature 380 (1996) 141.

[48] G. Cao, S. McCall, and J. E. Crow, Phys. Rev. B 55 (1997) 672.

[49] B. J. Kim, H. Ohsumi, T. Komesu, S. Sakai, T. Morita, H. Takagi, and T. Arima, Science 323 (2009) 1329.

[50] N. Motoyama, H. Eisaki, and S. Uchida, Phys. Rev. Lett. 76 (1996) 3212.

[51] M. Takigawa, N. Motoyama, H. Eisaki, and S. Uchida, Phys. Rev. Lett. 76 (1996) 4612.

[52] W. C. Mackrodt and H. J. Gotsis, Phys. Rev. B 62 (2000) 10728.

[53] H. Suzuura, H. Yasuhara, A. Furusaki, N. Nagaosa, and Y. Tokura, Phys. Rev. Lett. 76 (1996) 2579.

[54] T. Nagata, M. Uehara, J. Goto, J. Akimitsu, N. Motoyama, H. Eisaki, S. Uchida, H. Takahashi, T. Nakanishi, and N. Môri, Phys. Rev. Lett. 81 (1998) 1090.

[55] K. Urita, Y. Shiga, T. Fujimori, *et al*, J. Am. Chem. Soc. 133 (2011) 10344.

**Table 5.1.** Rietveld refinement for $A_2MO_3$ (A = Sr, Ca; M = Cu, Pd).[a]

| | $Sr_2PdO_3$ (34.7 GPa) | $Sr_2CuO_3$ (37.4GPa) | $Ca_2CuO_3$ (51.3GPa) |
|---|---|---|---|
| *a* (Å) | 3.0277(2) | 2.9859(3) | 2.7496(3) |
| *b* (Å) | 3.9293(3) | 3.8445(7) | 3.7044(5) |
| *c* (Å) | 11.8447(9) | 11.497(2) | 11.029(1) |
| *z* for A | 0.6570(2) | 0.6589(2) | 0. 6587(4) |
| *z* for O(1) | 0.8298(8) | 0.840(2) | 0.830(1) |
| *B* for A ($Å^2$) | 0.14(8) | 1.3(1) | 0.2(2) |
| *B* for M ($Å^2$) | 0.31(7) | 2.3(1) | 0.3(2) |
| *B* for O(1) and O(2) ($Å^2$) | 0.2(2) | 1.8(2) | 0.5(2) |
| $R_{wp}$ (%) | 1.21% | 1.20% | 1.24% |
| $R_p$ (%) | 0.75% | 0.90% | 0.69% |
| $\chi^2$ | 2.83 | 2.49 | 1.59 |
| $R_I$ (%) | 0.97% | 0.57% | 1.08% |
| $R_F$ (%) | 0.46% | 0.31% | 0.49% |

[a] All the refinements were performed using *Ammm* space group with A on 4*j* (0.5, 0, *z*), M on 2*a* (0, 0, 0), O(1) on 4*i* (0, 0, *z*) and O(2) on 2*b* (0, 0.5, 0).

**Table 5.2.** Interatomic distances and ratios between B–O(1) and B–O(2) for $A_2MO_3$ (A = Sr, Ca; M = Cu, Pd).

| Bond (Å) | $Sr_2PdO_3$ | | $Sr_2CuO_3$ | | $Ca_2CuO_3$ | |
|---|---|---|---|---|---|---|
| | 0 GPa[a] | 34.7 GPa | 0 GPa[a] | 37.4GPa | 0 GPa[a] | 51.3GPa |
| A–O(1) × 1 | 2.467 | | 2.510 | | 2.289 | |
| A–O(1) × 2 | | 2.3982(14) | | 2.360(2) | | 2.226(3) |
| A–O(1) × 4 | 2.671 | 2.545(8) | 2.629 | 2.4339(3) | 2.490 | 2.3103(7) |
| A–O(2) × 2 | 2.588 | 2.4851(6) | 2.570 | 2.564(15) | 2.466 | 2.332(9) |
| M–O(1) × 2 | 2.068 | 2.016(9) | 1.967 | 1.84(2) | 1.959 | 1.880(11) |
| M–O(2) × 2 | 1.993 | 1.9646(2) | 1.958 | 1.9223(3) | 1.884 | 1.8522(3) |
| Ratio | | | | | | |
| M–O(1)/M–O(2) | 1.038 | 1.026 | 1.005 | 0.957 | 1.040 | 1.015 |

[a] References [27] and [28] are used.

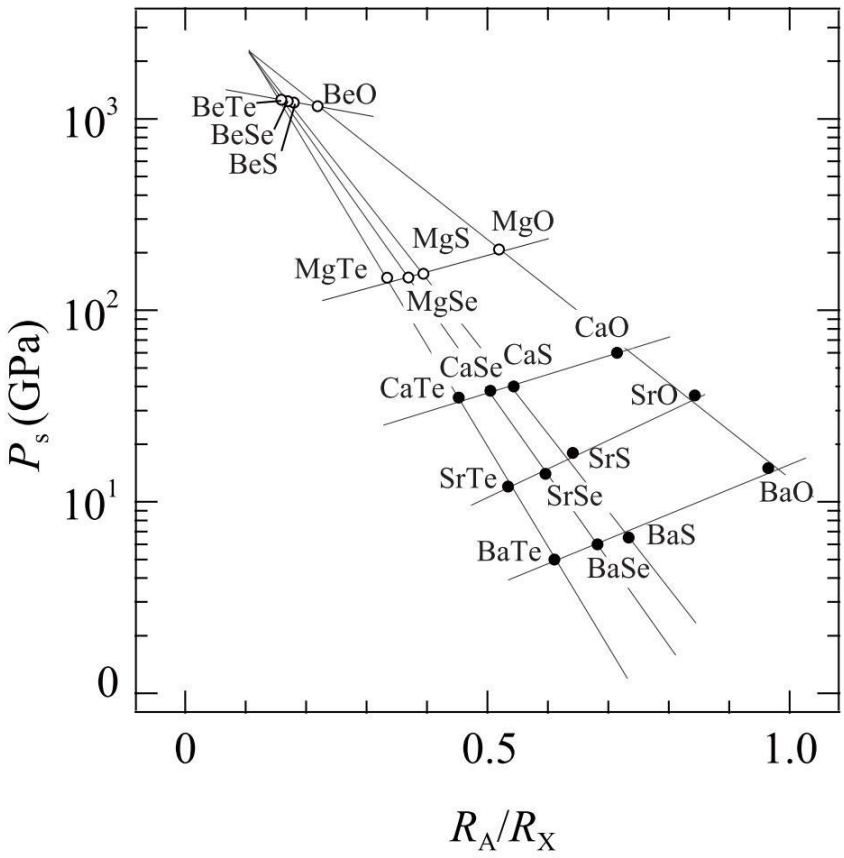


**Figure 5.1**. $P_s$ vs $R_A/R_X$ plot shown by Narayana *et al* [8]. $R_A$ = *A*-site ion radius and $R_X$ = chalcogenide ion radius.

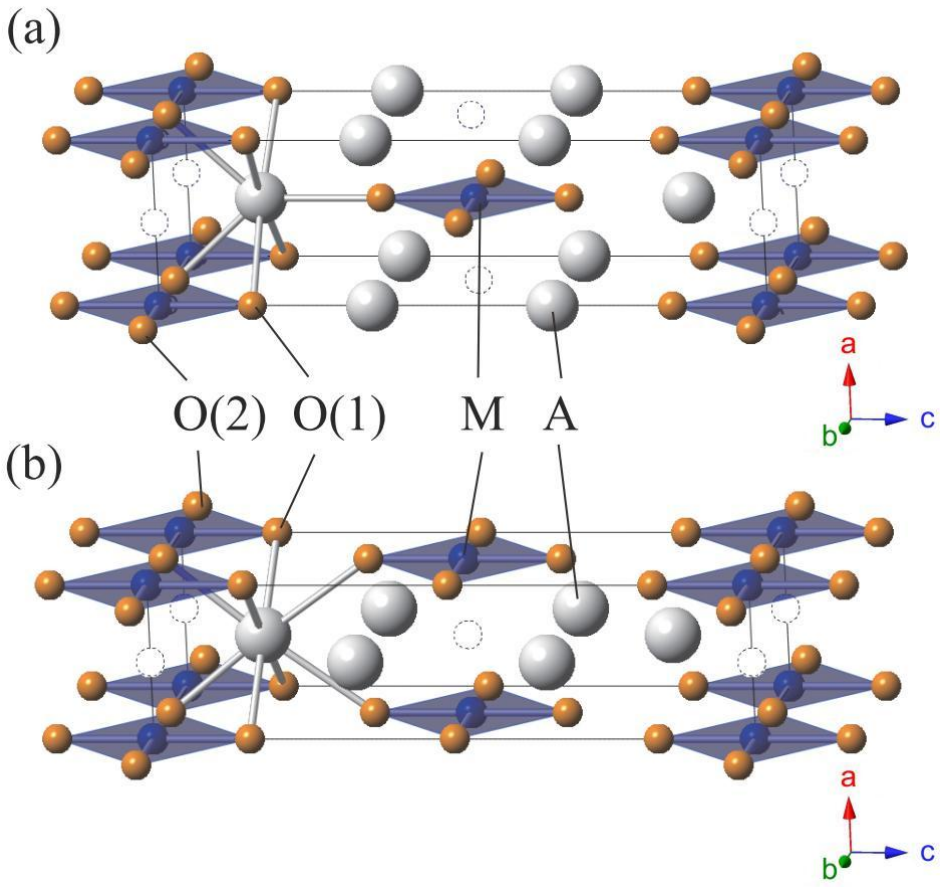


**Figure 5.2**. The $A_2MO_3$ structures (a) at low pressure ($P < P_s$) and (b) at high pressure ($P_s < P$). White, blue, and orange spheres represent A, M and O atoms, respectively. Dotted circles represent apical vacant oxygen sites.

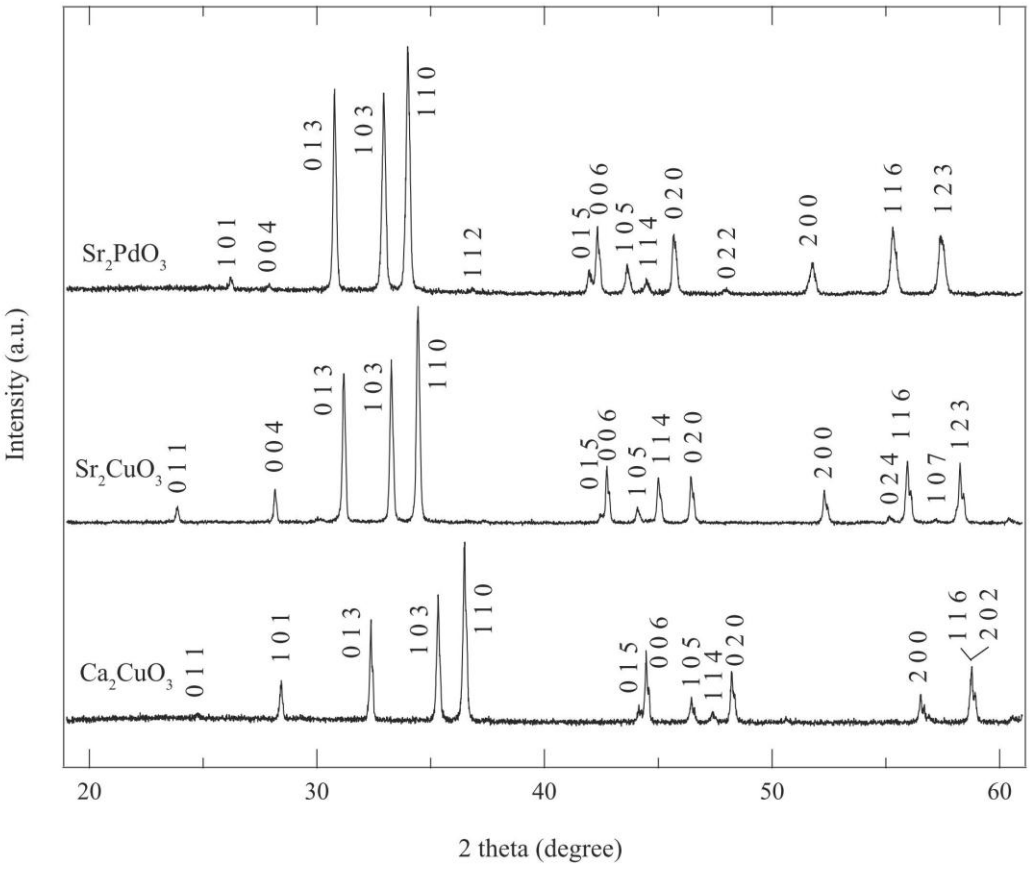


**Figure 5.3**. Powder XRD patterns of $Sr_2PdO_3$, $Sr_2CuO_3$ and $Ca_2CuO_3$ at ambient pressure at room temperature. All the patterns could be indexed by the *I*-centered orthorhombic lattice.

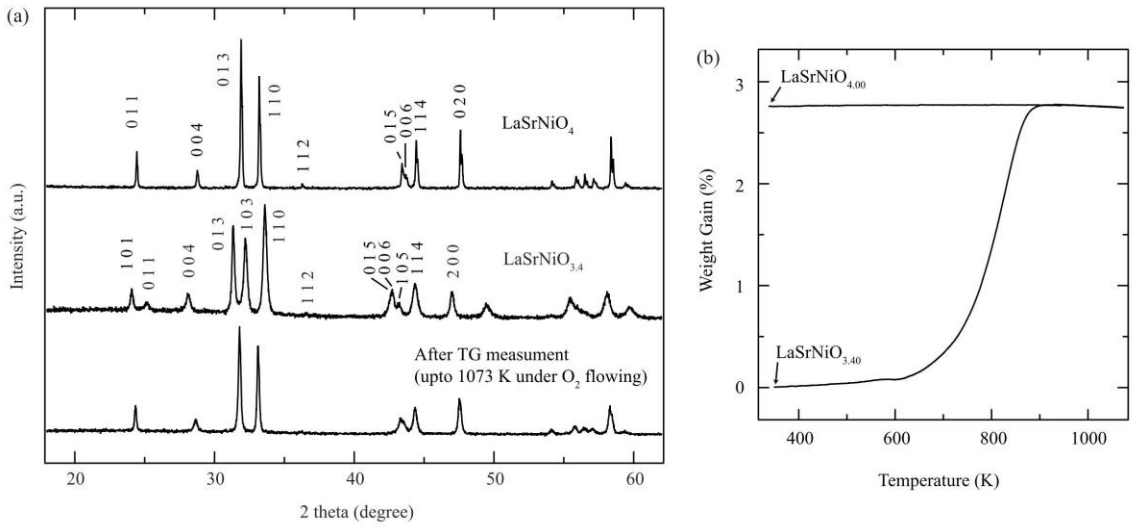


**Figure 5.4**. (a) Powder XRD patterns of (top) $LaSrNiO_4$ with the tetragonal *I*-centered cell and (middle) $LaSrNiO_{3.4}$ with the orthorhombic *I*-centered cell. After TG measurement of $LaSrNiO_{3.4}$ (see Figure 4S), the sample get back to $LaSrNiO_4$ (bottom). (b) Oxidation behavior from $LaSrNiO_{3.4}$ to $LaSrNiO_4$ under a flow of oxygen.

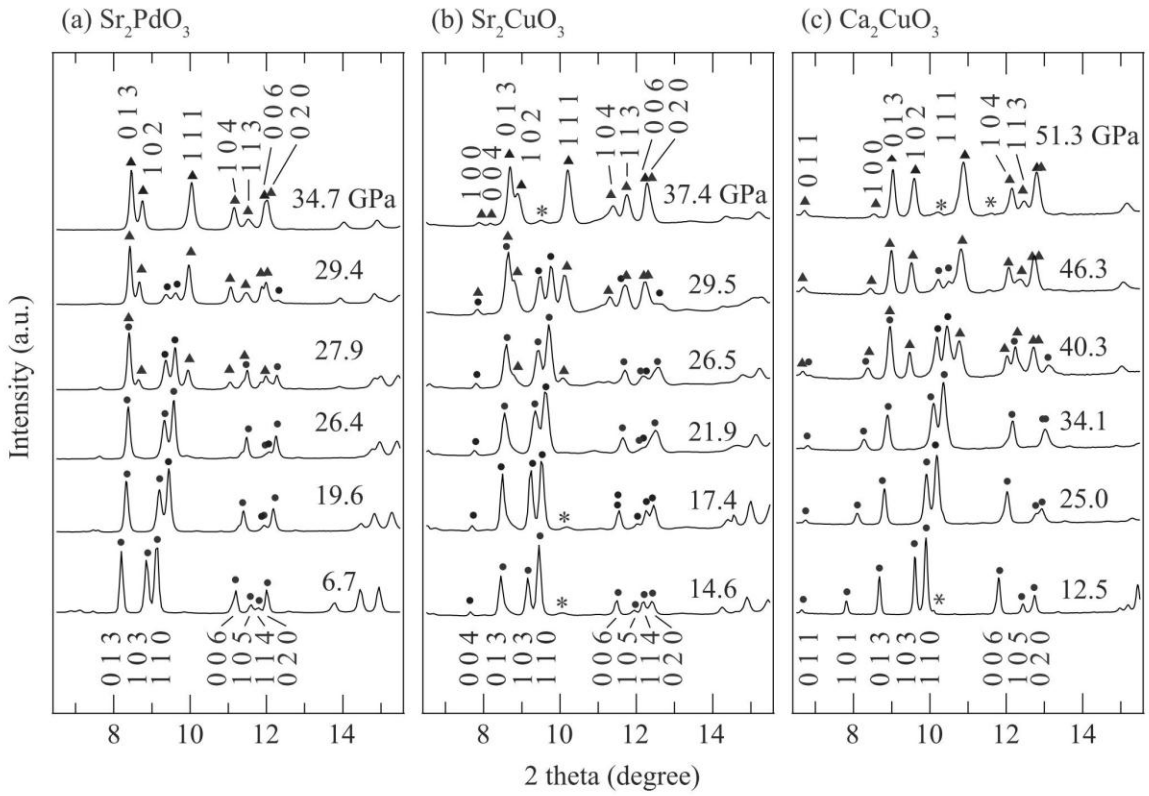


**Figure 5.5.** Selected powder synchrotron XRD patterns of (a) $Sr_2PdO_3$, (b) $Sr_2CuO_3$ and (c) $Ca_2CuO_3$ at room temperature under high pressures. For each specimen, the patterns can be indexed using the orthorhombic *I*-centered cell for $P < P_s$ and the orthorhombic *A*-centered cell for $P > P_s$. Peaks marked by circles and triangles, respectively, represent the low and high pressure phases. Peaks with asterisks denote unknown impurity.

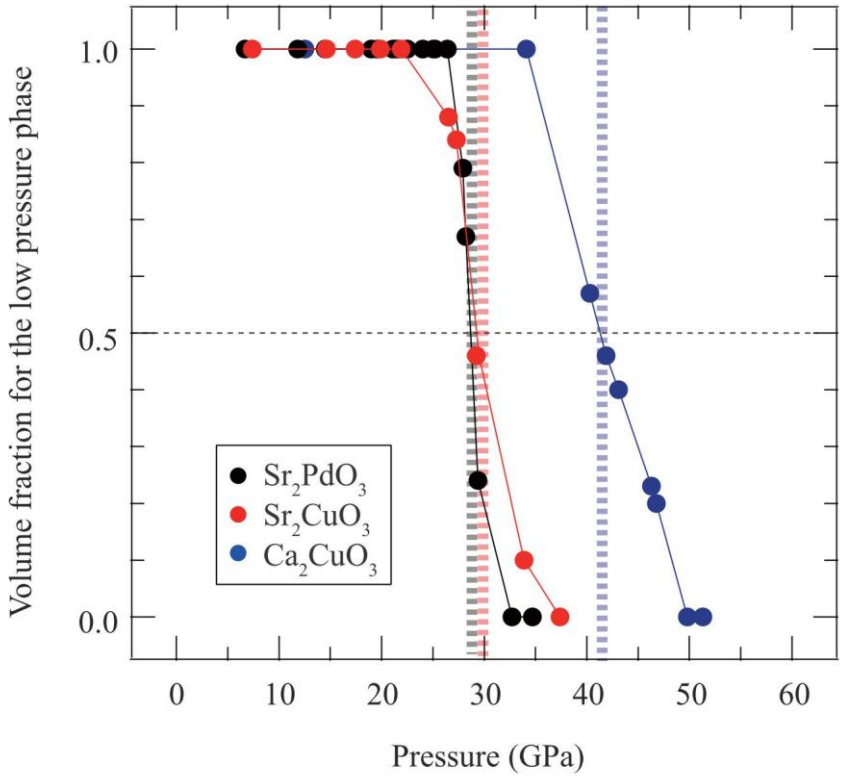


**Figure 5.6**. Volume fractions of the low and high pressure phases for $A_2MO_3$. The volume fractions are estimated from the Rietveld refinements. The values of $P_s$ are 29 GPa for $Sr_2PdO_3$, 30 GPa for $Sr_2CuO_3$, and 41GPa for $Ca_2CuO_3$.

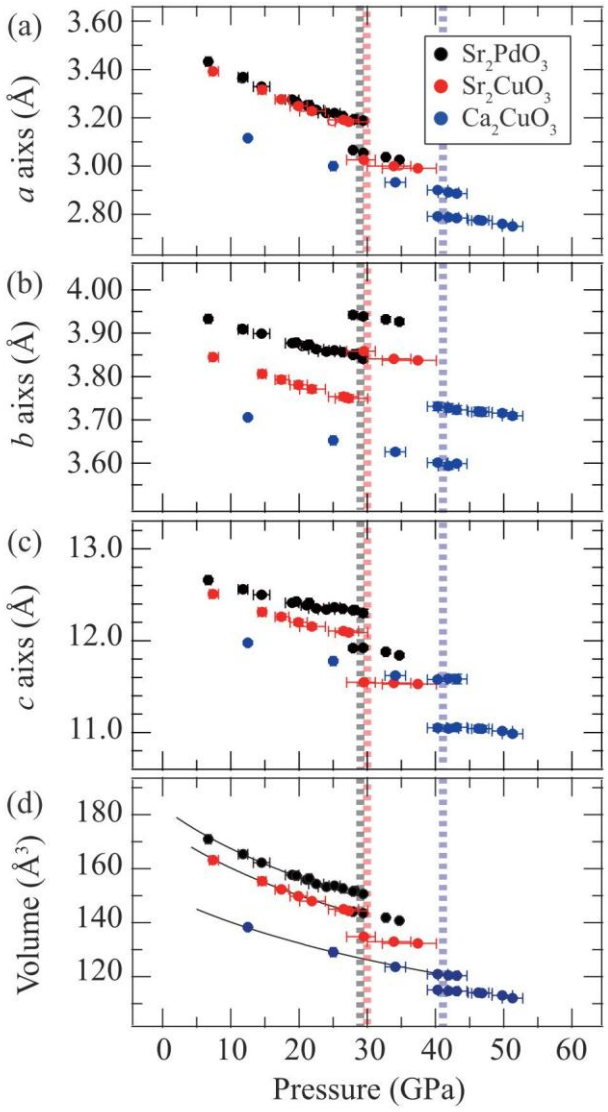


**Figure 5.7.** Pressure dependence of (a)-(c) the lattice parameters and (d) the volume for $Sr_2CuO_3$ (red), $Sr_2PdO_3$ (black), and $Ca_2CuO_3$ (blue). The parameters were obtained from synchrotron XRD measurements. Solid lines in (d) represent Birch-Murnaghan fitting for the low pressure phase below $P_s$.

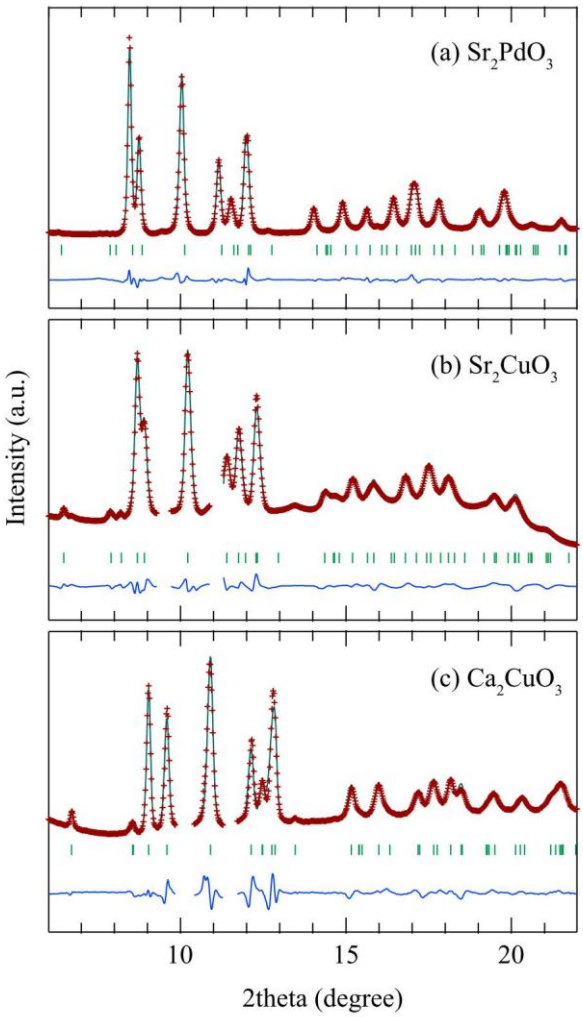


**Figure 5.8**. Observed (crosses), calculated (lines) and difference plots from the structural refinements of the powder synchrotron XRD data for (a) $Sr_2PdO_3$ at 34.7 GPa, (b) $Sr_2CuO_3$ at 37.4GPa and (c) $Ca_2CuO_3$ at 51.3GPa. The ticks represent the positions of the calculated Bragg reflections. Ranges for 9.3° - 9.7°, 10.9° - 11.3° in (b) and 9.8° - 10.4°, 11.3° - 11.7° in (c) are excluded from the refinement because of the existence of unknown impurities.

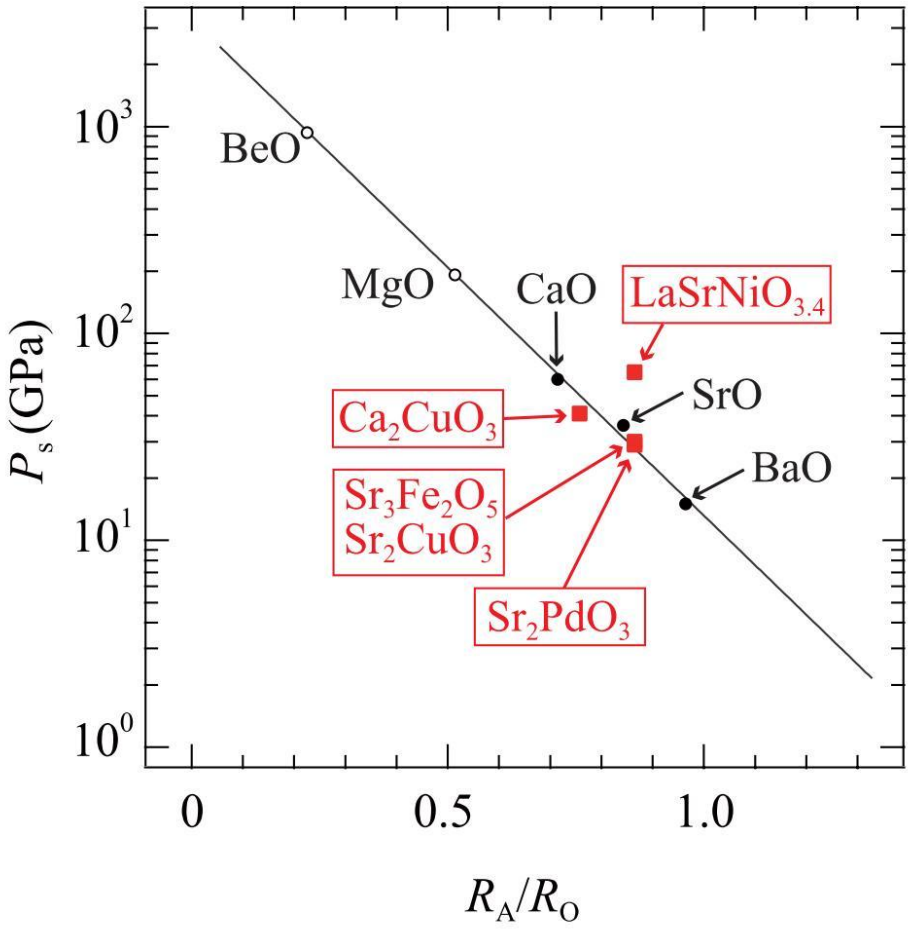


**Figure 5.9**. $P_s$ vs the A-site ion radius ($R_A$) to the oxide ion radius ($R_O$). $R_A$ in 6-, 7- and 8-fold coordination is used [45], respectively, for the low pressure structure of AO, $A_2MO_3$ ($Sr_3Fe_2O_5$) and $LaSrNiO_{3.4}$. Experimental (black closed circles) and theoretical (black open circles) values for binary systems AO (A = Ca, Sr, Ba) are from the references [9--11]. Red Closed squares represent the data obtained in this study.

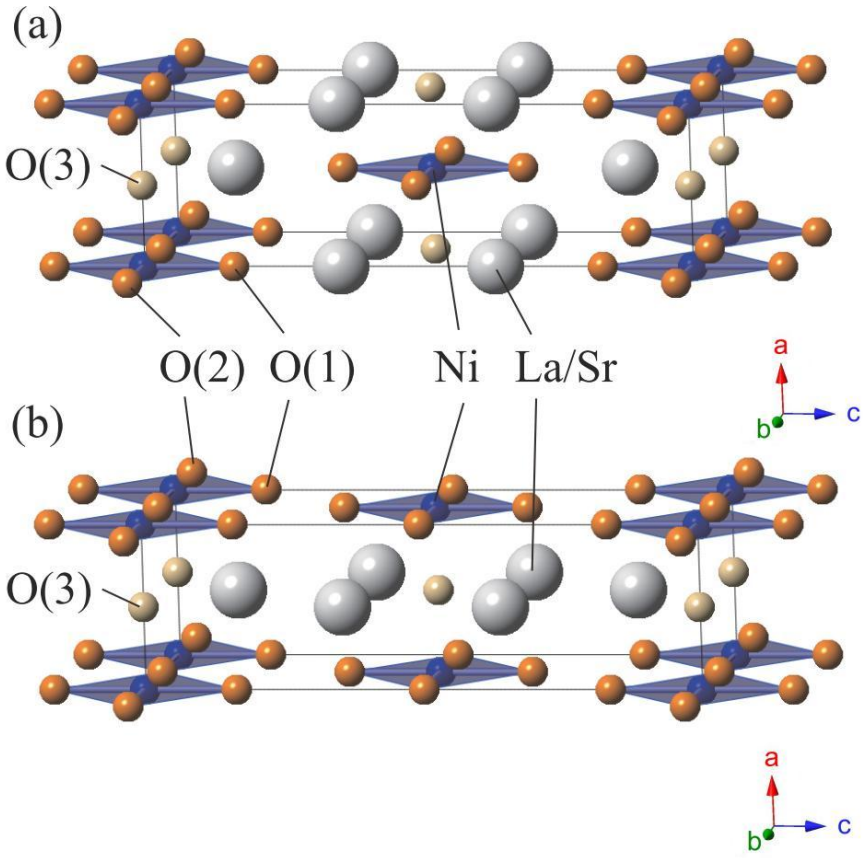


**Figure 5.10**. The $LaSrNiO_{3.4}$ structures (a) at low pressure ($P < P_s$) and (b) at high pressure ($P_s < P$). White, blue, and orange spheres represent La/Sr, Ni and O atoms, respectively. Light orange spheres represent O atoms at apical oxygen sites (2*d*).

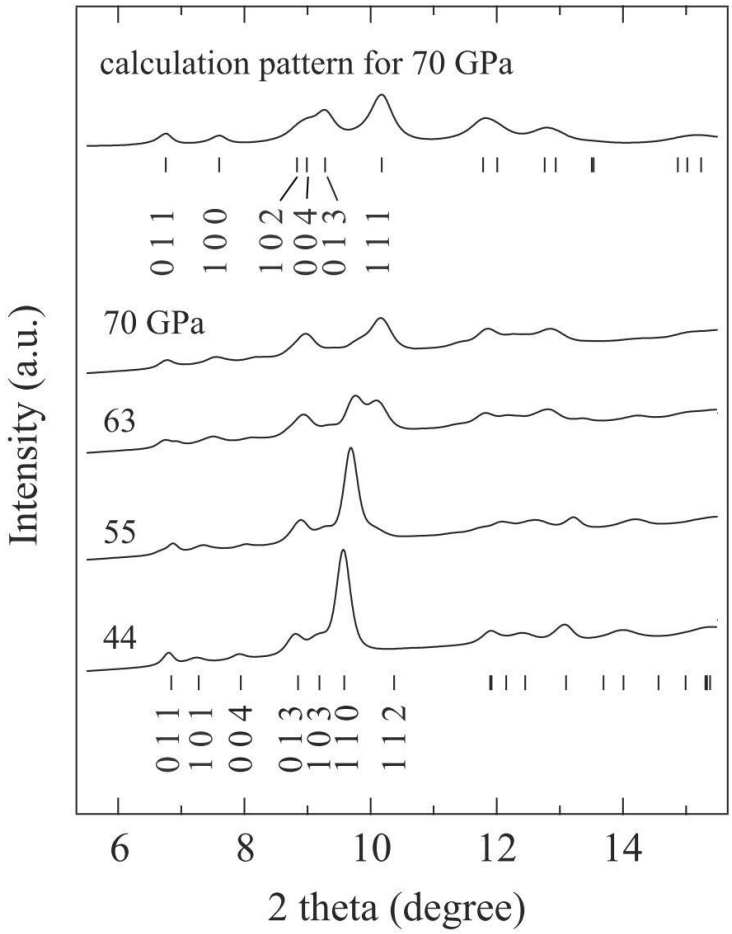


**Figure 5.11.** Powder synchrotron XRD patterns of $LaSrNiO_{3.4}$ under high pressures collected at room temperature. The data at 44 GPa were indexed by the *I*-centered orthorhombic unit cell, while those at 70 GPa by the *A*-centered orthorhombic unit cell. The ticks represent the positions of the allowed Bragg reflections. The calculation pattern for 70 GPa is obtained by the expected high pressure structure.

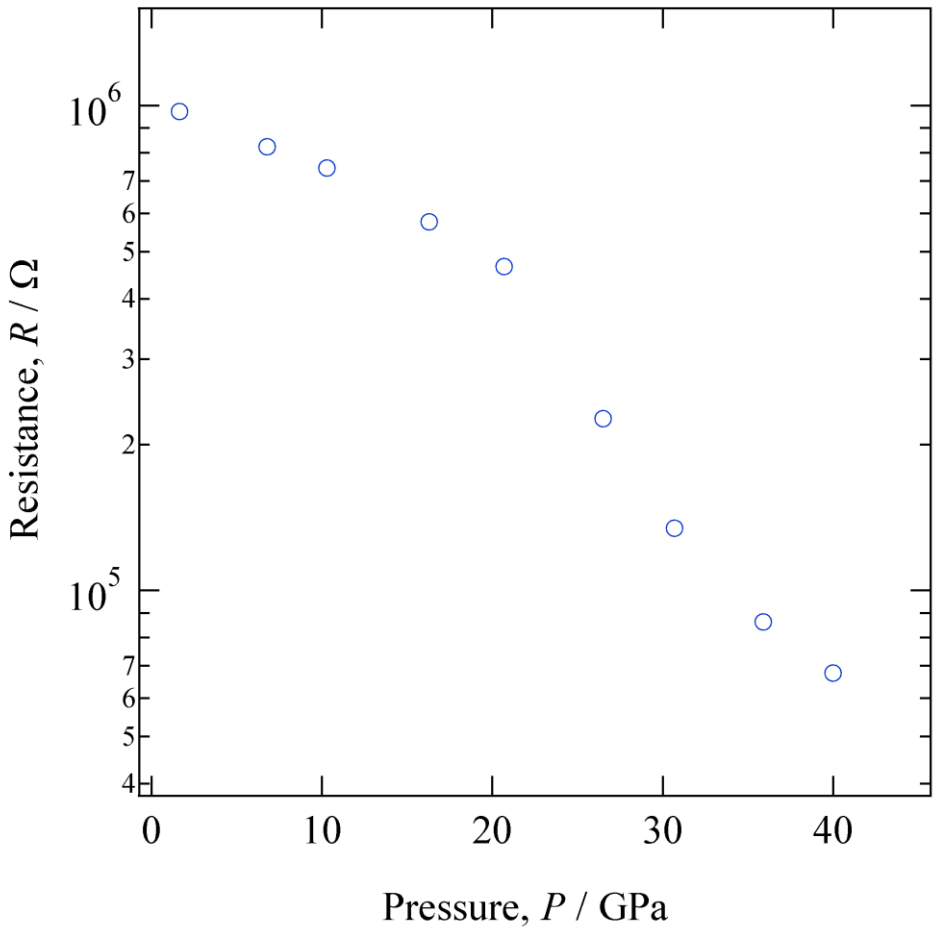


**Figure 5.12.** Room-temperature electrical resistance of $Sr_2CuO_3$ as a function of $P$.

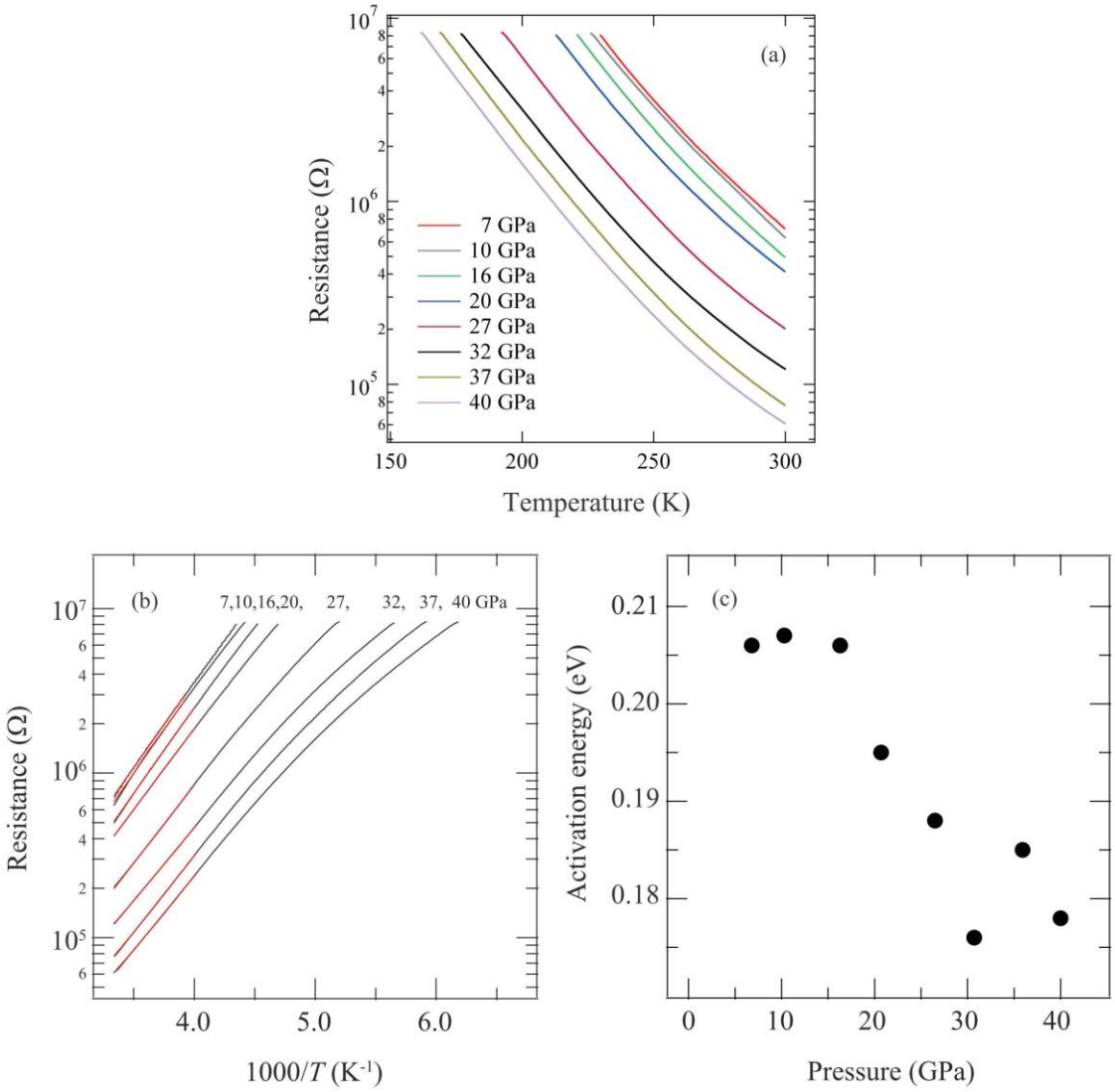


**Figure 5.13.** (a) Temperature dependence of the electrical resistance under various pressures for $Sr_2CuO_3$. (b) Room temperature electrical resistance as a function of 1000/*T* for $Sr_2CuO_3$. Red lines represent Arrhenius plots performed above 250 K. (c) Activation energy as a function of *P*.

# *Chapter 6. $BaFeO_3$: A Ferromagnetic Iron Oxide*

## 6.1. Introduction

A small class of oxides that contain iron in a high valence state of $Fe^{4+}$ ($d^4$) are known. The most representative phase is $SrFeO_3$ (SFO) that crystallizes in the cubic perovskite structure containing corner-sharing $(FeO_6)^{8-}$ octahedra and $Sr^{2+}$ ions that occupy the resulting large open voids. It has been shown that SFO and related oxides behave very differently from $Fe^{2+}$ and $Fe^{3+}$ oxides such as FeO, $Fe^{2+/3+}{}_3O_4$, and $LaFe^{3+}O_3$ (LFO). To the best of our knowledge, all these $Fe^{2+}$ and $Fe^{3+}$ oxides are antiferromagnetic (or ferrimagnetic) insulators in their ground states. Valence mixing often generates good electrical conductivity, but even for the most well-known case of $Fe_3O_4$, an insulating gap of 0.11 eV [1] eventually opens at 119 K (the Verwey transition). $Fe_3O_4$ and $Y_3Fe^{3+}{}_5O_{12}$ have nontrivial spontaneous magnetizations of approximately 1 $\mu_B$ per Fe ion, but these values are due to simple imbalance between the antiferromagnetic sublattices and not to ferromagnetism. In contrast, the $Fe^{4+}$ oxides commonly exhibit a shift toward metallicity and ferromagnetism. SFO maintains cubic symmetry down to low temperatures in spite of the instability inherent to the twofold orbitally degenerate $t_{2g}{}^3e_g{}^1$ configuration and, at the same time, maintains metallic conductivity down to low temperatures [2,3]. SFO is seemingly an antiferromagnet ($T_N$ = 134 K), but the nearest neighboring spins make an angle of only approximately 46˚ (3.1 $\mu_B$ per Fe ion at 4 K) in the helicoidal spin structure with a long wavelength [4,5]. Moreover, genuine ferromagnetism appears when the specific volume is compressed to $V$(7 GPa)/$V$(0 GPa) = 0.95 [6].

As discussed in the recent report on an $Fe^{4+}$ oxide $SrCu^{2+}{}_3Fe^{4+}{}_4O_{12}$ [7], the specificity of $Fe^{4+}$ oxides can be assigned to the fact that the approximate effective charge transfer energy

$\Delta_{eff}$ drastically drops from 8 eV for FeO and 5.5 eV for LFO to -3 eV for SFO. Thus, $Fe^{3+}(O_6)^{11-}$ or $Fe^{3+}L$ (L: ligand hole) is the realistic picture rather than $Fe^{4+}(O_6)^{12-}$ [8,9]. The aforementioned characteristics of "$Fe^{4+}$" oxides should thus be considered to result from interplay of Fe d electrons and O p holes [10].

Oxygen-stoichiometric SFO and $CaFeO_3$ (CFO) have been obtained by applying high oxygen pressures of 30 MPa – 2 GPa at elevated temperatures (typically ca. 1300 K) to easily obtainable oxygen-deficient phases $SrFeO_{3-\delta}$ and $CaFeO_{2.5}$ [2,3,11]. On the other hand, it has been known that $BaFeOO_{3-\delta}$ ($\delta \sim 0.1$) prepared in a similar way crystallizes in the 6H or 12H perovskite structure where not only corner-sharing but also face-sharing Fe–O octahedra are contained (Figure 6.1) [12]. However, by using the following process (see the Experimental Section for details), we succeeded in obtaining fully oxidized $BaFeO_3$ (BFO), which crystallizes in the normal perovskite structure. The starting material was a powder of the easily obtained oxygen-deficient 6H phase. The undesirable face-sharing configuration was eliminated by reducing $BaFeO_{2.5}$ before oxidation. In the constituent $FeO_6$ octahedra of $BaFeO_{2.5}$, $FeO_5$ pyramids and $FeO_4$ tetrahedra are connected only by corner sharing [13]. The powder was subsequently oxidized topochemically at low temperatures by using ozone as an oxidant. Ozone is usually considered to be suitable for strong superficial oxidation such as overlayering of silver metal with AgO [14]. Oxidation to $Fe^{4+}$, $Co^{4+}$, and $Cu^{3+}$ by ozone has also been limited to the cases of thin films (ca. 50 nm) of SFO, CFO, $SrCoO_3$ [10], and $Ba_2CuO_{3+\delta}$ [15]. However, we show below that the $BaFeO_{2.5}$ powder approximately 1 mm in diameter could be oxidized completely by this oxidant.

## 6.2. Experimental

The sample was prepared as follows: appropriate amounts of $Ba(NO_3)_2$ (99.9%) and $Fe(NO_3)_3 \cdot 9H_2O$ (99.9%) were dissolved in distilled water, to which a fivefold excess of citric acid, a onefold excess of propylene glycol, and an ammonia solution were added while stirring. The solution was condensed at 393 K for 10 h, and the resulting polymerized solid was heated first at 723 K for 2 h and then at 1073 K for 5 h in air to obtain a fine powder of 6H-$BaFeO_{3-\delta}$. The powder was converted to $BaFeO_{2.5}$ by heating in a vacuum of approximately $10^{-4}$ Pa at 1073 K for 5 h. Oxygen-stoichiometric BFO was obtained by heating the $BaFeO_{2.5}$ at 473 K for 4 h in oxygen-containing ozone (ca. 10 vol%) flowing at a rate of 100 $mLmin^{-1}$. The ozone was generated by using an ozonizer (Ecodesign, ED-OG-R2).

High-resolution synchrotron X-ray diffraction (XRD) experiments were performed using a monochromated incident beam ($\lambda$ = 0.65297 Å) at the JASRI SPring-8 BLXU15 line, and the obtained profile was analyzed by the Rietveld method using a RIETAN-2000 program. Powder neutron diffraction (ND) experiments were carried out at $\lambda$= 1.82646 Å on a sample powder packed in a vanadium can using the Kinken powder diffractometer, HERMES, installed at JAEA, Tokai. The temperature and field dependence of the magnetization was measured by using a SQUID magnetrometer (Quantum Design, MPMS2) between 5 K and 300 K up to 5 T. $^{57}$Fe Mössbauer measurements were performed in transmission geometry using $^{57}$Co/Rh as a radiation source and α-Fe as a control for velocity calibration and center shift. The collected spectra were computer-fitted using the Lorenzian function.

## 6.3. Results and Discussions

Figure 6.2a shows the room-temperature synchrotron XRD pattern, which suggests a cubic cell of a ~3.97 Å. The sharpness of the signals indicates that the powder is well-crystallized

and chemically homogeneous, and also that the powder remains stable. The Rietveld refinement, assuming cubic perovskite structure (*Pm*-3*m*) as an initial model, quickly converged to small *R* factors with reasonable magnitudes of temperature factor (*B*; Figure 6.2a and Table 6.1). Essentially the same conclusion was obtained from powder ND measurements (Figure 6.2b and Table 6.1). It was also confirmed that the cubic symmetry is preserved to at least 8 K. Since neutrons are sensitive to oxygen, we checked the oxygen content by analyzing the ND data; when allowed to vary, the oxygen site occupancy factor converged to 0.994(7). We thus conclude that BFO is a cubic perovskite that is fully oxidized within experimental error. The Mössbauer spectrum collected at room temperature (Figure 6.3a) is consistent with this conclusion and consists of a sharp singlet signal with a center shift (*CS*) of 0.146 $mms^{-1}$.

Mössbauer measurements also provided firm evidence of magnetic order. A single magnetically split sextet with a hyperfine field (*HF*) of 22.1 T and 29.1 T appears at 77 K (not shown) and 4 K (Figure 6.3b), respectively. Interestingly, application of an external field (*H*) of 0.5 T and above along the g-ray beam changed the relative peak intensity from the normal 3:2:1:1:2:3 to the 3:0:1:1:0:3 pattern (Figure 6.3c) and, at the same time, the *HF* value decreased by the value of *H*. These results clearly indicate the ferromagnetism of BFO. Consistent with this observation, the magnetization (*M*) measured at $H = 0.1$ T on cooling showed a pronounced increase followed by saturation at around 120 K (Figure 6.4a). We have estimated the transition temperature to be 111 K, where the temperature derivative of magnetization shows an anomalous change. The *M*-*H* curve (Figure 6.4b), however, was complex and consisted of a low-field linear part that changed to a high-field ferromagnetic part at approximately 0.3 T at 5 K (ca. 0.2 T at 77 K). A field-induced switching from antiferromagnetism to ferromagnetism was thus suggested. The saturation magnetization

corresponds to a large atomic moment of $3.5\mu_B$ per Fe ion ($3.2\mu_B$ per Fe ion at 77 K), which is consistent with the $Fe^{3+}L$ picture with $S = 2$. The usual Curie–Weiss estimation of the atomic moment in the paramagnetic temperature region failed because the curve of $(M/H)^{-1}$ versus $T$ curve has a nonlinear, concave shape (Figure 6.4a). SFO also behaves similarly although the reason for this is not clear [4].

The spin state at zero field was examined by ND measurements. Figure 6.5a shows the profile around the 100 and 110 reflections between 8 K and 303 K, where weak satellite reflections that indicate the formation of a superstructure with a propagation vector of $\boldsymbol{q}/\boldsymbol{a}^* = [0.06,0,0]$ can clearly be seen. As shown in Figure 6.5b, these peaks disappear at around 110 K, which is close to the temperature of the magnetic transition. On the other hand, the synchrotron XRD pattern at 80 K did not show these additional signals. We thus conclude that BFO is an antiferromagnet with a spiral spin structure of the A type ($\boldsymbol{q}//\boldsymbol{a}$) that shows a field-induced transition to ferromagnetism at approximately 0.3 T at 5 K (0.2 T at 77 K).

The spiral spin order of BFO is somewhat different from that of SFO, as SFO has its propagation vector along the <111> axis, and the Fe (111) layers rotate their spin axis by approximately 46˚ from one layer to another. For BFO, however, the propagation vector is along the <100> direction and the Fe (100) layers rotate the *yz* component of their spin axis by approximately 22˚ from one layer to another. In this respect it may be concluded that BFO is closer to ferromagnetism than SFO. We believe that BFO must "show metallic properties" better but could not confirm it experimentally because well-sintered pellets could not be produced.

The proper screw spin structure of SFO was classically explained based on the RKKY interaction model featuring a ferromagnetic nearest-neighbor interaction ($J_1$ = 1.2 meV) and antiferromagnetic second-nearest and fourth-nearest neighbor interactions ($J_2$ = -0.1 meV, $J_4$

= -0.3 meV) [5]. More recently, Mostovoy [16] proposed another theoretical framework and constructed a phase diagram including various spin structures. The study starts from the ferromagnetic Kondo lattice model involving itinerant electrons of Fe $e_g$ parentage in strongly hybridized $d_\gamma$-$p_\sigma$ orbitals and also localized, spin-polarized $t_{2g}$ electrons. The theoretical consideration was made in terms of p–d charge transfer energy $\Delta$, p–d transfer integral ($pd\sigma$), p–p transfer integral $t_{pp}$, and the superexchange coupling $J$ between the $t_{2g}$ spins. When $J$ is neglected, the ferromagnetic state (FM) and the proper screw spin state with $\boldsymbol{q}$//<111> (A-HM) dominate the phase diagram spanned by $\Delta/(pd\sigma)$ and $t_{pp}/(pd\sigma)$. When $J$ is taken into account, the A-type antiferromagnetic state (A-AFM) and the proper screw spin state with $\boldsymbol{q}$//<111> (G-HM) appear in lower $\Delta/(pd\sigma)$ regions below the A-HM state. Because the cubic lattice constant and hence the Fe–O distance $r$ increase on going from SFO ($r$ = 1.925 Å) to BFO ($r$ = 1.985 Å), the parameters in the model Hamiltonian should change accordingly. According to Harrison's rule [17], $r$ varies according to $(pd\sigma)\propto 1/r^{3.5}$, $t_{pp}\propto 1/r^2$, and $J\propto(pd\sigma)^4\propto 1/r^{14}$, while $\Delta$ changes much less. Therefore, the most remarkable difference between SFO and BFO is that the $J$ value is reduced roughly by a factor of two owing to the lattice expansion; that is, in the theoretical treatment developed by Mostovoy, the shift from the G-HM structure of SFO to the A-type spiral structure and ferromagnetism of BFO may be ascribed to the weakening of the antiferromagnetic interactions between the $t_{2g}$ cores. It is interesting to note here that both lattice compression under external pressure [6] and lattice expansion by chemical substitution lead SFO to ferromagnetism.

Recently, two research groups independently prepared $BaFeO_{3-\delta}$ films on the $SrTiO_3$ (001) substrate, but the results are controversial [18–20]. One research group claimed that their film was highly insulating and ferromagnetic ($T_C$ > 300 K) [18,19], while the other claimed

metallicity and ferromagnetism with $T_C$ ~ 235 K [20]. The observed moments were as small as 0.6 $\mu_B$ per Fe ion. This diversity indicates the necessity of careful control of film quality.

### 6.4. Conclusion

A new cubic $Fe^{4+}$ perovskite, BFO, was prepared by low-temperature oxidation using ozone. This oxide has an A-type spiral spin structure below 111 K, while application of a small external field induces ferromagnetism with a large atomic moment of 3.5$\mu_B$ per Fe ion. BFO is thus the first reported Fe oxide that shows ferromagnetism at ambient pressure.

**References**

[1] U. Buchenau, I. Müller, Solid State Commun. 11 (1972) 1291.

[2] J. B. MacChesney, R. C. Sherwood, and J. F. Potter, J. Chem. Phys. 43 (1965) 1907.

[3] T. Takeda, R. Kanno, Y. Kawamoto, M. Takano, S. Kawasaki, T. Kamiyama, F. Izumi, Solid State Sci. 2 (2000) 673.

[4] T. Takeda, Y. Yamaguchi, N. Watanabe, J. Phys. Soc. Jpn. 33 (1972) 967.

[5] T. Takeda, S. Komura, N. Watanabe, Ferrites, Proceedings of the Third International Conference of Ferrites (ICF3), Kyoto (1980) 385.

[6] T. Kawakami, S. Nasu, J. Phys. Condens. Matter 17 (2005) S789.

[7] I. Yamada, K. Tsuchida, K. Ohgushi, N. Hayashi, J. Kim, N. Tsuji, R. Takahashi, M. Matsushita, N. Nishiyama, T. Inoue, T. Irifune, K. Kato, M. Takata, M. Takano, Angew. Chem. Int. Ed. 50 (2011) 6579.

[8] A. E. Bocquet, A. Fujimori, T. Mizokawa, T. Saitoh, H. Namatame, S. Suga, N. Kimizuka, Y. Takeda, M. Takano, Phys. Rev. B 45 (1992) 1561.

[9] M. Abbate, F. M. F. de Groot, J. C. Fuggle, A. Fujimori, O. Strebel, F. Lopez, M. Domke, G. Kaindl, G. A. Sawatzky, M. Takano, Y. Takeda, H. Eisaki, S. Uchida, Phys. Rev. B 46 (1992) 4511.

[10] N. Hayashi, T. Terashima, M. Takano, J. Mater. Chem. 11 (2001) 2235.

[11] P. M. Woodward, D. E. Cox, E. Moshopoulou, A. W. Sleight, S. Morimoto, Phys. Rev. B 62 (2000) 844.

[12] K. Mori, T. Kamiyama, H. Kobayashi, T. Otomo, K. Nishiyama, M. Sugiyama, K. Itoh, T. Fukunaga, S. Ikeda, J. Appl. Cryst. 40 (2007) s501.

[13] M. Parras, M. Vallet-Regí, J. M. González-Calbet, M. A. Alario-Franco, J. C. Grenier, P. Hagenmuller, Mater. Res. Bull. 22 (1987) 1413.

[14] R. O. Suzuki, T. Ogawa, K. Ono, J. Am. Ceram. Soc. 82 (1999) 2033.

[15] H. Yamamoto, M. Naito, H. Sato, Jpn. J. Appl. Phys. 36 (1997) L341.

[16] M. Mostovoy, Phys. Rev. Lett. 94 (2000) 137205.

[17] W. A. Harrison, Electronic Structure and the Properties of Solids, (1989) Dover: New York.

[18] T. Matsui, H. Tanaka, N. Fujimura, T. Ito, H. Mabuchi, K. Morii, Appl. Phys. Lett. 81 (2002) 2764.

[19] E. Taketani, T. Matsui, N. Fujimura, K. Morii, IEEE Trans. Magn. 40 (2004) 2736.

[20] C. Callender, D. P. Norton, R. Das, A. F. Hebard, J. D. Budai, Appl. Phys. Lett. 92 (2008) 012514.

**Table 6.1.** Structural parameters for $BaFeO_3$.[a]

| atom | site | *x* | *y* | *z* | *B* /Å$^2$ (XRD, RT) | *B* /Å$^2$ (ND, 150K) |
|---|---|---|---|---|---|---|
| Ba | 1*b* | 0.5 | 0.5 | 0.5 | 0.247(5) | 0.19(5) |
| Fe | 1*a* | 0 | 0 | 0 | 0.49(1) | 0.36(3) |
| O | 3*c* | 0.5 | 0 | 0 | 0.73(3) | 0.72(4) |

[a] space group : *Pm*-3*m*, $a$ = 3.97106(1) Å. $R_{wp}$ = 7.01%, $R_I$ = 1.46%, $R_e$ = 0.42%, $R_F$ = 1.34%, $R_p$ = 4.75% for synchrotron XRD at room temperature. $a$ = 3.95435(8) Å. $R_{wp}$ = 6.11%, $R_I$ = 2.58%, $R_e$ = 4.62%, $R_F$ = 1.37%, $R_p$ = 4.80% for ND at 150 K.

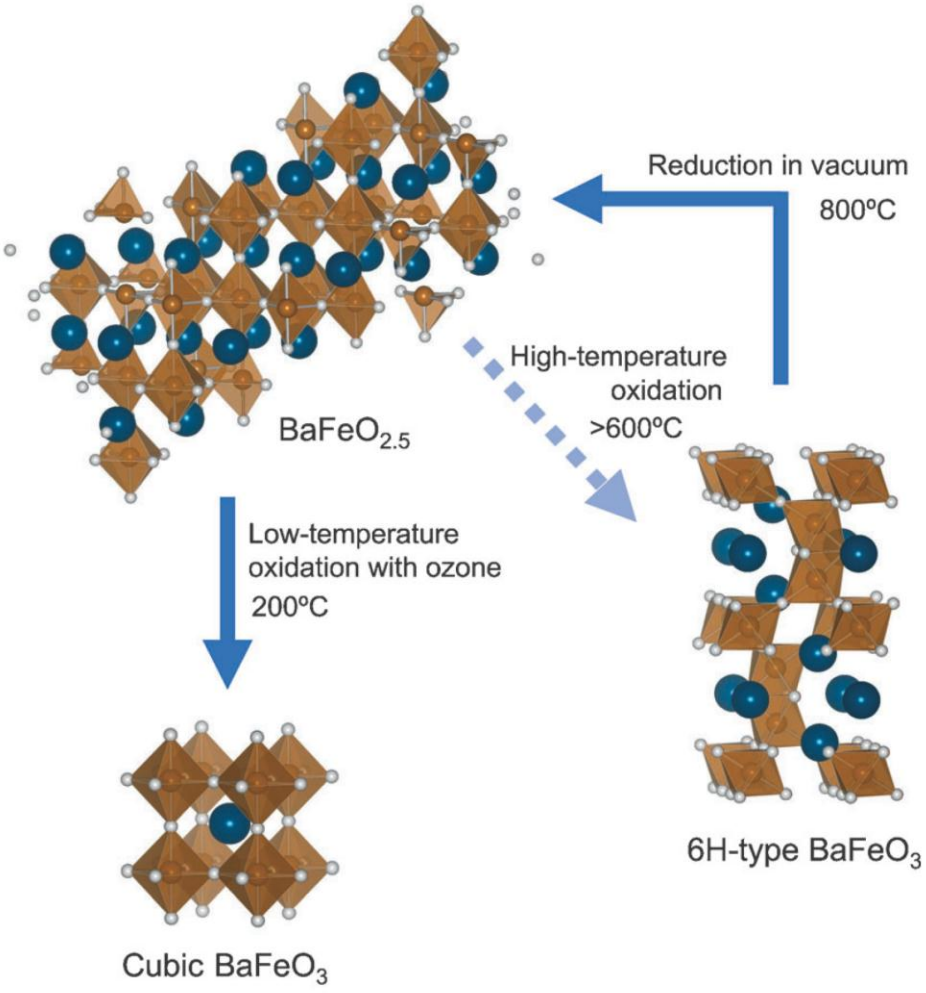


**Figure 6.1.** Synthetic route for cubic $BaFeO_3$. Ba Blue, Fe brown, O white.

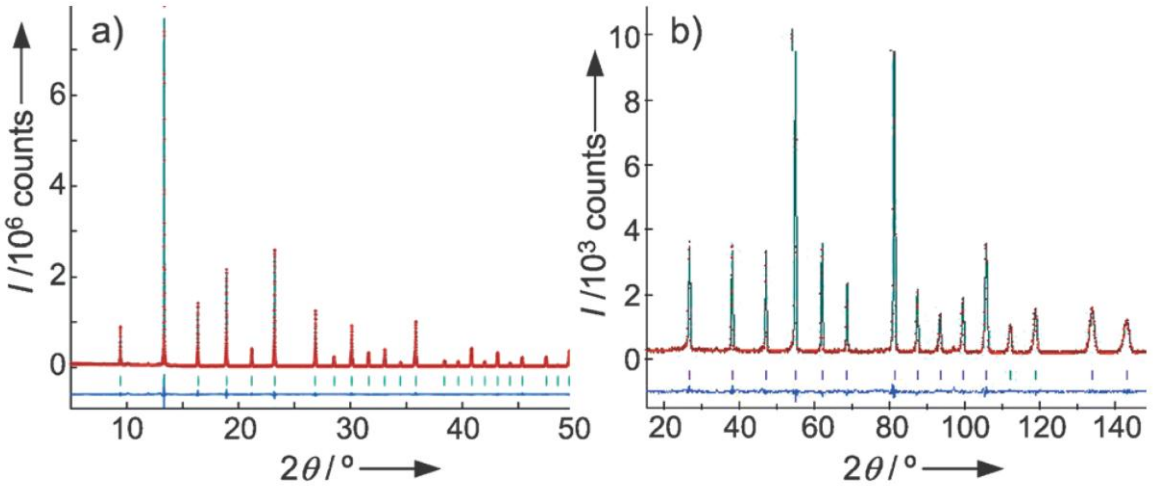


**Figure 6.2.** Synchrotron powder XRD profile taken at room temperature (a) and the powder ND profile taken at 150 K (b) for $BaFeO_3$. The overlying crosses and solid lines represent the observed and calculated intensities, respectively. The solid line at the bottom of the spectrum represents the difference between the observed intensity and the calculated intensity. The ticks indicate the calculated peak positions.

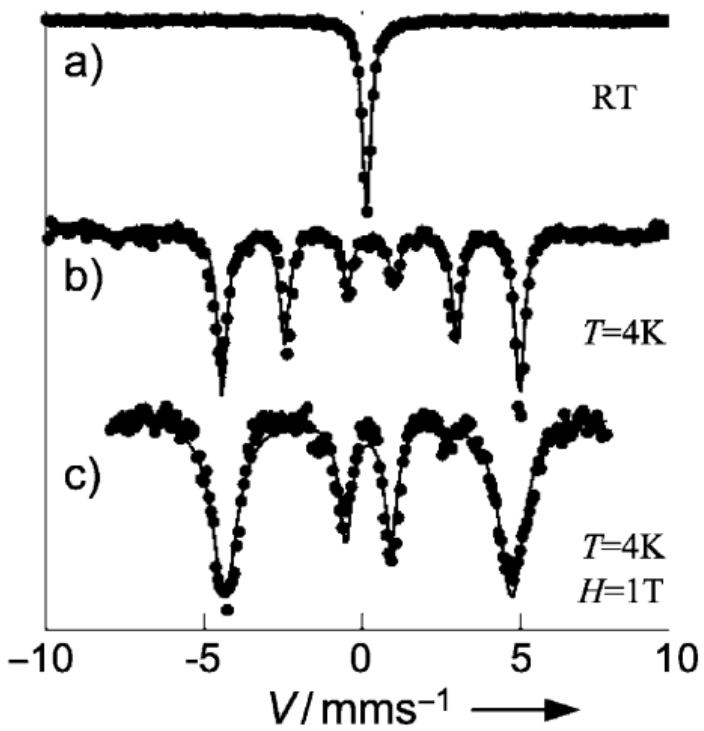


**Figure 6.3.** Mössbauer spectra of $BaFeO_3$ taken at room temperature (a) and 4 K (b). The spectrum (c) was obtained from a sample enriched with $^{57}Fe$ at 4 K in an external field of 1 T applied parallel to the γ-ray beam. The peaks of this spectrum are broadened because of the saturation effect arising from the enrichment. Dotted lines: experimental data points, solid lines: best-fit curves.

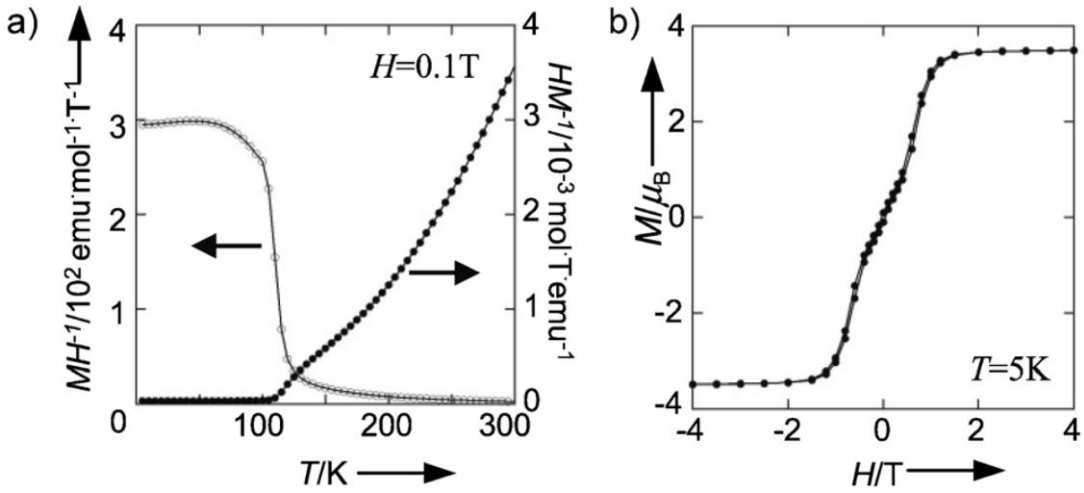


**Figure 6.4.** Temperature dependence of magnetization divided by field *M*/*H*, and its inverse measured at *H* = 0.1 T on cooling (a) and the M-H curve recorded at 5 K (b).

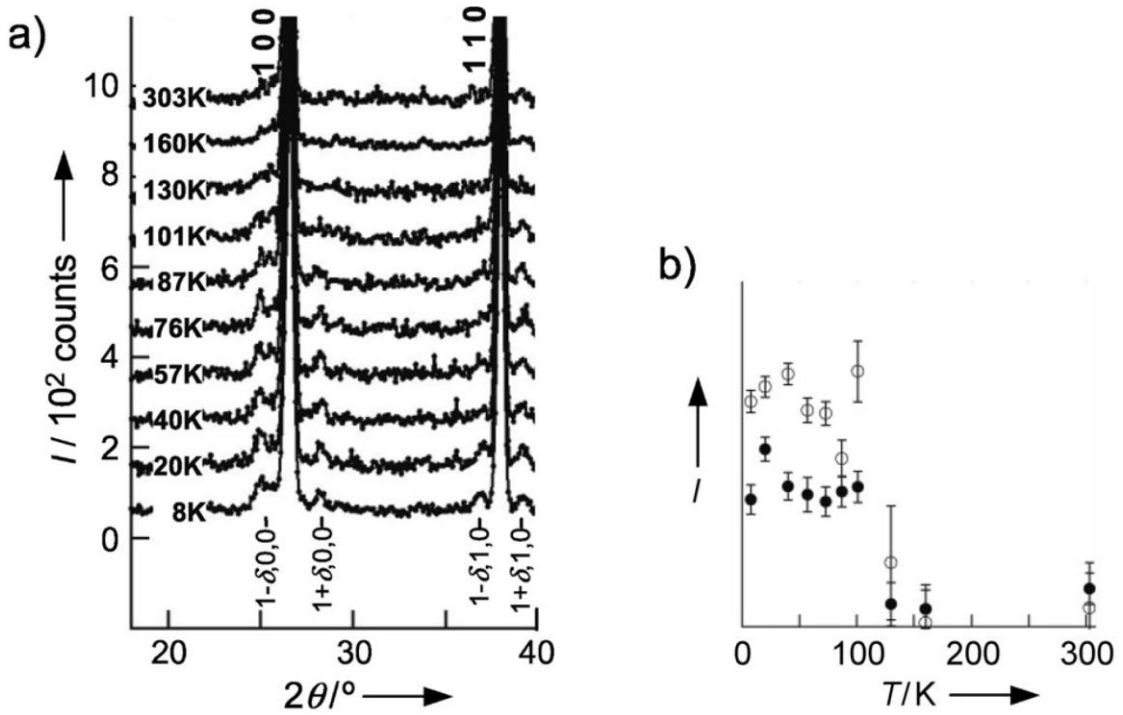


**Figure 6.5.** ND profiles showing satellites in the vicinity of the (100) and (110) peaks (a). Temperature dependences of relative intensity for 1+$\delta$,0,0 (solid circles) and 1+$\delta$,1,0 (open circles) satellite peaks (b).

# *General Conclusion*

This thesis reported the synthesis, structure, and physical properties of novel iron oxides prepared by topotactic reactions. Especially, this thesis focused on the square planar coordinated iron oxides and a perovskite oxide with the high valence state of $Fe^{4+}$.

In Chapter 1, the author demonstrated that $SrFeO_2$ with the IL structure can tolerate only up to 30% substitution of Ba unlike the case of Ca-substitution. The long Fe-O distance caused by the Ba-substitution destabilizes the IL structure. The negative pressure effect does not drastically change the magnetic properties in contrast to the theoretical anticipation, meaning that iron atoms are still very strongly bonded to oxide ion. The oxidation temperature and rate are controllable to a great extent by *A*-site cation size.

In Chapter 2, $(Sr_{1-x}Ba_x)FeO_2$ ($0.4 \leq x \leq 1.0$) with a novel perovskite-related structure was successfully obtained by low temperature topotactic reaction with calcium hydride ($0.4 \leq x \leq 0.9$) and sodium hydride ($x = 1.0$). The new structure is partly analogous to the $LaNiO_{2.5}$ structure with one-dimensional chains of octahedra linked by planar units, but differs in that one of the octahedral sites has a significant amount of oxygen vacancies and that all the iron ions have the same spin and valence state. Unlike recently reported iron oxides with square planar coordination, this structure demonstrates the ability of the iron square planar coordination to coexist with other types of coordination. Thus, it is expected that a large family of square–planar based iron oxides will be prepared in future. The Mössbauer spectra indicate that the Fe(2) and Fe(3) ions have extremely strong covalency, and this may contribute to the formation of the unique structure. At the same time, the rigidity of a 3D Fe-O-Fe connection which consists of [-Fe(1)-O(3)-] along the *c* axis and [-Fe(1)-O(1)-Fe(2)-O(1)-] along the *a*(*b*) axis acts to strengthen the framework. The extreme covalency of planar

coordinate iron and its preferential valence (+2) stabilize this compound as a line phase with a defined composition, despite the presence of structural disorders and partial occupations.

In Chapter 3, the author demonstrated that the A-site substitution in the IL structure $SrFeO_2$ is tolerable up to ca. 30% for all Ln (= Nd, Sm, Eu, Ho). For the Nd, Sm and Ho substitution, an increase of out-of-plane cell parameters is observed, which is explained by an insertion of apical oxygen atoms to compensate for trivalent doping. This compound represents the first example of the IL related structure that oxygen content slightly deviates from 2. On the other hand, $(Sr_{1-x}Eu_x)FeO_2$ adopts an ideal infinite layer structure by forcing the europium ions to be divalent. The Ho-substitution results in a significant reduction of the Néel temperature, while the Eu-substitution has a little influence on the magnetic property. Although this represents a success of heterovalent A-site substitution into square planar iron oxide, we failed to inject carriers into a $FeO_2$ layer, indicating significant stability of a divalent iron in the square-planar-based iron oxide.

In Chapter 4, the author repoted that $Sr_3Fe(II)_2O_5$ exhibits a spin state transition from $S = 2$ to $S = 1$ state at $P_c = 34$ GPa with an AFM-FM transition. Signs suggesting an I-M transition were also observed at pressure around $P_c$. $SrFeO_2$ shows the same behavior, suggesting a general intrinsic character for square planar coordinated iron oxides. The critical pressure $P_c$ is insensitive to the dimensionality, but further studies especially using other systems $Sr_{n+1}Fe_nO_{2n+1}$ are needed to understand the spin-ladder physics for $S = 2$. Most importantly, unlike $SrFeO_2$, we also observed a pressure-induced structural transition at $P_s = 30$ GPa, which involves a change in the stacking sequence of the ladder blocks. The SrO block of the original seven-fold rock-salt structure adopts the eight-fold CsCl structure. This allows an efficient contraction of the volume.

In Chapter 5, the author demonstrated that the intergrowth structures $A_2MO_3$ (A = Sr, Ca; M = Cu, Pd) exhibit a pressure-induced structural transition with the space group changing from *Immm* to *Ammm*, involving change of the structure of AO block from rock salt structure to CsCl structure. Together with $Sr_3Fe_2O_5$, the present study demonstrates the generality of the *B*1-to-*B*2 structural transition in the intergrowth structure of $(AO)(AMO_2)_n$ ($n$ = 1, 2, 3…). It is remarkable that the critical pressures $P_s$ for the intergrowth compounds are determined solely by $R_A/R_O$, showing quantitatively the same trend as the binary AO compounds, which make it possible to predict $P_s$ of other related compounds. Given the *B*1-to-*B*2 structural transition in binary chalcogenides, the rock-salt/ladder intergrowth chalcogenides may also exhibit the *B*1-to-*B*2 structural transition with $P_s$ scaled by $R_A/R_S$, $R_A/R_{Se}$, and $R_A/R_{Te}$. Introduction of oxygen atom at the apical site leads to a significantly deviation from the $P_s$ vs $R_A/R_O$ relation. It is expected that the high pressure structures consisting of "quasi" infinite layers have different electronic structures due to inter-ladder(chain) interaction within the layer, leading to new or improved chemical and physical properties.

In Chapter 6, a new cubic $Fe^{4+}$ perovskite, $BaFeO_3$, was prepared by low-temperature oxidation using ozone. This oxide has an A-type spiral spin structure below 111 K, while application of a small external field induces ferromagnetism with a large atomic moment of $3.5\mu_B$ per Fe ion. $BaFeO_3$ is thus the first reported Fe oxide that shows ferromagnetism at ambient pressure.

# *List of Pablications*

Chapter 1.

**Synthesis and Thermal Stability of the Solid Solution $A$FeO$_2$ ($A$ = Ba, Sr, Ca)**

Takafumi Yamamoto, Zhafei Li, Cédric Tassel, Naoaki Hayashi, Mikio Takano, Masahiko Isobe, Yutaka Ueda, Kenji Ohoyama, Kazuyoshi Yoshimura, Yoji Kobayashi, and Hiroshi Kageyama

*Inorganic Chemistry* 49 (2010) 5957-5962.

Chapter 2.

**(Sr$_{1-x}$Ba$_x$)FeO$_2$ ($0.4 \leq x \leq 1$): a New Oxygen-Deficient Perovskite Structure**

Takafumi Yamamoto, Yoji Kobayashi, Naoaki Hayashi, Cédric Tassel, Takashi Saito, Shoji Yamanaka, Mikio Takano, Kenji Ohoyama, Yuichi Shimakawa, Kazuyoshi Yoshimura, and Hiroshi Kageyama

*Journal of the American Chemical Society* 134 (2012) 11444–11454.

Chapter 3.

**An Infinite Layer Structure with Partially Filled Apical Oxygen**

Takafumi Yamamoto, Cédric Tassel, Naoaki Hayashi, Yoji Kobayashi, Hiroshi Ohkubo, Shota Kawasaki, Yoshitaka Matsushita, James Hester, Maxim Avdeev, Mikio Takano, and Hiroshi Kageyama

*in preparation.*

Chapter 4.

**Pressure-Induced Structural, Magnetic, and Transport Transitions in the Two-Legged Ladder $Sr_3Fe_2O_5$**

Takafumi Yamamoto, Cédric Tassel, Yoji Kobayashi, Takateru Kawakami, Taku Okada, Takehiko Yagi, Hideto Yoshida, Takanori Kamatani, Yoshitaka Watanabe, Takumi Kikegawa, Mikio Takano, Kazuyoshi Yoshimura, and Hiroshi Kageyama

*Journal of the American Chemical Society* 133 (2011) 6036–6043.

Chapter 5.

**B1-to-B2 Structural Transitions in Rock Salt Intergrowth Structures**

Takafumi Yamamoto, Yoji Kobayashi, Taku Okada, Takehiko Yagi, Takateru Kawakami, Cédric Tassel, Shota Kawasaki, Naoyuki Abe, Ken Niwa, Takumi Kikegawa, Naohisa Hirao, Mikio Takano, and Hiroshi Kageyama

*Inorganic Chemistry* 50 (2011) 11787-11794.

Chapter 6.

**$BaFeO_3$: A Ferromagnetic Iron Oxide**

Naoaki Hayashi, Takafumi Yamamoto, Hiroshi Kageyama, Masakazu Nishi, Yoshitaka Watanabe, Takateru Kawakami,Yoshitaka Matsushita, Atsushi Fujimori, and Mikio Takano

*Angewandte Chemie International Edition* 50 (2011) 12547-12550.

*The following papars are not included in this thesis*

**Oxyhydrides of (Ca,Sr,Ba)$TiO_3$ perovskite solid solution**

Tatsunori Sakaguchi, Yoji Kobayashi, Takeshi Yajima, Masatoshi Ohkura, Cédric Tassel, Fumitaka Takeiri, Shingo Mitsuoka, Hiroshi Ohkubo, Takafumi Yamamoto, Jungeun Kim, Naruki Tsuji, Akihiko Fujihara, Yoshitaka Matsushita, James Hester, Maxim Andeev, Kenji Ohoyama, and Hiroshi Kageyama
*submitted for publication.*

**Quadruple-layered perovskite (CuCl)$Ca_2NaNb_4O_{13}$**

Atsushi Kitada, Yoshihiro Tsujimoto, Takafumi Yamamoto, Yoji Kobayashi, Yasuo Narumi, Koichi Kindo, Adam A. Aczel, Greame M. Luke, Yasutomo J. Uemura, Yoko Kikuchi, Yutaka Ueda, Kazuyoshi Yoshimura, Yoshitami Ajiro, and Hiroshi Kageyama
*Journal of Solid State Chemistry* 185 (2012) 10-17.

**Fe-Site Substitution Effect on the Structural and Magnetic Properties in $SrFeO_2$**

Liis Seinberg, Takafumi Yamamoto, Cédric Tassel, Naoaki Hayashi, Atsushi Kitada, Yuji Sumida, Takashi Watanabe, Masakazu Nishi, Kenji Ohoyama, Kazuyoshi Yoshimura, Mikio Takano, Waner Paulus, and Hiroshi Kageyama
*Inorganic Chemistry* 50 (2011) 3988-3995.

**Random fan-out state induced by site-random interlayer couplings**

Ryo Tamura, Naoki Kawashima, Takafumi Yamamoto, Cédric Tassel, and Hiroshi Kageyama
*Physical Review B* 84 (2011) 214408.

**Superconducting state coexisting with a phase-separated static magnetic order in $(Ba,K)Fe_2As_2$ ,$(Sr,Na)Fe_2As_2$ , and $CaFe_2As_2$**

Tatsuo Goko, Adam A. Aczel, Elisa Baggio-Saitovitch, Sergey L. Bud'ko, Paul C. Canfield, Jeremy P. Carlo, Gen-Fu Chen, Pengcheng Dai, Andreas C. Hamann, Wan-Zheng Hu, Hiroshi Kageyama, Greame M. Luke, Jian-Lin Luo, Benjamin Nachumi, Ni Ni, Dmitry Reznik, Dalber R. Sanchez-Candela, Andrei T. Savici, Kenneth J. Sikes, Nan-Lin Wang, Christopher R. Wiebe, Travis J. Williams, Takafumi Yamamoto, Weiqiang Yu, and Yasutomo J. Uemura
*Physical Review B* 80 (2009) 024508.

**Muon spin relaxation studies of the frustrated quasi-two-dimensional square-lattice spin system $Cu(Cl,Br)La(Nb,Ta)_2O_7$ : Evolution from spin-gap to antiferromagnetic state**

Yasutomo J. Uemura, Adam A. Aczel, Jeremy P. Carlo, Tatsuo Goko, Dorian A. Goldfeld, Atsushi Kitada, Greame M. Luke, Greg J. MacDougall, Ion G. Mihailescu, Jose A. Rodriguez, Peter L. Russo, Yoshihiro Tsujimoto, Christopher R. Wiebe, Travis J. Williams, Takafumi Yamamoto, Kazuyoshi Yoshimura, and Hiroshi Kageyama
*Physical Review B* 80 (2009) 174408.

**Synthesis, structure, and magnetic properties of the two-dimensional quantum antiferromagnets $(CuBr)A_2B_3O_{10}$ (A=Ca, Sr, Ba, Pb; B=Nb, Ta) with the 1/3 magnetization plateau**

Yoshihiro Tsujimoto, Hiroshi Kageyama, Yoichi Baba, Takafumi Yamamoto, Yasuo Narumi, Koichi Kindo, Masakazu Nishi, Jeremy P. Carlo, Adam A. Aczel, Travis J. Williams, Greame M. Luke, Yasutomo J. Uemura, Yutaka Ueda, Yoshitami Ajiro, and Kazuyoshi Yoshimura

*Physical Review B* 78 (2008) 214410.

**Stability of the Infinite Layer Structure with Iron Square Planar Coordination**

Cédric Tassel, Takashi Watanabe, Yoshihiro Tujimoto, Naoaki Hayashi, Atsushi Kitada, Yuji Sumida, Takafumi Yamamoto, Hiroshi Kageyama, Mikio Takano, and Kazuyoshi Yoshimura

*Journal of the American Chemical Society* 130 (2008) 3764-3765.

# *Acknowledgement*

This thesis summarizes the author's studies at Kageyama Laboratory, the Department of Energy and Hydrocarbon Chemistry, Graduate School of Engineering, Kyoto University.

The author wishes to express his greatest gratitude to Professor Hiroshi Kageyama for his invaluable advises and suggestions throughout the course of this work. The author is also grateful to Professor Ryu Abe and Professor Katsuhisa Tanaka for their kind guidance and comments.

The author is also grateful to Professor Mikio Takano, Professor Yuich Shimakawa, Professor Kazuyoshi Yoshimura, Professor Yoshitami Ajiro (Kyoto University), Professor Takehiko Yagi, Professor Yutaka Ueda, Professor Atsushi Fujimori (University of Tokyo), Professor Shoji Yamanaka (Hiroshima University), for their kind guidance and comments.

The author would like to express his gratitude to Dr. Yoji Kobayashi, Dr. Naoaki Hayashi, Dr. Cédric Tassel, Dr. Takeshi Yajima, Dr. Atsushi Kitada, Dr. Takashi Saito (Kyoto University), Dr. Takateru Kawakami (Nihon University), Dr. Taku Okada, Dr. Masahiko Isobe, Dr. Masakazu Nishi (Tokyo University), Dr. Yoshihiro Tsujimoto, Dr. Yoshitaka Matsushita (National Institute of Material Science (NIMS)), Dr. Kenji Ohoyama (Tohoku University), Dr. Takumi Kikegawa (High Energy Acceleration Research Organization (KEK)), Dr. Naohisa Hirao (Japan Synchrotron Radiation Research Institute (JASRI)), Dr. Ken Niwa (Nagoya University), Dr. James Hester, Dr. Maxim Avdeev (Australian Nuclear Science and Technology Organisation (ANSTO), Dr. Zhafei Li for their valuable discussions and supports.

Sincere guidance is also expressed to all the members of the Professor Hiroshi Kageyama's Laboratory for their kind encouragements, supports, and collaborations. A

special debt of gratitude goes to coauthors in the author's publications: Dr. Subodh Ganesan Potti, Mr. Yoichi Baba, Mr. Takashi Watanabe, Mr. Yuji sumida, Ms. Liis Seinberg, Mr. Tatsunori Sakaguchi, Mr. Naoyuki Abe, Mr. Hiroshi Ohokubo, Mr. Shota Kawasaki, Mr. Masatoshi Ohokura, Mr. Fumitaka Takeiri, Mr. Shingo Mitsuoka.

The author would like to thank for financial support from Japan Society of the Promotion of Science (JSPS) for Young Scientists.

Finally, the author would like to thank his family immensely, particularly, his parents Noboru and Chikako Yamamoto, for their understanding, supports, and encouragement.

*Takafumi Yamamoto*

2012